THE UNIVERSITY
of ADELAIDE

Faculty of Sciences
School of Physical Sciences
Department of Physics

Transverse Properties of Baryons using Lattice Quantum Chromodynamics

Jacob M. Bickerton

Supervisors:
A. Prof. Ross Young
A. Prof. James Zanotti

August 2020

Abstract

Utilising lattice Quantum Chromodynamics (QCD) to calculate nucleon matrix elements allows us to gain great insight into the internal structure of baryons that would be prohibitively difficult to access in physical experiments. We can extract the electromagnetic and tensor form factors for not only the proton but also the heavier octet baryons, including the sigma Σ and cascade Ξ baryons. By utilising the properties of SU(3) flavour breaking in a new method only recently published, we extrapolate our electromagnetic and tensor form factors to the physical point.

We also investigate the transverse spin-dependent quark densities and how the choice of baryon spin and quark spin polarisation affects the distribution of quarks in a plane transverse to the baryon's momentum. Presenting the first lattice calculation extrapolated to the physical point, we compare the proton to those in the heavier octet baryons. These densities show interesting distortions that occur when the quark spin and baryon spin polarisation are both aligned or anti-aligned and shows the dominance of the baryon spin when determining the quark distribution inside the baryon.

Following a similar procedure to the transverse spin density, we analyse the transverse 'colour' Lorentz force acting on a struck quark in deep inelastic scattering experiments. Understanding the distribution of these forces could offer a significant conceptual advance in the understanding of the force mechanisms underlying confinement in QCD.

Declaration

I certify that this work contains no material which has been accepted for the award of any other degree or diploma in my name, in any university or other tertiary institution and, to the best of my knowledge and belief, contains no material previously published or written by another person, except where due reference has been made in the text. In addition, I certify that no part of this work will, in the future, be used in a submission in my name, for any other degree or diploma in any university or other tertiary institution without the prior approval of the University of Adelaide and where applicable, any partner institution responsible for the joint-award of this degree. I give permission for the digital version of my thesis to be made available on the web, via the University's digital research repository, the Library Search and also through web search engines, unless permission has been granted by the University to restrict access for a period of time. I acknowledge the support I have received for my research through the provision of an Australian Government Research Training Program Scholarship.

Jacob M. Bickerton

Contents

Chapter 1

Introduction

Our understanding of modern particle physics has given us insight into the sub-atomic world, including the particles that exist in this space and the corresponding interactions between them, with the ultimate goal being a unified model to map such particles and their interactions. One of the most important theories postulated in modern physics is the Standard Model (SM), which provides a unified theory of the electromagnetic, weak and strong interactions between fundamental particles.

Quantum Chromodynamics (QCD) is the field theory describing the strong interactions, with an unbroken symmetry group, SU(3), associated with the 'colour' charge of the massless gauge bosons of the theory, gluons, and of the fundamental spin-$\frac{1}{2}$ spinor fields, named quarks, which are bound together to form hadrons such as the protons and neutrons, alongside more exotic matter. Prominent in QCD is asymptotic freedom, which states that the strength of the interaction of the particles of the theory, quarks and gluons, becomes weaker at higher energies until the particles can be treated as quasi-free. Conversely, at very small energy scales, colour confinement occurs that makes it impossible to find free quarks or gluons. For the low energy regime we are interested in, we must employ non-perturbative methods to calculate the QCD spectrum or hadron matrix elements.

Lattice QCD is a non-perturbative tool that has been developed over the past forty years, that allows for first principle calculations of low energy hadronic quantities, by calculating path integrals on a finite-volume discretised lattice of points, approximating space-time. On this lattice, a discrete version of the QCD action is developed, which allows for large-scale computer simulations, with the outcome of numerical results of physical observables. Lattice QCD has been able to provide remarkably precise measurements of these low energy quantities. Discretising space-time and calculating observables comes with its own systematics that need to be taken into consideration, with high computational expenses at low quark masses in the physical regime and divergent effects that arise from the discretisation of the action, requiring renormalisation.

1. INTRODUCTION

The quarks defined in QCD come in six 'flavours', which are found to have significantly different masses in certain cases. The Lie SU(3) group plays a role here as an approximate symmetry of the three lightest flavours of quarks: the 'up', 'down' (collectively 'light') and 'strange' quarks. This symmetry is broken due to the mass splittings between these quarks. The effects of flavour symmetry breaking are of great theoretical interest, and one of our aims is to utilise this effect on the matrix elements of octet hyperons (baryons containing the strange quarks) in order to develop new methods of overcoming the computational expense of physical mass quark calculations.

In this thesis, we will apply lattice QCD to investigate the inner structure of hadrons. More precisely, we compute matrix elements that are related to the probability densities of quarks inside baryons. While the global features like charge, spin and isospin are well known, there is still little known about their internal structure because of the aforementioned confining nature of QCD. A detailed description of the internal structure of hadrons in terms of the quarks and gluons can be obtained from generalised parton distributions (GPDs). These generalised distributions have over the years become a powerful tool leading to many new observations, including the transverse quark spin distribution inside hadrons.

To this day the transverse spin structure of quarks in the proton is an intriguing and relatively unknown aspect of baryon structure, and provides a unique perspective on the structure of a hadron. We are able to access this spin structure through lattice QCD and the calculation of the electromagnetic and tensor form factors of the octet baryons as the lowest x moment of the GPDs.

While twist-2 GPDs allow for a determination of the distribution of partons on the transverse plane, the twist-3 GPDs contain quark-gluon correlations that provide information about the distribution of average transverse colour Lorentz force acting on quarks across the proton. These two transverse properties greatly expand our understanding of the internal structure of hadrons and the distribution of quarks and forces within the octet baryons.

Outline of this work

We begin with Chapter 2 as an opportunity to introduce some of the fundamental theories that will be used through out this thesis, beginning with an outline of the Standard Model and its relevance in our understanding of the quarks and the gauge bosons. Following on from this we introduce the processes and challenges of QCD and its mathematical formulation. We then seek to introduce the phenomenological processes behind elastic scattering and deep inelastic scattering (DIS) experiments, and how these processes lead to a deeper understanding of the internal structure of matter through form factors and structure functions.

In Chapter 3, we introduce the non-perturbative numerical technique known as 'lattice QCD'. This method involves looking into the fermion and gauge components of the QCD action introduced in Chapter 2, and the necessary steps to discretise space-time and momentum. We move on to constructing the necessary two-point and three-point correlation functions that are vital to determining the matrix elements relevant for determining the form factors of interest. We briefly discuss the systematics of our computational simulations and the benefits and challenges we face when using the lattice QCD method.

Following on in Chapter 4, we give a more in-depth look into the form factors, and the information we can derive from their calculation. Using the matrix elements discussed in the previous chapter, we demonstrate our method of calculating the electromagnetic and tensor form factors. We provide an updated lattice calculation of these form factors with a new determination of the tensor form factors, and compare the proton with heavier octet baryons while hinting at how we will later use and improve upon our determination of these form factors.

In Chapter 5, in order to remove additional divergences that arise during the discretisation of the action when using lattice QCD, we look to using the Regularisation Independent Momentum (RI'-MOM) renormalisation scheme and later a conversion to the more widely adapted Modified Minimal Subtraction ($\overline{\text{MS}}$) scheme. We show the method and the work done in order to calculate the multiplicative renormalisation constants for a variety of operators across a large number of lattice volumes, spacings and quark mass configurations.

In the next Chapter 6, we investigate the properties of SU(3) flavour symmetry breaking with the aim of extrapolating our results to the physical quark mass, and so introduce an extended method to include hadronic matrix elements. Using the unique properties that come about from the construction of our lattice, where the singlet mass is held constant along a mass trajectory, we find the mass expansion of the matrix elements to be highly constrained. This property provides the opportunity for extrapolation to the physical point of our matrix elements, and hence form factor calculations. The work in this chapter has already appeared in a published form [1] only recently, with additional tensor form factor results presented for the first time in this thesis.

We use the form factors extrapolated to the physical point in Chapter 6 in order to investigate the transverse spin structure of the octet baryons in Chapter 7. In this chapter we will be looking at transverse spin density contour plots that allow us to investigate the internal structure of the baryons with the transverse spin polarisation for both quarks and the baryons chosen independently. This entails looking for correlations between the quark and baryon spin, and the position of the quark in the transverse plane with respect to the spin polarisations. These densities show the interesting effects that

occur when the quark spin and baryon spin polarisation are both aligned or anti-aligned and shows the dominance of the baryon spin when determining the quark distribution inside the baryon.

Finally in Chapter 8, we look into the twist-3 component of the second moment of the g_2 structure function, d_2. This matrix element has the semi-classical interpretation as the average colour Lorentz force acting on the quark structure in DIS, the instant after being hit by a virtual photon. This then motivates us to calculate the off-forward matrix elements of d_2, in order to construct a form factor describing this force. We can then follow the procedure used in Chapter 7, in order to view the transverse 'force' form factors for the first time. Calculating and understanding these 'force' form factors can lead to a significant conceptual advance in our understanding of the force mechanisms underlying confinement in QCD.

We finish with concluding remarks in Chapter 9.

Chapter 2

Quantum Chromodynamics

In this chapter we will be giving a brief introduction to some of the important theories required to set the stage for work done in later chapters. We will begin with an introduction to the Standard Model and its relevance in our understanding of the quarks and bosons. Following this we briefly introduce the theory of Quantum Chromodynamics (QCD) and its mathematical formulation which is important in understanding the reasoning and limitations behind our computational simulation technique, lattice QCD, which we go on to explain in Chapter 3. We then seek to discuss two phenomenological processes and the part QCD has to play in describing them, with elastic scattering giving rise to form factors discussed further in Chapter 4, and in-elastic scattering providing the structure functions discussed in more depth in Chapter 8.

The Standard Model (SM) is one of the most important theories postulated in modern physics, describing electromagnetism and both the strong and weak nuclear forces, three quarters of the fundamental forces. The SM has lead to predictions of the existence of the $W^{\pm}$ and Z^0 bosons, and the top and charm quarks, long before being experimentally proven and has survived countless challenges from experimental results. With the confirmation of the Higgs boson [2, 3], all of the elementary particles predicted in the Standard Model have been experimentally observed.

The theory explains how all atoms are constructed of the fundamental quarks, leptons and gluons, with the three generations of quark flavours split into pairs, with the lightest being the up and down flavour quarks, the heavier strange and charm pair, and finally the top and bottom flavour pair as the heaviest. Similar to the quarks, we have leptons paired into generations with the electron and corresponding electron neutrino, the muon and muon neutrino, and finally tau and tau neutrino. The interaction of these particles is through the exchange of spin-one gauge bosons, where these arise as a consequence of a local gauge symmetry of $SU(3)_{\text{colour}} \times SU(2)_{\text{weak isospin}} \times U(1)_{\text{weak hypercharge}}$. The electromagnetic force is facilitated by the charge neutral massless photon, while the weak nuclear force is mediated by the massive charged and neutral weak bosons

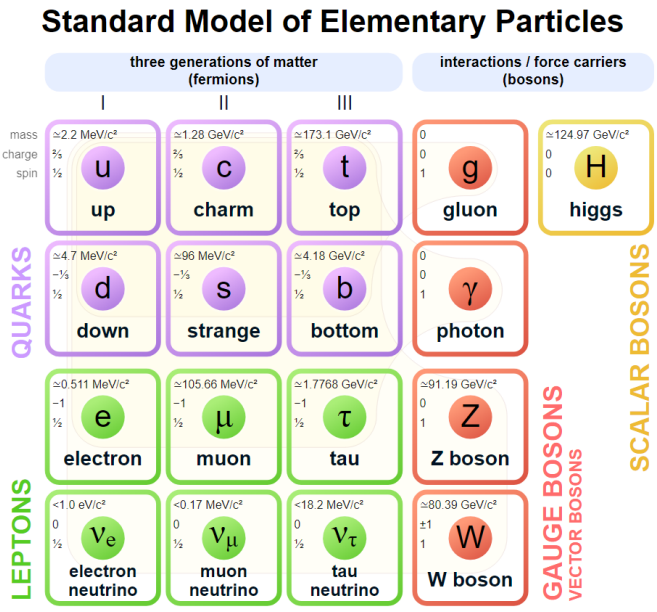

Figure 2.1: Elementary particles of the Standard Model. Showing each generation of quark and lepton pairs, with their mass, charge and spin. Figure from [4].

($W^{\pm}$ and Z^0) and the strong nuclear force by a set of 8 gluons. These quarks, leptons and Z and W bosons couple with the Higgs field to gain mass, the excitations of which display the last boson described by SM, the spin-zero Higgs boson. These Elementary SM particles are summarised in Fig. 2.1.

With our interest in investigating the internal structure of the nucleon, we focus on the theory of Quantum Chromodynamics (QCD) and the relevant interactions for baryons. We begin our discussion considering the three lightest quark flavours (up, down and strange), we find the baryons, which are comprised of three quarks, can be identified as belonging to either the decuplet, octet or singlet irreducible representations of $SU(3)$:

$$3 \otimes 3 \otimes 3 \rightarrow 10 \oplus 8 \oplus 8 \oplus 1 \tag{2.1}$$

In this case, for the proton and neutron, which correspond to a spin-$\frac{1}{2}$ particle, with hyper charge of $Y = 2(Q - I_3) = 1$, with electric charge $Q = +1$ and 0, and iso-spin $I_3 = \frac{1}{2}(n_u - n_d)$, defined as the number of up and down quarks, n_u and n_d respectively. The only possible combination of quarks to produce these quantum numbers are u, u, d and d, d, u for the proton and neutron. We then must introduce a 'colour' charge into our theory to account for the discovery of the $\Delta^{++}(uuu)$ particle with three up quarks all spin-up, which should not be allowed due to the Pauli exclusion theory. We do this by simply attaching a colour $SU_c(3)$ charge to our quarks, but since all observed objects are 'colour neutral' with this colour charge never observed, we must then assume that

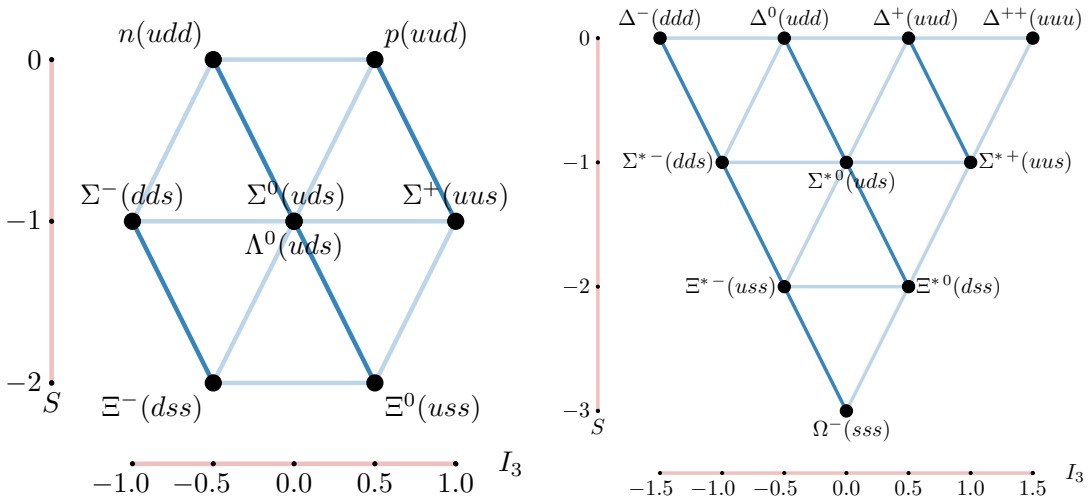

Figure 2.2: Diagram of the Octet (left) and Decuplet (right) multiplets for the spin $\frac{1}{2}$ and $\frac{3}{2}$ baryons. The horizontal axes shows Iso-spin I_3, the vertical axes shows Strangeness S, and the diagonal lines depict electric charge Q.

we only find hadrons containing three colour charges anti-symmetrised to form a colour singlet, or mesons with a colour charged quark and a colour anti-charged anti-quark.

In Fig. 2.2 we show the octet and decuplet baryon multiplets broken down in eq. 2.1. These plots show the 3$^{\text{rd}}$ component of Iso-spin (I_3) along the horizontal axis, and the strangeness (S) in the baryons along the vertical axis. The electric charge (Q) of the baryons is aligned along the diagonal axes. In this work, we will focus primarily on the Octet baryons, with specific focus on the proton p and the hyperons, sigma plus Σ^+ and the cascade zero Ξ^0.

The theory of Quantum Chromodynamics describes all the strong-interaction physics at all distance scales. Using the particles described above, we can begin to describe how the quarks and gluons interact through a non-Abelian gauge field theory, where this diverse physics is encapsulated in the Lagrangian of QCD, which despite it's apparently simple form poses tremendous theoretical challenges when it comes to deriving the physical dynamics of a system. In the next section, we will look at the mathematical formulation of the Lagrangian, and how we can use it to calculate the physical processes we are interested in.

2.1 Mathematical Formulation

The theory of Quantum Chromodynamics describes the strong interactions in physics at every energy scale, from high energy particle collisions, to the low energy regime where gluons and quarks bind together to form hadrons, as well as heavy matter decays and properties of matter in extreme conditions. These physical situations are all described by the Lagrangian of QCD, which is fully constrained by renormalisability, and invariance under the local $SU(3)$ gauge transformations of

$$\psi(x) \to \psi'(x) = U(x)\psi(x), \tag{2.2}$$

$$A_\mu(x) \to A'_\mu(x) = U(x)A_\mu(x)U^{-1}(x) + \frac{i}{g}(\partial_\mu U(x))U^{-1}(x), \tag{2.3}$$

where $U(x) = \exp(i\phi^a(x)t^a)$ defines an independent SU(3) transformation at every point in space-time. The Lagrangian that describes these gauge field interactions is:

$$\mathcal{L}_{QCD} = \sum_q \overline{\psi}^i_q (i\gamma^\mu D^{ij}_\mu - \delta^{ij} m_q)\psi^j_q - \frac{1}{4}F^{(a)}_{\mu\nu}F^{(a)\mu\nu} \tag{2.4}$$

$$= \overline{\psi}(i\not{D} - M_q)\psi - \frac{1}{4}F_{\mu\nu}F^{\mu\nu} \tag{2.5}$$

where the second line shows the simplified notation where the colour indices i, j, the flavour labels $q = u, d, s$ and the $SU(3)$ adjoint representation indices (a) are suppressed. We see the vector nature of the strong force in the form of the γ_μ with Lorentz index μ, and our non-zero quark masses on the diagonals of $M_q = diag(m_u, m_d, m_s, ...)$. The theory is based on the non-Abelian, compact and simple Lie group $SU(3)$, which we represent by a group of 3×3 complex unitary matrices with a unit determinant. QCD is a gauge field theory describing the interactions between these 'colour' charged particles, thus we find the gluon field A_μ correpsonds to the (spin-1) gauge bosons and denote quark fields ψ, describing spin-$\frac{1}{2}$ fermions that carry colour and flavour labels. Quarks transform in the fundamental representation where the dimension is the degree of the group, $N = 3$ for SU(3), and so the quarks form colour triplets. Through QCD, the covariant derivative allows the coupling of the quarks to the gluons through a coupling g, where the covariant derivative D^{ij}_μ is defined as:

$$D^{ij}_\mu = \delta^{ij}\partial_\mu - igt^{ij}_a A^a_\mu \tag{2.6}$$

where $t_a = \lambda_a/2$ where the $\lambda_a, a = 1, 2, 3, ..., 8$ are the Gell-Mann matrices with $\mathrm{Tr}(\lambda_a\lambda_b) = \delta_{ab}$ defined in Appendix C. The non-Abelian gluon field strength tensor is

$$F^{(a)}_{\mu\nu} = \partial_\mu A^a_\nu - \partial_\nu A^a_\mu + g f_{abc} A^b_\mu A^c_\nu \tag{2.7}$$

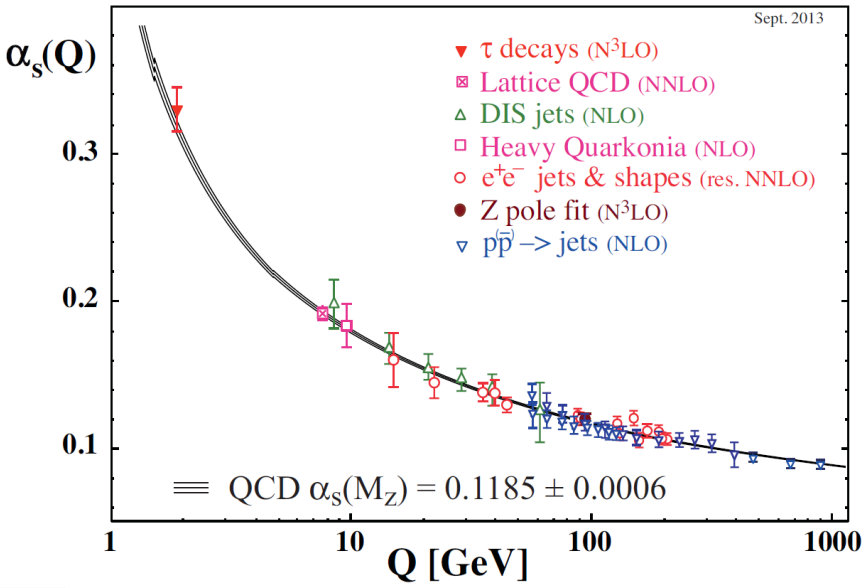

Figure 2.3: Running of the effective strong coupling α_s as a function of the energy scale Q from experimental results. Figure from [5].

with structure constants from the SU(3) Lie group. Since we find a non-linear term in the gauge fields $f_{abc}A^b_\mu A^c_\nu$, we find that the kinetic energy of the gluons generate self interactions between three or four gluons. It is these gluon self interactions which generate many of the interesting features in QCD.

As a result of these gluon self interactions, the QCD coupling $\alpha_s = g^2/4\pi$ becomes very small at high energies, thus allowing high-energy QCD to become almost a theory of free partons that only interact with small quantum corrections, and as a result allows us to use perturbative methods to calculate them. However at lower energies the coupling term becomes much stronger and free quarks are never observed, instead quarks are strongly-bound into colour-singlet hadrons. This phenomenon is termed confinement, where the force between two colour charges doesn't diminish as the distance between them increases. In Fig. 2.3, we show the QCD coupling α_s as a function of the energy scale Q. The asymptotic freedom of the QCD theory is where high-energy reactions allow perturbative methods to be used at small distance scales, but low energy reactions employ strong QCD interactions and thus perturbation theory is not applicable. To work at low-energy requires numerically discretising the QCD equations using a non-perturbative method Lattice QCD, which we will investigate in detail in Chapter 3.

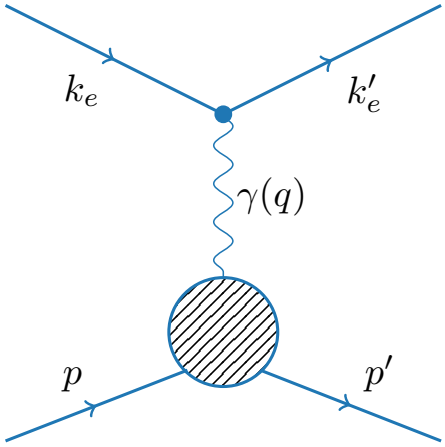

Figure 2.4: Figure showing the electron-nucleon interaction with initial momenta p and k_e and final momenta $p'$and k'_e respectively.

2.2 Form Factors

Elastic electron-nucleon scattering is an experiment that has been studied extensively, where electrons are scattered elastically off a nucleon. These experiments allow the probing of the spatial, charge and magnetisation densities through the measurement of the electromagnetic form factors [6]. With the first studies into the proton and neutron back in the 1950's [7, 8], even to this day, there is still much we have left to uncover from determinations of these form factors [9]. With the increased precision of many modern experimental determinations of the form factors [10–13], in order to match this there have been many low-energy calculations using the non-perturbative method lattice QCD [14–30].

During the process of elastic scattering, as depicted in Fig. 2.4, an electron with initial momentum k_e elastically scatters with a nucleon at initial momentum p, with a momentum transfer of $q \equiv p' - p = k_e - k'_e$. The experimental ranges for the (Lorentz) invariant, $Q^2 = -q^2$ are accessed in different experiments[11–13]. Using the assumption of a single photon exchange (which can be justified by the small size of the fine structure constant $\alpha \sim \frac{1}{137}$), we can obtain the scattering amplitude

$$T_{fi} = (-ie)^2 \overline{u}_e(\vec{k}'_e)\gamma_\mu u_e(\vec{k}_e)\frac{-i}{q^2}\langle \vec{p}'|J^\mu(\vec{q})|\vec{p}\rangle \tag{2.8}$$

Where J^μ is the electromagnetic current describing the interaction of the photon with the (electrically) charged quarks

$$J^\mu = \frac{2}{3}\overline{u}\gamma^\mu u - \frac{1}{3}\overline{d}\gamma^\mu d + \left[-\frac{1}{3}\overline{s}\gamma^\mu s\right] + \ldots \tag{2.9}$$

By considering all of the unique vector terms, we find the decomposition of the hadronic matrix element in eq. 2.9:

$$\langle \vec{p}' | J^{\mu}(\vec{q}) | \vec{p} \rangle = \overline{u}(\vec{p}') \left[\gamma_{\mu} F_1(q^2) + \frac{i\sigma^{\mu\nu} q_{\nu}}{m_N} F_2(q^2) \right] u(\vec{p}), \tag{2.10}$$

where m_N is the mass of the nucleon, and $F_1(q^2)$ and $F_2(q^2)$ are the Dirac and Pauli form factors respectively. At vanishing momentum transfer $q^2 \equiv q^{\mu} q_{\mu} = 0$, $F_1(0)$ gives the electric charge, while F_2 gives the anomalous magnetic moment of the nucleon. We will continue our investigation of these form factors in more detail in Chapter 4, where we will demonstrate the construction of the matrix elements and some of the properties obtained from the electromagnetic and tensor form factors.

2.3 Structure functions

2.3.1 Deep Inelastic Scattering

Aside from form factors, another way to describe the structure of hadrons is through Parton Distribution Functions (PDF), which describe the way momentum is distributed among the quarks and gluons inside an unpolarised hadron, and spin-dependent PDF's for polarised hadrons. These PDF's are determined via deep inelastic scattering experiments (DIS), in which we still have the lepton-nucleon (usually electron-proton) collisions, only now the transferred momentum is large enough such that the nucleon is destroyed, as demonstrated in Fig. 2.5, where we depict an electron with initial momentum k collide with a proton with initial momentum p via the exchange of a virtual photon γ with transferred momentum q, where we now differ from Fig. 2.4 and the final state is no longer a proton, instead all possible final states X are included, with total final momentum p'. In order to try and understand this field, there have been many models formulated see for example [31–37], and experiments undertaken [38–41].

The scattering amplitude for deep inelastic scattering is similar to that of the form factors,

$$T_{fi} = (-ie)^2 \overline{u}_e(\vec{k}_e') \gamma_{\mu} u_e(\vec{k}_e) \frac{-i}{q^2} \langle X | J^{\mu}(\vec{q}) | \vec{p} \rangle, \tag{2.11}$$

only now the final hadronic state X is an unknown state, where the initial and final momenta of the target are still p and p' and similarly the initial and final momenta of the lepton $k = (E_e, \vec{k})$ and $k' = (E_e', \vec{k}')$ respectively. With the Bjorken scaling parameter x and inverse ω defined as

$$\omega \equiv \frac{1}{x} \equiv \frac{2 m_N \nu}{Q^2} = \frac{-2 p \cdot q}{q^2}, \qquad \nu \equiv \frac{p \cdot q}{m_N}. \tag{2.12}$$

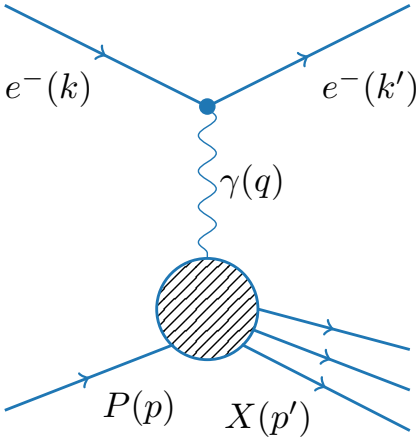

Figure 2.5: Figure demonstrating the deep inelastic scattering process of a Proton and electron collision, producing a final state X.

The invariant mass in elastic scattering $M_X^2 = (p+q)^2$ has to be fixed to a proton final state $M_X^2 = m_N^2$ with $x = \omega = 1$, but for the case in inelastic scattering, $M_X^2 \geq (m_N + m_\pi)^2$ (from baryon number conservation) and so we can have any $x \leq 1$, but require a large enough $Q^2 = -q^2$, and for large Q^2, x_max approaches 1. The cross section for DIS can be written in the nucleon laboratory frame as

$$\left.\frac{\mathrm{d}^2\sigma}{\mathrm{d}\Omega \mathrm{d}E_e'}\right|_{\text{N lab. frame}} = \frac{\alpha^2}{m_N Q^4}\frac{E_e'}{E_e} L_{\mu\nu} W^{\mu\nu} \tag{2.13}$$

where the leptonic tensor $L_{\mu\nu}$ is given by

$$L_{\mu\nu} = k_\mu' k_\nu + k_\nu' k_\mu - g_{\mu\nu} k' \cdot k + i\epsilon_{\mu\nu\rho\sigma} s_e^\rho q^\sigma. \tag{2.14}$$

If we consider inclusive processes, by summing over the final states X, we see that the unknown hadronic tensor $W^{\mu\nu}$ is then given as

$$\begin{aligned} W^{\mu\nu} &= \frac{1}{4\pi}\int d^4x e^{-iq\cdot x}\langle p|[J^\mu(x), J^\nu(0)]|p\rangle \\ &\equiv W_S^{\mu\nu} + iW_A^{\mu\nu} \end{aligned} \tag{2.15}$$

where we have split the tensor into its symmetric and anti-symmetric pieces. By conserving the current and using parity and time reversal invariance, the Lorentz decomposition of these tensors is given by

$$\begin{aligned} W_S^{\mu\nu} &= \left(-g^{\mu\nu} + \frac{q^\mu q^\nu}{q^2}\right) F_1(x, Q^2) + \frac{1}{m_N \nu}\left(p_\mu - \frac{p\cdot q}{q^2} q_\nu\right) F_2(x, Q^2) \\ W_A^{\mu\nu} &= \frac{1}{m_N \nu}\epsilon^{\mu\nu\rho\sigma} q_\rho s_\sigma g_1(x, Q^2) + \frac{1}{m_N \nu}\epsilon^{\mu\nu\rho\sigma} q_\rho \left(s_\sigma - \frac{q\cdot s}{m_N \nu} p_\sigma\right) g_2(x, Q^2). \end{aligned} \tag{2.16}$$

From eq. 2.14 and 2.16, the cross section in eq. 2.13 is then given by the unpolarised structure functions F_1 and F_2, which carry information about the longitudinal parton structure when summing over beam and target polarisations, and g_1 and g_2, which encode the corresponding longitudinal spin distributions when both the beam and target are suitably polarised. The polarised structure functions g_1 and g_2, can be found experimentally from the asymmetry factor A. For example, if considering a longitudinally polarised muon ($\Uparrow$) with respect to the beam direction and consider target protons polarised either $\uparrow$ or $\downarrow$, we form

$$\begin{aligned} A &= \frac{\frac{d^2\sigma^{\Uparrow\uparrow}}{d\Omega dE'_e} - \frac{d^2\sigma^{\Uparrow\downarrow}}{d\Omega dE'_e}}{\frac{d^2\sigma^{\Uparrow\uparrow}}{d\Omega dE'_e} + \frac{d^2\sigma^{\Uparrow\downarrow}}{d\Omega dE'_e}} \\ &\propto (E_e E'_e) g_1 - 2x m_N g_2 \\ &\propto g_1 \end{aligned} \tag{2.17}$$

This style of experiment only measures the g_1 structure function as g_2 is suppressed by $O(1/E_e)$ with comparison to g_1. If we instead use a transversely polarised proton ($\perp, \top$), we find A as

$$\begin{aligned} A &= \frac{\frac{d^2\sigma^{\Uparrow\perp}}{d\Omega dE'_e} - \frac{d^2\sigma^{\Uparrow\top}}{d\Omega dE'_e}}{\frac{d^2\sigma^{\Uparrow\perp}}{d\Omega dE'_e} + \frac{d^2\sigma^{\Uparrow\top}}{d\Omega dE'_e}} \\ &\propto \nu g_1 + 2E_e g_2 \\ &\propto g_2, \end{aligned} \tag{2.18}$$

which picks out the g_2 structure function. The g_1 structure function has been measured experimentally for years now [42] while the g_2 is much more challenging to obtain.

2.3.2 Operator Product Expansion

In order to relate the structure functions to the matrix elements of local operators, we have to use an Operator product expansion (OPE). When considering the product of two currents eq. 2.15 at the limit $x \to 0$ or ($q \to \infty$), for scales larger than x, the product instead looks like a single operator. We can then write [43]

$$\lim_{x\to 0} \mathcal{O}_i(x)\mathcal{O}_j(0) = \sum_k E_{ijk}(x)\mathcal{O}_{ijk}(0), \tag{2.19}$$

where E are the Wilson coefficients calculated perturbatively for small distances. In order to determine possible operators for the right hand side of eq. 2.19, a dimensional analysis finds that we have an expansion in inverse powers of Q^2, with expansion power given by $t-2$, where t is the twist of an operator defined by its *dimension − spin*. 'Leading order' terms must then be of twist $t = 2$ and are given by the symmetrised,

traceless parts of the quark bilinear operators, where all allowable operators must have the form

$$\mathcal{O}_q^{\mu_1\cdots\mu_n} = i^{n-1}\overline{q}\gamma^{\mu_1}\overset{\leftrightarrow}{D}^{\mu_2}\ldots\overset{\leftrightarrow}{D}^{\mu_n} q$$
$$\mathcal{O}_{5q}^{\mu_1\cdots\mu_n} = i^{n-1}\overline{q}\gamma^{\mu_1}\gamma_5\overset{\leftrightarrow}{D}^{\mu_2}\ldots\overset{\leftrightarrow}{D}^{\mu_n} q, \tag{2.20}$$

where $\overset{\leftrightarrow}{D} = \vec{D} - \overset{\leftarrow}{D}$ and the symmetrised, traceless part of the operator is defined as

$$\mathcal{S}\mathcal{O}^{\mu_1\cdots\mu_n} \overset{def}{=} \mathcal{O}^{\{\mu_1\cdots\mu_n\}} - \text{Tr}, \tag{2.21}$$

where the subtracted trace terms are defined such that $\eta_{\mu_i\mu_j}\mathcal{O}^{\mu_1\cdots\mu_i\cdots\mu_j\cdots\mu_n} = 0$. This entire operation produces an operator with spin n, so where for example $\mathcal{S}\mathcal{O}_{(5)q}$, the derivatives and fields give dimension $3 + (n-1)$, and so these operators all must have twist 2. Thus for $n = 2$ we have

$$\mathcal{S}\mathcal{O}_q^{\mu_1\mu_2} = i\overline{q}\left[\gamma^{\{\mu_1}\overset{\leftrightarrow}{D}^{\mu_2\}} - \frac{1}{4}\eta^{\mu_1\mu_2}\gamma^{\mu}\overset{\leftrightarrow}{D}_{\mu}\right] q, \tag{2.22}$$

and as n increases, so too does the complexity of these expressions.

The local operators eq. 2.20 as well as the hadron structure observables that are based on them are related through moments in the momentum fraction x, given by the integral

$$f^n = \int_{-1}^{1} dx\ x^{n-1} f(x). \tag{2.23}$$

If we consider moments of the polarised structure functions g_1 and g_2 from eq. 2.16, we find

$$2\int_0^1 dx x^n g_1(x,Q^2) = \frac{1}{2}\sum_f e_{g_1,n}^{(f)} a_n^{(f)}(\mu) + O(1/Q^2) \tag{2.24}$$
$$2\int_0^1 dx x^n g_2(x,Q^2) = \frac{1}{2}\frac{n}{n+1}\sum_f (e_{g_2,n}^{(f)} d_n^{(f)}(\mu) - e_{g_1,n}^{(f)} a_n^{(f)}(\mu)) + O(1/Q^2),$$

where $e \equiv e^{\overline{\text{MS}}}(\mu^2/Q^2, g^{\text{MS}}(\mu))$ are the Wilson coefficients defined in the $\overline{\text{MS}}$ renormalisation scheme (described in more detail in Chapter 5). Here n is even and starts at $n = 2$ and so a_n and d_n are defined by [44]

$$\langle\vec{p},\vec{s}|\mathcal{O}_{5q}^{\{\sigma\mu_1\cdots\mu_n\}} - \text{Tr}|\vec{p},\vec{s}\rangle = \frac{1}{2}a_n^{(q)}\mathcal{S}\overline{u}(\vec{p},\vec{s})\gamma^{\sigma}\gamma_5 p^{\mu_1}\ldots p^{\mu_n}u(\vec{p},\vec{s})$$
$$\equiv a_n^{(q)}\left[s^{\{\sigma}p^{\mu_1}\ldots p^{\mu_n\}} - \text{Tr}\right] \tag{2.25}$$
$$\langle\vec{p},\vec{s}|\mathcal{O}_{5q}^{[\sigma\{\mu_1]\cdots\mu_n\}} - \text{Tr}|\vec{p},\vec{s}\rangle = \frac{1}{2}\frac{n}{n+1}d_n^{(q)}\overline{u}(\vec{p},\vec{s})\left[(\gamma^{\sigma}\gamma_5 p^{\{\mu_1}\gamma_5 p^{|\sigma|})p^{\mu_2}\ldots p^{\mu_n\}} - \text{Tr}\right]u(\vec{p},\vec{s})$$
$$\equiv \frac{n}{n+1}d_n^{(q)}\left[(s^{\sigma}p^{\{\mu_1} - s^{\{\mu_1}p^{|\sigma|})p^{\mu_2}\ldots p^{\mu_n\}} - \text{Tr}\right] \tag{2.26}$$

where, for example for three indices, the operator $\mathcal{O}_{5q}^{\sigma\{\mu_1\mu_2\}}$ has been split into its symmetric and mixed symmetric component pieces,

$$\mathcal{O}_{5q}^{\sigma\{\mu_1\mu_2\}} \equiv \mathcal{O}_{5q}^{\{\sigma\mu_1\mu_2\}} + \mathcal{O}_{5q}^{[\sigma\{\mu_1]\mu_2\}}. \tag{2.27}$$

The mixed symmetric term $\mathcal{O}_{5q}^{[\sigma\{\mu_1]\mu_2\}}$ does not contain a totally symmetric piece, thus it has a spin of $n-1$ and is thus twist-3. This means that g_2 not only contains a_n the so-called twist-2 Wandzura-Wilczek contribution to g_2 [45], but also a separate twist-3 contribution d_n. In Chapter 8, we will calculate the d_2 twist-3 contribution to the g_2 structure function, and further investigate the unique properties demonstrated by its form factors.

Chapter 3

Lattice QCD

Lattice QCD, first proposed in 1974 [46], is a method of calculating non-perturbative QCD observables numerically and is derived from first-principles. Being the only direct theoretical probe of QCD at low energies, lattice calculations are able to give us important insight into a variety of physical phenomena such as hadron structure [47–49], the hadron spectrum [50, 51], the vacuum structure [52–54] and the QCD phase diagram [55–57] among others.

Based on the path integral formulation of QCD [58], expectation values of operators are expressed as weighted integrals over fermion and gauge field configurations, using a discretised version of the QCD theory to be solved explicitly on a four dimensional lattice with three space dimensions and a time dimension. These lattices are defined by a finite distance between each lattice grid point where the lattice spacing a must be taken to the continuum limit $a \to 0$ to connect to a physical interpretation. One of the key advantages to lattice QCD is the precise control over the variables involved in QCD, such as 'turning off' the disconnected vacuum loops and using non-physical quark masses to better understand the non-perturbative results.

In this chapter we will be looking at the definitions of the fermion and gauge actions, and the necessary steps to discretise the observable expectation values. We then move on to using the actions of the fermions and gauge fields to construct two-point and three-point correlation functions, vital to determining the expectation value of observables relevant for studying baryon properties that we are interested in. A more comprehensive overview of lattice QCD can be found in [59–62].

3.1 The Action

Being based on the Feynman path integral in quantum field theory [58], the observables calculated using lattice gauge theory are given by expectation values of field operators.

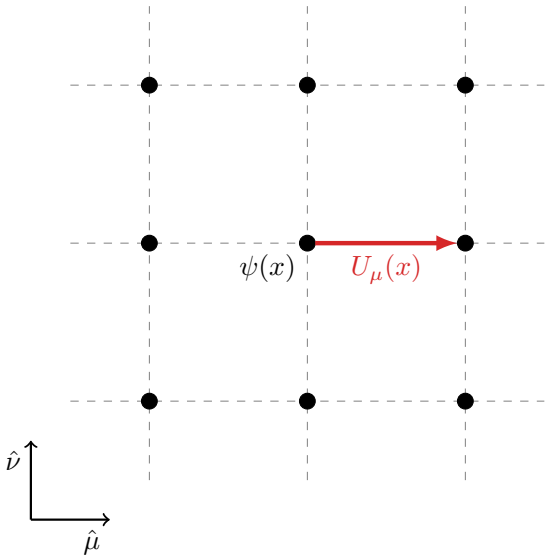

Figure 3.1: Two dimensional representation of the lattice grid, displaying the fermion fields defined on the lattice grid points $\psi(x)$ and the gauge fields through link variables U_μ(x).

The expectation values are then defined as Green's functions, and are expressed as derivatives of a generating functional,

$$Z_{QCD} = \int \delta A_\mu \delta\overline{\psi}\delta\psi e^{iS^M_{QCD}}, \tag{3.1}$$

which is not easily calculated in Minkowski space, due to the complex term $e^{iS^M_{QCD}}$ creating an oscillatory integral and cancelling between different regions of phase space. Thus lattice calculations are done in the Euclidean space-time and our partition function is then obtained from a Wick rotation of $(t \to -it_E)$ of eq. 3.1,

$$Z^E_{QCD} = \int \delta A_\mu \delta\overline{\psi}\delta\psi e^{-S_{QCD}}. \tag{3.2}$$

This forms the probabilistic interpretation of the integral, where the exponential factor corresponds to the Boltzmann weighting of a statistical ensemble and we treat S_{QCD} as the discretised action for QCD.

In order to discretise the integral in eq. 3.2, we define a hypercubic grid of spacetime points with size $N_L^3 \times N_T$ and an isotropic separation a. We can then define the fermion and adjoint fermion fields on the grid points without modification, where the gauge fields are discretised in terms of link variables,

$$U_\mu(x) \equiv \mathcal{P}\exp\left[ig\int_0^a A_\mu(x + a'\hat{\mu})da'\right]. \tag{3.3}$$

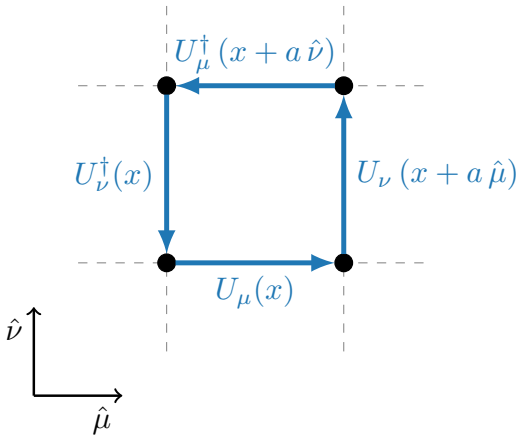

Figure 3.2: The plaquette term $P_{\mu\nu}(x)$ shown on the lattice.

Here $\mathcal{P}$ indicates a path ordering of the gauge field A_μ, g is the coupling constant, and we omit color indices for simplicity. In Fig. 3.1, we show that the fermion fields are located the points of the grid, while the link variables now provide a gauge covariant method of transporting quantities across adjacent lattice sites $x \to x + \hat{\mu}$, where $\hat{\mu}$ is an adjacent site corresponding the direction chosen ($\hat{\mu} = 1, 2, 3, 4$). The 'reverse' of such a link is defined through its Hermitian conjugate,

$$U_\mu^\dagger(x) \equiv U_{-\mu}(x + a\hat{\mu}). \tag{3.4}$$

Gauge invariance is still imposed on the lattice, and we require our gauge links $U_\mu(x)$ belonging to $SU(3)$ to have the transformation,

$$U_\mu(x) \to \Lambda(x) U_\mu(x) \Lambda(x + a\hat{\mu})^{-1}, \tag{3.5}$$

where the gauge transformation $\Lambda(x)$ is defined in eq. 2.2. With the fermion fields and gauge links defined, we can now evaluate the lattice action S_{QCD} from eq. 3.2 as,

$$S_{QCD} = S_F[U, \psi, \overline{\psi}] + S_G[U] \tag{3.6}$$

which is split into the action of the fermion and gauge components as S_F and S_G respectively.

3.1.1 Gluon Action

We begin by looking into the pure gauge action term $S_G[U]$, where we have defined a link variable $U_\mu(x)$ in eq. 3.3, which maintains gauge invariance and acts as the gauge transporter connecting adjacent lattice sites. With the transformation in eq. 3.5, it is possible to construct a traced loop of gauge links that share a start and end point which

maintains gauge invariance, and so a series of loops used in combination allow us to build the lattice version of the QCD gauge action. A precise construction is arbitrary so long as we maintain the continuum action in the limit $a \to 0$. The first quantity to consider is the simplest loop called a plaquette, which is the shortest closed loop consisting of four links as seen in Fig.(3.2). In terms of link variables the plaquette is defined as

$$P_{\mu\nu}(x) = \frac{1}{3}\mathcal{R}e\mathrm{Tr}U_{sq}, \tag{3.7}$$

where,

$$\begin{aligned} U_{sq} &\equiv U_\mu(x)U_\nu(x+a\hat{\mu})U_{-\mu}(x+a\hat{\mu}+a\hat{\nu})U_{-\nu}(x+a\hat{\nu}) \\ &= U_\mu(x)U_\nu(x+a\hat{\mu})U_\mu^\dagger(x+a\hat{\nu})U_\nu^\dagger(x). \end{aligned} \tag{3.8}$$

Using eq. 3.3, $P_{\mu\nu}$ can be rewritten as an integration around a closed loop $\Box$, Taylor expanding the resulting exponential, the plaquette can be expressed in terms of the field A_μ,

$$P_{\mu\nu}(x) = \mathcal{R}e\mathrm{Tr}\mathcal{P}\left[1 - \frac{1}{2}\left(g\oint_\Box A\cdot dx\right)^2 + \mathcal{O}(g^4)\right]. \tag{3.9}$$

Now using Stoke's theorem gives us the expression for the integral,

$$\begin{aligned} \oint_\Box A\cdot dx &= \int_{-\frac{a}{2}}^{\frac{a}{2}} dx_\mu dx_\nu \left[\partial_\mu A_\nu(x_0+x) - \partial_\nu A_\mu(x_0+x)\right] \\ &= \int_{-\frac{a}{2}}^{\frac{a}{2}} dx_\mu dx_\nu F_{\mu\nu}(x_0+x) \end{aligned} \tag{3.10}$$

where $F_{\mu\nu} = \partial_\mu A_\nu - \partial_\nu A_\mu$ is the Abelian field strength tensor and x_0 is the centre of the integration loop. We then take a Taylor expansion of $F_{\mu\nu}(x_0+x)$ about the origin x_0,

$$\oint_\Box A\cdot dx = a^2 F_{\mu\nu}(x_0) + \frac{a^4}{24}(\partial_\mu^2+\partial_\nu^2)F_{\mu\nu}(x_0) + \mathcal{O}(a^6, g^2), \tag{3.11}$$

and so by inserting eq. 3.11 into eq. 3.9, the plaquette simply becomes,

$$P_{\mu\nu}(x_0) = 1 - \frac{1}{2}g^2a^4\mathrm{Tr}[F_{\mu\nu}(x_0)^2] + \mathcal{O}(g^2a^6, a^8, g^4a^6). \tag{3.12}$$

The Wilson action for the gluons is then simply written in terms of this new plaquette operator term,

$$S_G^W[U] = \frac{2}{g^2}\sum_{x,\mu>\nu}[1 - P_{\mu\nu}(x)] = \frac{a^4}{2g^2}\sum_{x,\mu>\nu}\mathrm{Tr}[F_{\mu\nu}(x)^2] + \mathcal{O}(a^6, a^2g^2) \tag{3.13}$$

As we mentioned before the construction of the gluon action is arbitrary as long as it agrees with the continuum gluon action, and since we are not limited to only squares, we can improve on our action by incorporating additional rectangular $R_{\mu\nu}$ and parallelogram shaped terms $L_{\mu\nu}$ in order to correct the $\mathcal{O}(a^2)$ effects by using the Lüscher-Weisz gauge action [63]. These add in a way to improve the action up to $\mathcal{O}(a^4)$ at tree level and $\mathcal{O}(g^2a^2)$

$$S_G^{LW}[U] = \frac{\beta}{3}\sum_{x,\mu>\nu}\left[c_0(1-P_{\mu\nu}(x)) + c_1(1-R_{\mu\nu}(x)) + c_2(1-L_{\mu\nu}(x))\right] \tag{3.14}$$

where here $\beta \equiv \frac{6}{g^2}$ is the inverse bare coupling, and the coefficients c_i are generally functions of g^2 and are chosen to satisfy $c_0 + 8c_1 + 8c_2 = 1$, which ensures that discretisation errors are cancelled to $\mathcal{O}(a^4)$. Two avaliable choices to these coefficients are the Iwasaki gauge action [64] and the tree-level improved action, which we have used in this work where we set $c_0 = 20/12, c_1 = -1/12, c_2 = 0$.

3.1.2 Fermion Action

Whilst the gauge fields by themselves provide information on the structure of the vacuum, we require the inclusion of fermions into lattice QCD in order to analyse the fermionic particles and their interaction with the rest of QCD. The Dirac action for a fermion is then formulated in Euclidean space-time as,

$$\int d^4x\overline{\psi}(x)(\not{D} + m)\psi(x), \tag{3.15}$$

for a single flavour, where ψ is a Dirac spinor that carries a colour index. The quark fields are now located on the sites of the lattice, separated by the lattice spacing a and the derivatives are simply reduced to finite differences, with forward and backward neighbours,

$$\begin{aligned} D_\mu^{(f)}\psi(x) &= \frac{1}{a}\left[U_\mu(x)\psi(x+a\hat{\mu}) - \psi(x)\right], \\ D_\mu^{(b)}\psi(x) &= \frac{1}{a}\left[U_\mu^\dagger(x-a\hat{\mu})\psi(x-\hat{\mu}) - \psi(x)\right], \end{aligned} \tag{3.16}$$

where again the $U_\mu(x)$ are the gauge links and elements of the SU(3) gauge group defined in eq. 3.3, and these gauge fields lie along the links between the lattice sites x and $x + a\hat{\mu}$. The symmetric nearest neighbour derivative is then constructed via

$$D_\mu\psi(x) = \frac{1}{2}\left[D_\mu^{(f)}\psi(x) - D_\mu^{(b)}\psi(x)\right] = \frac{1}{2a}\left[U_\mu(x)\psi(x+a\hat{\mu}) - U_\mu^\dagger(x-a\hat{\mu})\psi(x-a\hat{\mu})\right], \tag{3.17}$$

where appropriate gauge links maintain the gauge invariance of the action. Thus our first form for the fermion action on the lattice can be constructed by discretising the derivative of the fermion action in eq. 3.15 using the symmetrised finite difference,

$$S_F^N[U,\psi,\overline{\psi}] = \sum_{n\in Lat} \overline{\psi}(x) \left(\frac{1}{2a} \sum_{\mu=1}^{4} \gamma_\mu \left[U_\mu(x)\psi(x+a\hat{\mu}) - U_\mu^\dagger(x-a\hat{\mu})\psi(x-a\hat{\mu}) \right] + m\psi(x) \right) \tag{3.18}$$

$$= \sum_{x,y\in Lat} \overline{\psi}(x) M_{xy}^N[U] \psi(y) \tag{3.19}$$

where here we have the interaction matrix

$$M_{xy}^N[U] = m\delta_{xy} + \frac{1}{2a} \sum_{\mu=1}^{4} \gamma_\mu \left[U_\mu(x)\delta_{x(y-\mu)} - U_\mu^\dagger(x-a\hat{\mu})\delta_{x(y+\mu)} \right]. \tag{3.20}$$

Using Taylor expansions of the gauge links U_μ and fermion fields ψ in powers of a, we find errors of $\mathcal{O}(a^2)$ in the naive fermion action. The first-order derivative can only couple lattice sites $2a$ apart. As a result of this on the lattice, high-momentum modes no longer correspond to a large portion of the action, causing additional long-range degrees of freedom to emerge called doublers. One method to suppress the doublers is to stagger the quark degrees of freedom as seen in [62], but we use a second method where to suppress this doubling problem, we add additional operators to the quark action by pushing them to higher energy levels. The term that we add is known as the Wilson term, which when added to our standard lattice fermion action S_F gives us the Wilson action [65, 66],

$$S_F^W[U,\psi,\overline{\psi}] = \sum_{x\in Lat} \overline{\psi}(x) \left[\sum_{\mu=1}^{4} \left(\gamma_\mu \nabla_\mu - \frac{1}{2} ra \triangle_\mu \right) + m \right] \psi(x). \tag{3.21}$$

The $\nabla_\mu = D_\mu^{(f)} - D_\mu^{(b)}$ defines the finite difference we saw in the previous action, and the new operator $\triangle$ enables us to remove the doublers by coupling together adjacent lattice sites, where

$$\triangle_\mu \psi(x) = \frac{1}{a^2} \left[U_\mu(x)\psi(x+a\hat{\mu}) + U_\mu^\dagger(x-a\hat{\mu})\psi(x-a\hat{\mu}) - 2\psi(x) \right]. \tag{3.22}$$

To simplify the Wilson action, we write it in terms of the interaction matrix and link variables

$$S_F^W[U,\psi,\overline{\psi}] = \sum_{x,y\in Lat} \overline{\psi}^L(x) M_{xy}^W[U] \psi^L(y) \tag{3.23}$$

where the interaction matrix is

$$M_{xy}^W[U]a = \delta_{xy} - \kappa \sum_{\mu=1}^{4} \left[(r-\gamma_\mu) U_\mu(x)\delta_{x(y-\mu)} + (r+\gamma_\mu) U_\mu^\dagger(x-a\hat{\mu})\delta_{x(y+\mu)} \right] \tag{3.24}$$

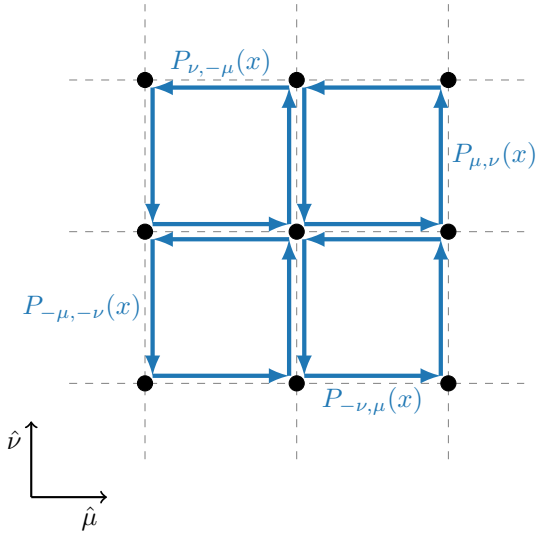

Figure 3.3: The clover term $F_{\mu\nu}(x)$ shown on the lattice.

with the renormalisation $\kappa = 1/(2ma + 8r)$ and $\psi^L = \psi/\sqrt{2\kappa}$. Taking the standard choice of $r = 1$, the quark mass then becomes

$$m_q = \frac{1}{2}\left(\frac{1}{\kappa} - \frac{1}{\kappa_c}\right). \tag{3.25}$$

The parameter κ_c is the critical kappa value which describes when the quark mass vanishes. In the free theory, kappa critical is $\kappa_c = 1/8r$, but with our interacting theory, we require additive and multiplicative renormalisation due to the explicit chiral symmetry breaking by the Wilson term in eq. 3.21. The $\mathcal{O}(a)$ error is present at finite lattice spacing which affects the approach to the continuum limit. At finite lattice spacing the Dirac action picks up an discretisation artefact from the Wilson term of order $\mathcal{O}(a)$, and thus

$$\int d^4x \overline{\psi}(x)\left(\not{D} + m - a\frac{r\not{D}^2}{2}\right)\psi(x) + \mathcal{O}(a^2) \tag{3.26}$$

Simulations run purely using Wilson fermions are computationally 'cheap', but due to the large $\mathcal{O}(a)$ artefacts, one requires very fine lattices, hence large volumes to calculate, which are computationally 'expensive'. Thus it is beneficial to improve the action by adding operators of increasing dimensions that vanish at the continuum limit which is known as the Symanzik improvement program [67]. This work makes use of the Sheikholeslami-Wohlert function [68] that includes a 'clover' term, a sum of plaquettes,

$$F_{\mu\nu}(x) \equiv P_{\mu,\nu}(x) + P_{\nu,-\mu}(x) + P_{-\mu,-\nu}(x) + P_{-\nu,\mu}(x). \tag{3.27}$$

It is a gauge invariant, local, dimension five operator which is included along side the original Wilson action and has been continually improved [69–71]. The explicit form for the action is

$$S_F^{SW}[U,\psi,\overline{\psi}] = S_F^W[U,\psi,\overline{\psi}] - \frac{ac_{SW}r}{4}\sum_{x\in Lat}\sum_{\mu,\nu=1}^{4}\overline{\psi}(x)\sigma_{\mu\nu}F_{\mu\nu}\psi(x), \tag{3.28}$$

where c_{SW} is the 'clover' coefficient and is tuned depending on the situation to eliminate all the $\mathcal{O}(a)$ errors, most often non-perturbatively using the axial Ward identity [71] and is referred to as the non-perturbative improved clover fermion action.

3.1.3 Gauge Configurations and Quark Propagators

In lattice QCD, the partition function is the basic building block to begin extracting quantities. We define the partition function as

$$Z = \int DU_\mu D\psi D\overline{\psi}e^{-S}, \qquad S = S_G + S_F = S_G + \sum_x \overline{\psi}M\psi, \tag{3.29}$$

where S is the chosen QCD action separated into its gauge and fermion components as defined in the previous section, and M is the interaction matrix. It is possible to separate and integrate the Grassmann fermion fields $\overline{\psi}$ and ψ, thus simplifying the partition function,

$$Z = \int DU_\mu \det[M]e^{-S_G}. \tag{3.30}$$

We can then calculate observables using lattice QCD through their corresponding expectation values,

$$\langle\mathcal{O}\rangle = \frac{1}{Z}\int DU_\mu \det[M]\mathcal{O}e^{-S_G}, \tag{3.31}$$

where $\langle\mathcal{O}\rangle$ is the expectation value of an operator $\mathcal{O}$ corresponding to the average value of its associated physical observable. This expectation value has a dependence on the background gauge field $U[A]$ integrated via DU_μ. Since we cannot integrate over a continuous range, we take the approximate of the integral defined by a finite sum over some set of N gauge fields

$$\langle\mathcal{O}\rangle \approx \frac{1}{N}\sum_{i=1}^{N}\mathcal{O}[U^{[i]}], \tag{3.32}$$

and here $\mathcal{O}[U^{[i]}]$ represents the measurement of the operator $\mathcal{O}$ on the i^{th} background gauge field 'configuration' $U^{[i]}$. The field configurations are randomly generated using an acceptance probability from the weight function $\det[M[U]]e^{-S_G}$ and an iterative Markov process using a Hybrid Monte-Carlo style algorithm for the transition probability between configurations [72].

We also require the introduction of quarks on our lattice via a 'quark propagator', the goal of which is to remove the dependence of the quark operators on the field by performing Wick contractions. We can generate these quark propagators by performing an inversion of the interaction matrix on a particular gauge field U

$$S^{ab}_{\alpha\beta}(x, y, U, m_q) = (M^{ab}_{\alpha\beta})^{-1}(x, y, U, m_q), \tag{3.33}$$

where we define α as the spin, a the colour and y as the lattice site of the annihilation 'sink' operator and β, b, x the spin, colour and lattice site of the quark creation 'source' operator respectively. Using this, we can calculate a propagator for each gauge field configuration U for a particular quark mass m_q. These propagators are the base for any lattice QCD calculation of hadronic observables, as different combinations of propagators allow different ways to analyse a particular particle system. Generally to calculate results we would require propagators from all x to all y locations on the lattice, which is prohibitively expensive, so we mitigate this problem by invoking translational invariance and fix the source to be a single space-time point y and only calculate $y \to x$ for all x.

3.2 Correlation Functions

In order to investigate the structure of the hadron and relevant form factors, we need calculations of nucleon masses and matrix elements which in turn require the construction of two-point and three-point correlation functions. For this section we use the following notation convention. Upper indices in English $a, b, c...$, represent the colour indices, while lower indices α, β, γ, label the spin indices, any other sub/super-script is for labelling. We use a split space-time notation $x = x^\mu = (\vec{x}, t)$, where the source will be represented generally at space-time position $x_0 = (\vec{x_0}, t_0) \equiv 0 = (\vec{0}, 0)$, while the 'sink' position at $x = (\vec{x}, t)$. When taking a trace Tr(), we imply tracing over both colour and spin matrices.

3.2.1 Two-point Correlation Functions

We begin by considering baryon interpolating fields χ_α and $\overline{\chi}_\beta$ corresponding to annihilation and creation operators at a 'sink' and 'source' respectively. This leads to the definition of the baryon two-point correlation function,

$$C_{2pt}(\Gamma; \vec{p}, t - t_0) \equiv \sum_{\vec{x}-\vec{x_0}} e^{-\vec{p}\cdot(\vec{x}-\vec{x_0})} \mathrm{Tr}\left\{\Gamma \langle \Omega | \chi(\vec{x}, t) \overline{\chi}(\vec{x_0}, t_0) | \Omega \rangle\right\}, \tag{3.34}$$

as depicted in Fig. 3.4. Here Γ is the spin matrix used to project on to definite baryon spin, $\vec{p}$ the momentum of our system and t and t_0 are times of the annihilation and

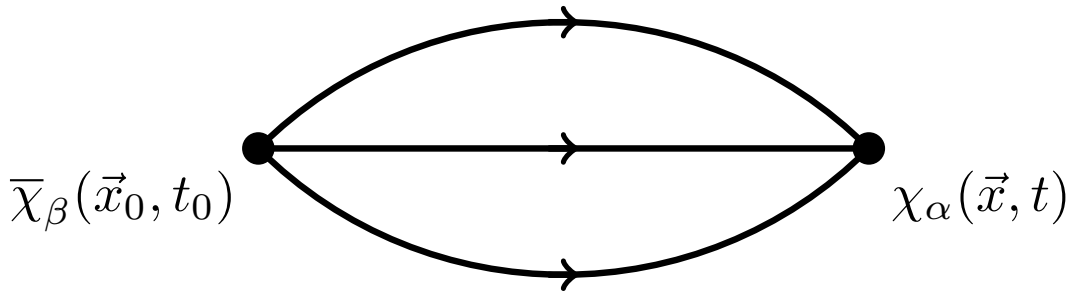

Figure 3.4: Diagram of a two-point function described in equation (3.34)

creation of the particle on the lattice respectively. We choose the point of creation as $(\vec{x_0}, t_0) = (\vec{0}, 0)$ for simplicity. In order to reduce eq. 3.34 into a more useful term, we first translate the operator $\chi(\vec{x}, t)$ with translational invariance

$$\begin{aligned}\chi(\vec{x}, t) &= e^{\hat{H}t} e^{-i\hat{\vec{p}}\cdot\vec{x}} \chi(\vec{0}, 0) e^{-\hat{H}t} e^{i\hat{\vec{p}}\cdot\vec{x}} \\ C_{2pt}(\Gamma; \vec{p}, t) &= \sum_{\vec{x}} e^{-i\vec{p}\cdot\vec{x}} \mathrm{Tr}\left\{\Gamma\langle\Omega| e^{\hat{H}t} e^{-i\hat{\vec{p}}\cdot\vec{x}} \chi(\vec{0}, 0) e^{-\hat{H}t} e^{i\hat{\vec{p}}\cdot\vec{x}} \overline{\chi}(\vec{0}, 0)|\Omega\rangle\right\},\end{aligned} \tag{3.35}$$

using the Hamiltonian $\hat{H}$ and momentum operators $\hat{\vec{p}}$. Next we insert a complete set of states into the trace,

$$\hat{I} = \sum_N \frac{|N, \vec{p}', s'\rangle\langle N, \vec{p}', s'|}{2E_{p'}} + |\Omega\rangle\langle\Omega|, \tag{3.36}$$

where the index N is summed over all the eigenstates, with the operators action on $|N\rangle$ as

$$\hat{H}|N, \vec{p}, s\rangle = E_{p'}|N, \vec{p}, s\rangle \qquad \hat{\vec{p}}|N, \vec{p}, s\rangle = \vec{p}'|N, \vec{p}, s\rangle, \tag{3.37}$$

where each eigenstate has energy $E_{p'}$, momentum $\vec{p}'$ and spin s'. This leaves

$$C_{2pt}(\Gamma; \vec{p}, t) = \sum_{\vec{x}, N} \frac{1}{2E_{p'}} e^{-i(\vec{p}-\vec{p}')\cdot\vec{x}} e^{-E_{p'}t} \mathrm{Tr}\left\{\Gamma\langle\Omega|\chi(\vec{0}, 0)|N, \vec{p}', s'\rangle\langle N, \vec{p}', s'|\overline{\chi}(\vec{0}, 0)|\Omega\rangle\right\}. \tag{3.38}$$

By splitting the sum over eigenstates into their energy, momentum and spin $N = E_{p'}, \vec{p'}, s'$, we can evaluate the sum over $\vec{x}$ which leaves us a δ-function which helps sum over $\vec{p}'$,

$$\sum_{\vec{p}', \vec{x}} = e^{-i\vec{x}\cdot(\vec{p}-\vec{p}')} F(\vec{p}') = \sum_{\vec{p}'} \delta^3(\vec{p} - \vec{p}') F(\vec{p}') = F(\vec{p}), \tag{3.39}$$

which equates to us replacing $\vec{p}'$ with $\vec{p}$ in eq. 3.38,

$$C_{2pt}(\Gamma; \vec{p}, t) = \sum_{N, s} \frac{1}{2E_p} e^{-E_p t} \mathrm{Tr}\left\{\Gamma\langle\Omega|\chi(\vec{0}, 0)|N, \vec{p}, s\rangle\langle N, \vec{p}, s|\overline{\chi}(\vec{0}, 0)|\Omega\rangle\right\}. \tag{3.40}$$

From here we can create two-point correlators on the lattice by combining different quark propagators defined in eq. 3.33 in order to construct the system of interest. We can write down the interpolating fields for the proton,

$$\chi_\alpha(x) = \epsilon^{abc} u^a_\alpha(x) u^b_\beta(x) \tilde{C}_{\beta\gamma} d^c_\gamma(x) \qquad \overline{\chi}_\alpha(x) = \epsilon^{a'b'c'} \overline{u}^{a'}_\alpha(x) \overline{d}^{b'}_\beta(x) \tilde{C}_{\beta\gamma} \overline{u}^{c'}_\gamma(x) \tag{3.41}$$

with quark fields u and d here generalised as the 'doubly' and 'singly' represented quarks respectively, to describe any octet baryon defined in Chapter 2, and $\tilde{C} = C\gamma_5$, where $C = \gamma_4\gamma_2$ is the charge conjugation matrix. Substituting these interpolating fields into eq. 3.34 then gives us the forward propagating two-point correlator in terms of the quark fields,

$$C_{2pt}(\Gamma; \vec{p}, t) \equiv \sum_{\vec{x}} e^{-i\vec{p}\cdot\vec{x}} \epsilon^{abc} \epsilon^{a'b'c'} \tilde{C}_{\beta\gamma} \tilde{C}_{\beta'\gamma'} \Gamma_{\alpha'\alpha} \langle u^a_\alpha(x) u^b_\beta(x) d^c_\gamma(x) \overline{u}^{a'}_{\alpha'}(0) \overline{d}^{b'}_{\beta'}(0) \overline{u}^{c'}_{\gamma'}(0) \rangle. \tag{3.42}$$

We then perform all possible Wick contractions between these quark propagators, where we define the Wick contraction between two of the quark fields as eq. 3.33

$$S^{(q)aa'}_{\alpha\alpha'} \equiv \overbrace{q^a_\alpha(x) \overline{q}^{a'}_{\alpha'}}(y), \tag{3.43}$$

where q is the quark flavour involved in the contraction. We have two ways to contract all the quark fields in eq. 3.42,

$$\begin{aligned} C_{2pt}(\Gamma; \vec{p}, t) = \sum_{\vec{x}} & e^{-i\vec{p}\cdot\vec{x}} \epsilon^{abc} \epsilon^{a'b'c'} \tilde{C}_{\beta\gamma} \tilde{C}_{\beta'\gamma'} \Gamma_{\alpha\alpha'} \\ & \left\langle S^{(d)cb'}_{\gamma\beta'}(x,0) \left(S^{(u)aa'}_{\alpha\alpha'}(x,0) S^{(u)bc'}_{\beta\gamma'}(x,0) + S^{(u)ac'}_{\alpha\gamma'}(x,0) S^{(u)ba'}_{\beta\alpha'}(x,0) \right) \right\rangle. \end{aligned} \tag{3.44}$$

To simplify this equation, we define

$$\overline{S^{(q)cb'}_{\gamma'\beta}}(x,0) \equiv \tilde{C}_{\beta\gamma} S^{(q)cb'}_{\gamma\beta'} \tilde{C}_{\beta'\gamma'} \tag{3.45}$$

giving us the expression

$$\begin{aligned} C_{2pt}(\Gamma; \vec{p}, t) = \sum_{\vec{x}} & e^{-i\vec{p}\cdot\vec{x}} \epsilon^{abc} \epsilon^{a'b'c'} \\ & \Big[\left\langle \mathrm{Tr}\left\{ \Gamma S^{(u)aa'}(x,0) \right\} \mathrm{Tr}\left\{ \overline{S^{(d)cb'}}(x,0) S^{(u)bc'}(x,0) \right\} \right\rangle + \\ & \left\langle \mathrm{Tr}\left\{ \Gamma S^{(u)ac'}(x,0) \overline{S^{(d)cb'}}(x,0) S^{(u)ba'}(x,0) \right\} \right\rangle \Big]. \end{aligned} \tag{3.46}$$

Once we have constructed the S and $\overline{S}$ propagators on each gauge field, the combination of traces in eq. 3.46 gives us the two-point correlation function C_{2pt}.

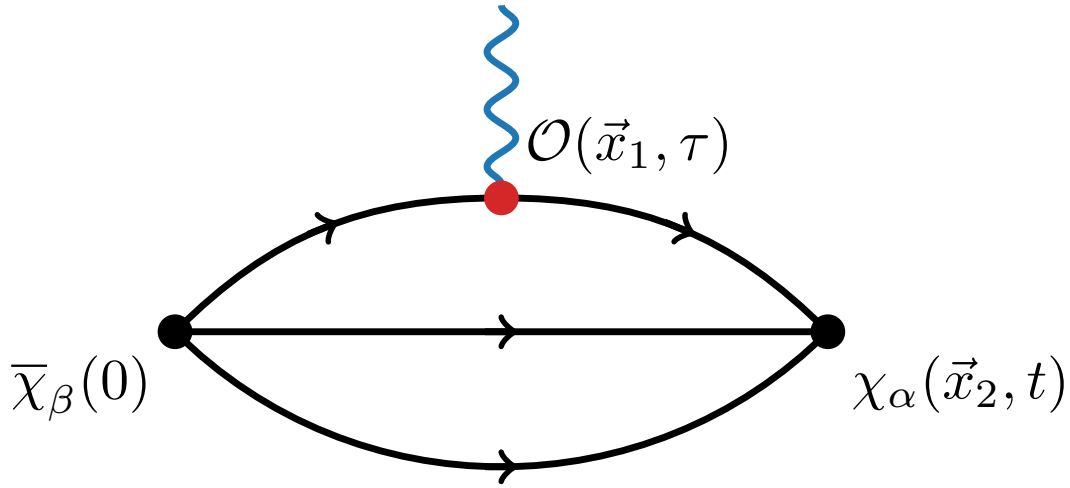

Figure 3.5: Diagram of a three-point function described in equation (3.47)

3.2.2 Three-point Correlation Functions

In order for us to probe the internal structure of the octet baryons, we need to construct an additional correlator, analogous to the two-point correlator only with an added current insertion operator $\mathcal{O}^{(q)}$, for example the vector current J^μ defined in eq. 2.9. In this three-point case, where some insertion operator $\mathcal{O}^{(q)}$ now interacts with one of the quark lines at some intermediate point $(\vec{x}_1, \tau)$ between the annihilation operator at the 'sink' $(\vec{x}_2, t)$ and the creation operator at the 'source' $(\vec{0}, 0)$. For simplicity we again assume the creation operator exists at the origin as illustrated in Fig. 3.5,

$$C_{3pt}(\Gamma; \vec{p}', t; \vec{q}, \tau; \mathcal{O}^{(q)}) = \sum_{\vec{x}_1, \vec{x}_2} e^{-i\vec{p}'\cdot\vec{x}_2} e^{i\vec{q}\cdot\vec{x}_1} \mathrm{Tr}\left\{\Gamma\langle\Omega|\chi(\vec{x}_2, t)\mathcal{O}^q(\vec{x}_1, \tau)\overline{\chi}(\vec{0}, 0)|\Omega\rangle\right\}. \tag{3.47}$$

In this case, there are two independent momentum, where $\vec{q}$ corresponds to the momenta at the point of current insertion $(\vec{x}_1, \tau)$ and $\vec{p}'$ corresponding to the 'sink' now at $(\vec{x}_2, t)$. The source momentum is then defined as the difference $p^\mu = p'^\mu - q^\mu$ due to momentum conservation.

Following the same method used for the two-point correlation function, we first use the translational invariance from eq. 3.35 followed by inserting complete sets of states

eq. 3.36 into eq. 3.47 with two state sets N_1, N_2,

$$C_{3pt}(\Gamma;\vec{p}',t;\vec{q},\tau;\mathcal{O}^{(q)}) = \sum_{\vec{x}_1,\vec{x}_2}\sum_{N_1,N_2}\frac{1}{4E_{N_1}E_{N_2}}e^{-i\vec{p}'\cdot\vec{x}_2}e^{i\vec{q}\cdot\vec{x}_1} \\ \mathrm{Tr}\Big\{\Gamma\langle\Omega|e^{\hat{H}t}e^{-i\hat{\vec{p}}\cdot\vec{x}_2}\chi(\vec{0},0)e^{-\hat{H}t}e^{i\hat{\vec{p}}\cdot\vec{x}_2}|N_1\rangle \\ \langle N_1|e^{\hat{H}\tau}e^{-i\hat{\vec{p}}\cdot\vec{x}_1}\mathcal{O}^{(q)}(0)e^{-\hat{H}\tau}e^{i\hat{\vec{p}}\cdot\vec{x}_1}|N_2\rangle\langle N_2|\overline{\chi}(\vec{0},0)|\Omega\rangle\Big\}. \tag{3.48}$$

Each state is once again split into energy E_{p_i}, momentum $\vec{p}_i$ and spin s_i, and by using the eigenvalues in eq. 3.37, for each eigenstate

$$C_{3pt}(\Gamma;\vec{p}',t;\vec{q},\tau;\mathcal{O}^{(q)}) = \sum_{N_1,N_2}\sum_{\vec{x}_1,\vec{x}_2}\frac{1}{4E_{p_1}E_{p_2}}e^{-i\vec{p}'\cdot\vec{x}_2}e^{i\vec{q}\cdot\vec{x}_1} \\ \mathrm{Tr}\Big\{\Gamma\langle\Omega|\chi(\vec{0},0)e^{-E_{p_1}t}e^{\vec{p}_1\cdot\vec{x}_2}|N_1\rangle\langle N_1|e^{E_{p_1}\tau}e^{-\vec{p}_1\cdot\vec{x}_1} \\ \mathcal{O}^{(q)}(0)e^{-E_{p_2}\tau}e^{\vec{p}_2\cdot\vec{x}_1}|N_2\rangle\langle N_2|\overline{\chi}(\vec{0},0)|\Omega\rangle\Big\}. \tag{3.49}$$

By evaluating the sum $\sum_{\vec{x}_1,\vec{x}_2}$ over $\vec{x}_1$ and $\vec{x}_2$ we find now two δ-functions as demonstrated in eq. 3.39, which amounts to replacing $\vec{p}_1 \to \vec{p}'$ and $\vec{p}_2 \to \vec{p} \equiv \vec{p}' - \vec{q}$, thus simplifying eq. 3.49

$$C_{3pt}(\Gamma;\vec{p}',t;\vec{q},\tau;\mathcal{O}^{(q)}) = \sum_{N_1,N_2,s_1,s_2}\frac{1}{4E_pE_{p'}}e^{-E_{p'}t}e^{-(E_p-E_{p'})\tau} \tag{3.50}$$

$$\mathrm{Tr}\left\{\Gamma\langle\Omega|\chi(\vec{0},0)|N_1,\vec{p}',s_1\rangle\langle N_1,\vec{p}',s_1|\mathcal{O}^{(q)}(0)|N_2,\vec{p},s_2\rangle\langle N_2,\vec{p},s_2|\overline{\chi}(\vec{0},0)|\Omega\rangle\right\}.$$

Again following the same procedure as for the two-point function, we substitute the interpolating fields from eq. 3.41 into eq. 3.47 for octet baryons, thus the forward propagating three-point correlator in terms of quark fields is given by

$$C_{3pt}(\Gamma;\vec{p}',t;\vec{q},\tau,\mathcal{O}^{(q)}) = \sum_{\vec{x}_1,\vec{x}_2}e^{-i\vec{p}'\cdot\vec{x}_2}e^{i\vec{q}\cdot\vec{x}_1}\epsilon^{abc}\epsilon^{a'b'c'}\tilde{C}_{\beta\gamma}\tilde{C}_{\beta'\gamma'}\Gamma_{\alpha'\alpha} \tag{3.51}$$

$$\left\langle u^a_\alpha(x_2)u^b_\beta(x_2)d^c_\gamma(x_2)\overline{q}^d_\delta(x_1)\mathcal{O}^{de}_{\delta\epsilon}q^e_\epsilon(x_1)\overline{u}^{a'}_{\alpha'}\overline{d}^{b'}_{\beta'}(0)\overline{u}^{c'}_{\gamma'}(0)\right\rangle, \tag{3.52}$$

where $q, \overline{q}$ are either u or d, the doubly or singly represented quark respectively.

At this point, we have the choice of using two common methods for calculating the three-point functions [73, 74], the first is known as 'sequential source through the sink', and the second, 'through the operator'. In this work, we will only focus on the first method and consider only the connected diagrams, since as we will soon see, the primary benefits of using this method over the second is the free choice of current

insertion operator $\mathcal{O}$, the insertion time τ and the current (or source) momentum $\vec{q}(\ \vec{p}\ )$ for each sequential propagator.

We begin by rewriting the three-point correlator into three terms,

$$C_{3pt}(\Gamma;\vec{p}\,',t;\vec{q},\tau;\mathcal{O}^{(q)}) = \sum_{\vec{x}_1} e^{i\vec{q}\cdot\vec{x}_1}\langle \mathrm{Tr}\left\{\Sigma_\Gamma^{(q)}(\vec{x}_2,t;\vec{x}_1,\tau;\vec{0},0)\mathcal{O}(\vec{x}_1,\tau)S^{(q)}(\vec{x}_1,\tau;0)\right\}\rangle, \tag{3.53}$$

where we now have a separate *fixed sink* propagator $\Sigma^{(q)}$ defined as

$$\Sigma_\Gamma^{(q)}(\vec{x}_2,t;\vec{x}_1,\tau;\vec{0},0) = \sum_{\vec{x}_2} S_\Gamma^{(q)}(\vec{x}_2,t;\vec{0},0)S^{(q)}(\vec{x}_2,t;\vec{x}_1,\tau) \tag{3.54}$$

where all the quark lines excluding the line with the current vertex are represented by $S_\Gamma^{(q)}(\vec{x}_2,t;\vec{0},0)$ as pictured in Fig. 3.6. The source is defined separately from all of the connected Wick contractions, for the case where the current vertex is located on one of the doubly represented quark lines,

$$\begin{aligned} S_\Gamma^{(u)a'a}(\vec{x}_2,t;\vec{0},0;\vec{p}\,') \equiv e^{-i\vec{p}\,'\cdot\vec{x}_2}\epsilon^{abc}\epsilon^{a'b'c'}\times \\ \Big[\overline{S^{(d)bb'}}(\vec{x}_2,t;\vec{0},0)S^{(u)cc'}(\vec{x}_2,t;\vec{0},0)\Gamma + \mathrm{Tr}[\overline{S^{(d)bb'}}(\vec{x}_2,t;\vec{0},0)S^{(u)cc'}(\vec{x}_2,t;\vec{0},0)]\Gamma + \\ \Gamma\overline{S^{(u)bb'}}(\vec{x}_2,t;\vec{0},0)\overline{S^{(d)cc'}}(\vec{x}_2,t;\vec{0},0) + \mathrm{Tr}[\Gamma S^{(u)bb'}(\vec{x}_2,t;\vec{0},0)\overline{S^{(d)cc'}}(\vec{x}_2,t;\vec{0},0)]\Big]. \end{aligned} \tag{3.55}$$

and for the alternate case of the singly represented quark vertex

$$\begin{aligned} S_\Gamma^{(d)cb'}(\vec{x}_2,t;\vec{0},0;\vec{p}\,') \equiv e^{-i\vec{p}\,'\cdot\vec{x}_2}\epsilon^{abc}\epsilon^{a'b'c'}\times \\ \Big[\overline{S^{(u)bb'}}(\vec{x}_2,t;\vec{0},0)\overline{\Gamma}\,\overline{S^{(u)cc'}}(\vec{x}_2,t;\vec{0},0) + \mathrm{Tr}[\Gamma S^{(u)bb'}(\vec{x}_2,t;\vec{0},0)\overline{S^{(u)cc'}}(\vec{x}_2,t;\vec{0},0)]\Big], \end{aligned} \tag{3.56}$$

In Fig. 3.7 we show a diagram that demonstrates the construction of the fixed sink propagator, $\Sigma^{(q)}$, from eq. 3.54, which is obtained via a second inversion

$$\sum_x M^{(q)}(\vec{x}\,'_1,\vec{x}_1)\gamma_5\Sigma^{(q)\dagger}(\vec{0},0;x_1,\tau;\vec{p}\,',t) = \gamma_5 S_\Gamma^{(q)\dagger}(\vec{x}_1,\tau;\vec{0},0,;\vec{p}\,')\delta_{x'_0,t}, \tag{3.57}$$

where we sum over the space-time point $(\vec{x}_1,\tau)$. We then insert the operator at the vertex and tie everything together with an ordinary propagator $S^{(q)}(\vec{x}_1,\tau;0)$ from eq. 3.53 as demonstrated in Fig. 3.8.

For this fixed sink method of generating the three-point correlation function, we are forced to fix the sink momentum $\vec{p}\,'$, the spin projector Γ, the choice of interpolating fields χ and the quark flavours interacting with the current before creating the fixed sink propagator. This then gives us the freedom to choose the current (source) momentum $\vec{q}$ $(\vec{p})$, the insertion time τ and the current insertion operator after the inversion. We must now isolate the matrix elements of interest through the construction of ratios of these two-point and three-point correlation functions.

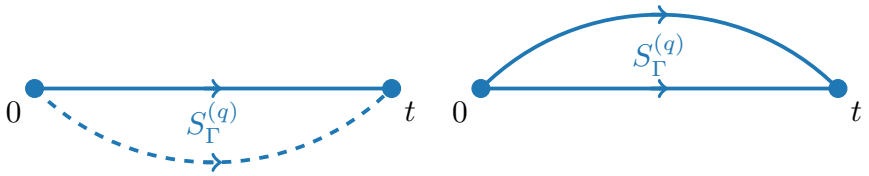

Figure 3.6: Diagram of the term $S_\Gamma^{(q)}(\vec{x}_2, t; \vec{0}, 0)$ from eq. 3.54, representing all the quark lines, excluding the quark with the current vertex. The solid blue lines, showing the doubly represented quark lines, and the dashed blue lines showing the singly represented quark line. The diagram on the left shows $S_\Gamma^{(u)}$ for when the a doubly represented quark line interacts with the current insertion, and on the right $S_\Gamma^{(d)}$ for when the singly represented quark interacts with the current insertion.

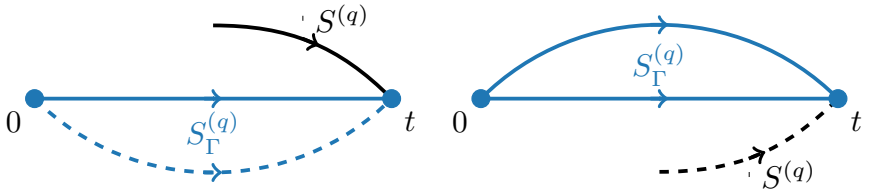

Figure 3.7: Similar to Fig. 3.6, only here we show $\Sigma_\Gamma^{(q)}(\vec{x}_2, t; \vec{x}_1, \tau; \vec{0}, 0)$ where we introduce the term $S^{(q)}(\vec{x}_2, t; \vec{x}_1)$ from eq. 3.54 as the black quark-line.

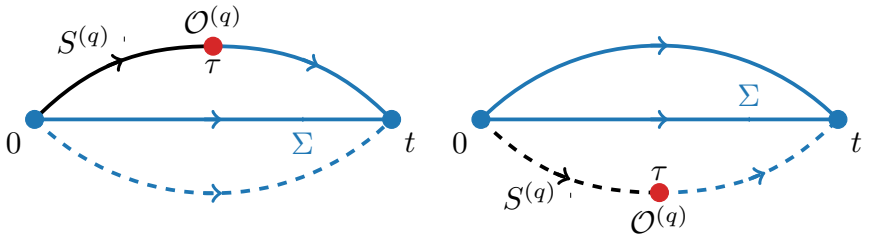

Figure 3.8: Similar to Fig. 3.6, only now showing the full three-point correlation function in eq. 3.53, where the blue lines represent $\Sigma_\Gamma^{(q)}(\vec{x}_2, t; \vec{x}_1, \tau; \vec{0}, 0)$, the red point indicates the location of the current operator insertion $\mathcal{O}^{(q)}$ and the black quark-line represents $S^{(q)}(\vec{x}_1, \tau; 0)$.

3.2.3 Ratios of Functions

The reason it is necessary to calculate both the two-point functions and three-point correlation functions is because we wish to determine matrix elements

$$\langle N(p',s')|\mathcal{O}(q)|N(p,s)\rangle \tag{3.58}$$

however the three-point function carries exponential time-dependent factors, along with the momentum dependent wave function overlaps as seen in eq. 3.50. To cancel off these additional terms we create a ratio of the two-point and three-point functions, where we take the two-point function from eq. 3.40,

$$C_{2pt}(\Gamma;\vec{p},t) = \sum_{E_p,s} \frac{1}{2E_p} e^{-E_p t} \mathrm{Tr}\left\{\Gamma\langle\Omega|\chi(\vec{0},0)|E_p,\vec{p},s\rangle\langle E_p,\vec{p},s|\overline{\chi}(\vec{0},0)|\Omega\rangle\right\}. \tag{3.59}$$

and the three-point correlation function from eq. 3.50

$$\begin{aligned} C_{3pt}(\Gamma;\vec{p}\,',t;\vec{q},\tau;\mathcal{O}^{(q)}) = &\sum_{E_p,E_{p'},s_1,s_2} \frac{1}{4E_pE_{p'}} e^{-E_{p'}t} e^{-(E_p-E_{p'})\tau} \\ &\mathrm{Tr}\left\{\Gamma\langle\Omega|\chi(\vec{0},0)|E_{p'},\vec{p}\,',s_1\rangle\langle E_{p'},\vec{p}\,',s_1|\mathcal{O}^{(q)}(0)|E_p,\vec{p},s_2\rangle\langle E_p,\vec{p},s_2|\overline{\chi}(\vec{0},0)|\Omega\rangle\right\}. \end{aligned} \tag{3.60}$$

By taking a specific combination of these two-point and three-point correlation functions, in the form of the ratio function,

$$R(t,\tau;p',p;\mathcal{O}) = \frac{C_{3pt}(\Gamma;\vec{p}\,',t;\vec{q},\tau;\mathcal{O}^{(q)})}{C_{2pt}(\Gamma;\vec{p},t)} \left[\frac{C_{2pt}(\Gamma;\vec{p}\,',\tau)C_{2pt}(\Gamma;\vec{p}\,',t)C_{2pt}(\Gamma;\vec{p},t-\tau)}{C_{2pt}(\Gamma;\vec{p},\tau)C_{2pt}(\Gamma;\vec{p},t)C_{2pt}(\Gamma;\vec{p}\,',t-\tau)}\right]^{\frac{1}{2}}. \tag{3.61}$$

all time dependence is removed from our correlation function at the large time approximation $0 \ll \tau \ll t < T/2$. With this ratio of two-point and three-point correlation functions we can calculate the matrix elements required to find the form factors, as described in the next chapter.

3.3 Lattice Systematics

In our formulation of the lattice, we have introduced the lattice spacing a and volume, and the quark flavours and masses. For us to then compare these lattice results with experiments, we must quantify our systematics. For example, where heavier than physical quark masses are chosen, appropriate extrapolations have to be considered.

3.3.1 Quark Mass

As we have mentioned, many lattice simulations are performed with larger than physical quark masses, which improves the speed at which we can invert the Dirac operator to compute quark propagators. As a result, we must then extrapolate the results obtained from these simulations to the physical point. For our work, we have chosen to simulate $2+1$ flavours of quarks, where this corresponds to the two mass degenerate u and d quarks, and a separate heavier s quark. There are several choices on the path taken to the physical point. It is common to fix the mass of the heavy strange quark at its physical value, and to then vary the masses of the light u and d quarks. In this work, however, we choose to start our trajectory to the physical point at the simplest point where all three quark flavours are degenerate, having the same mass at the $SU(3)$ flavour symmetric point, then vary the individual quark masses towards their physical value whilst keeping the flavour singlet quark mass fixed at its physical value,

$$\overline{m} \equiv \frac{1}{3}(2m_l + m_s) = constant. \tag{3.62}$$

This method of setting the quark masses has several advantages [75], the most prevelent in which is the fact that as we move away from the $SU(3)$ symmetric point, the flavour symmetry breaking effects can be easily investigated. By keeping the singlet quark mass fixed, we constrain expansions in the flavour-symmetry breaking, with flavour-singlet quanities constant at the leading order. We will look into these flavour-symmetry breaking expansions later in Chapter 6.

3.3.2 Finite Spacing and Volume

In lattice calculations, all dimensionful quantities are calculated with respect to the spacing a, where the values of the quark masses and the bare coupling β are set with a scale determined to match their physical value[76]. In these simulations, the scale is set by extrapolating for a fixed value of β and by varying the κ, a series of $SU(3)$ symmetric points along trajectories to the physical point [75, 77–79], and once determined, the lattice spacing is the same for all configurations with a fixed β. We have already seen the effect of the discrete lattice spacing on the action, but for continuum extrapolation, multiple values of a, or in our case β are required. By decreasing the lattice spacing, we are also decreasing the volume, and so as we go to smaller and smaller lattice spacings, we are required to increase the number of lattice sites in order to avoid increasing finite-volume artefacts.

We are forced to introduce a periodic in space and anti-periodic in time, boundary condition on our lattice from needing to have a finite number of lattice sites, which has been understood to introduce errors from potential 'wrap-around' effects [80]. To investigate these potential finite-volume effects on our results, it would be ideal to

	β	Lattice Volume	κ_0	κ_l	κ_s	$m_\pi(MeV)$	$m_K(MeV)$
1	5.5	$32^3 \times 64$	0.120900	0.120900	0.120900	465	465
2				0.121040	0.120620	360	505
3				0.121095	0.120512	310	520
4		$48^3 \times 96$		0.121166	0.120371	220	540
5		$32^3 \times 64$	0.120920	0.120920	0.120920	440	440
6			0.120950	0.120950	0.120950	400	400
7				0.121040	0.120770	330	435

Table 3.1: Details of the lattice simulation parameters. The parameter κ_0 denotes the value of $\kappa_l = \kappa_s$ at the SU(3)-symmetric point. Including the β value and lattice volumes with values for the κ_l indicating the kappa of the light quark and κ_s the strange quark with their equivalent pion and kaon masses.

perform lattice calculations on a variety of different volumes to determine whether such effects are significant.

For the majority of this work, we have used the first three mass configurations 1-3 on Table 3.1, on ensembles with lattice volumes $L^3 \times T = 32^3 \times 64$, with spacing $a = 0.074(2)$ fm [75, 77, 79]. This is less of a 'precision' study, with our focus more on the $SU(3)$ patterns and physical pictures.

In Fig. 3.9, we show the locations of each of the ensembles listed in Table 3.1 in relation to their trajectory towards the physical point, following a line of constant singlet mass $m_q = (m_u + m_d + m_s)/3 = (2m_l + m_s)/3$. It is clear that the primary trajectory beginning at $\kappa_0 = 0.120900$ does not quite match the physical singlet-mass line, and so extrapolation will require shifting not only along the simulation trajectory but also in a direction perpendicular to it. This is constrained by the addition of several singlet masses listed as simulations 5-7 in Table 3.1. We additionally have a an individual ensemble along the primary trajectory using a larger volume $L^3 \times T = 48^3 \times 96$, with at a pion mass of 220 MeV, much lighter than any of the other ensembles. This individual point can be used as a test of the finite-volume effects.

3.3.3 Renormalisation

For us to be able to match our lattice results with experimental results renormalised in another scheme (generally the modified minimal-subtraction ($\overline{\text{MS}}$) scheme), we must connect the regulators of two different renormalisation schemes. We approach this non-perturbatively, and use the regularisation-independent' momentum (RI'-MOM) subtraction scheme [81] to determine the renormalisation of our various lattice operators. We will investigate these renormalisation schemes further in Chapter 5.

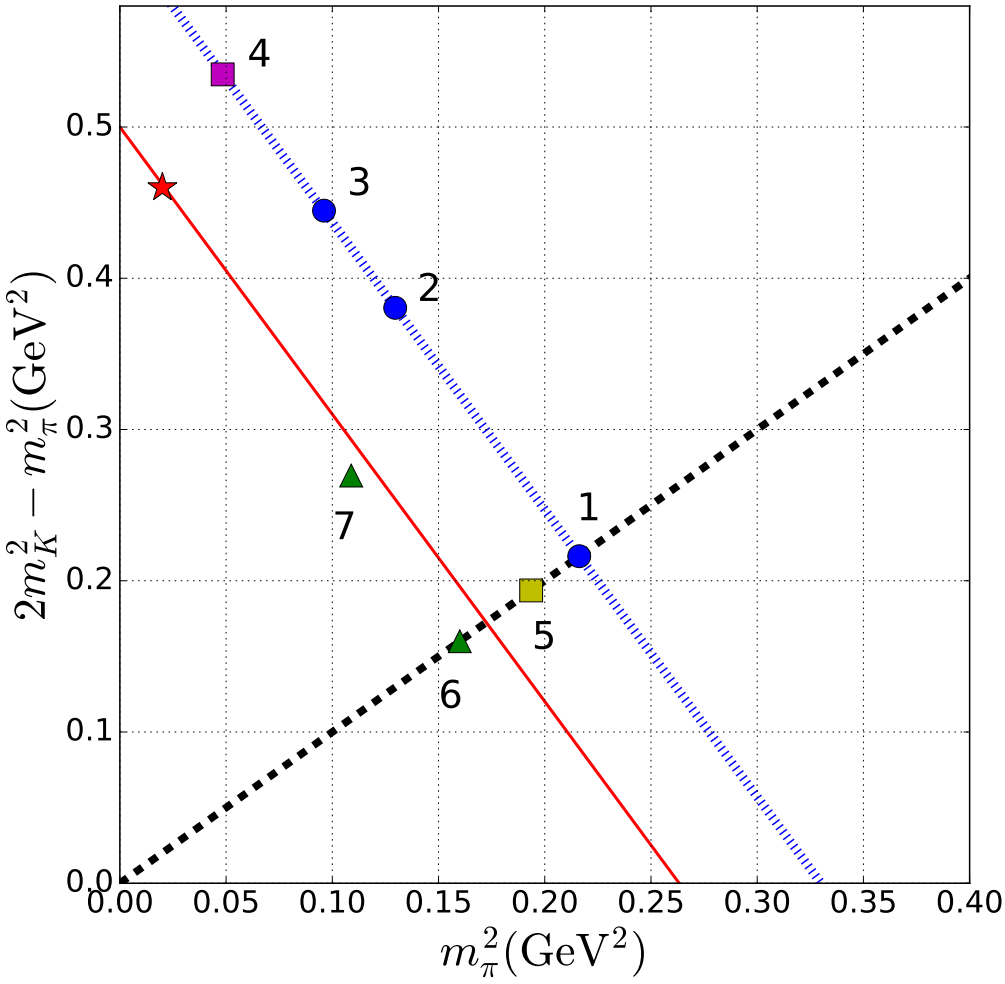

Figure 3.9: Labeled locations of the lattice ensembles from Table 3.1 in the $m_l - m_s$ plane. The black dashed line indicates the flavour-symmetric line where $m_l = m_s$. The primary simulation trajectory is shown by the blue dotted line, with the three blue circles representing configurations 1-3, and the purple square configuration 4. The red star denotes the physical point, while the solid red line indicates the physical value of the singlet mass. The green triangles represent simulation sets 6-7, and the yellow square represents the third symmetric configuration 5.

Chapter 4

Form Factors

As we discussed in Chapter 2, one of the key ways in which we extract information about the structure of the nucleon is through elastic electron-proton scattering experiments, which probe the spatial distribution of properties of the nucleon. These charge and magnetic densities within the nucleon are then represented by electromagnetic form factors [6], which we express as functions of the momentum Q^2 transferred from the electron to the proton. With the constant improvement of experimental measurements of these form factors and their deviation from a phenomenological dipole form[10–13], it is more important than ever to calculate precise computational QCD results for these functions. Lattice QCD provides a first principles approach to quantitatively probe non-perturbative QCD [15–17, 20–30, 82], while giving theoretical predictions of the hyperon form factors [16, 17, 26, 29, 30, 83] that are challenging to measure and poorly determined experimentally.

As well as giving us precise calculations of the form factors, lattice QCD is able to provide an interpretation of experimental results of these form factors within QCD. In the context of a lattice simulation, we are able to probe the individual quark-flavour contributions to the form factors, giving us some insight into the sensitivity of the distributions of quarks inside the hadron [26, 83]. It is also possible to probe the quark mass dependence of these quantities[84–86], as well as separate the quark-line connected and disconnected terms.

This chapter will use the methods described in Chapter 3 using our 2 + 1-flavour lattice QCD simulations, in order to calculate a range of form factors including the electromagnetic form factors and tensor form factors. A novel feature of this work is the investigation of the hyperon form factors, since they provide significant interest both in looking at the heavier baryons, as well as some valuable insight into the distribution of quarks inside the hadron, as we will be able to observe how the distribution of u quarks in the Σ^+ changes from those in the proton due to the presence of s spectator quarks.

4.1 Electromagnetic Form Factors

4.1.1 Dirac and Pauli Form Factors

The electromagnetic form factors in the form of the Dirac and Pauli form factors $F_1(Q^2)$ and $F_2(Q^2)$ are obtained from the decomposition of matrix elements of the electromagnetic current j_μ [87]

$$\langle B(p',s')|j_\mu(q)|B(p,s)\rangle = \overline{u}(p',s')\left[\gamma_\mu F_1(Q^2) + \frac{i\sigma_{\mu\nu}q^\nu}{2m_B}F_2(Q^2)\right]u(p,s) \tag{4.1}$$

where $u(p,s)$ are Dirac spinors with momentum p and spin polarisation s, the transfer momentum $q = p' - p$ and $Q^2 = -q^2$ and the mass of the B baryon m_B. These form factors F_1 and F_2 can additionally be written in a linear combination to form what are known as the Sachs electric and magnetic form factors respectively, where

$$G_E(Q^2) = F_1(Q^2) - \tau F_2(Q^2) \tag{4.2}$$

$$G_M(Q^2) = F_1(Q^2) + F_2(Q^2) \tag{4.3}$$

where $\tau = Q^2/4M^2$, which are the quantities that are more commonly determined from elastic electron-proton scattering experiments. From these Sachs electric and magnetic form factors, we can find the commonly-defined electric and magnetic mean-square radii at low Q^2,

$$\langle r^2\rangle_{E/M} = -\frac{6}{G^B_{E/M}(0)}\frac{d}{dQ^2}G^B_{E/M}(Q^2)\bigg|_{Q^2=0}. \tag{4.4}$$

For simple physical interpretations of the Sachs electric and magnetic form factors, we assume that the initial and final states of the nucleon are fixed within the same location and thus have the same internal structure. Thus a three-dimensional Fourier transforms of $G^B_E(Q^2)$ describes the charge density distribution within baryon B, similarly for the magnetic form factor $G^B_M(Q^2)$, encoding the magnetic current density distribution. In the limit as $Q^2 \to 0$, [88] the electric form factor $G^B_E(0)$ simply gives the charge of baryon B, while $G^B_M(0) = (G^B_E(0) + \kappa_B) = \mu_B$ defines the baryon magnetic moment, where $F_2^{B,q}(0) = \kappa^{B,q}$ is the anomalous magnetic moment.

As we go to larger values of Q^2 however, the wave function of the initial and final states will be different and the Fourier transform no longer applies since the nucleon mass is finite and the nucleon's recoil effect becomes important in the interpretation. Thus we consider the Breit frame, where the initial and final state nucleons have momenta with the same magnitude, minimising any nucleon recoil effect and acting similar to a Lorentz contraction, or a boost to the infinite momentum frame which is used in this work, presenting us with a pancake like structure leaving only the transverse plane, which we will briefly demonstrate with our lattice results and in more detail in Chapter 7 on transverse spin densities.

To find the electromagnetic form factors using the two-point and three-point functions on the lattice, we use the ratio Eq. 3.61 found in Chapter 3. By considering anti-periodic boundary conditions in time, the two point and three point functions can be rewritten in terms of nucleon spinors, thus

$$C_{2pt}(t;\vec{p}) = \sum_{\vec{s}} \mathrm{Tr}\left[\overline{u}(\vec{p},\vec{s})\Gamma u(\vec{p},\vec{s})\right]\left[\frac{\sqrt{Z\overline{Z}}}{2E_{\vec{p}}}e^{-E_{\vec{p}}t} + \frac{\sqrt{Z'\overline{Z}'}}{2E'_{\vec{p}}}e^{-E'_{\vec{p}}(T-t)}\right] \tag{4.5}$$

where the Z and $\overline{Z}$ are the wave function overlaps with the proton and the source and the sink respectively, and T is the total lattice time extent. In Euclidean space, we have the spinor sum

$$\sum_{s} u(\vec{p},\vec{s})\overline{u}(\vec{p},\vec{s}) = -i\not{p} + m, \tag{4.6}$$

and using the projection matrix $\Gamma_{unpol.} = \frac{1}{2}(1+\gamma_4)$, for a large enough t such that the lowest state dominates, we get

$$C_{2pt}(t,\vec{p}) = \left[\sqrt{Z\overline{Z}}\left(\frac{E_{\vec{p}}+m}{E_{\vec{p}}}\right)e^{-E_{\vec{p}}t} + \sqrt{Z'\overline{Z}'}\left(\frac{E'_{\vec{p}}+m'}{E'_{\vec{p}}}\right)e^{-E'_{\vec{p}}(T-t)}\right] \tag{4.7}$$

and similarly for the three point function from eq. 3.50,

$$C_{3pt}(t,\tau;\vec{p}\,',\vec{p};\mathcal{O}) = \sqrt{Z(\vec{p}\,')\overline{Z}(\vec{p})}F(\Gamma,J^\mu)e^{-E_{\vec{p}\,'}(t-\tau)}e^{-E_{\vec{p}}\tau} \tag{4.8}$$

where we have

$$F(\Gamma,J^\mu) = \frac{1}{4}\mathrm{Tr}\left[\left(\gamma_4 - i\frac{\vec{p}\,'\cdot\vec{\gamma}}{E_{\vec{p}\,'}} + \frac{m}{E_{\vec{p}\,'}}\right)J^\mu\left(\gamma_4 - i\frac{\vec{p}\cdot\vec{\gamma}}{E_{\vec{p}}} + \frac{m}{E_{\vec{p}}}\right)\right]. \tag{4.9}$$

Thus the matrix elements in the form

$$\langle N(\vec{p}\,',\vec{s}\,')|\mathcal{O}(\vec{q})|N(\vec{p},\vec{s})\rangle = \overline{u}(\vec{p}\,',\vec{s}\,')J^\mu u(\vec{p},\vec{s}) \tag{4.10}$$

can be solved. Thus for the electromagnetic form factors from eq. 4.1, we have

$$j^\mu = \gamma^\mu F_1(Q^2) + i\sigma^{\mu\nu}\frac{q_\nu}{2M}F_2(Q^2). \tag{4.11}$$

Now for example, we can show the calculation required to find the $F_1(Q^2=0)$ value, where $p = p' = 0$, and thus the term with $F_2(Q^2)$ vanishes. Since the lattice calculations are done in Euclidean space and the matrix elements are written in Minkowski space, the transformations required are

$$\gamma_0^M = \gamma_4^E \quad , \quad \gamma_i^M = -i\gamma_i^E \quad , \quad p_4^E = ip_0^M \equiv iE(p) \quad , \quad p_i^E = -p_i^M. \tag{4.12}$$

And so for $Q^2 = 0$, eq. 4.1 reduces to

$$\langle N(p',s')|\overline{q}\gamma_\mu^E q|N(p,s)\rangle = \overline{u}(p',s')\gamma_\mu^E u(p,s)F_1(Q^2=0) \tag{4.13}$$

where now we have the simple form $J^\mu = \gamma^\mu F_1(0)$. Inserting these into $F(\Gamma, J^\mu)$, we find the time and spatial components

$$F(\Gamma_{unpol.},\gamma_4) = \frac{1}{2E_pE'_p}[(E_p+m)(E'_p+m)+p'\cdot p] \tag{4.14}$$

and

$$F(\Gamma_{unpol.},\gamma_i) = \frac{-i}{2E_pE'_p}[(E_p+m)p'+(E'_p+m)p]. \tag{4.15}$$

In the case of $p' = p = 0$ we are simply left with $F(\Gamma_{unpol.},\gamma_4) = 2F_1(0)$ and the spatial components vanish. Returning to the ratio of three-point and two-point functions in eq. 3.61, we find that it is in a simple form

$$R(t,\tau;p',p;J^\mu) = \sqrt{\frac{E'_pE_p}{(E'_p+m)(E_p+m)}}F(\Gamma,J^\mu) \tag{4.16}$$

and thus for our example we find exactly that the ratio $R(t,\tau;p',p;J^\mu) = F_1(Q^2=0)$. More generally we consider all the combinations at each fixed value of Q^2 and compute these as simultaneous equations to solve for the form factors $F_1(Q^2)$ and $F_2(Q^2)$. For a specific non-physical mass configuration, we follow this procedure to compute the form factors at various fixed Q^2 values.

4.1.2 Lattice Results

In order to demonstrate our lattice result, we choose a source sink separation of $t_{\text{sink}} = 13$ for a physical separation of around one fermi, and take plateaus of the ratio function eq. 4.16 for a third of the time slices from $[5,8]$ in order avoid the source and sink. In this work we do not consider the effects of excited state contamination, but there are methods avaliable to reduce these effects including the variational method [89–94], locally split sink interpolating fields [95] and the 'Pencil of function' method [96–98].

In Fig. 4.1 we show results for the first electromagnetic form factor $F_1(Q^2)$ for the doubly represented quark contributions from ensemble 7 on Table. 3.1. The three different baryons that we consider; the proton p, the sigma Σ and the cascade Ξ, are represented by the blue diamond, green circle and red triangle respectively. As the current operator j^μ isn't conserved under these processes, we enforce charge conservation on each ensemble through a multiplicative renormalisation of

$$Z_V = \frac{2}{F_1^u(0)} \quad \text{or} \quad \frac{1}{F_1^d(0)}. \tag{4.17}$$

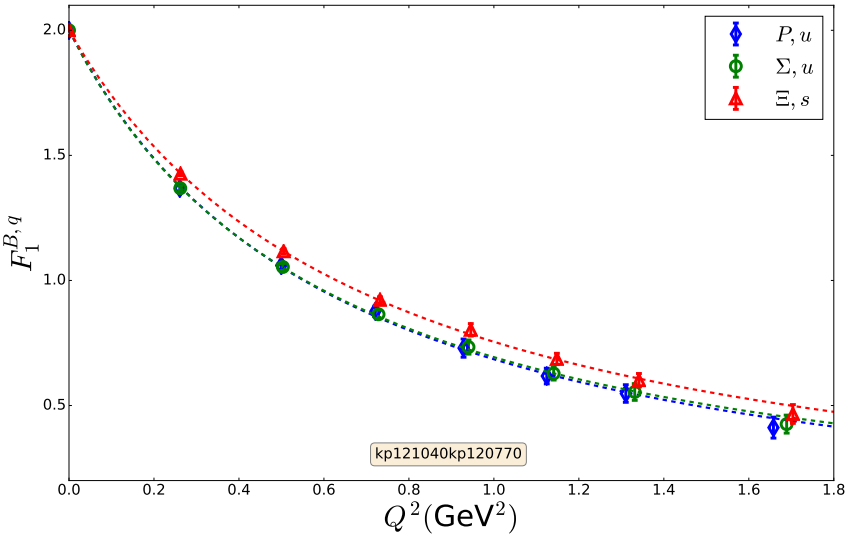

Figure 4.1: Electromagnetic form factor $F_1^u(Q^2)$ for the $\kappa_l = 0.12104$, $\kappa_s = 0.12077$ lattice configuration ensemble 7 on Table 3.1. Comparing the doubly represented quark contribution of the up quark in the proton and Σ and the strange quark in the Ξ baryon.

This ensures the correct quark counting in the double and singly represented quarks. We then fit F_1 with a 2 parameter ansätz [16]:

$$F_1(Q^2) = \frac{F_1(0)}{1 + c_{12}Q^2 + c_{14}Q^4} \tag{4.18}$$

and similarly F_2 with,

$$F_2(Q^2) = \frac{F_2(0)}{(1 + c_{22}Q^2)^2}, \tag{4.19}$$

where c_{ij} and the anomalous magnetic moment $F_2^{B,q}(0) = \kappa^{B,q}$ are fit parameters.

As we can see from Fig. 4.1, the heavier particle Ξ (cascade) is higher, corresponding to it being more compact, than both the proton and Σ (Sigma), due to the mass difference between the doubly represented strange quark and the up quarks of the Σ and proton.

In Figs.(4.2-4.4), we can see both the doubly and singly represented quark contributions for the $F_1(Q^2)$ and $F_2(Q^2)$ form factors. We can see again for the singly represented quark contribution of the F_1 form factor in Fig. 4.2 that the value at $Q^2 = 0$ is set to 1 thus enforcing charge conservation. With the presence of the helicity flip operator $\sigma_{\mu\nu}$ in the pre-factor term of F_2, the form factor is senstive to the polarisation of the nucleon, and we see the doubly represented contribution gives a positive result, while the singly represented contribution is negative. We also cannot measure

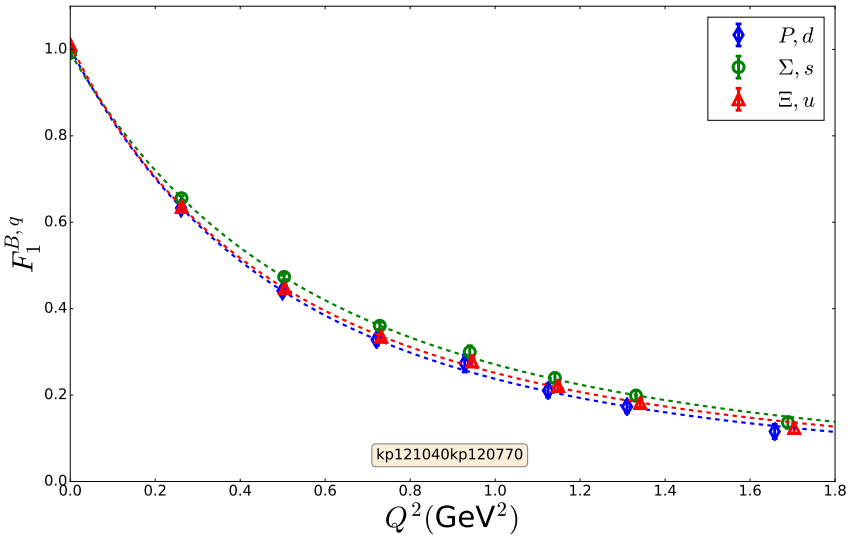

Figure 4.2: Similar to Fig. 4.1, only now comparing the singly represented quark contribution of the down quark in the proton, strange quark in the Σ and the up quark in the Ξ baryon.

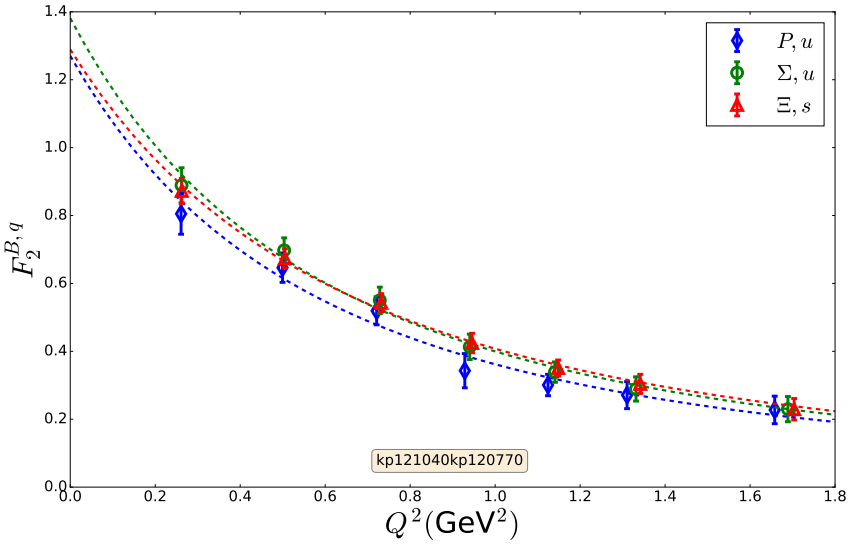

Figure 4.3: Electromagnetic form factor $F_2^u(Q^2)$ for the $\kappa_l = 0.12104$, $\kappa_s = 0.12077$ lattice configuration ensemble 7 on Table 3.1. Comparing the doubly represented quark contribution of the up quark in the proton and Σ and the strange quark in the Ξ baryon.

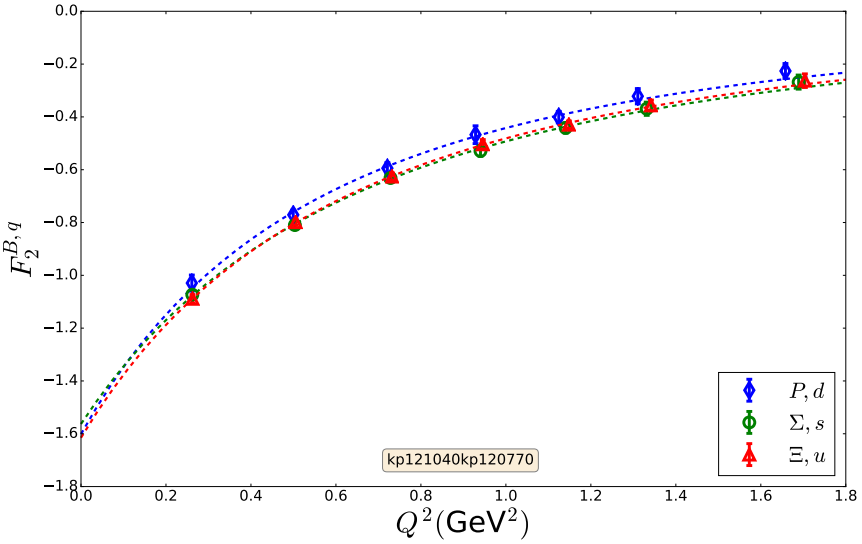

Figure 4.4: Similar to Fig. 4.3, only now comparing the singly represented quark contribution of the down quark in the proton, strange quark in the Σ and the up quark in the Ξ baryon.

directly a value for $F_2(Q^2 = 0)$ due to the q dependence in the pre-factor, thus we instead extrapolate backwards using the dipole fit given in eq. 4.19.

As an example of using the infinite momentum frame in order to look at the spatial distributions within the proton on a transverse plane, we can take a two-dimensional Fourier transform from transverse momentum space to the $b_\perp$ dependent form:

$$f(b_\perp) \equiv \int \frac{d^2q}{(2\pi)^2} e^{-ib_\perp \cdot\, q} f(-q^2), \tag{4.20}$$

where $Q^2 = -q^2$ is the transverse momentum transferred to the nucleon. By applying this Fourier transform to the F_1 Dirac form factor, we can create an example of the transverse spatial quark density distribution in an unpolarised proton as seen in Fig. 4.5.

The x and y axes in Fig. 4.5 correspond to the b_x and b_y respectively, $b_\perp$ describing the quark's transverse distance from the centre of momentum of the proton. Here we are showing the u quark in a proton, where the shading on the contour plot corresponds to an increased probability density of the quark within the proton. Due to the form of the F_1^u form factor, we observe rotational symmetry about the origin of the proton. We will use this technique further in Chapter 7 to gain further understanding on quark density distributions within the octet baryons.

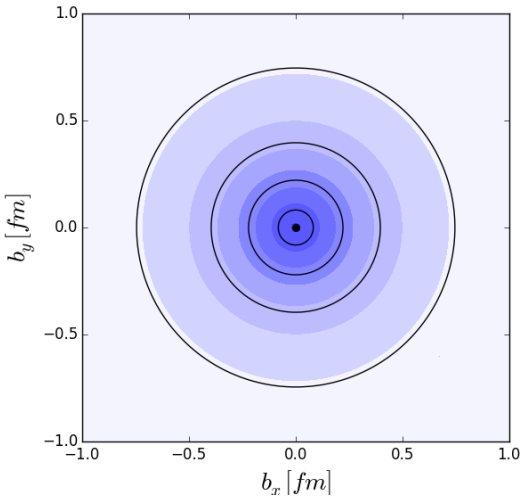

Figure 4.5: Quark density distribution of the F_1^u Dirac form factor in an unpolarised Proton.

4.2 Tensor Form Factors

Following the calculation of the electromagnetic form factors, we now move on to the tensor form factors. Similar to the EM form factors, we are able to find the anomalous tensor charge from the calculation of $A_{T10}(Q^2 = 0) = g_T$, and also using a combination of the EM and tensor form factors, we are later able to create a transverse spin density distribution through a similar method to a charge distribution. We only need to consider the first order $n = 1$ tensor generalised form factors GFF's, $A_{Tn0}, B_{Tn0}, \tilde{A}_{Tn0}$ found in the form [99]

$$\langle P'\Lambda' \mid \overline{\psi}(0) i\sigma^{\mu\nu}\psi(0) \mid P\Lambda\rangle = \overline{u}(P',\Lambda')\{i\sigma^{\mu\nu}A_{T10}(t) \tag{4.21}$$

$$+ \frac{\overline{P}^{[\mu}\Delta^{\nu]}}{m^2}\tilde{A}_{T10}(t) + \frac{\gamma^{[\mu}\overline{P}^{\nu]}}{2m}B_{T10}(t)\}u(P,\Lambda) \tag{4.22}$$

where $\gamma^{[\mu}\overline{P}^{\nu]} \equiv \gamma^{\mu}\overline{P}^{\nu} - \gamma^{\nu}\overline{P}^{\mu}$, $\Delta = P' - P$, $\overline{P} = \frac{P'+P}{2}$ and $i\sigma^{\mu\nu} = i\gamma^{\mu}\gamma^{\nu}$. Again we need to transform this from Minkowski space to Euclidean space, where the transformation is given by the same transformation laws from eq. 4.12, and so we want to simplify the pre-factor terms in the expression to allow us to form the systems of linear equations required to solve for the tensor form factors. After the conversion from Minkowski to

Euclidean space, we now evaluate the second pre-factor

$$i\frac{\overline{P}^{[\mu}\Delta^{\nu]}}{m^2} = i\frac{1}{2m^2}((P'_\mu + P_\mu)(P'_\nu - P_\nu) - (P'_\nu + P_\nu)(P'_\mu - P_\mu)) \tag{4.23}$$

$$= \frac{i}{2m^2}((P'_\mu P'_\nu - P'_\mu P_\nu + P_\mu P'_\nu - P_\mu P_\nu) - (P'_\nu P'_\mu - P'_\nu P_\mu + P_\nu P'_\mu - P_\nu P_\mu)) \tag{4.24}$$

$$= \frac{i}{m^2}(P'_\nu P_\mu - P'_\mu P_\nu), \tag{4.25}$$

while the third pre-factor

$$\frac{-i\gamma^{[\mu}\overline{P}^{\nu]}}{2m} = \frac{-i}{4m}(\gamma_\mu(P'_\nu + P_\nu) - \gamma_\nu(P'_\mu + P_\mu)). \tag{4.26}$$

We then evaluate these equations for the values of $\sigma^{\mu\nu}$ where $\mu < \nu = 0, 1, 2, 3$, beginning with the evaluation of σ^{01} where $\mu = 0,\ \nu = 1$, and so for the second pre-factor

$$\frac{i\overline{P}^{[\mu}\Delta^{\nu]}}{m^2} = \frac{i}{m^2}(P'_1 P_0 - P'_0 P_1) \tag{4.27}$$

$$= \frac{i}{m^2}(iEP'_1 - iP_1 E') \tag{4.28}$$

$$= \frac{-1}{m^2}(EP'_1 - P_1 E'), \tag{4.29}$$

and similarly the third pre-factor term

$$\frac{-i\gamma^{[\mu}\overline{P}^{\nu]}}{2m} = \frac{-i}{4m}(\gamma_0(P'_1 + P_1) - \gamma_1(P'_0 + P_0)) \tag{4.30}$$

$$= \frac{-i}{4m}(-i\gamma_0(P'_1 + P_1) + i\gamma_1(iE' + iE)) \tag{4.31}$$

$$= \frac{1}{4m}(-\gamma_0(P'_1 + P_1) + i\gamma_1(E' + E)). \tag{4.32}$$

Thus we find for σ_{01} in Euclidean space

$$\langle P'\Lambda' \mid \overline{\psi}(0)\sigma_{01}\psi(0) \mid P\Lambda\rangle \tag{4.33}$$

$$= \overline{u}(P', \Lambda')\{\sigma_{01}A_{T10} - \frac{1}{m^2}(EP'_1 - P_1 E')\tilde{A}_{T10} \tag{4.34}$$

$$+ \frac{1}{4m}(-\gamma_0(P'_1 + P_1) + i\gamma_1(E' + E))B_{T10}\}u(P, \Lambda). \tag{4.35}$$

Similarly for σ_{02} and σ_{03}, we find

$$\langle P'\Lambda' \mid \overline{\psi}(0)\sigma_{0i}\psi(0) \mid P\Lambda\rangle \tag{4.36}$$

$$= \overline{u}(P', \Lambda')\{\sigma_{0i}A_{T10} - \frac{1}{m^2}(EP'_i - P_i E')\tilde{A}_{T10} \tag{4.37}$$

$$+ \frac{1}{4m}(-\gamma_0(P'_i + P_i) + i\gamma_i(E' + E))B_{T10}\}u(P, \Lambda), \tag{4.38}$$

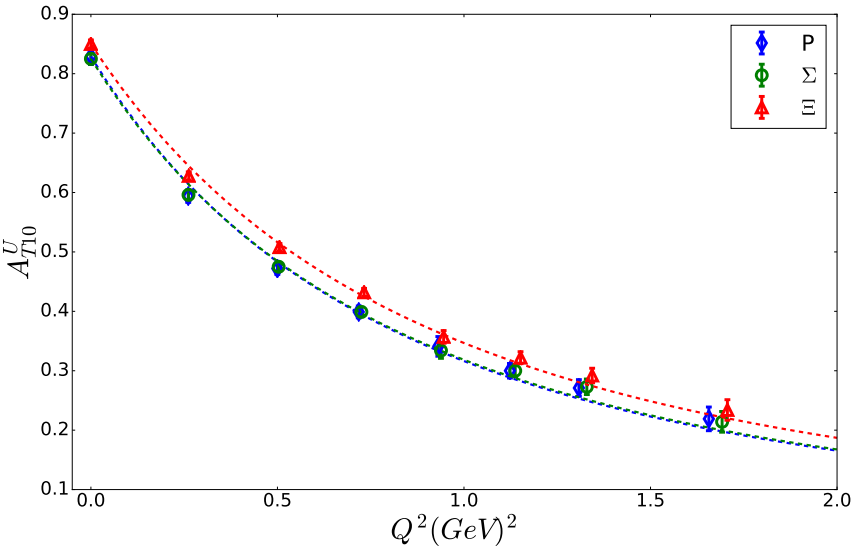

Figure 4.6: The unrenormalised tensor form factor $A^u_{T10}(Q^2)$ for the $\kappa_l = 0.12104$, $\kappa_s = 0.12062$ lattice configuration. Comparing the Doubly represented quark contribution of the up quark in the Proton and Σ and the strange quark in the Ξ baryon.

and for σ_{12}, σ_{13} and σ_{23}, we find

$$\langle P'\Lambda' \mid \overline{\psi}(0)\sigma_{ij}\psi(0) \mid P\Lambda\rangle \tag{4.39}$$

$$= \overline{u}(P',\Lambda')\{\sigma_{ij}A_{T10} + \frac{i}{m^2}(P'_jP_i - P'_iP_j)\tilde{A}_{T10} \tag{4.40}$$

$$+ \frac{1}{4m}(\gamma_j(P'_i + P_j) + \gamma_i(P'_j + P_j))B_{T10}\}u(P,\Lambda), \tag{4.41}$$

where these are our 6 equations in Euclidean space.

4.2.1 Lattice Results

Similarly to the electromagnetic form factors, by using the ratio of two-point and three-point functions and solving for the tensor form factors using the matrix elements at various q momenta as linear equations, the unrenormalised results are shown in the following figures.

Figs. (4.6-4.7) show the first tensor form factor A_{T10} for the three baryons that are considered: the proton p, the sigma Σ and the cascade Ξ, displayed in blue, green and red respectively. Fig. 4.6 displays the doubly represented quark contributions, so for the proton and sigma we would consider the up quark to be doubly represented, whereas for the cascade, the strange quark replaces the up quark. The dashed lines in

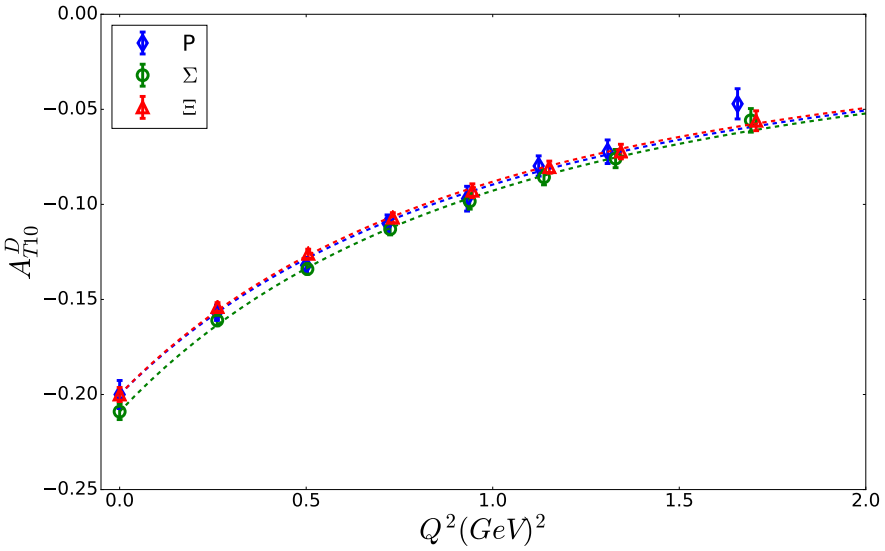

Figure 4.7: The unrenormalised tensor form factor $A^d_{T10}(Q^2)$ for the $\kappa_l = 0.12104$, $\kappa_s = 0.12062$ lattice configuration. Comparing the Singly represented quark contribution of the down quark in the Proton, strange quark in the Σ and the up quark in the Ξ baryon.

their respective colours show the dipole like fit used on each of the tensor form factors where

$$A_{T10}(Q^2) = \frac{A_{T10}(0)}{(1 + Q^2/(m_D)^2)^2} \tag{4.42}$$

for each tensor form factor respectively. Thus when analysing Fig. 4.6, we see that the three baryons carry the same shape, where as we might expect, the heavier cascade particle has a larger magnitude as Q^2 increases, compared to the lighter up quark contributions from the proton and sigma. We note that the dipole appears to struggle to describe the inital steepness followed by the flattening of the curve, and in Chapter 7, we will look at alternative fits. In Fig. 4.7, we see a similar Q^2 dependence only now the values are negative as was the case for the singly represented F_2 Pauli form factor, due to the helicity flip operator $\sigma_{\mu\nu}$ present in the pre-factor of both A_{T10} and F_2. In this case, the sigma, which has the heavier singly represented strange quark, the value is larger in magnitude in comparison to the up and down from the proton and cascade baryons.

The second and third tensor form factor plots are avaliable in Appendix F with Figs. (F.1-F.2) for tensor form factor $\tilde{A}_{T10}$, and Figs. (F.3-F.4) where instead of plotting B_{T10}, which is a very small value, we instead plot the much more useful $\overline{B}_{T10} \approx 2\tilde{A}_{T10} + B_{T10}$ [25], which we require later in Chapter 7 for the transverse spin density. The two plots show again the same form of dipole, only due to the Δ

dependence in the pre-factors of these two tensors, it is impossible to get a value at $Q^2 = 0$ as it was for A_{T10}, thus we fit to the same dipole form to allow the least squares fitting to determine a value for $\overline{B}_{T10}(0)$ and $\tilde{A}_{T10}(0)$.

4.3 Summary

In this chapter we have demonstrated how to calculate the electromagnetic and tensor form factors on the lattice using the processes discussed in Chapter 3. These calculations are limited to the masses and configurations shown in Table 3.1, and having looked at the form of their Q^2 dependence, we have fitted these values to appropriate ansätze in order to find a functional form for the Dirac and Pauli electromagnetic and first order ($n = 1$) tensor form factors. As we progress, we will find that improvements can be made to the calculation of these form factors, with the implementation of renormalisation as will be shown in Chapter 5, and with techniques bringing a series of configurations together and, using the properties of $SU(3)$ flavour breaking, extrapolate our results to the physical point in Chapter 6. These results, along side their improvements, will then be essential in the calculation of the transverse spin densities of the octet baryons in Chapter 7.

Chapter 5

Renormalisation

When calculating the Feynman path integrals in continuum QCD, we run into problems with divergent integrals, and so we must at some point cut off the integral to remove such divergences. When using lattice QCD, we instead introduce the lattice spacing which regulates the integral by cutting off the higher frequency modes. Unfortunately when comparing the correlation functions and values extracted from our lattice to experimental results, the cut off provided by the lattice spacing is insufficient and so we must include an additional renormalisation on our lattice operators to remove any further divergences. One such method is the Regularisation Independent Momentum (RI-MOM) renormalisation scheme. This scheme attempts to copy the procedure used in continuum perturbation theory, but in practical applications, we require a variant of the RI-MOM scheme, which differs in the renormalisation factor of the quark field. This modified RI-MOM denoted as RI'-MOM can be converted into the Modified Minimal Subtraction scheme ($\overline{\text{MS}}$) using continuum perturbation theory, which is useful since phenomenological results are often presented in this $\overline{\text{MS}}$ scheme.

The work in this chapter follows closely the work and method used in [100], extending it in order calculate the multiplicative renormalisation constants over a wide range of lattice volumes, spacings and configurations.

5.1 RI'-MOM

The RI'-MOM method involves comparing lattice calculations of off-shell Green's functions directly to continuum perturbation theory results. Matching these results works best at short distances, where we have a small running coupling constant, and effects such as chiral symmetry breaking are no longer a problem.

We start by constructing the Greens functions on the lattice with source four-momentum p and sink four-momentum p'.

$$G_{\alpha\beta}(p,p',\mathcal{O}) \equiv \frac{a^{12}}{V}\sum_{x,y,z} e^{-ip'\cdot(x-z)}e^{-ip\cdot(z-y)}\langle \mathcal{O}_{\alpha\beta}(x,y,z)\rangle, \tag{5.1}$$
$$\mathcal{O}_{\alpha\beta}(x,y,z) \equiv q_\alpha(x)\mathcal{O}(z)\overline{q}_\beta(y),$$

where V is the volume of the lattice and q is an up/down/strange quark field. Next we define the amputated Greens function as

$$\Gamma(p,p',\mathcal{O}) = S^{-1}(p)G(p,p',\mathcal{O})S^{-1}(p'), \tag{5.2}$$

with the definition of a quark propagator being

$$S(p) \equiv \frac{a^8}{V}\sum_{x,z} e^{-ip\cdot(x-y)}\langle q_\alpha(x)\overline{q}_\beta(y)\rangle \tag{5.3}$$

This is easiest to calculate when $p = p'$ when there is zero momentum transfer, such that we can impose a renormalisation condition on the vertex function, and so following [101–103],

$$\Gamma_R(p) = Z_q^{-1}Z_{\mathcal{O}}\Gamma(p) \tag{5.4}$$

where Z_q is the renormalisation for the fermion field, and $Z_{\mathcal{O}}$ is the renormalisation value required for the operator $\mathcal{O}$. The renormalisation value Z_q can be written as the projection of the propagator onto the Born massless quark $\Lambda_q(p)$,

$$Z_q = \Lambda_q(p)|_{p^2=\mu^2}, \qquad \Lambda_q(p) = \frac{Tr(-i\sum_\mu \sin(ap_\mu)aS^{-1}(p)}{12\sum_\mu \sin^2(ap_\mu)}. \tag{5.5}$$

We can then fix $Z_{\mathcal{O}}$ by the renormalisation condition

$$\frac{1}{12}Tr[\Gamma_R(p,p,\mathcal{O})\Gamma^{-1}_{Born}(p,p',\mathcal{O})]_{p^2=\mu^2} = 1 \tag{5.6}$$

with the renormalisation scale set to $p^2 = \mu^2$ for some μ^2. By using the Born term Γ_{Born} for the vertex function, we can rearrange it into an expression for the renormalisation constant $Z_{\mathcal{O}}$,

$$Z = 12Z_q Tr[\Gamma(p,p,\mathcal{O})\Gamma^{-1}_{Born}(p,p,\mathcal{O})]^{-1}_{p^2=\mu^2} \tag{5.7}$$

The Born term $\Gamma_{Born}(p,p,\mathcal{O})$ changes with our choice of operator $\mathcal{O}$, the momentum p and the momentum transfer $p'-p$ (if non-zero),

$$\Gamma_{Born}(p,p,I) = -iI, \qquad \Gamma_{Born}(p,p,\gamma_\mu) = -i\gamma_\mu$$
$$\Gamma_{Born}(p,p,\gamma_\mu\gamma_\nu) = -i\gamma_\mu\gamma_\nu, \qquad \Gamma_{Born}(p,p,\gamma_\mu\gamma_5) = -i\gamma_\mu\gamma_5. \tag{5.8}$$

We can calculate these renormalisation quantities on the lattice by first finding the Fourier transformed quark propagator in Eq. (5.3), by taking a space-time Fourier transform of the inverse Dirac Matrix

$$\hat{S}(p) = \sum_x e^{-ip.x}\hat{S}(x,0). \tag{5.9}$$

where we represent the operator under study in the form

$$\sum_z \mathcal{O}(z) = \sum_{z,z'} \overline{q}(z)J(z,z')q(z'). \tag{5.10}$$

We calculate the nonamputated Greens function defined in Eq. (5.1) as the gauge field average of the quantity

$$\hat{G}(p) = \frac{1}{V}\sum_{x,y,z,z'} e^{-ip\cdot(x-y)}\hat{S}(x,z)J(z,z')\hat{S}(z',y), \tag{5.11}$$

constructed from the quark propagator $\hat{S}$ on the same gauge field configuration. With the relation

$$\hat{S}(x,y) = \gamma_5\hat{S}(y,x)^+\gamma_5 \tag{5.12}$$

we can rewrite $\hat{G}(p)$ as

$$\hat{G}(p) = \frac{1}{V}\sum_{z,z'}\gamma_5\left(\sum_x \hat{S}(z,x)e^{ip\cdot x}\right)^+\gamma_5 J(z,z')\left(\sum_y \hat{S}(z',y)e^{ip\cdot y}\right). \tag{5.13}$$

These quantities

$$\sum_x \hat{S}(z,x)e^{ip\cdot x} \tag{5.14}$$

are calculated by solving the lattice Dirac equation using a momentum source,

$$\sum_x M(y,z)\left(\sum_x \hat{S}(z,x)e^{ip\cdot x}\right) = e^{ip\cdot y}, \tag{5.15}$$

where $M(x,y)$ represents the fermion matrix, and the number of matrix inversions required is proportional to the number of momenta we consider [104].

The result from this renormalisation calculation is a variant of the Regularisation Independent Momentum scheme (RI'-MOM). This is a convenient scheme for us to compute renormalisation factors in, but phenomenological results are usually given in the Modified Minimal Subtraction scheme ($\overline{\text{MS}}$), and so we need to go through a process to convert our calculated RI'-MOM renormalisation factors into the $\overline{\text{MS}}$ scheme.

5.1.1 Moving to MS scheme

In order to convert our RI'-MOM renomalisation factors into the $\overline{\text{MS}}$ scheme, we take eq. 5.7 at various scales of μ, and convert them into a reference scale which we set to 2 GeV and move to an intermediary stage using the Renormalisation Group Invariant (RGI) scheme before converting from RI'-MOM to $\overline{\text{MS}}$, giving us

$$Z_{\mathcal{O}}^{RGI} = Z_{\mathcal{O}}^{\overline{\text{MS}}}(2\text{GeV})\Delta Z_{\mathcal{O}}^{\overline{\text{MS}}}(2\text{GeV}) = Z_{\mathcal{O}}^{\text{RI'-MOM}}(\mu)\Delta Z_{\mathcal{O}}^{\text{RI'-MOM}}(\mu) \tag{5.16}$$

and thus

$$\begin{aligned} Z_{\mathcal{O}}^{\overline{\text{MS}}}(2\text{GeV}) &= C_{\mathcal{O},\text{RGI}}^{\text{RI'-MOM},\overline{\text{MS}}}(2\text{GeV},\mu) Z_{\mathcal{O}}^{\text{RI'-MOM}}(\mu), \\ C_{\mathcal{O},\text{RGI}}^{\text{RI'-MOM},\overline{\text{MS}}}(2\text{GeV},\mu) &= \frac{\Delta Z_{\mathcal{O}}^{\text{RI}'-\text{MOM}}(\mu)}{\Delta Z_{\mathcal{O}}^{\overline{\text{MS}}}(2\text{GeV})}. \end{aligned} \tag{5.17}$$

To then perturbatively calculate the conversion factors ΔZ, we start with a three loop approximation of the coupling constant $g^{\mathcal{S}}(\mu)$ [105] with scheme $\mathcal{S}$,

$$\frac{g^{\mathcal{S}}(\mu)^2}{16\pi^2} = \frac{1}{\beta_0^{\mathcal{S}} L} - \frac{\beta_1^{\mathcal{S}}}{\beta_0^{\mathcal{S}3}} \frac{\log L}{L^2} + \frac{1}{\beta_0^{\mathcal{S}5}} \frac{\beta_1^{\mathcal{S}2} \log L^2 - \beta_1^{\mathcal{S}2} \log L + \beta_2^{\mathcal{S}} \beta_0^{\mathcal{S}} - \beta_1^{\mathcal{S}2}}{L^3}, \tag{5.18}$$

$$L \equiv \log \frac{\mu^2}{\Lambda_{\mathcal{S}}^2}, \tag{5.19}$$

Where the coefficients in the definition of $\beta^{\mathcal{S}}$ functions in the $\overline{\text{MS}}$ and RI'-MOM scheme coincide up to three loops and are given by [106, 107]

$$\begin{aligned} \beta_0 &= 11 - \frac{2}{3} N_f, \\ \beta_1 &= 102 - \frac{38}{3} N_f, \\ \beta_2 &= \frac{2857}{2} - \frac{5033}{18} N_f + \frac{325}{54} N_f^2. \end{aligned} \tag{5.20}$$

With the calculation of the coupling constant eq. 5.18 complete, we can then solve for the conversion factor by expressing the quantity $\Delta Z_{\mathcal{O}}^{\mathcal{S}}(\mu)$ in scheme $\mathcal{S}$ through the $\beta-$functions and the anomalous dimension of the operator under $\gamma_{\mathcal{O}}^{\mathcal{S}} \equiv \gamma^{\mathcal{S}}$:

$$\Delta Z_{\mathcal{O}}^{\mathcal{S}}(\mu) = \left(2\beta_0 \frac{g^{\mathcal{S}}(\mu)^2}{16\pi^2}\right)^{\frac{\gamma_0}{2\beta_0}} \exp\left\{\int_0^{g^{\mathcal{S}}(\mu)} \mathrm{d}g' \left(\frac{\gamma^{\mathcal{S}}(g')}{\beta^{\mathcal{S}}(g')} + \frac{\gamma_0}{\beta_0 g'}\right)\right\}. \tag{5.21}$$

Again to the three-loop approximation $\Delta Z_{\mathcal{O}}^{\mathcal{S}}(\mu)$ equates to:

$$\begin{aligned} \Delta Z_{\mathcal{O}}^{\mathcal{S}}(\mu) = \left(2\beta_0 \frac{g^{\mathcal{S}}(\mu)^2}{16\pi^2}\right)^{\frac{\gamma_0}{2\beta_0}} \Bigg(1 + \frac{g^{\mathcal{S}}(\mu)^2}{16\pi^2} \frac{\beta_1\gamma_0 - \beta_0\gamma_1^{\mathcal{S}}}{2\beta_0^2} + \\ \frac{g^{\mathcal{S}}(\mu)^4}{(16\pi^2)^2} \frac{-2\beta_0^3\gamma_2^{\mathcal{S}} + \beta_0^2(\gamma_1^{\mathcal{S}}(2\beta_1 + \gamma_1^{\mathcal{S}}) + 2\beta_2\gamma_0) - 2\beta_0\beta_1\gamma_0(\beta_1 + \gamma_1^{\mathcal{S}}) + \beta_1^2\gamma_0^2}{8\beta_0^4}\Bigg). \end{aligned} \tag{5.22}$$

For the quark fields in the $\overline{\text{MS}}$ and RI'-MOM schemes are given by [108]

$$\begin{aligned}
\gamma_0 &= 0, \\
\gamma_1 &= \frac{134}{3} - \frac{8}{3}N_f, \\
\gamma_2^{\overline{\text{MS}}} &= \frac{20729}{18} - 79\zeta_3 - \frac{1100}{9}N_f + \frac{40}{27}N_f^2, \\
\gamma_2^{\text{RI'-MOM}} &= \frac{52321}{18} - 79\zeta_3 - \frac{1100}{9}N_f + \frac{40}{27}N_f^2,
\end{aligned} \tag{5.23}$$

where $\zeta_3 = 1.20206...$, for the scalar/pseudoscalar operators [109, 110],

$$\begin{aligned}
\gamma_0 &= -8, \\
\gamma_1^{\overline{\text{MS}}} &= -\frac{404}{3} - \frac{40}{9}N_f, \\
\gamma_1^{\text{RI'-MOM}} &= -252 + \frac{104}{9}N_f, \\
\gamma_2^{\overline{\text{MS}}} &= -2498 + \left(\frac{4432}{27} - \frac{320}{3}\zeta_3\right)N_f + \frac{280}{81}N_f^2, \\
\gamma_2^{\text{RI'-MOM}} &= -\frac{40348}{3} + \frac{6688}{3}\zeta_3 - \left(\frac{35176}{27} - \frac{256}{9}\zeta_3\right)N_f - \frac{1712}{81}N_f^2,
\end{aligned} \tag{5.24}$$

and for the tensor [106, 111]

$$\begin{aligned}
\gamma_0 &= \frac{8}{3}, \\
\gamma_1 &= \frac{724}{9} - \frac{104}{27}N_f, \\
\gamma_2^{\overline{\text{MS}}} &= \frac{105110}{81} - \frac{1856}{27}\zeta_3 - \left(\frac{10480}{81} + \frac{320}{9}\zeta_3\right)N_f - \frac{8}{9}N_f^2, \\
\gamma_2^{\text{RI'-MOM}} &= \frac{358012}{81} - \frac{26144}{27}\zeta_3 + \left(-\frac{39640}{81} - \frac{512}{27}\zeta_3\right)N_f + \frac{2288}{243}N_f^2.
\end{aligned} \tag{5.25}$$

Each calculation at $p = \mu$ in the RI'-MOM scheme is dependent on momentum, but we require a zero momentum renormalisation value, thus we must take a value in the acceptable momentum range for an RGI scheme and chirally extrapolate to zero momentum. Then we are able to convert to the $\overline{\text{MS}}$ scheme at our chosen value of $\mu = 2$ GeV.

5.2 Calculation

We are now looking to calculate in the RI'-MOM scheme to find the initial renormalisation values for a series of operators as shown in Table 5.1. We then convert the appropriate renormalisation constants into the $\overline{\text{MS}}$ scheme with the aim to tabulate the resultant renormalisation constants for each of the operators across all lattice configurations.

Operators	Quark Bilinear	Renormalising Constant
$\mathcal{O}^S$	$\overline{q}q$	$Z_S^{\overline{\rm MS}}$
$\mathcal{O}^P$	$\overline{q}\gamma_5 q$	$Z_P^{\overline{\rm MS}}$
$\mathcal{O}^V_\mu$	$\overline{q}\gamma_\mu q$	Z_V
$\mathcal{O}^A_\mu$	$\overline{q}\gamma_\mu\gamma_5 q$	Z_A
$\mathcal{O}^T_{\mu\nu}$	$\overline{q}\gamma_{\mu\nu} q$	$Z_T^{\overline{\rm MS}}$

Table 5.1: The operators and their corresponding structure and renormalisation constants.

5.40 $24^3\times 48$ $a=0.0818$		5.50 $32^3\times 64$ $a=0.074$		5.65 $32^3\times 64$ $a=0.068$	
$\kappa_l=\kappa_s$	am_π	$\kappa_l=\kappa_s$	am_π	$\kappa_l=\kappa_s$	am_π
0.119820	0.2288(5)	0.120900	0.1759(8)	0.121975	0.1562(5)
0.119860	0.2085(5)	0.120920	0.1653(3)	0.122005	0.1461(4)
0.119895	0.1895(4)	0.120950	0.1511(6)	0.122030	0.1355(3)
0.119930	0.1724(8)	0.120990	0.1288(7)	0.122050	0.1260(4)
0.1200000	0.1371(8)	0.121021	0.1130(6)		

5.80 $48^3\times 96$ $a=0.0588$		5.95 $48^3\times 96$ $a=0.05$	
$\kappa_l=\kappa_s$	am_π	$\kappa_l=\kappa_s$	am_π
0.122760	0.1448(9)	0.123411	0.1267(4)
0.122810	0.1276(7)	0.123460	0.1105(8)
0.122920	0.0802(9)	0.123510	0.0927(5)

Table 5.2: Parameters $\kappa_l=\kappa_s$ where $l=u,d$ and the pion masses of the lattice ensembles over the five separate values of β, lattice extent and spacing.

5.2.1 Lattice Parameters

A variety of lattice spacings, quark masses and volumes are analysed, as shown in Table 5.2. With the 3 degenerate quarks ($N_f=3$), which allows at each value of β a controlled extrapolation to the $N_f=3$ chiral limit required for the $\overline{\rm MS}$ scheme. In order to convert these renormalisation factors into the physical scales μ, we need the lattice spacing a, using the singlet quantities to set the scale [112]. We choose our lattice momenta according to

$$\Lambda^2_{QCD} \ll p^2 \leq \left(\frac{\pi}{a}\right)^2 \tag{5.26}$$

$\theta = (0,0,0,-\frac{1}{2})$		$\theta = (\frac{1}{2},\frac{1}{2},\frac{1}{2},-\frac{1}{2})$		$\theta = (\frac{1}{4},\frac{1}{4},\frac{1}{4},0)$	
n	$(a\ p)^2$	n	$(a\ p)^2$	n	$(a\ p)^2$
(1, 1, 1, 2)	0.1542	(0, 0, 0, 1)	0.0385	(0, 0, 0, 0)	0.0096
(2, 2, 2, 4)	0.6169	(1, 1, 1, 3)	0.3470	(1, 1, 1, 2)	0.2410
(3, 3, 3, 6)	1.3879	(2, 2, 2, 5)	0.9638	(2, 2, 2, 4)	0.7807
(4, 4, 4, 8)	2.4674	(3, 3, 3, 7)	1.8891	(3, 3, 3, 6)	1.6289
(5, 5, 5, 10)	3.8553	(4, 4, 4, 9)	3.1228	(4, 4, 4, 8)	2.7855
(6, 6, 6, 12)	5.5517	(5, 5, 5, 11)	4.6649	(5, 5, 5, 10)	4.2505
(7, 7, 7, 14)	7.5564	(6, 6, 6, 13)	6.5155	(6, 6, 6, 12)	6.0239
(8, 8, 8, 16)	9.8696	(7, 7, 7, 15)	8.6745	(7, 7, 7, 14)	8.1058

Table 5.3: The Twist angles and lattice momenta in lattice units for the $32^3 \times 64$ lattices.

on our $L^3 \times T$ lattice, where we use a periodic spatial and antiperiodic temporal boundary condition, where the allowed momenta are given by,

$$p = \left(\frac{2\pi}{L}n_x, \frac{2\pi}{L}n_y, \frac{2\pi}{L}n_z, \frac{2\pi}{T}\left(n_t + \frac{1}{2}\right)\right). \tag{5.27}$$

In order to improve the resolution of our calculation we increase the number of momenta measured by employing a twisted boundary condition to these quark fields[113], where $p \to p + B$, using a B defined as,

$$B = \left(\frac{2\pi}{L}\theta_x, \frac{2\pi}{L}\theta_y, \frac{2\pi}{L}\theta_z, \frac{2\pi}{T}\theta_t\right) \tag{5.28}$$

and so for our lattice where the temporal extent is double the spatial extent $T = 2L$, our momenta are then

$$p = \frac{2\pi}{L}\left(n_x + \theta_x, n_y + \theta_y, n_z + \theta_z, \frac{1}{2}\left(n_t + \frac{1}{2} + \theta_t\right)\right). \tag{5.29}$$

By varying our p^2 whilst holding a fixed direction along a diagonal [75], we are left with an overall correction of $O((a\ p)^2)$. These twist angles and momenta are shown on Table 5.3.

5.2.2 Results

We start by calculating the renormalisation constants in the RI'-MOM scheme, calculating them over multiple momenta. By plotting all of the lattice ensembles and twist angles over the renormalisation scale $(a\ p)^2$, in Fig. 5.1, we see that at each of the defined renormalisation scale points, the ensembles differ from each other, showing a

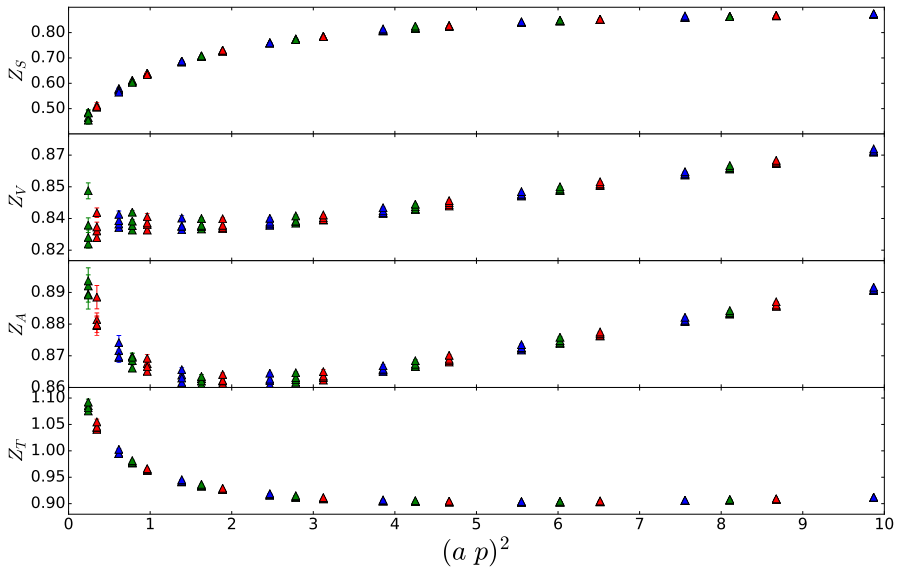

Figure 5.1: Results of the Z renormalisation values for all pion masses versus the renormalisation scale in lattice units. The different colours represent the different twist angles, and the overlapping points are the different ensembles.

small amount of pion mass dependence within each of Z at each p^2. For illustration, by taking a single point along the renormalisation scale at approximately $(ap)^2 \approx 2.5$, we plot those individual Z from each ensemble against their pion mass in Fig. 5.2. On this figure, we can see a small pion mass dependence, and with a linear fit, we can extrapolate these Z-factors to the chiral limit for each value of $(ap)^2$.

The renormalisation of the pseudoscalar operator needs to be treated differently, as within the Green's function of the pseudoscalar we find a pion pole, which to extrapolate to the chiral limit needs to be subtracted from its vertex function. This is achieved by constructing a two-parameter ansätze for each momentum p

$$f^{(2)}(p, m_\pi) = a_P(p) + \frac{c_P(p)}{m_\pi^2}, \tag{5.30}$$

and fit this equation to the ratio

$$R(p, m_\pi) = \frac{\Lambda_P(p, m_\pi)}{Z_q(p, m_\pi) C_{P,\mathrm{RGI}}^{\mathrm{RI'\text{-}MOM},\overline{\mathrm{MS}}}(p, 2GeV)}. \tag{5.31}$$

We employ this local two-parameter fit to subtract the pion pole and extrapolate Z_P along with the other renormalisation factors to the chiral limit, as shown in Fig. (5.3,5.4).

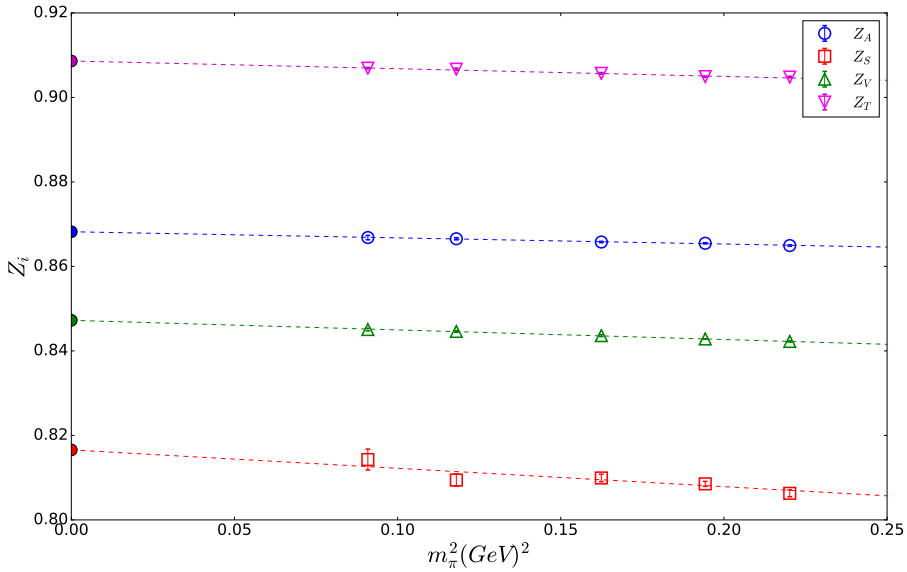

Figure 5.2: The dependence of the Z renormalisation values on the pion mass of $\beta = 5.50$ at $(a\ p)^2 \approx 2.5$, with a linear chiral extrapolated fit.

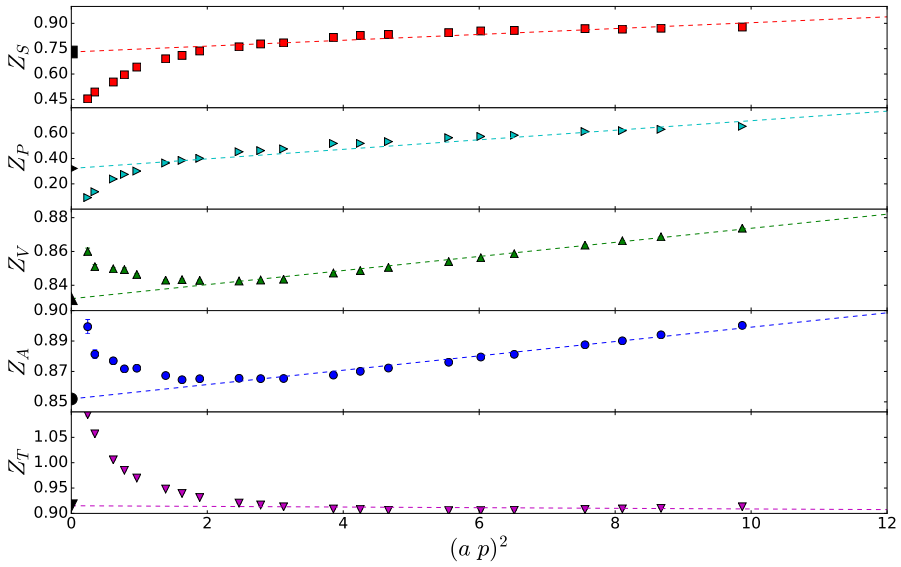

Figure 5.3: Results of the Z renormalisation value of the $\beta = 5.50$, with the chiral extrapolation to zero momentum. Each renormalisation value is plotted with separate colours and symbols to differentiate each operator, using a fitting range of $(a\ p)^2 \in [4, 12]$.

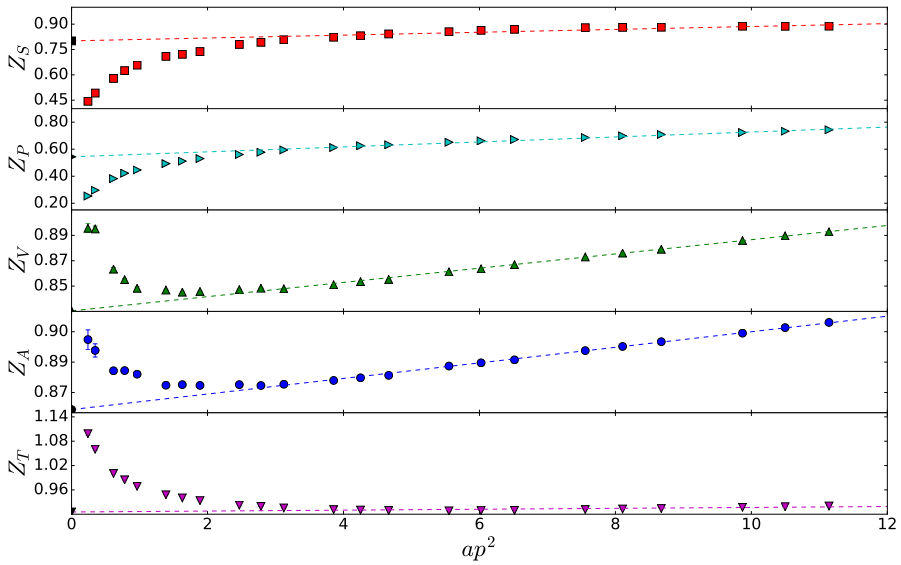

Figure 5.4: Similar to Fig. 5.3 for $\beta = 5.65$

As we can see in these two figures, the values of Z_V, Z_A, Z_S, Z_P and Z_T, each lies on an approximately linear curve after the renormalisation scale value $(a\ p)^2 \geq 2$ for Fig. 5.3 and $(a\ p)^2 \geq 4$ on Fig. 5.4, which allows us to fit these points to a straight line and extrapolate back to zero momentum. On these plots the the dashed lines represent the fit interval of $(a\ p)^2 \in [2, 10]$ and $(a\ p)^2 \in [4, 12]$ for Figs 5.3 and 5.4 respectively.

We then convert our Z_S, Z_P and Z_T to the $\overline{\text{MS}}$ scheme at 2 GeV, and in Fig. (5.5, 5.6, 5.7) show the difference between the RI'-MOM and $\overline{\text{MS}}$ schemes respectively in the $\beta = 5.65$ lattice configurations, with the dashed line representing the extrapolation of the $\overline{\text{MS}}$ scheme with a fit interval of $(a\ p)^2 \in [4, 12]$ in each.

The renormalisation constants in the vector and axial case have the same coefficients in the RI'-MOM and $\overline{\text{MS}}$ schemes, thus their renormalisation values will be equivalent up to the third order between these two cases, and so we leave Z_V and Z_A in their RI'-MOM form.

The renormalisation values for each of the operators, at each β are presented in Table 5.4.

5.2.2.1 Complete subtraction of one-loop lattice artifacts

Our previous renormalisation factor has reduced the level of lattice aftifacts, such that we can use this renormalisation to compare our lattice results to experimental, but there are still remaining degrees of one-loop lattice aftifacts remaining in our lattice QCD

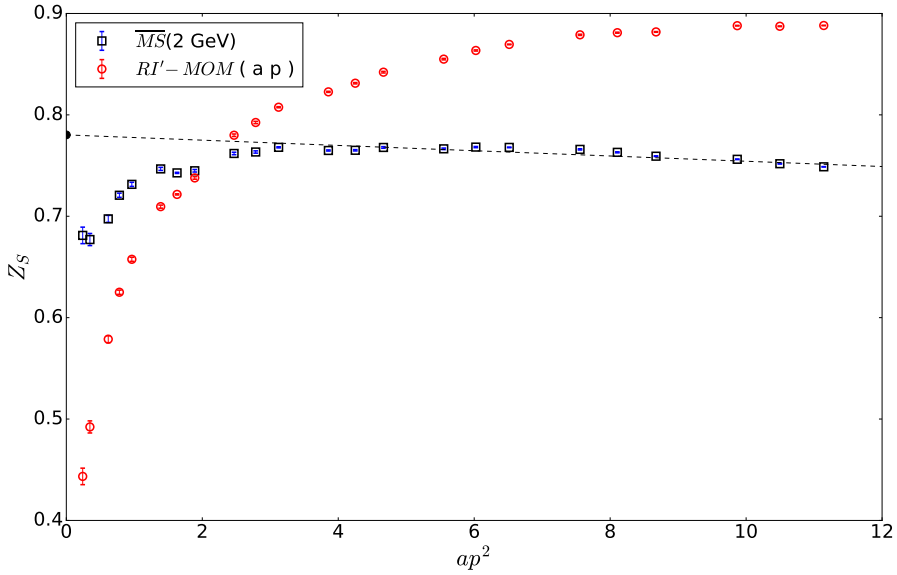

Figure 5.5: The dependence of $Z_S^{\text{RI'-MOM}}$ and $Z_S^{\overline{\text{MS}}}$ on the momentum scale, for the chirally extrapolated non-perturbative data. Dashed line represents the continuum extrapolation of the $\overline{\text{MS}}$ fit, for $\beta = 5.65$

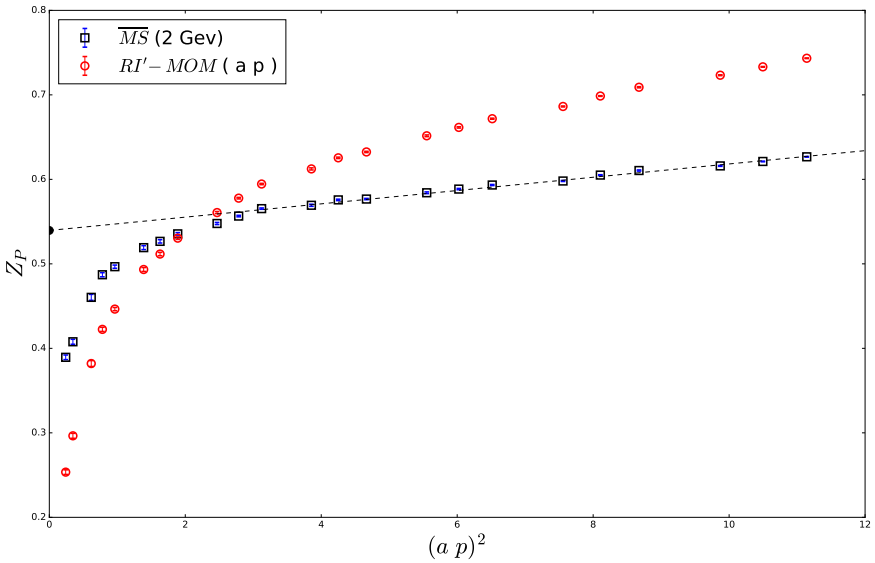

Figure 5.6: Similar to Fig. 5.5 for $Z_P^{\overline{\text{MS}}}$.

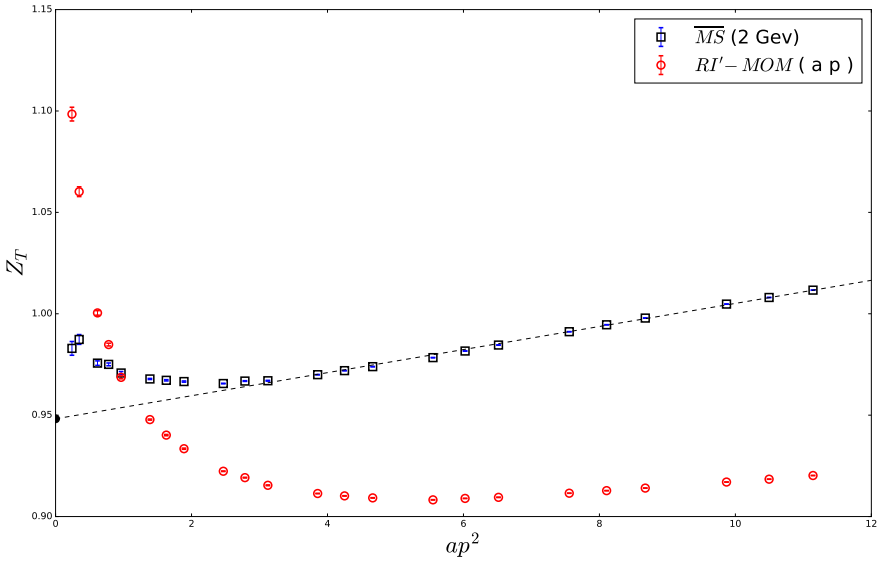

Figure 5.7: Similar to Fig. 5.5 for $Z_T^{\overline{\text{MS}}}$.

β	$Z_S^{\overline{\text{MS}}}$	$Z_P^{\overline{\text{MS}}}$	$Z_V^{\text{RI'-MOM}}$	$Z_A^{\text{RI'-MOM}}$	$Z_T^{\overline{\text{MS}}}$
5.40	0.7759(19)	0.4902(66)	0.8317(17)	0.8535(43)	0.9462(70)
5.50	0.7667(23)	0.4959(40)	0.8341(25)	0.8578(49)	0.9479(22)
5.65	0.7802(89)	0.5395(06)	0.8403(40)	0.8616(37)	0.9482(58)
5.80	0.7408(69)	0.5477(82)	0.8545(15)	0.8749(18)	0.9667(89)
5.95	0.7406(04)	0.5739(57)	0.8608(53)	0.8817(13)	0.9708(46)

Table 5.4: Renormalisation constants at each value of β after chiral extrapolation across multiple masses with conversion from RI'-MOM to $\overline{\text{MS}}$ at $\mu = 2$ GeV, for the tensor and scalar renormalisation constants, with statistical error.

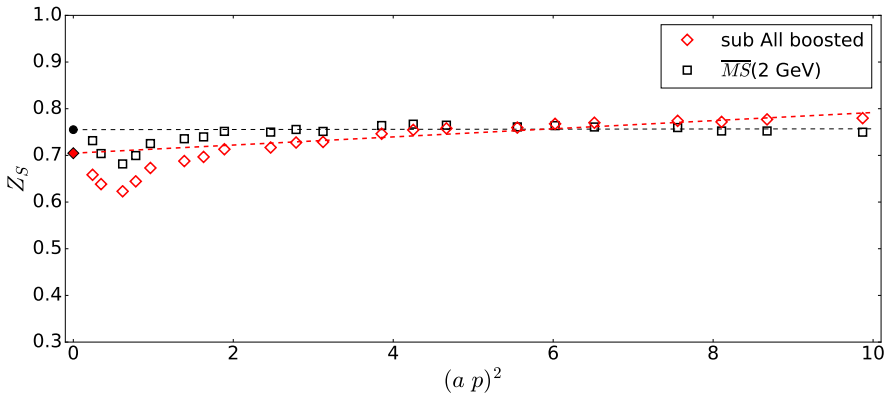

Figure 5.8: The $\beta = 5.50$ chirally extrapolated values of $Z_S^{\overline{\rm MS}}$ prior to the subtraction (black circles) and after the complete subtraction of one-loop lattice artifacts using g_b (red diamonds).

calculations. We can attempt to improve our determination of the renormalisation factors Z_i by performing a 'complete' subtraction of these one-loop lattice artifacts [102]. It has been shown in previous studies [100] that at high values of $(a\ p)^2$, the $\mathcal{O}(g^2\ a^2)$ terms become large and are no longer under control. Due to the way we compute to all orders of our lattice spacing a, we have a dependence on the momentum included in the propagators that cannot be given in a closed form, so we compute the one-loop expressions separately for each value of the external momentum used in our calculations. We can omit the $\mathcal{O}(a^0)$ contributions by subtracting $\mathcal{O}(g^2\ a^0)$ terms, which have been computed analytically in [100]. For this case we are subtracting the complete one-loop lattice artifacts and so we employ the boosted coupling,

$$g_b^2 = \frac{g^2}{P(g)} \tag{5.32}$$

where $P(g)$ is the plaquette at each lattice β taken from each of the ensembles, and we use the tree-level value of the improvement coefficient $c_{sw} = 1$. The effects of this subtraction are shown in Figs. 5.8 - 5.12 for the chirally extrapolated $Z_S^{\overline{\rm MS}}$,$Z_P^{\overline{\rm MS}}$, $Z_V^{\text{RI'-MOM}}$,$Z_A^{\text{RI'-MOM}}$ and $Z_T^{\overline{\rm MS}}$, where these figures show the renormalisation factors $Z_i^{\overline{\rm MS}}$ determined previously, alongside the renormalisation factor after a complete subtraction of all the one-loop lattice artifacts. We then take the continuum extrapolation of these subtracted renormalisation factors and tabulate them for each of the lattice β ensembles in Table 5.5.

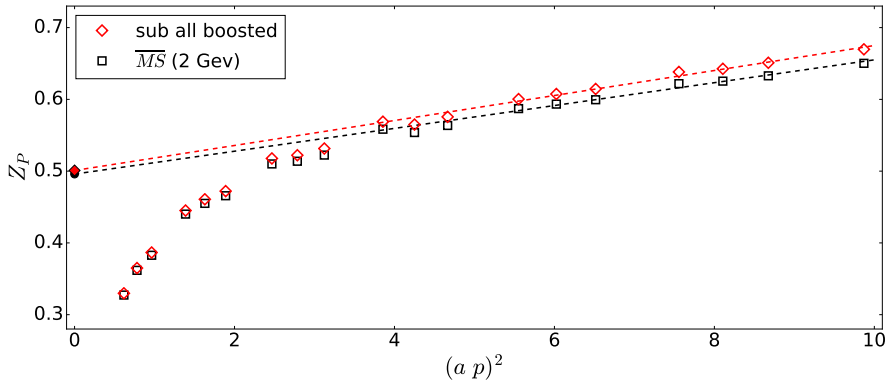

Figure 5.9: Similar to Fig. 5.8 for $Z_P^{\overline{\rm MS}}$

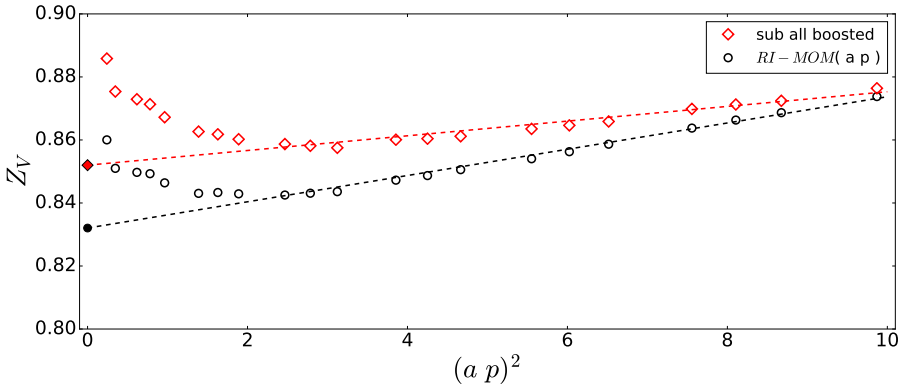

Figure 5.10: Similar to Fig. 5.8 for $Z_V^{\rm RI'\text{-}MOM}$

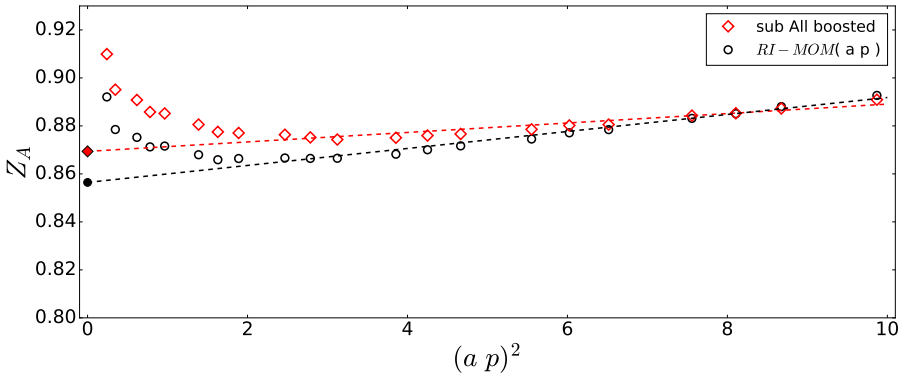

Figure 5.11: Similar to Fig. 5.8 for $Z_A^{\rm RI'\text{-}MOM}$

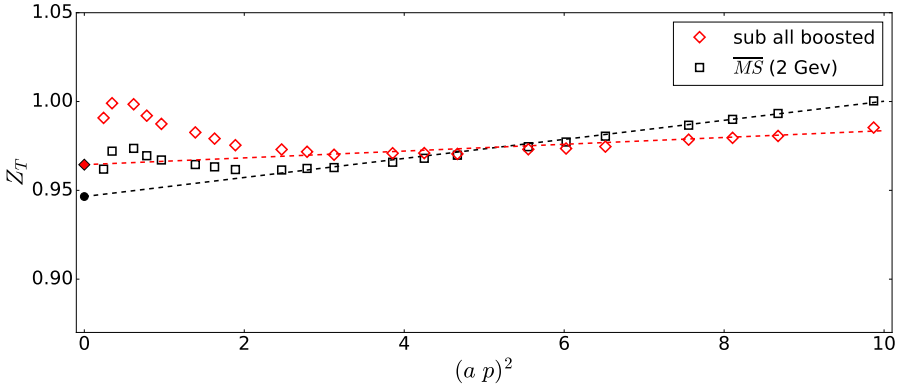

Figure 5.12: Similar to Fig. 5.8 for $Z_T^{\overline{\text{MS}}}$

β	$Z_S^{\overline{\text{MS}}}$	$Z_P^{\overline{\text{MS}}}$	$Z_V^{\text{RI'-MOM}}$	$Z_A^{\text{RI'-MOM}}$	$Z_T^{\overline{\text{MS}}}$
5.40	0.7034(48)	0.5021(87)	0.8503(14)	0.8671(77)	0.9637(23)
5.50	0.7046(89)	0.5009(24)	0.8519(95)	0.8693(38)	0.9644(49)
5.65	0.7153(86)	0.5428(51)	0.8615(59)	0.8754(19)	0.9684(54)
5.80	0.6709(23)	0.5647(34)	0.8796(75)	0.8913(49)	0.9945(11)
5.95	0.6683(94)	0.6134(17)	0.8856(25)	0.8983(43)	0.9980(42)

Table 5.5: Renormalisation constants at each value of β after chiral and continuum extrapolation across multiple masses with conversion from RI'-MOM to $\overline{\text{MS}}$ at $\mu = 2$ GeV with the added improvement of the subtraction of one-loop lattice artifacts using g_b. Numbers in brackets indicate statistical error only.

5.3 Summary

We finally take the lattice data that has been improved by the complete subtraction of the one-loop lattice artifacts with the boosted coupling g_b to be our final results, with the renormalisation factors tabulated in Table 5.5. We have calculated the Green's function on each of our lattice ensembles, and through this process found renormalisation factors Z in a variant of the Regularisation Independent Momentum (RI'-MOM) scheme, and using a transformation from this scheme into the Renormalised Group Invariant (RGI) scheme to get a conversion into the Modified Minimal Subtraction scheme ($\overline{\text{MS}}$). We then further improved our calculation of the renormalisation factors, by performing a complete subtraction of the one-loop lattice artifacts by omitting all the $\mathcal{O}(a^0)$ contributions by subtracting the $\mathcal{O}(g^2\ a^0)$ terms.

When comparing our unsubtracted results in Table 5.4; specifically of the $\beta = 5.50$ $Z_V^{\text{RI'-MOM}} = 0.8341$, we find compared to previous values calculated in [17] of $Z_V = 0.857(1)$ at a pion mass of $m_\pi = 220$ MeV, that our initial calculation was underestimating previous calculations. However our result after improvement in Table 5.5, of $Z_V^{\text{RI'-MOM}} = 0.8519(95)$ is in much better agreement with previously calculated results, which gives us encouragement that the subtraction of these lattice artifacts has improved our calculation of the renormalisation factors.

Chapter 6

Flavour Symmetry Breaking

The QCD interaction is flavour-blind, which means that when we ignore the weak interactions and electromagnetism, the only difference between flavour comes from the quark masses. This allows us to investigate the properties of flavour symmetry breaking and mixing, one of the remaining outstanding problems in particle physics. A program to systematically investigate the patterns of flavour symmetry breaking in meson and baryon masses based on group theory, as opposed to effective field theory as would be seen in chiral perturbation, has been proposed [75, 79] with an extension to incorporate QED effects described in [114–116]. In the recently published [1] this procedure was extended to include hadronic matrix elements, and in this chapter we will present our results for the electromagnetic and tensor form factors.

It is easiest to understand the theory behind these interactions when all three quark flavours share the same mass, as this allows us to use all the tools available to us in flavour SU(3) group theory. As we have seen earlier in Chapter 3, when constructing our lattice, we have kept the bare quark mass $\overline{m} = (m_u + m_d + m_s)/3$ constant while then expanding the matrix elements around the SU(3) flavour symmetric point, further restricting ourselves to $n_f = 2 + 1$ where we have degenerate u and d quark masses $m_u = m_d \equiv m_l$.

The work in this chapter uses the theory discussed in [1], where the local currents covering all possible Dirac gamma matrix structures were split into 'first' and 'second' class currents. Using group theory, we define the expansion parameters and the general structure of the expansion. Then using the Wigner-Eckart theorem, give the reduced matrix elements and discus the group theory classification of the $SU(3)$ tensors, determining those which are useful to the study and give the required Leading Order expansions. We briefly demonstrate the amplitudes restricted to the symmetric point, constructed from the group theory classifications in [1], and then move on to the linear combinations of the matrix elements constructed from various baryons, that produce

Index	Baryon (B)	Meson (F)	Current (J^F)
1	n	K^0	$\overline{d}\gamma s$
2	p	K^+	$\overline{u}\gamma s$
3	Σ^-	π^-	$\overline{d}\gamma u$
4	Σ^0	π^0	$\frac{1}{\sqrt{2}}(\overline{u}\gamma u - \overline{d}\gamma d)$
5	Λ^0	η	$\frac{1}{\sqrt{6}}(\overline{u}\gamma u + \overline{d}\gamma g - 2\overline{s}\gamma s)$
6	Σ^+	π^+	$\overline{u}\gamma d$
7	Ξ^-	K^-	$\overline{s}\gamma u$
8	Ξ^0	$\overline{K}^0$	$\overline{s}\gamma d$
0		η'	$\frac{1}{\sqrt{3}}(\overline{u}\gamma u + \overline{d}\gamma d + \overline{s}\gamma s)$

Table 6.1: The conventions for the generalised currents. We use the convention that the current (i.e operator) numbered by i has the same effect as absorbing a meson with the index i. γ here represents an arbitrary Dirac matrix.

functions which share the same value at the $SU(3)$ flavour symmetric point, but deviate as masses change.

6.1 Mass Dependence of Amplitudes

To find the allowed mass dependence of the matrix elements of octet operators in octet hadrons we need the $SU(3)$ decomposition of the $8 \otimes 8 \otimes 8$. We regard the baryons and mesons as vectors of length 8, using the ordering in Table 6.1. The group theory classification of the $SU(3)$ octet tensors in [1] leads us to using a mass Taylor expansion of the operator amplitudes. We tabulate the $SU(3)$ singlet and octet coefficients into Table 6.2. These coefficients are used to construct equations allowing linear expansion of the hadronic amplitudes along the fixed $\overline{m}$ line described in Chapter 3, to the physical point. Using the definitions on Table 6.1 and referring back to Chapters 3 and 4 with the construction of matrix elements, the notation for the matrix element transition of $B \to B'$ is,

$$A_{\overline{B}'FB} = \langle B'|J^F|B\rangle, \tag{6.1}$$

where J^F is the appropriate operator from Table 6.1 and F denotes the flavour structure of the operator. In our operator expressions $\overline{q}\gamma q$, q is the annihilation operator and $\overline{q}$ the creation operator, with γ representing an arbitrary Dirac matrix. We use our convention for the flavour structure F, where the current i has the same effect as absorbing a meson with the same index. For example creating a π^+ annihilates one d

quark while creating a u quark, such that

$$J^{\pi^+}|0\rangle \propto |\pi^+\rangle, \tag{6.2}$$

and so

$$\langle p|\overline{u}\gamma d|n\rangle = \langle p|J^{\pi^+}|n\rangle \tag{6.3}$$

represents $p = \pi^+ n$.

We can use this notation to write out the quark electromagnetic current as we saw in Chapter 4, in the form of an appropriate flavour matrix F

$$\begin{aligned} J_{em} &\propto \frac{1}{\sqrt{2}}J^{\pi^0} + \frac{1}{\sqrt{6}}J^{\eta} \\ &= \frac{2}{3}\overline{u}\gamma u - \frac{1}{3}\overline{d}\gamma d - \frac{1}{3}\overline{s}\gamma s. \end{aligned} \tag{6.4}$$

Table 6.2 is then to be read as such, where the f and d terms are independent of the quark mass, while the r_1, r_2, r_3 and s_1, s_2 coefficients are the leading order or δm_l terms. Thus as an example of how the Amplitudes of the various matrix elements are read off Table 6.2 we look at the $\overline{\Sigma}\pi\Sigma$ term, which gives to first or leading order in δm_l,

$$\langle \Sigma^+|J^{\pi^0}|\Sigma^+\rangle = A_{\overline{\Sigma}\pi\Sigma} = 2f + (-2s_1 + \sqrt{3}s_2)\delta m_l \tag{6.5}$$

6.1.1 Amplitude at the symmetric point

If we look at the pattern of amplitudes at the symmetric point, where there is no breaking of $SU(3)$ flavour symmetry, we can read off the corresponding matrix elements from Table 6.2, and construct many matrix element combinations which have to be equal at the symmetric point. For example

$$\begin{aligned} \frac{\sqrt{3}}{2}\langle p|J^{\eta}|p\rangle + \frac{1}{2}\langle p|J^{\pi^0}|p\rangle &= \langle \Sigma^+|J^{\pi^0}|\Sigma^+\rangle \\ &= -\frac{\sqrt{3}}{2}\langle \Xi^0|J^{\eta}|\Xi^0\rangle + \frac{1}{2}\langle \Xi^0|J^{\pi^0}|\Xi^0\rangle \\ &= 2f, \end{aligned} \tag{6.6}$$

writing the operators out in their $\overline{q}\gamma q$ form

$$\begin{aligned} \frac{1}{\sqrt{2}}\langle p|(\overline{u}\gamma u - \overline{s}\gamma s)|p\rangle &= \frac{1}{\sqrt{2}}\langle \Sigma^+|(\overline{u}\gamma u - \overline{d}\gamma d)|\Sigma^+\rangle \\ &= \frac{1}{\sqrt{2}}\langle \Xi^0|(\overline{s}\gamma s - \overline{d}\gamma d)|\Xi^0\rangle \qquad (6.7) \\ &= 2f. \qquad (6.8) \end{aligned}$$

		$1, 1^{st}$ class		$8, 1^{st}$ class				
		$O(1)$		$O(\delta m_l)$				
		f	d	d	d	d	f	f
I	$A_{\overline{B}'FB}$	f	d	r_1	r_2	r_3	s_1	s_2
0	$\overline{N}\eta N$	$\sqrt{3}$	-1	1	0	0	0	-1
0	$\overline{\Sigma}\eta\Sigma$	0	2	1	0	$2\sqrt{3}$	0	0
0	$\overline{\Lambda}\eta\Lambda$	0	-2	1	2	0	0	0
0	$\overline{\Xi}\eta\Xi$	$-\sqrt{3}$	-1	1	0	0	0	1
1	$\overline{N}\pi^0 N$	1	$\sqrt{3}$	0	0	-2	2	0
1	$\overline{\Sigma}\pi^0\Sigma$	2	0	0	0	0	-2	$\sqrt{3}$
1	$\overline{\Xi}\pi^0\Xi$	1	$-\sqrt{3}$	0	0	2	2	0

Table 6.2: Coefficients in the mass Taylor expansion of $A_{\overline{B}'FB}$ operator amplitudes: $SU(3)$ singlet and octet, for first class currents. The first row gives whether singlet or octet, the second row gives the order in δm_l. The third row gives whether the associated tensor is f-like or d-like according to the definition given in [1]. These coefficients are sufficient for the linear expansion of hadronic amplitudes. Table from [1].

It is clear why these three matrix elements have to be the same at the symmetric point. The u contribution of the proton is the same as the u contribution of the Σ^+ or the s component of the Ξ^0, because each is their respective 'doubly-represented' valence quark. Much the same for the s in the proton being equal to the d in the Σ^+ or the d in the Ξ^0, because in each case it is the non-valence flavour. Thus the relations in eq. 6.7 are simply consequences of each baryon's flavour permutations, each belonging in the S_3 subgroup of $SU(3)$. Similarly

$$\begin{aligned}\frac{1}{\sqrt{6}}\langle p|(\overline{u}\gamma u + \overline{s}\gamma s - 2\overline{d}\gamma d)|p\rangle &= \frac{1}{\sqrt{6}}\langle \Sigma^+|(\overline{u}\gamma u + \overline{d}\gamma d - 2\overline{s}\gamma s)|\Sigma^+\rangle \\ &= \frac{1}{\sqrt{6}}\langle \Xi^0|(\overline{s}\gamma s + \overline{d}\gamma d - 2\overline{u}\gamma u)|\Xi^0\rangle \qquad (6.9)\\ &= 2d. \qquad (6.10)\end{aligned}$$

These elements all have the same pattern with 'doubly-represented + non-valence $-2\times$ singly-represented', and so we can see why they must be the same at the symmetric point.

6.2 Fan Plots

Moving away from the symmetric point, we keep $\overline{m}$ fixed, and so we only consider the non-singlet polynomials in the quark mass. Using only first order in δm_l, we can consider the octets, allowing us to read off the mass coefficients from Table 6.2 as in eq. 6.5. By constructing quantities which are equal in the fully symmetric case and differ for our case of $n_f = 2 + 1$ quark masses, we can examine the violation of the $SU(3)$ symmetry that arises from the $m_s - m_l$ mass difference.

6.2.1 The *d*-fan

We can construct a so-called 'fan' plot, by constructing combinations of $\overline{B}'FB$ amplitudes that have the same value ($2d$) at the symmetric point, but fan out once the $SU(3)$ symmetry is broken. From Table 6.2 we can construct seven quantities D_i for our d-fan,

$$\begin{aligned}
D_1 \equiv -\left(A_{\overline{N}\eta N} + A_{\overline{\Xi}\eta\Xi}\right) &= 2d - 2r_1\delta m_l, \\
D_2 \equiv A_{\overline{\Sigma}\eta\Sigma} &= 2d + \left(r_1 + 2\sqrt{3}r_3\right)\delta m_l, \\
D_3 \equiv -A_{\overline{\Lambda}\eta\Lambda} &= 2d - (r_1 + 2r_2)\,\delta m_l, \\
D_4 \equiv \frac{1}{\sqrt{3}}\left(A_{\overline{N}\pi N} - A_{\overline{\Xi}\pi\Xi}\right) &= 2d - \frac{4}{\sqrt{3}}r_3\delta m_l, \\
D_5 \equiv A_{\overline{\Sigma}\pi\Lambda} &= 2d + \left(r_2 - \sqrt{3}r_3\right)\delta m_l, \\
D_6 \equiv \frac{1}{\sqrt{6}}\left(A_{\overline{N}K\Sigma} + A_{\overline{\Sigma}K\Xi}\right) &= 2d + \frac{2}{\sqrt{3}}r_3\delta m_l, \\
D_7 \equiv -\left(A_{\overline{N}K\Lambda} + A_{\overline{\Lambda}K\Xi}\right) &= 2d - 2r_2\delta m_l.
\end{aligned} \tag{6.11}$$

By constructing these quantities, we find a 'fan' plot with 7 lines constrained by only 3 slope parameters (r_1, r_2 and r_3), so the split between these observables is highly constrained. These are not the only 7 quantities that can be chosen as an infinite set of linear combinations exist. For this work, we only calculate the flavour diagonal equations D_1, D_2 and D_4, as we have not calculated the off-diagonal terms in the other equations. We can construct an 'average D' from the diagonal amplitudes

$$X_D \equiv \frac{1}{6}\left(D_1 + 2D_2 + 3D_4\right) = 2d + O(\delta m_l^2) \tag{6.12}$$

chosen such that the $O(\delta m_l)$ coefficient vanishes. These average quantities can be useful for helping to set the lattice scale in the mass case [78]. It is helpful when constructing the fan plots from these equations to plot D_i/X_D to find the average fit to reduce statistical fluctuations, however for the construction of our F_1 form factor as

an example of the method, X_D vanishes at $Q^2 = 0$ and is always small, so instead we use the alternative $\tilde{D}_i \equiv D_i/X_F$, where X_F is defined next in eq. 6.14.

6.2.2 The f-fan

By using Table 6.2 again, we can construct another five quantities F_i, which again have the same value $(2f)$ at the symmetric point, but differ when the $SU(3)$ symmetry is broken.

$$\begin{aligned}
F_1 \equiv \frac{1}{\sqrt{3}}\left(A_{\overline{N}\eta N} - A_{\overline{\Xi}\eta\Xi}\right) &= 2f - \frac{2}{\sqrt{3}}s_2\delta m_l, \\
F_2 \equiv \left(A_{\overline{N}\pi N} + A_{\overline{\Xi}\pi\Xi}\right) &= 2f + s_1\delta m_l, \\
F_3 \equiv A_{\overline{\Sigma}\pi\Sigma} &= 2f + \left(-2s_1 + \sqrt{3}s_2\right)\delta m_l, \\
F_4 \equiv \frac{1}{\sqrt{2}}\left(A_{\overline{\Sigma}K\Xi} - A_{\overline{N}K\Sigma}\right) &= 2f - 2s_1\delta m_l, \\
F_5 \equiv \frac{1}{\sqrt{3}}\left(A_{\overline{\Lambda}K\Xi} - A_{\overline{N}K\Lambda}\right) &= 2f + \frac{2}{\sqrt{3}}\left(\sqrt{3}s_1 - s_2\right)\delta m_l.
\end{aligned} \tag{6.13}$$

Once again we can construct these quantities to find a fan plot with 5 lines, but in this case with only 2 slope parameters (s_1 and s_2), so the split between these observables is highly constrained. Again, we only calculate the flavour diagonal terms F_1, F_2 and F_3. At quadratic and higher level there are no constraints between the coefficients for the f-fan. We can then find an 'average F' from the diagonal amplitudes

$$X_F \equiv \frac{1}{6}\left(3F_1 + F_2 + 2F_3\right) = 2f + O(\delta m_l^2) \tag{6.14}$$

and using this we can construct normalised fan plots of $\tilde{F}_i \equiv F_i/X_F$.
Unlike the d-fan, the f-fan to linear order, has no error from dropping the quark-line disconnected contributions, as only the r_1 parameter has a quark-line disconnected piece, and none of the r_i parameters appear in the f-fan, i.e it's purely connected.

6.3 Flavour-diagonal matrix elements

In order to calculate the flavour diagonal matrix elements, we need the additional expansion of $\langle B|J^{\eta'}|B\rangle$, which requires the $SU(3)$ analysis of the $8 \otimes 1 \otimes 8$ tensors, which are just the $8 \otimes 8$ matrices previously analysed in [75]. This leads the conclusion that the matrix elements of flavour singlet operators follow the same formulae as the hadron masses. For leading order the expansion is found by

$$\begin{aligned} A_{\overline{N}\eta' N} &= a_0 + 3a_1\delta m_l, \\ A_{\overline{\Sigma}\eta'\Sigma} &= a_0 + 3a_2\delta m_l, \\ A_{\overline{\Xi}\eta'\Xi} &= a_0 - 3(a_1 - a_2)\delta m_l, \end{aligned} \tag{6.15}$$

with higher order terms available in [75].

The diagonal flavour states are then given by π^0 and η, together with the singlet flavour state η'. These can then be inverted to give individual quark states $\overline{u}\gamma u$, $\overline{d}\gamma d$ and $\overline{s}\gamma s$ in terms of these $J^{\eta'}$, J^{π^0} and J^{η} as

$$\begin{aligned} \overline{u}\gamma u &= \frac{1}{\sqrt{3}}J^{\eta'} + \frac{1}{\sqrt{2}}J^{\pi^0} + \frac{1}{\sqrt{6}}J^{\eta}, \\ \overline{d}\gamma d &= \frac{1}{\sqrt{3}}J^{\eta'} - \frac{1}{\sqrt{2}}J^{\pi^0} + \frac{1}{\sqrt{6}}J^{\eta}, \\ \overline{s}\gamma s &= \frac{1}{\sqrt{3}}J^{\eta'} - \sqrt{\frac{2}{3}}J^{\eta}. \end{aligned} \tag{6.16}$$

Using eq. 6.16 together with eq. 6.15 and Table 6.2, allows us to construct the $SU(3)$ flavour breaking expansion for the flavour diagonal matrix elements. Whilst from eq. 6.15, we will gain extra coefficients a_0, a_1 and a_2 that we don't calculate from our 'fan' plots, we can alleviate this with the consideration of connected and disconnected matrix elements. If we consider separate expansions for both connected and disconnected pieces,

$$\langle p|\overline{u}\gamma u|p\rangle = \langle p|\overline{u}\gamma u|p\rangle^{con} + \langle p|\overline{u}\gamma u|p\rangle^{dis} \tag{6.17}$$

which now adds additional constraints.

If we explicitly consider the flavour diagonal amplitudes, in each baryon the disconnected u and d terms will be equal as $m_u = m_d$, and so

$$\langle p|J^{\pi^0}|p\rangle^{dis}, \quad \langle\Sigma^+|J^{\pi^0}|\Sigma^+\rangle^{dis}, \quad \langle\Xi^0|J^{\pi^0}|\Xi^0\rangle^{dis} \tag{6.18}$$

will then vanish, leaving the terms

$$f^{dis} + \sqrt{3}d^{dis} = 0, \quad f^{dis} = 0, \quad f^{dis} - \sqrt{3}d^{dis} = 0 \tag{6.19}$$

and

$$-r_3^{dis} + s_1^{dis} = 0, \quad -2s_1^{dis} + \sqrt{3}s_2^{dis} = 0, \quad r_3^{dis} + s_1^{dis} = 0. \tag{6.20}$$

This gives us that all of these disconnected terms f^{dis}, d^{dis}, r_3^{dis}, s_1^{dis} and $s_2^{dis} = 0$, leaving us with only the r_1^{dis} contributing to the disconnected result. Thus from now on we only need to distinguish the r_1 term between our connected and disconnected contributions.

6.3.1 Connected terms

For the octet baryons that we are interested in, $p(uud)$, $\Sigma^+(uus)$ and $\Xi^0(ssu)$, there are no connected pieces for the components of $\langle p|\overline{s}\gamma s|p\rangle$, $\langle\Sigma^+|\overline{d}\gamma d|\Sigma^+\rangle$ and $\langle\Xi^0|\overline{d}\gamma d|\Xi^0\rangle$. This gives us new conditions on the connected terms for a_0, a_1 and a_2, from previous expansion parameters, giving

$$\begin{aligned} a_0^{con} &= \sqrt{6}f - \sqrt{2}d, \\ 3a_1^{con} &= \sqrt{2}r_1^{con} - \sqrt{2}s_2, \qquad (6.21) \\ 3a_2^{con} &= \frac{1}{\sqrt{2}}r_1^{con} + \sqrt{6}r_3 - \frac{3}{\sqrt{2}}s_2. \qquad (6.22) \end{aligned}$$

Using these new expressions for a_0^{con}, a_1^{con} and a_2^{con}, gives us the individual quark flavour expansions for the octet baryons p, Σ^+ and Ξ^0

$$\begin{aligned} \langle p|\overline{u}\gamma u|p\rangle^{con} &= 2\sqrt{2}f + \left(\sqrt{\frac{3}{2}}r_1^{con} - \sqrt{2}r_3 + \sqrt{2}s_1 - \sqrt{\frac{3}{2}}s_2\right)\delta m_l, \qquad (6.23) \\ \langle p|\overline{d}\gamma d|p\rangle^{con} &= 2\sqrt{2}(f - \sqrt{3}d) + \left(\sqrt{\frac{3}{2}}r_1^{con} + \sqrt{2}r_3 - \sqrt{2}s_1 - \sqrt{\frac{3}{2}}s_2\right)\delta m_l, \end{aligned}$$

and

$$\begin{aligned} \langle\Sigma^+|\overline{u}\gamma u|\Sigma^+\rangle^{con} &= 2\sqrt{2}f + \left(-2\sqrt{2}s_1 + \sqrt{6}s_2\right)\delta m_l, \qquad (6.24) \\ \langle\Sigma^+|\overline{s}\gamma s|\Sigma^+\rangle^{con} &= \sqrt{2}(f - \sqrt{3}d) + \left(\sqrt{-\frac{3}{2}}r_1^{con} - \sqrt{2}r_3 - \sqrt{2}s_1 + \sqrt{\frac{3}{2}}s_2\right)\delta m_l, \end{aligned}$$

and

$$\begin{aligned} \langle\Xi^0|\overline{u}\gamma u|\Xi^0\rangle^{con} &= \sqrt{2}(f - \sqrt{3}d) + \left(2\sqrt{2}r_3 + 2\sqrt{2}s_1\right)\delta m_l, \\ \langle\Xi^0|\overline{s}\gamma s|\Xi^0\rangle^{con} &= 2\sqrt{2}f + \left(-\sqrt{\frac{3}{2}}r_1^{con} + \sqrt{2}r_3 + \sqrt{2}s_1 - \sqrt{\frac{3}{2}}s_2\right)\delta m_l. \qquad (6.25) \end{aligned}$$

We can also use these individual quark contribution to find the result for the electromagnetic current J_{em} as seen earlier in Chapter 4, for the octet baryons p, Σ^+ and Ξ^0,

$$\begin{aligned}
\langle p|J_{em}|p\rangle^{con} &= \sqrt{2}f + \sqrt{\frac{2}{3}}d + \left(\frac{1}{\sqrt{6}}r_1^{con} - \sqrt{2}r_3 + \sqrt{2}s_1 - \frac{1}{\sqrt{6}}s_2\right)\delta m_l, \\
\langle \Sigma^+|J_{em}|\Sigma^+\rangle^{con} &= \sqrt{2}f + \sqrt{\frac{2}{3}}d + \left(\frac{1}{\sqrt{6}}r_1^{con} + \sqrt{2}r_3 - \sqrt{2}s_1 - \frac{1}{\sqrt{6}}s_2\right)\delta m_l, \\
\langle \Xi^0|J_{em}|\Xi^0\rangle^{con} &= -2\sqrt{\frac{2}{3}}d + \left(\frac{1}{\sqrt{6}}r_1^{con} + \sqrt{2}r_3 + \sqrt{2}s_1 + \frac{1}{\sqrt{6}}s_2\right)\delta m_l, \qquad (6.26)
\end{aligned}$$

for the quark line connected terms, and then for the disconnected terms we simply find

$$\langle p|J_{em}|p\rangle^{dis} = \langle \Sigma^+|J_{em}|\Sigma^+\rangle^{dis} = \langle \Xi^0|J_{em}|\Xi^0\rangle^{dis} = \frac{1}{\sqrt{6}}r_1^{dis}\delta m_l. \qquad (6.27)$$

6.4 Renormalisation and $O(a)$ improvement for the vector current

As we saw in Chapter 5, the computed matrix elements require renormalisation and $O(a)$ improvement. We expect the $O(a)$ improvment to merely modify the $SU(3)$ flavour breaking expansion coefficients, and so following on from the previous section we look at the diagonal sector where $B' = B$ and using the vector current. We use the notation and results from [117] and [118] for the onshell improvement with simplification from [1] to find the vector currents,

$$\begin{aligned}
V_\mu^{\pi^0 R} &= \hat{Z}_V\left[1 + \hat{b}_V\delta m_l\right]\mathcal{V}_\mu^{\pi^0}, \\
V_\mu^{\eta R} &= \hat{Z}_V\left[(1 - \hat{b}_V\delta m_l)\mathcal{V}_\mu^{\eta} + \sqrt{2}(\hat{b}_V + 3\hat{f}_V)\delta m_l\mathcal{V}_\mu^{\eta'}\right], \qquad (6.28) \\
V_\mu^{\eta' R} &= \hat{Z}_V\hat{r}_V\left[\mathcal{V}_\mu^{\eta'} + 2\sqrt{2}\hat{d}_V\delta m_l\mathcal{V}_\mu^{\eta}\right],
\end{aligned}$$

here $\mathcal{V}$ denotes for the local vector current,

$$\mathcal{V}_\mu^F = V_\mu^F + ic_V\partial_\nu T_{\mu\nu}^F \qquad (6.29)$$

with $T_{\mu\nu}^F = \overline{q}F\sigma_{\mu\nu}q$ and $\partial_\mu\phi(x) = [\phi(x+\hat{\mu}) - \phi(x-\hat{\mu})]/2$. These improvement coefficients b_V, d_V and c_V are functions of the coupling constant g_0, where r_V accounts for the fact that the singlet renormalisation differs from the non-singlet renormalisation $Z_V(g_0)$, depending on the chosen scheme and scale. We have absorbed a constant $\overline{m}$ into the renormalisation constant and improvement coefficients

$$\begin{aligned}\hat{Z}_V &= Z_V(1+(b_V+3\bar{b}_V)\overline{m})\\ \hat{b}_V &= b_V(1+(b_V+3\bar{b}_V)\overline{m})^{-1},\\ \hat{f}_V &= f_V(1+(b_V+3\bar{b}_V)\overline{m})^{-1}.\end{aligned} \tag{6.30}$$

We can then use eq. 6.28 as our definition of the improvement coefficients, as we already have the $SU(3)$ flavour breaking expansion coefficients as functions of $\overline{m}$.

If we consider $V_\mu^{\pi^0 R}$ in eq. 6.28 together with $\langle p|V_\mu^{\pi^0}|p\rangle^R$, $\langle\Sigma^+|V_\mu^{\pi^0}|\Sigma^+\rangle^R$ and $\langle\Xi^0|V_\mu^{\pi^0}|\Xi^0\rangle^R$. From our expansion coefficient Table 6.2 for $F=\pi^0$, we find from $A_{\overline{N}\pi N}$, $A_{\overline{\Sigma}\pi\Sigma}$ and $A_{\overline{\Xi}\pi\Xi}$ that our expansion coefficients simply change their value slightly by our renormalisation coefficients

$$\begin{aligned}s_1 \;&\to\; s_1' \;=\; s_1+\frac{1}{2}f\hat{b}_V,\\ s_2 \;&\to\; s_2' \;=\; s_2+\sqrt{3}f\hat{b}_V,\\ r_3 \;&\to\; r_3' \;=\; r_3-\frac{\sqrt{3}}{2}d\hat{b}_V.\end{aligned} \tag{6.31}$$

As we saw from eqs. (6.19, 6.20), the disconnected pieces for f, d, r_3, s_1 and s_2 vanish, implying that $\hat{b}_V$ must also vanish for the disconnected piece.

By repeating this process for $V_\mu^{\eta R}$, we get further results for r_1 which we then split into connected and disconnected pieces r_1^{con} and r_1^{dis}

$$\begin{aligned}r_1^{con} \;&\to\; r_1^{con'} \;=\; r_1^{con}+2\sqrt{3}f(\hat{b}_V+3\hat{f}_V^{con})-d(\hat{b}_V+6\hat{f}_V^{con}),\\ r_1^{dis} \;&\to\; r_1^{dis'} \;=\; r_1^{dis}+3\sqrt{2}a_0^{dis}\hat{f}_V^{dis}.\end{aligned} \tag{6.32}$$

And finally considering $V_\mu^{\eta' R}$

$$\begin{aligned}a_1 \;&\to\; a_1' \;=\; a_1+2\sqrt{\frac{2}{3}}(f-\frac{1}{\sqrt{3}}d)\hat{d}_V,\\ a_2 \;&\to\; a_2' \;=\; a_2-\frac{4}{3}\sqrt{2}d\hat{d}_V.\end{aligned} \tag{6.33}$$

Thus as we expected the improvement coefficients are simply the terms in the $SU(3)$ symmetry flavour breaking expansion that are slightly modified as given in eqs. (6.31,6.32,6.33).

6.4.1 Determination of $\hat{Z}_V$, $\hat{b}_V$ and $\hat{f}_V^{con}$

In order to determine some of the improvement coefficients, we implement a constraint in the form of a conserved vector current (CVC) using Noether's theorem. Due to the global symmetry of the lattice action; $q \to e^{-i\alpha_q} q$ is valid for each quark separately, so essentially the operator counts the number of u quarks and d quarks in the baryon. The local current is not exactly conserved $V_{CVC} = V + O(a)$, and so we can define the renormalisation constant and several improvement terms (used similarly in [119] for both 2 flavour and quenched QCD) by imposing CVC. We thus restrict our consideration to the forward matrix elements for V_4 at $Q^2 = 0$, with no momentum transfer to eliminate the $\hat{c}_V$ term.

Thus for the conserved vector current, the representative matrix elements are

$$\begin{aligned} \langle p|V_4^{\pi^0}|p\rangle^R &= A^R_{\overline{N}\pi N} = \frac{1}{\sqrt{2}}(2-1), \\ \langle \Sigma^+|V_4^{\pi^0}|\Sigma^+\rangle^R &= A^R_{\overline{\Sigma}\pi\Sigma} = \frac{1}{\sqrt{2}}(2-0), \\ \langle \Xi^0|V_4^{\pi^0}|\Xi^0\rangle^R &= A^R_{\overline{\Xi}\pi\Xi} = \frac{1}{\sqrt{6}}(1-0). \end{aligned} \tag{6.34}$$

And using this together with the equation for $V_\mu^{\pi^0}$ in eq. 6.28 gives us

$$f = \frac{1}{\sqrt{2}\hat{Z}_V}, \quad d = 0. \tag{6.35}$$

From this we can determine f from X_F at $Q^2 = 0$ via eq. 6.14 as

$$\hat{Z}_V = \frac{\sqrt{2}}{X_F}. \tag{6.36}$$

From eq. 6.31, due to the lack of $O(\delta m_l)$ terms in eq. 6.34, we would have the improvement terms $s_1' = 0$, $s_2' = 0$ and $r_3' = 0$, in other terms

$$s_1 = -\frac{1}{2} f \hat{b}_V, \quad s_2 = -\sqrt{3} f \hat{b}_V, \quad r_3 = 0. \tag{6.37}$$

Thus directly using $\tilde{s_i} = s_i / X_F$, which to leading order is $s_i/(2f)$, gives us the $\hat{b}_V$ improvement coefficient. Using the equivalent results from eq.6.34 for $V_4^{\eta R}$

$$\begin{aligned} \langle p|V_4^{\eta}|p\rangle^R &= A^R_{\overline{N}\eta N} = \frac{1}{\sqrt{6}}(2+1-0), \\ \langle \Sigma^+|V_4^{\eta}|\Sigma^+\rangle^R &= A^R_{\overline{\Sigma}\eta\Sigma} = \frac{1}{\sqrt{6}}(2+0-2), \\ \langle \Xi^0|V_4^{\eta}|\Xi^0\rangle^R &= A^R_{\overline{\Xi}\eta\Xi} = \frac{1}{\sqrt{2}}(1+0-4), \end{aligned} \tag{6.38}$$

which not only gives consistency with previous eqs. 6.35,6.36, but in addition we get $r_1^{con'} = 0$, $r_2' = 0$, or if rewritten from eqs. 6.33

$$r_1^{con} = -2\sqrt{3}f(\hat{b}_V + 3\hat{f}_V^{con}), \quad r_2 = 0. \tag{6.39}$$

6.5 Results

Using the method we have described in the previous sections, we now use our lattice calculations and the ensembles in Table 3.1. to demonstrate some of the features of this expansion.

6.5.1 X Plots

We consider first, the quantities from the lattice $X_D^{F_1\ con}$, $X_F^{F_1}$ and $X_F^{F_2\ con}$, $X_F^{F_2}$, where here F_1 and F_2 refer to the electromagnetic form factors, which we construct from the diagonal form factors; D_1^{con}, D_2^{con} and D_4 from eq. 6.11 and F_1, F_2 and F_3 in eq. 6.13. In Fig. 6.1 we show $X_D^{F_1\ con}$ and $X_F^{F_1}$ for the F_1 Dirac form factor for two fixed values of Q^2 at $Q^2 = 0$ and 0.49 GeV^2. As we expected, the Xs are constant across the ensembles and show almost no signs of $O(\delta m_l^2)$ or any curvature effects. To show how far we have to extrapolate to get the quark mass from our symmetric point to the physical point, we use a previous determination of $\delta m_l^* = -0.01103$ [120], where $*$ denotes the physical point. We see as noted earlier for $Q^2 = 0$, $X_D^{F_1\ con}$ vanishes as $d = 0$, which is visible on the plot.

This constant nature of the Xs does not depend on which form factor we use to calculate them, as in Fig. 6.2 we see a similar plot, only now for the F_2 Pauli form factor, with $X_D^{F_2}$ and $X_F^{F_2}$, for two fixed Q^2 values at $Q^2 = 0.25$ and 0.49 GeV^2. With again the plot showing the Xs to be constant within statistics. Due to the limitations of the F_2 Pauli form factor, we can only determine the $Q^2 = 0$ value via extrapolation, thus we show $Q^2 = 0.25$GeV^2 instead.

By taking a value at multiple fixed Q^2 points, we can plot the dependency of X on Q^2. In Fig. 6.3 we see the Q^2 dependence of $X_D^{F_1\ con}$ and $X_F^{F_1}$ as well as $X_D^{F_2}$ and $X_F^{F_2}$, using previously determined fitted values at δm_l^*, using fits as shown in Fig. 6.1 and 6.2. This gives us the dependence of Q^2 that both d and f show respectively. We can see that for $X_F^{F_1}$, d is initially zero and remains small, while f drops almost as $1/Q^2$ as we would expect from all f and d for large Q^2 for all form factors.

6.5.2 Fan Plots

We now look to the 'fan' plots that we defined in eq. 6.11 and 6.13. We are only considering the unimproved lattice quantities, as the improved operators would only

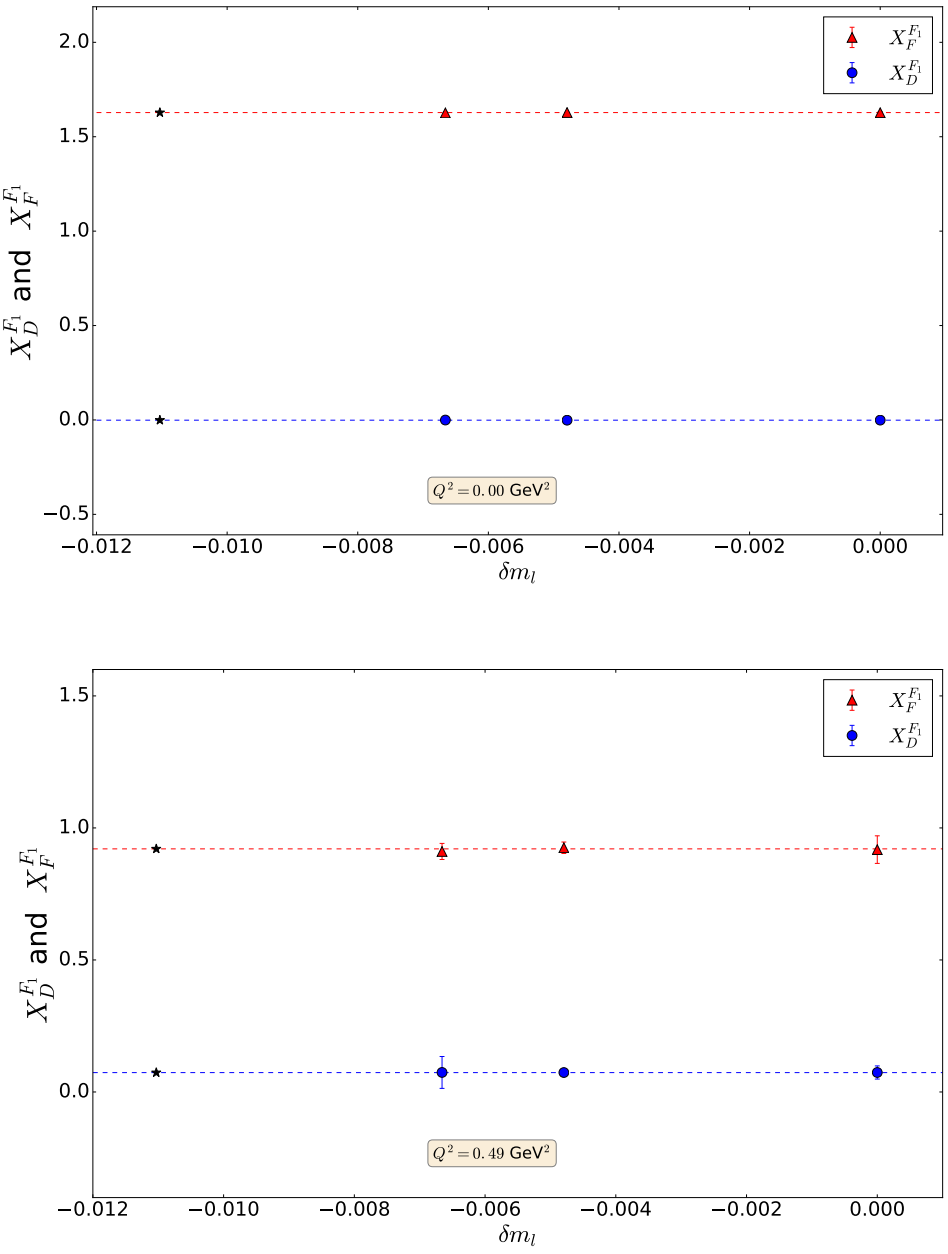

Figure 6.1: $X_D^{F_1 con}$ and $X_F^{F_1}$ for F_1 at $Q^2 = 0.00$ GeV^2, top panel and for $Q^2 = 0.49$ GeV^2, lower panel. The lower filled circles in each plot are$X_D^{F_1}$, the upper filled triangles are $X_F^{F_1}$. The dashed lines are constant fits and the stars represent the physical point.

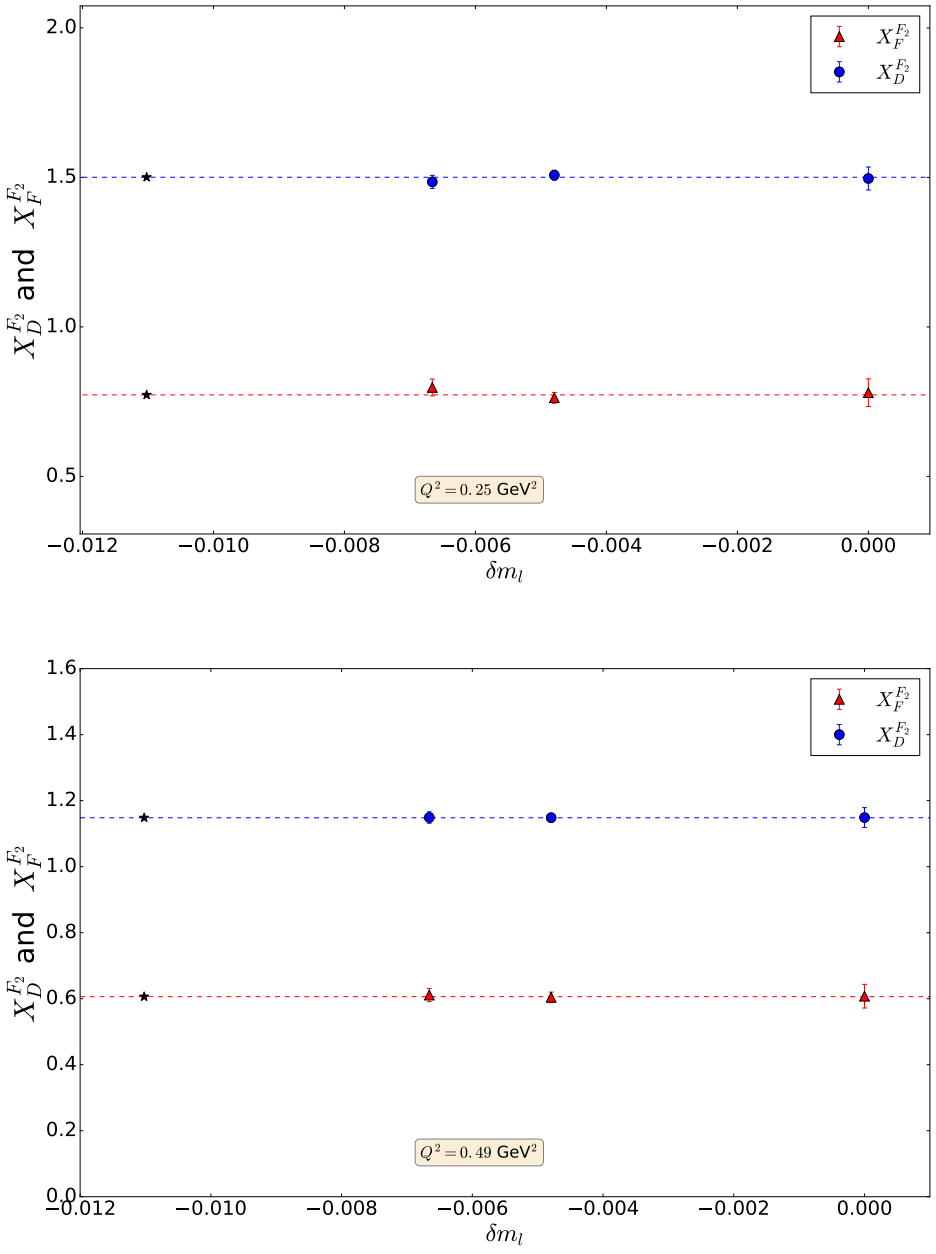

Figure 6.2: $X_D^{F_{2con}}$ and $X_F^{F_2}$ for F_2 at $Q^2 = 0.25$ Gev^2, top panel and for $Q^2 = 0.49$ GeV^2, lower panel. Same notation as Fig. 6.2.

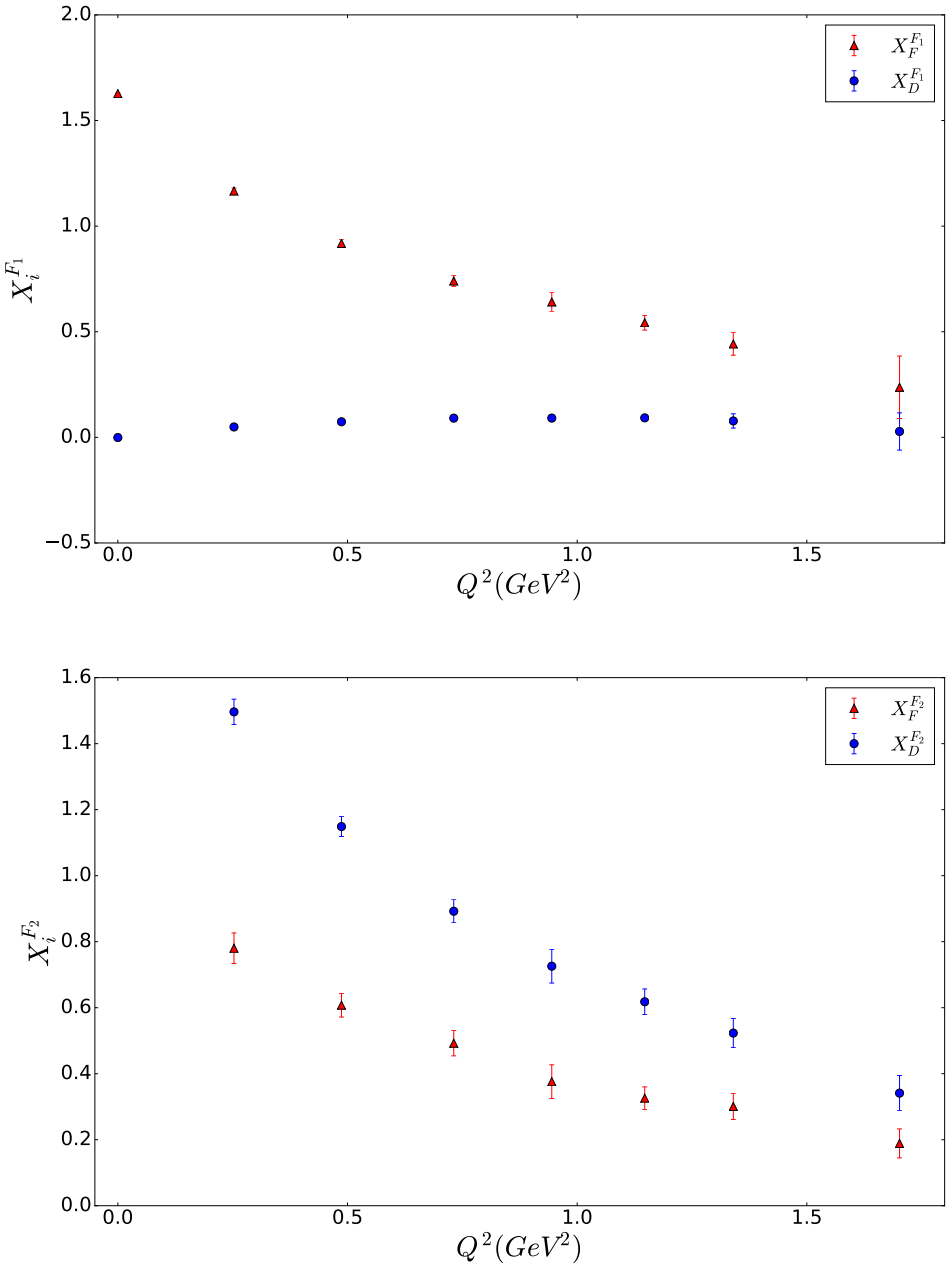

Figure 6.3: Top panel: $X_F^{F_1}$ (filled circles) and $X_D^{F_{1con}}$ (filled triangles) versus Q^2. Lower panel: similarly for F_2.

have minimal changes to the $SU(3)$ flavour breaking expansion, and also only consider once again the diagonal form factors in these equations D_1^{con}, D_2^{con} and D_4 from eq. 6.11 and F_1, F_2 and F_3 in eq. 6.13. To generate the 'fan' plots, we construct systems of linear equations for eq. 6.11, taking the parameters r_1^{con}, r_3 and d for the d-fan, and using eq. 6.13 with parameters s_1, s_2 and f for the f-fan.

In Fig. 6.4 we show the 'fan' plots for $\tilde{D_i}^{F_1} = D_i^{F_1}/X_F$ for $i = 1$, 2 and 4 and $\tilde{F_i}^{F_1} = F_i^{F_1}/X_F$ for $i = 1$, 2 and 3. We divide the D_i terms by X_F rather than X_D due to the fact that d vanishes for the F_1 Dirac form factor at $Q^2 = 0$ and remains small even away from $Q^2 = 0$, thus dividing by this value only causes unnessecary noise and is not beneficial. This is not the case for all form factors as seen in $X_D^{F_2}$, however for consistency, X_F is always used. This only causes our symmetric point for the D_i 'fan' plots to no longer be constrained to one.

The lines shown in Fig. 6.4 correspond to the linear fits of the $D_i^{F_1\ con}$ using eq. 6.11 in the upper plot and $F_i^{F_1\ con}$ using eq. 6.13 in the lower plot. The lines are generated from a least squares fit on the system of linear equations to determine r_1^{con}, r_3 and so these values are quite tightly constrained. By determining these two parameters, we can also predict the off-diagonal hyperon decays for $i = 6$, which is also shown. Similarly for $F_i^{F_1}$, we determine the constrained fit parameters $\tilde{s}_1 = s_1/X_F$, $\tilde{s}_2 = s_2/X_F$ and then plot the off-diagonal hyperon decays for $i = 4$, 5.

We show the equivalent results for F_2 in Fig. 6.5 where again we normalised the parameters $\tilde{r}_1^{con} = r_1^{con}/X_F$, $\tilde{r}_3 = r_3/X_F$ and $\tilde{s}_1 = s_1/X_F$, $\tilde{s}_2 = s_2/X_F$, with the addition of off-diagonal hyperon decays on the d-fan plot for $i = 6$; and on the f-fan plot for $i = 4$, 5.

From the fan plots, we can extract a dependence of the expansion coefficients r_1^{con},r_3, s_1 and s_2 on Q^2 by taking the fan plots at various fixed Q^2 points. In Fig. 6.6 we show the expansion coefficients r_1^{con},r_3, s_1 and s_2 for the F_1^{con} and F_2 form factors as functions of Q^2. As mentioned previously at $Q^2 = 0$ the expansion coefficients for F_1^{con} vanish, which determines the improvement coefficients b_V, f_V^{con}. Thus we see in the top panel of Fig. 6.6, at $Q^2 = 0$ the negative values of the expansion coefficients r_1^{con}, s_1 and s_2 show a clear indication of the nature of the improvement coefficients, which would force these expansion coefficients to vanish.

We can see that $|r_3|$,$|s_1| \approx 0$ and $|r_1^{con}|$ is a factor two – four larger than $|s_2|$. For the F_2 form factor, the coefficients are flatter, with $s_2 \approx 0$ as shown in Fig. 6.5, by the almost indistinguishable difference between $\tilde{F_3}^{F_2}$ and $\tilde{F_4}^{F_2}$.

6.5.3 Estimating $\hat{Z}_V$ and $\hat{b}_V$

As mentioned previously, $X_F^{F_1}$ at $Q^2 = 0$ determines the renormalisation constant $\hat{Z}_V$ via eq. 6.36. The constant fit described in eq. 6.14 and shown in Fig. 6.1 and 6.3,

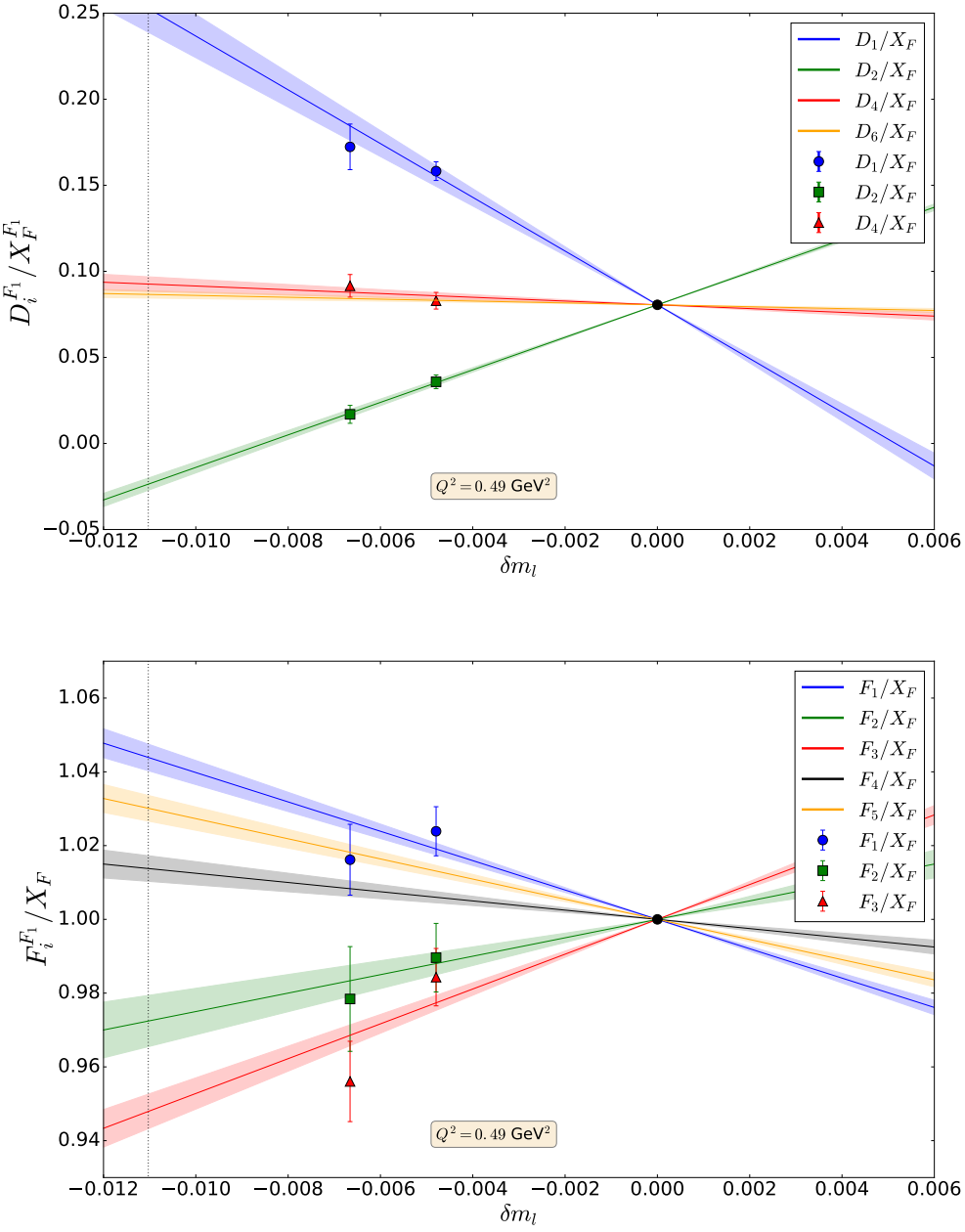

Figure 6.4: Top panel: $\tilde{D_i^{F_1}} \equiv D_i^{F_1}/X_F^{F_1}$ for i = 1 (filled circles), 2 (filled squares) and 4 (filled triangles) for $Q^2 = 0.49$ GeV^2. The three fits are from eq. 6.11, the line for $i = 6$ is also shown. The vertical dotted line represents the physical point. Lower panel: $\tilde{F_i^{F_1}} \equiv F_i^{F_1}/X_F^{F_1}$ again at $Q^2 = 0.49$ GeV^2 for i = 1 (filled circles), 2 (filled squares) and 3 (filled triangles) . The three fits are from eq. 6.13, and the lines for $i = 4, 5$ are also shown.

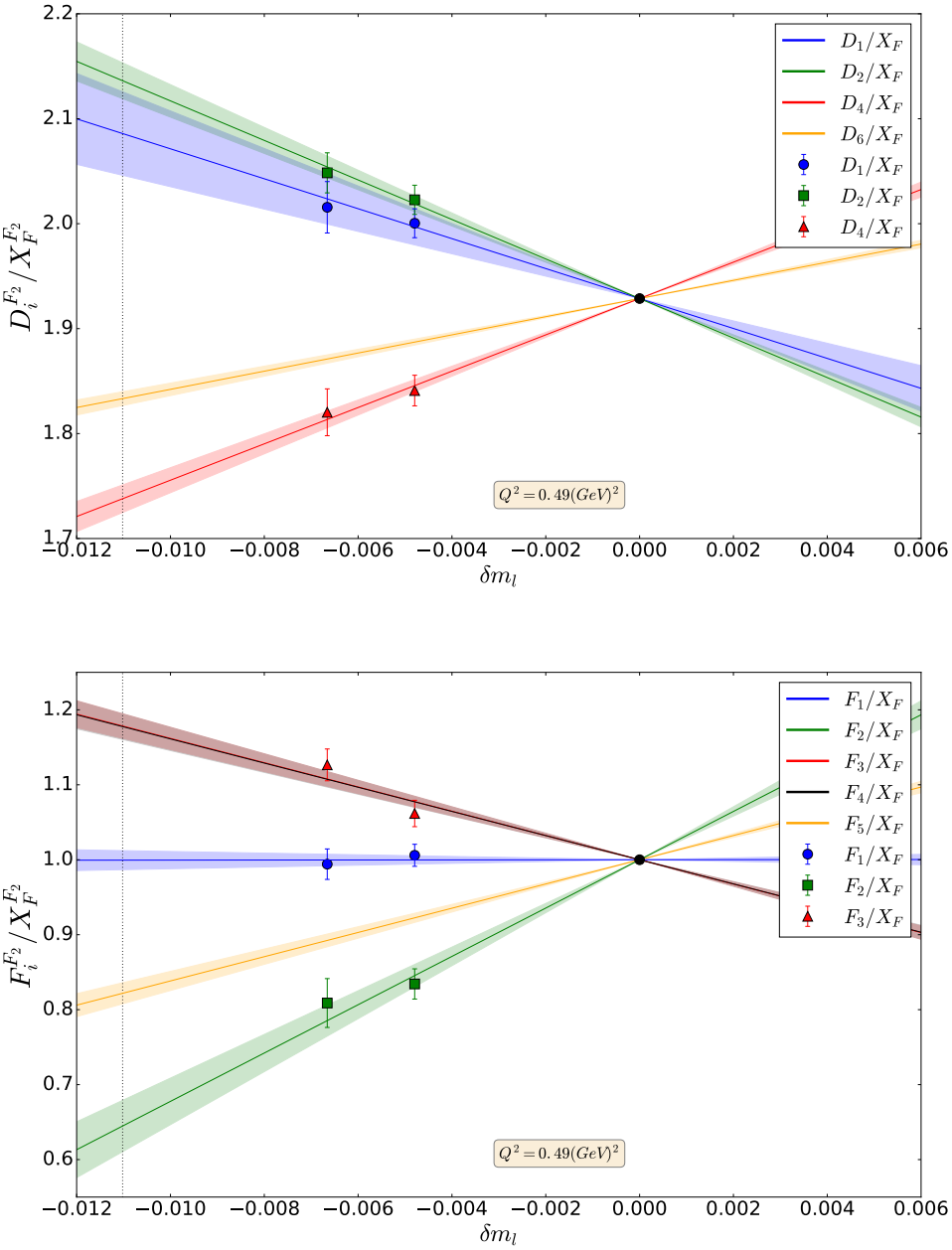

Figure 6.5: Top panel: $\tilde{D_i^{F_2}} \equiv D_i^{F_2}/X_F^{F_2}$ for i = 1 (filled circles), 2 (filled squares) and 4 (filled triangles) for $Q^2 = 0.49$ GeV^2. The three fits are from eq. 6.11 normalised by $X_F^{F_2}$, the line for $i = 6$ is also shown. The vertical dotted line represents the physical point. Lower panel: $\tilde{F_i^{F_2}} \equiv F_i^{F_2}/X_F^{F_2}$ again at $Q^2 = 0.49$ GeV^2 for i = 1 (filled circles), 2 (filled squares) and 3 (filled triangles) . The three fits are from eq. 6.13 normalised by $X_F^{F_2}$, and the line for $i = 5$ is also shown.

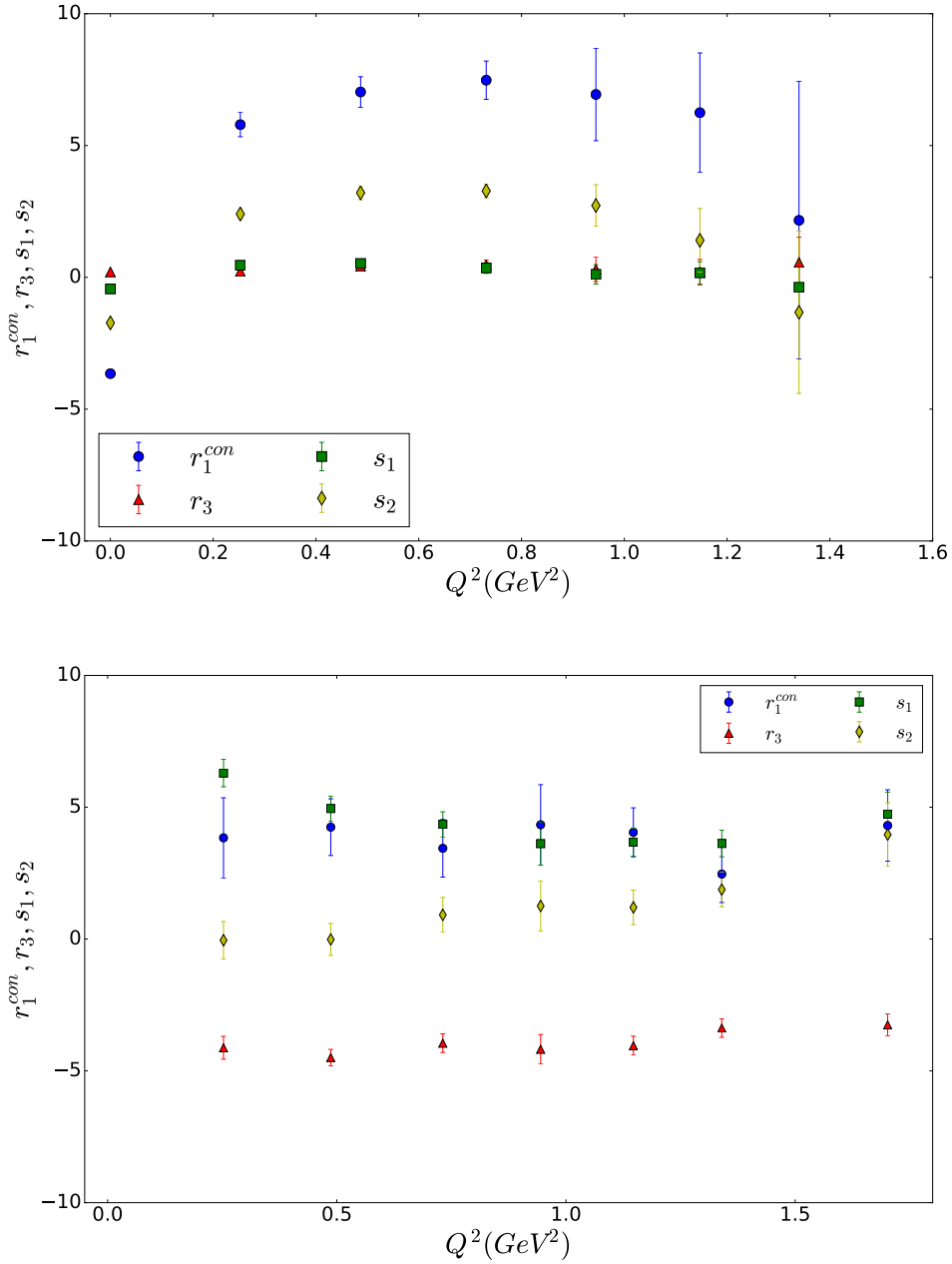

Figure 6.6: Top panel: r_1^{con} (filled circles), r_3 (filled triangles), s_1 (filled squares) and s_2 (filled diamonds) expansion coefficients for the vector F_1^{con} form factor as a function of Q^2. Lower panel: Similarly for the F_2 form factor.

leads to $f = 0.814(1)$ or

$$\hat{Z}_V = 0.869(1). \tag{6.40}$$

Previous non-perturbative estimates of Z_V at $\beta = 5.50$ are given in [100, 121] and Chapter 5 of 0.863(4), 0.857(1) and 0.8519(95) respectively, and are close to $\hat{Z}_V$ in eq. 6.40 with different determinations having $O(a)$ differences and the difference between the Z_V and $\hat{Z}_V$ of $\sim 1 + b_V\overline{m}$. For this calculation we have $b_V \sim O(1)$ and $\overline{m} \sim 0.01$ (from [75]), so there is another $\sim 1\%$ further difference.

From Fig. 6.6, the $Q^2 = 0$ value for r_3 is 0.06(2), which compared to other values is compatible with zero. The $Q^2 = 0$ values for $s_1 = -0.479(22)$ and $s_2 = -1.643(44)$ give the ratio $s_2/s_1 = 3.42$ which is in good agreement of the theoretical value for the ratio from eq. 6.37 of $2\sqrt{3} \sim 3.46$. Similarly using eq. 6.37, we find the weighted average of

$$\hat{b}_V = 1.174(21), \tag{6.41}$$

which is about a 15% increase from the tree level value. Although not a direct comparison to other computations, the value determined here is much closer to tree level as opposed to [118] and $n_f = 0$, 2 [119], suggesting that the improvement coefficients; including $\hat{c}_V$, are possibly small.

From this value of $\hat{b}_V$ together with $r_1^{con} = -3.65(8)$ using eq. 6.39 allows us to find a weighted average of

$$\hat{f}_V^{con} = 0.041(4), \tag{6.42}$$

which as we expect is quite small.

6.5.4 Electromagnetic form factor results

Having now calculated f,d and r_1^{con},r_3,s_1, and s_2 we can find the electromagnetic Dirac form factor $F_1^{con}(Q^2)$ and Pauli form factor $F_2^{con}(Q^2)$ using the electromagnetic current $J_{em\mu}^{con}$ and results from eq. 6.26 and the renormalisation values $\hat{Z}_V$, $\hat{b}_V$ and $\hat{f}_V^{con}$.

We are able to reconstruct the various contributions to the form factors from the expansion coefficients and here we shall consider the F_1^{con} form factor for p and Ξ^0. From eq. 6.26, we can write

$$\begin{aligned}
\langle p|J_{em}|p\rangle^{con\ R} &= \frac{X_F(Q^2,\overline{m})}{X_F(0,\overline{m})}\left[1 + \frac{2}{\sqrt{3}}\tilde{d}(Q^2,\overline{m}) + \tilde{\epsilon}'_p(Q^2,\overline{m})\delta m_l\right], \\
\langle \Xi^0|J_{em}|\Xi^0\rangle^{con\ R} &= \frac{X_F(Q^2,\overline{m})}{X_F(0,\overline{m})}\left[\frac{4}{\sqrt{3}}\tilde{d}(Q^2,\overline{m}) - \tilde{\epsilon}'_{\Xi^0}(Q^2,\overline{m})\delta m_l\right]
\end{aligned} \tag{6.43}$$

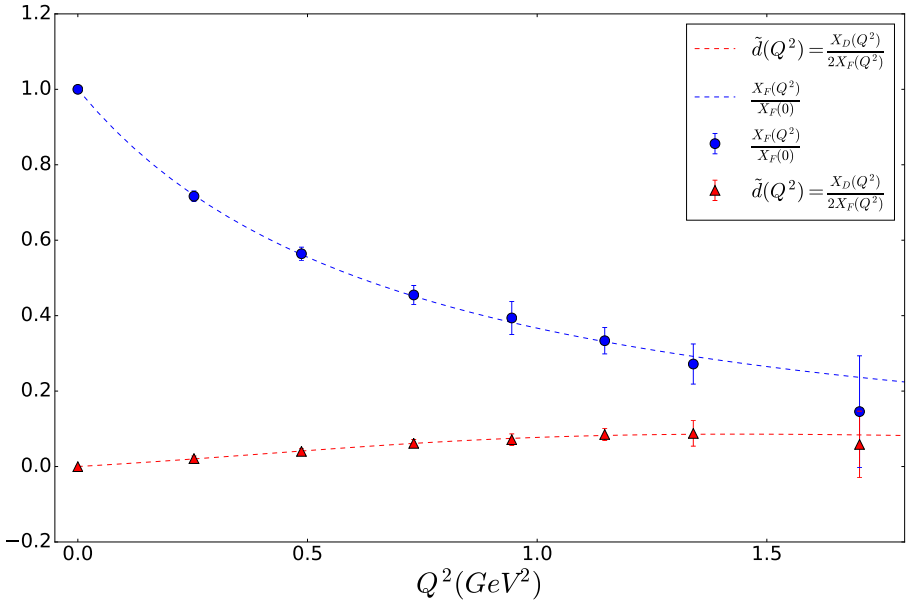

Figure 6.7: $X_F(Q^2)/X_F(0)$ (filled circles) and $\tilde{d}(Q^2)$ (filled triangles) for F_1^{con} against Q^2. The interpolation formulae used are given in eq. 6.45

with

$$\begin{aligned}\tilde{\epsilon}'_p &= \frac{1}{\sqrt{3}}\left(\tilde{r_1}^{con'} - \tilde{s_2}'\right) + 2\left(\tilde{s_1}' - \tilde{r_3}'\right) \\ \tilde{\epsilon}'_{\Xi^0} &= \frac{1}{\sqrt{3}}\left(\tilde{r_1}^{con'} + \tilde{s_2}'\right) + 2\left(\tilde{s_1}' + \tilde{r_3}'\right)\end{aligned} \tag{6.44}$$

where here $\tilde{r_1}^{con'} = r_1^{con'}(Q^2, \overline{m})/X_F(Q^2, \overline{m})$ and similarly for the other expansion coefficients, where the $'$ includes the improvement terms from eq. (6.31,6.32).

In Fig. 6.7, we show the results for the $X_F(Q^2)/X_F(0)$ and $\tilde{d}$ terms from eq. 6.43 and in Fig. 6.8 we show the improved expansion coefficients $\tilde{r_1}^{con'}$, $\tilde{r_3}'$, $\tilde{s_1}'$ and $\tilde{s_2}'$ versus Q^2. We use an interpolating function to fit all the terms in the form

$$\frac{AQ^2}{1 + BQ^2 + CQ^4}. \tag{6.45}$$

From Fig. 6.7, we can see that the leading term in eq. 6.43 for the proton form factor $X_F(Q^2, \overline{m})/X_F(Q^2, \overline{m})$ from the f term is the dominant contribution, while there is a smaller contribution from the d term in $\tilde{d}(Q^2, \overline{m})$. And from Fig. 6.8, we see clearly that there is essentially no contribution from $\tilde{s}'_1$ and $\tilde{r_3}'$ and so most of the contribution from the $\tilde{\epsilon}$ terms comes from $\tilde{r_1}^{con'}$ and $\tilde{s_2}'$.

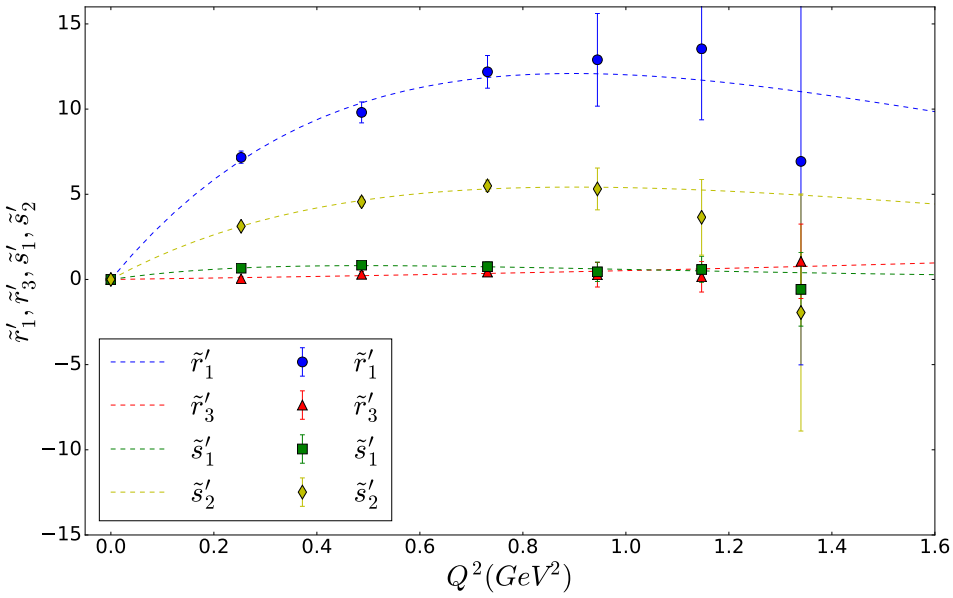

Figure 6.8: $\tilde{r}_1^{con'}$ (filled circles) and $\tilde{r}_3'$ (filled triangles), $\tilde{s}_1'$ (filled squares) and $\tilde{s}_2'$ (filled diamonds) against Q^2 together with interpolation formulae given in eq. 6.45

To show this effect more clearly, we take a plot of the F_1 Dirac form factor for the p and Ξ^0. In Fig. 6.9 we have the extrapolated results for the $F_1^{con\ R}$ form factor for these baryons at our physical point $\delta m_l^* = -0.01103$. This figure shows the individual contributions to the complete eq. 6.43 for p and Ξ^0, with the dashed line $X_F(Q^2)/X_F(0)$, the dashed-dotted lines are the leading terms; $X_F(Q^2,\overline{m})/X_F(0,\overline{m})(1+2/\sqrt{3}\tilde{d}(Q^2,\overline{m}))$ and $X_F(Q^2,\overline{m})/X_F(0,\overline{m})\times 4/\sqrt{3}\tilde{d}(Q^2,\overline{m})$ respectively. The full lines are then the complete expressions.

From this we can see that the f term from the proton $(X_F(Q^2,\overline{m})/X_F(0,\overline{m}))$ provides a result very close to the total numerical result, with the inclusion of the d term, pulling it in a slightly positive direction and the addition of the $O(\delta m_l)$ term, pushes it back in a negative direction. These additional terms only contribute a small percentage of the total final result. For the Ξ^0 fit, the inclusion of the $O(\delta m_l)$ term improves the agreement of the fit with the data.

6.5.5 Tensor form factor results

We can follow the same procedure we used previously for the electromagnetic form factor F_1; for the tensor form factors we looked at in Chapter 4, allowing us to then extrapolate using our SU(3) flavour symmetry breaking to find the form of the three

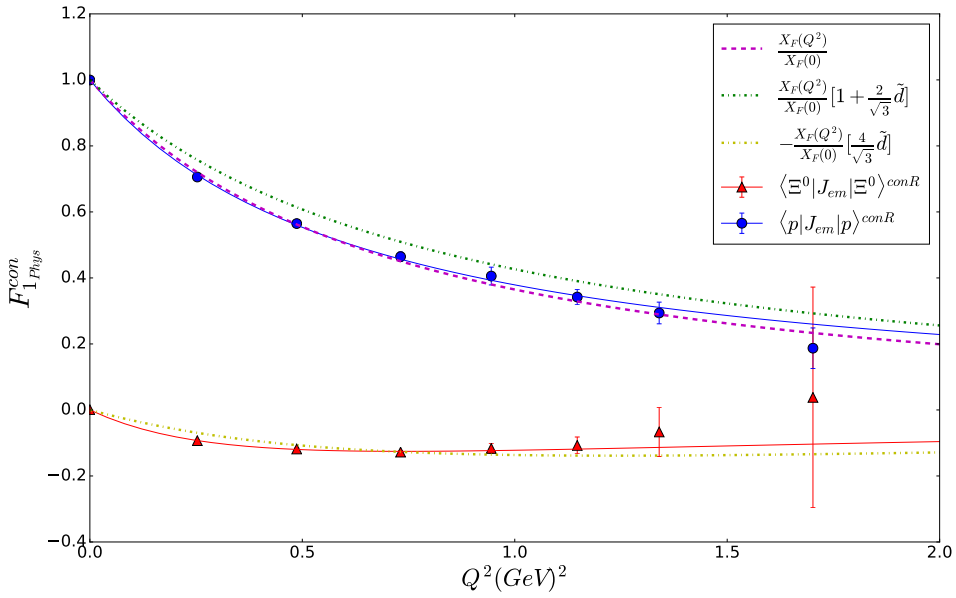

Figure 6.9: $F_1^{con\ R}$ for the proton (filled circles) and Ξ^0 (filled triangles) at the physical point. The dashed line is $X_F(Q^2)/X_F(0)$. The dashed-dotted lines are the complete leading terms, for the proton: $X_F(Q^2,\overline{m})/X_F(0,\overline{m})(1+2/\sqrt{3}\tilde{d}(Q^2,\overline{m}))$ and for Ξ^0: $X_F(Q^2,\overline{m}/X_F(0,\overline{m})\times 4/\sqrt{3}\tilde{d}(Q^2,\overline{m}))$, while the full lines are the complete expressions in eq. 6.43.

tensor form factors A_{T10}, $\tilde{A}_{T10}$ and $\overline{B}_{T10}$ at the physical mass point. Since the process is the same for each of the three tensor form factors, we will use the results from the first tensor form factor A_{T10} to demonstrate the results attainable from a different operator.

Looking at Fig. (6.10) of the X_i for the A_{T10} form factor, we can see the Q^2 dependence of the d and f. Previously we saw for the F_1, that the d stays nearer to zero across the Q^2 range, whilst the f has an approximate $1/Q^2$ dependence. For the A_{T10}, the difference between the d and the f is much more minimal, with both falling off approximately as $1/Q^2$ as we expected to see for other form factors.

For consistency with the electromagnetic results, we take the 'fan' plot results and divide both D_i and F_i by the X_F term rather than X_D term. Even though we no longer have the issue with d vanishing at $Q^2=0$, which is why our D_i 'fan' plot is not constrained to one. Viewing Fig. (6.11), we can see that for similar Q^2 values, the 'fan' plots of the A_{T10} are distinct to the 'fan' plots from both the F_1 and F_2 form factors, such that we expect each operator to generate unique 'fan' plots.

From the 'fan' plots and the equations used to generate them eq. (6.11 and 6.13),

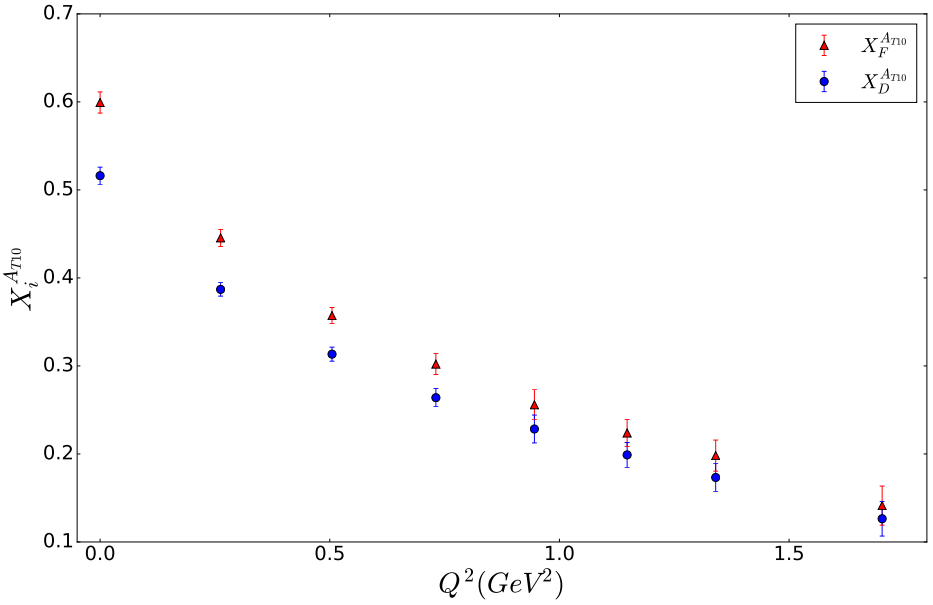

Figure 6.10: $X_D(Q^2)$ and $X_F(Q^2)$ plots of the Tensor form factor A_{T10}. The lower filled circles represent $X_D^{A_{T10}}$ and the upper filled triangles represent $X_F^{A_{T10}}$.

we can calculate the individual slope parameters r_1, r_3, s_1 and s_2 for A_{T10}, which we then plot in Fig. (6.12) as functions of their Q^2 dependence along side their improved expansion coefficients $\tilde{r_1}'$, $\tilde{r_3}'$, $\tilde{s_1}'$ and $\tilde{s_2}'$, fitted using the interpolating function eq. (6.45), where we now have a contribution from each of the expansion coefficients. Where once again we use an improvement in the expansion coefficients in the form, $\tilde{r_1}^{con'} = r_1^{con'}(Q^2, \overline{m})/X_F(Q^2, \overline{m})$ where the $'$ includes improvement terms from eq. (6.31,6.32).

Using these improved expansion coefficient terms $\tilde{r_1}'$, $\tilde{r_3}'$, $\tilde{s_1}'$ and $\tilde{s_2}'$, we can use a modified eq. (6.43) with eq. (6.44) to generate Fig. 6.13. This shows us from the $\tilde{d}(Q^2)$ term, that as we saw in Fig. (6.10), the contribution from the d and f are almost identical, forming an approximately horizontal linear fit, and the fit of $X_F(Q^2)/X_F(0)$ matches the shape of the tensor form factor A_{T10}.

Then following eq. (6.26), we can reconstruct the individual quark component forms of the Tensor form factors, now extrapolated to the physical mass point, where we see the doubly and singly represented contributions to A_{T10} in fig. (6.14). These improved tensor form factors will be of use in the next chapter alongside the improved electromagnetic form factors.

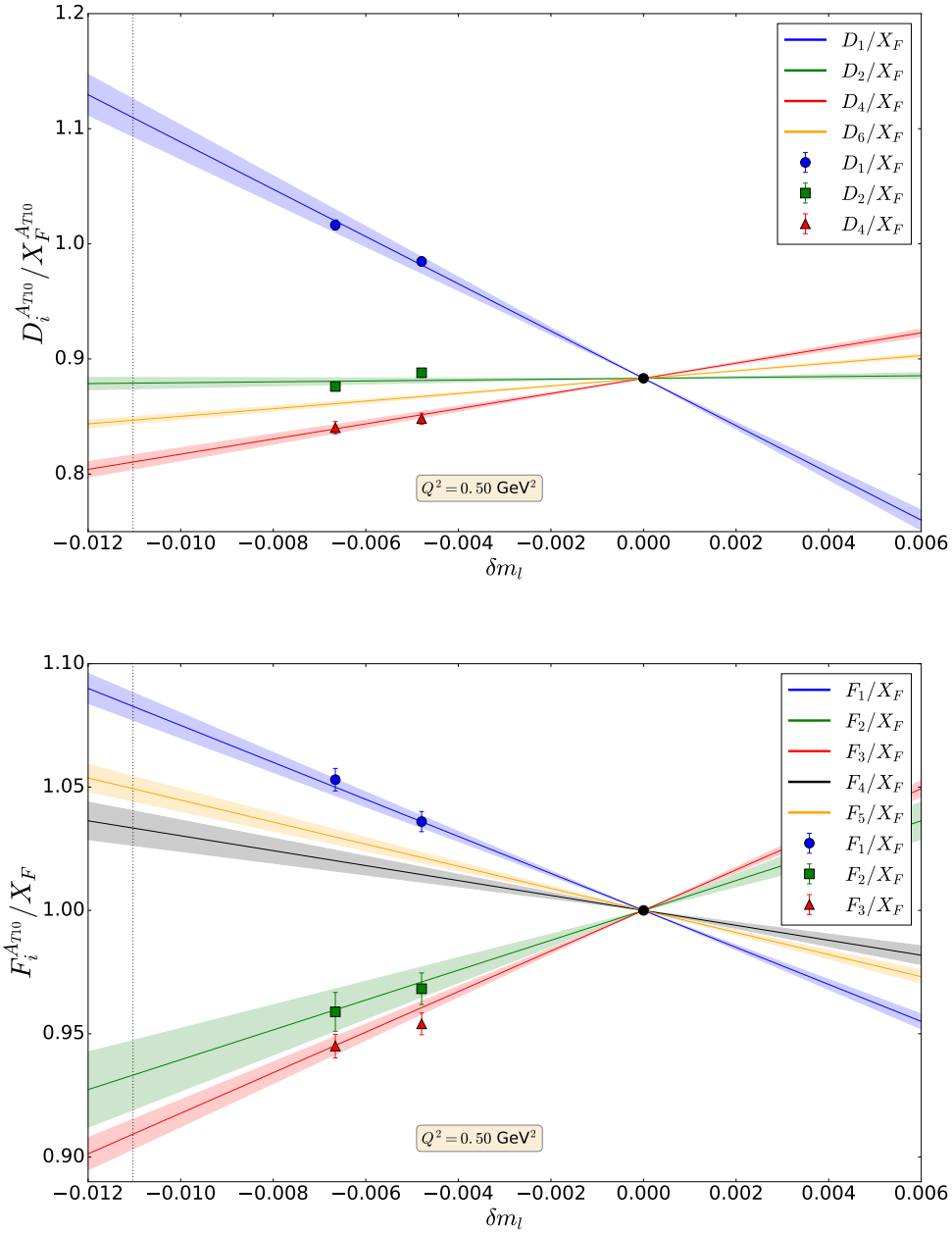

Figure 6.11: Top panel: $D_i^{\tilde{A}_{T10}} \equiv D_i^{A_{T10}}/X_F^{A_{T10}}$ for i = 1 (filled circles), 2 (filled squares) and 4 (filled triangles) for $Q^2 = 0.50$ GeV^2. The three fits are from eq. 6.11, the line for $i = 6$ is also shown. The vertical dotted line represents the physical point. Lower panel: $F_i^{\tilde{A}_{T10}} \equiv F_i^{A_{T10}}/X_F^{A_{T10}}$ again at $Q^2 = 0.50$ GeV^2 for i = 1 (filled circles), 2 (filled squares) and 3 (filled triangles) . The three fits are from eq. 6.13, and the lines for $i = 4, 5$ are also shown.

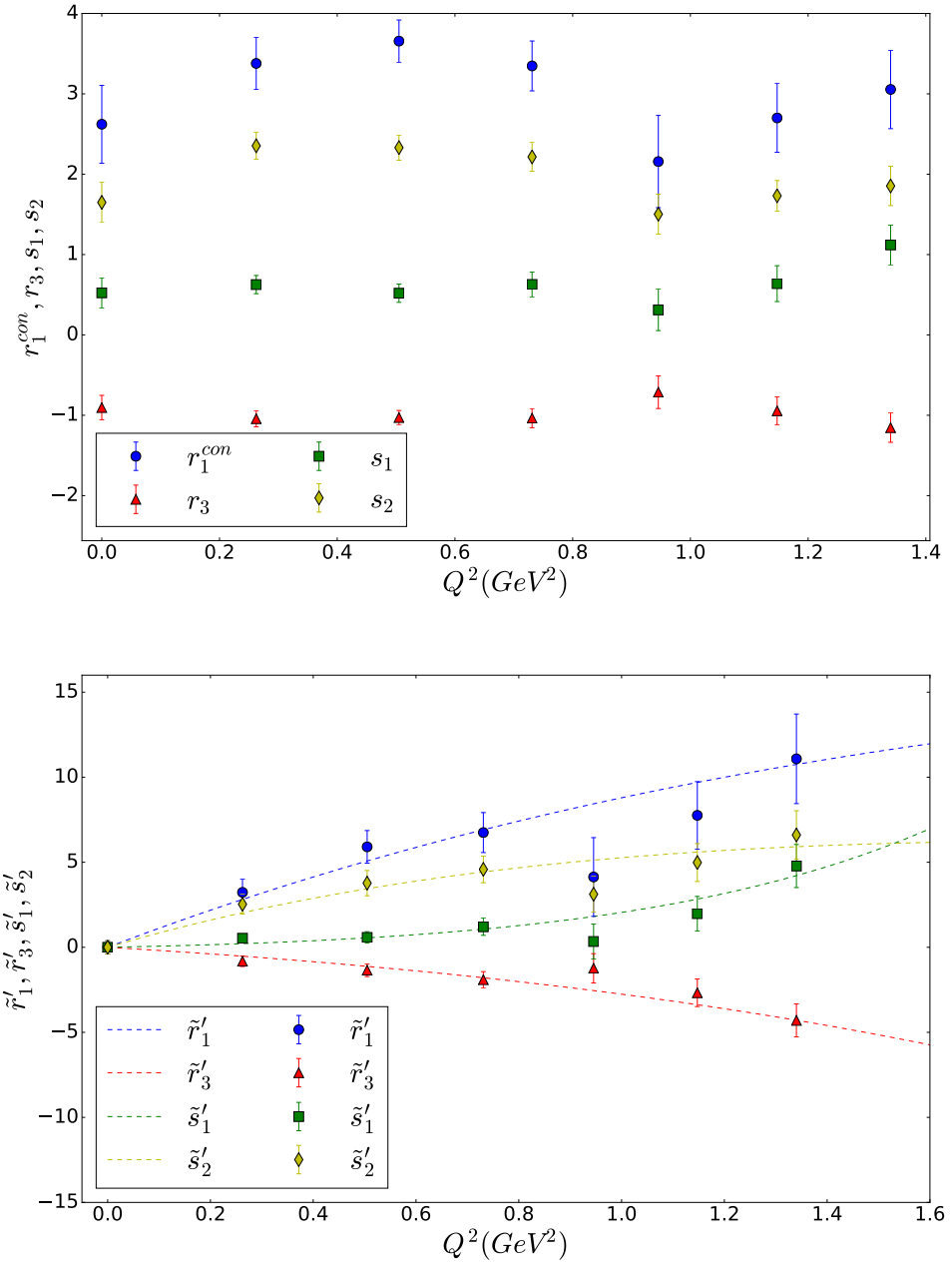

Figure 6.12: Top panel: r_1^{con} (filled circles), r_3 (filled triangles), s_1 (filled squares) and s_2 (filled diamonds) expansion coefficients for the tensor A_{T10} form factor as a function of Q^2. Lower panel: $\tilde{r}_1^{con'}$ (filled circles) and $\tilde{r}'_3$ (filled triangles), $\tilde{s}'_1$ (filled squares) and $\tilde{s}'_2$ (filled diamonds) against Q^2 together with interpolation formulae given in eq. 6.45 for the tensor form factor A_{T10}.

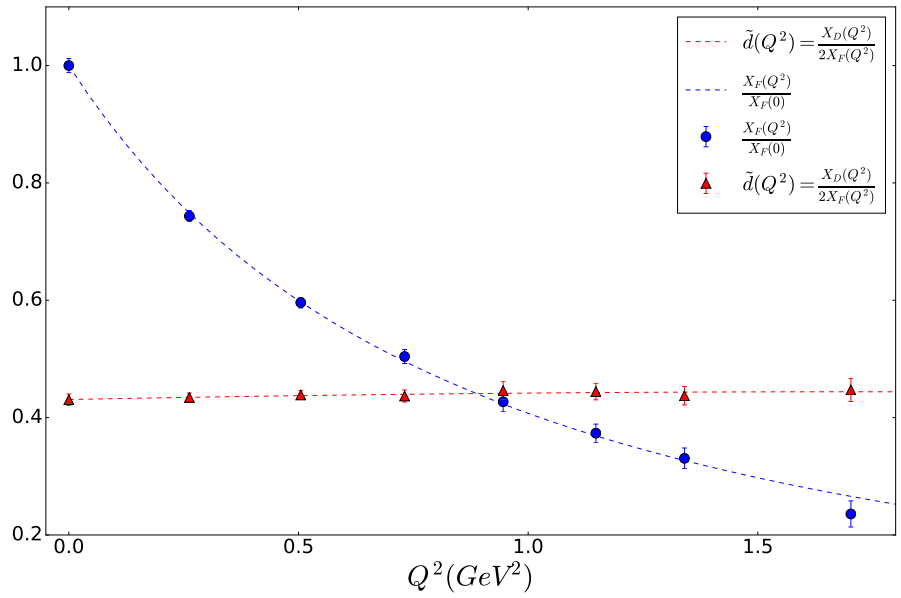

Figure 6.13: $X_F(Q^2)/X_F(0)$ (filled circles) and $\tilde{d}(Q^2)$ (filled triangles) for A_{T10} against Q^2. The interpolation formulae used are given in eq. 6.45.

6.6 Summary

By considering a flavour expansion about the SU(3)-flavour symmetric point, we have been able to investigate the flavour-breaking properties of octet baryon matrix elements after the point where SU(3) is broken by the mass difference between the quarks. Since we constrain our hadron masses to be linear along a mass trajectory where the singlet mass is held constant, we find the expansion similarly constrained, which allows us to look into the mechanics of flavour symmetry breaking, and provides an opportunity for extrapolation to the physical point by expanding upon a generalisation of techniques originally developed in [75, 79] further improved in [1].

We have found that upon the breaking of $SU(3)$ flavour symmetry, in the leading order and next leading order, the expansion is constrained, and there are a large number of relations between our expansion coefficients. We then were able to construct 'singlet-like' matrix elements, X, where the leading order term vanishes and these can be extrapolated to the physical point using a single parameter constant fit, and as we saw these X functions can isolate to either an f or d constant coupling. We also constructed 'fan' plots which are a linear combination of the matrix elements, which at the $SU(3)$ symmetric point have a shared value, but then deviate away from the common value as the quark masses change.

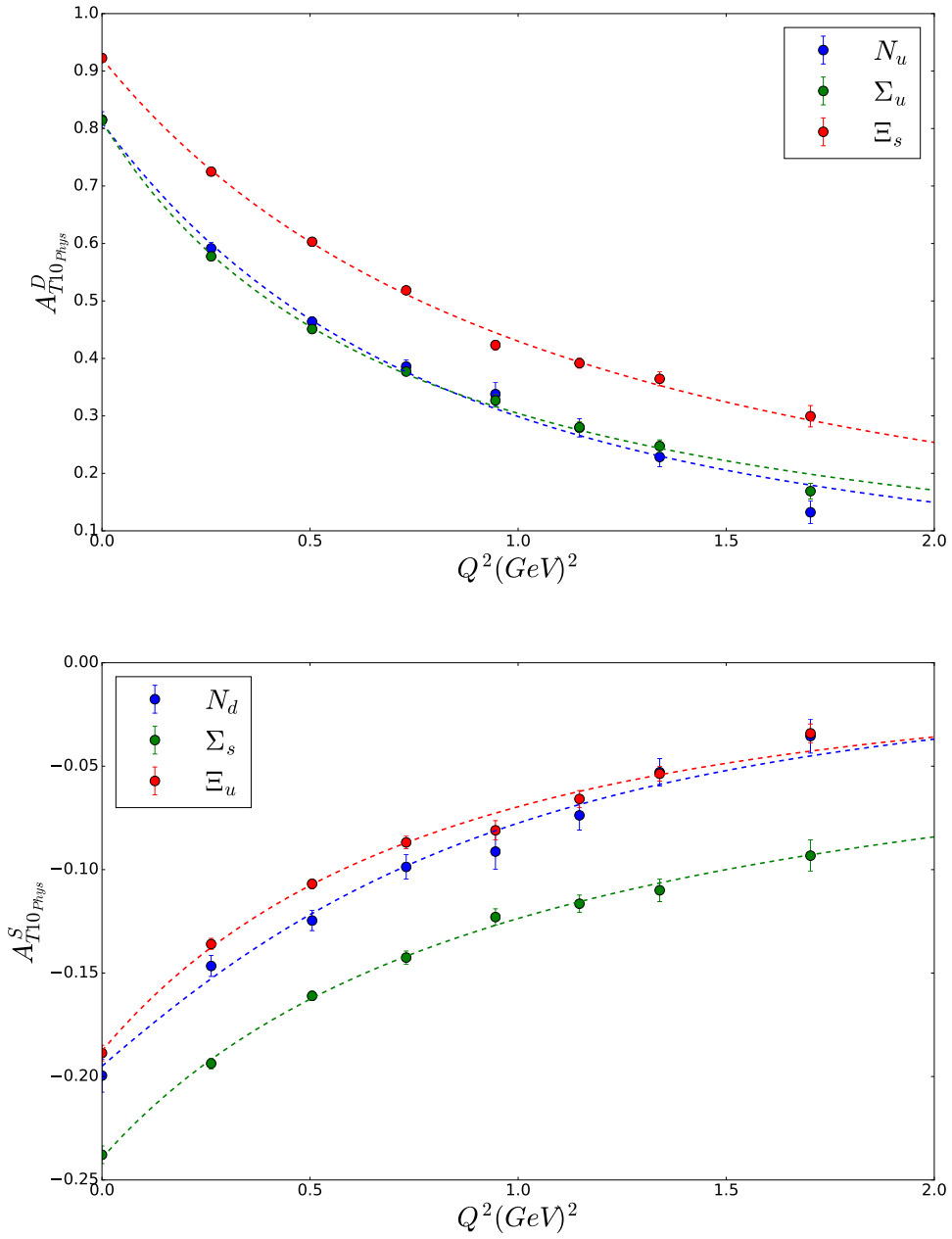

Figure 6.14: Top panel: Doubly represented quark contributions to A_{T10} at the physical mass point, where filled circle represents up-quarks in Nucleon, filled triangles represent up-quarks in Sigma (Σ), and filled squares represents strange-quarks in the Cascade (Ξ). Lower panel: Singly represented quark contributions to A_{T10} at the physical mass point, where filled circle represents the down-quark in Nucleon, filled triangles represent strange-quark in Sigma(Σ), and filled squares represents up-quark in the Cascade (Ξ).

Since we are using Wilson clover improved fermions, when applying these continuum expansions, we need to determine appropriate improvement coefficients. With the general structure for our $n_f = 2+1$ flavours of fermions previously determined [122], we have shown that these improvements are simply equivalent to modifying our expansion coefficients. Using the relation between the local and conserved vector current (CVC) simply being $O(a)$, allowed us to determine the two improvement terms along with a renormalisation constant for this process.

The results we obtain from fig. (6.14) and similarly for the electromagnetic form factors, will be especially useful in Chapter 7, where we require the individual quark contributions to both the Dirac and Pauli form factors of the electromagnetic current, and the three tensor form factors A_{T10}, $\tilde{A}_{T10}$, and $\overline{B}_{T10}$, to generate the transverse spin densities. Having extrapolated these results to the physical point, allows us to report the spin density at the physical point.

Chapter 7

Transverse Spin Structure

To this day the transverse spin structure of quarks in the proton is an intriguing and relatively unknown aspect of baryon structure, and provides a unique perspective on the structure of a hadron.

We have discussed how charge and magnetisation are distributed earlier in Chapter 4, and we wish to extend this to spin-dependent distributions. This entails looking for correlations between the quark and proton spin, and the position of the quark in the transverse plane with respect to these spin polarisations. These properties can all be described by the generalised parton distributions (GPDs) [123–125], which for the case we are interested in, the lowest moments of the GPD's are just the form factors that we calculated in Chapter 4. The Fourier transforms of the form factors then describe how the quarks are distributed into the transverse plane.

Of particular interest is the quark transversity distribution $\delta q(x) = h_1(x)$ which describes the probability of finding transversely polarised quarks with a longitudinal momentum fraction x in a transversely polarised baryon [126]. A number of studies have been done on the generalised transversity distributions introduced in [127–129], but since the operator measuring transversity is chiral-odd, it is difficult to find a process in which the transversity distribution can be accessed via experiment. Progress has been made in trying to understand transverse momentum dependent parton distribution functions (TMD PDFs) through the Boer-Mulders function $h_1^{\perp}(x, k_{\perp}^2)$ [130] describing the correlation of the quark transverse momentum $k_{\perp}$ and the transverse quark spin $s_{\perp}$, as well as through the Sivers function $f_{1T}^{\perp}$ [131], which measures a correlation between $k_{\perp}$ and the transverse baryon spin $S_{\perp}$. An approach to investigate the transverse spin structure through the use of lattice QCD has been accomplished in [132], where a first time quantitative prediction for the signs and sizes of the TMD PDF's was given, showing their relation to the mentioned Sivers and Boer-Mulders functions [133, 134]. As seen in [133], the correlation of transverse position with the transverse spin

of the proton can be shown as an explanation of the Sivers effect, which has been experimentally observed.

In this chapter, we will use the results and methods explained in previous chapters to give an expanded look into the transverse spin structure of these hadrons, where now we are able to view the structure after having extrapolated our form factor results to the physical point as shown in Chapter 6 and compare the structure of the hyperons.

7.1 Transverse Spin Density

Having seen how we calculate both the electromagnetic and tensor form factors in Chapter 4, renormalise quark bilinears in Chapter 5 and then extrapolate these results to the physical point in Chapter 6, we can now use a combination of these form factors to analyse the density distribution of quarks in a transverse baryon. As discussed in Chapter 4, by examining a baryon in the infinite momentum frame, such that we can view the baryon as simply a two dimensional flat object, the only remaining degrees of freedom of the quarks are their position within this transverse plane. Thus by choosing values for the spin of the baryons and the quarks individually we can create spin-dependent density distributions. The x moments of the transverse spin density are given by the following equation [132],

$$\rho(b_\perp, s_\perp, S_\perp) = \int_{-1}^{1} dx x^{n-1}\ \rho(x, b_\perp, s_\perp, S_\perp) \tag{7.1}$$

$$\begin{aligned}
&= \frac{1}{2}\{A_{n0}(b_\perp^2) + s_\perp^i S_\perp^i \left(A_{Tn0}(b_\perp^2) - \frac{1}{4m^2}\triangle_{b_\perp}\tilde{A}_{Tn0}(b_\perp^2)\right) \\
&+ \frac{b_\perp^j \epsilon^{ji}}{m}\left(S_\perp^i B'_{n0}(b_\perp^2) + s_\perp^i \overline{B}'_{Tn0}(b_\perp^2)\right) \\
&+ s_\perp^i \left(2b_\perp^i b_\perp^j - b_\perp^2 \delta^{ij}\right) S_\perp^j \frac{1}{m^2}\tilde{A}''_{Tn0}(b_\perp^2)\}
\end{aligned} \tag{7.2}$$

Here $b_\perp$ describes the quark's distance from the centre of momentum of the baryon, $s_\perp$ describes the transverse spin of a quark, $S_\perp$ describes the transverse spin of the baryon, x is the momentum fraction of the quark and m is the mass of the baryon, where ρ then describes the quark density dependent on these values.

For the lowest x moment of $n = 1$, we have $A_{10}(Q^2) = F_1(Q^2)$ and $B_{10}(Q^2) = F_2(Q^2)$ representing the Dirac and Pauli form factors calculated alongside the $A_{T10}(Q^2)$, $\tilde{A}_{T10}(Q^2)$ and $\overline{B}_{T10}(Q^2)$ tensor form factors, previously in Chapter 4. We then require a Fourier transform from transverse momentum space to the $b_\perp$ dependent form

$$f(\vec{b}_\perp) \equiv \int \frac{d^2q}{(2\pi)^2} e^{-i\vec{b}_\perp \cdot\ \vec{q}} f(-q^2), \tag{7.3}$$

where $Q^2 = -q^2$ is the transverse momentum squared transferred to the baryon.

Again we use the combination of two tensor form factors to form $\overline{B}_{T10}(Q^2)$ where [25],

$$\overline{B}_{T10}(Q^2) \approx 2\tilde{A}_{T10}(Q^2) + B_{T10}(Q^2). \tag{7.4}$$

The derivatives required of the form factors for eq. 7.1 and using the shorthand [132] are defined by

$$f' = \frac{\partial}{\partial b_\perp^2} f, \qquad f'' = \left(\frac{\partial}{\partial b_\perp^2}\right)^2 f, \tag{7.5}$$

and for the two-dimensional Laplace operator acting on functions f that depend on b^2 only

$$\triangle_{b_\perp} f = \frac{\partial}{\partial b_\perp^i}\frac{\partial}{\partial b_\perp^i} f = 4\frac{\partial}{\partial b_\perp^2}\left(b_\perp^2 \frac{\partial}{\partial b_\perp^2}\right) f. \tag{7.6}$$

If we analyse eq. (7.2) in further detail we recognise the orbitally symmetric monopole terms $A_{10}(b_\perp^2)$ and $s_\perp^i S_\perp^i \left(A_{T10}(b_\perp^2) - \frac{1}{4m^2}\triangle_{b_\perp}\tilde{A}_{T10}(b_\perp^2)\right)$, the two dipole structures $b_\perp^j \epsilon^{ji} S_\perp^i B_{10}(b_\perp^2)$ and $b_\perp^j \epsilon^{ji} s_\perp^i \overline{B}'_{T10}(b_\perp^2)$, and the term $s_\perp^i \left(2b_\perp^i b_\perp^j - b_\perp^2 \delta^{ij}\right) S_\perp^j \frac{1}{m^2}\tilde{A}''_{T10}(b_\perp^2)$ corresponds to a quadrupole structure [135]. Thus the derivatives of the EM and tensor form factors $B_{10}(b_\perp)$, $\overline{B}_{T10}(b_\perp)$ and $\tilde{A}_{T10}(b_\perp)$ all correspond to the strength of the distortion in the orbital symmetry in the transverse plane from these dipole and quadrupole terms. The remaining two form factors $A_{10}(b_\perp)$ and $A_{T10}(b_\perp)$ provide only a constant orbitally symmetric addition to the other form factors orbital distortion. To create a two dimensional spin density contour plot, we must transform our momentum space, Q^2 dependent form factors into the impact parameter space $b_\perp$ dependent form factors. We then can simply vary the values of our quark and baryon spin polarisation, $s_\perp^i$ and $S_\perp^i$ respectively, to create unique contour plots.

Where possible we will use a purely analytic solution, otherwise we compute the Fourier transform numerically. Our method of transforming the Q^2 dependent form factors into impact parameter form is to use the Fourier transform from eq. 7.3, only now considering a more general p-pole ansatz

$$A(Q^2) = \frac{A(0)}{(1 - Q^2/m_A^2)^p}, \tag{7.7}$$

where the power p and mass m_A are free parameters for any given form factor $A(Q^2)$. We can then construct modified Bessel functions by inserting eq. 7.7 into eq. 7.3 which gives,

$$A(b^2) = C(m_A b)^{b-1} K_{p-1}, \qquad C = \frac{m_A^2}{2^p \pi \Gamma(p)} A(0), \tag{7.8}$$

with the appropriate Bessel functions K and gamma function Γ, and then our derivatives defined in eqs. 7.5 and 7.6,

$$A'(b^2) = -\frac{1}{2}Cm_A^2(m_Ab)^{p-2}K_{p-2}(m_Ab), \qquad A''(b^2) = \frac{1}{4}Cm_A^4(m_Ab)^{p-3}K_{p-3}(m_Ab),$$
$$\delta_b A(b^2) = -Cm_A^2(m_Ab)^{p-2}\left[2K_{p-2}(m_Ab) - m_AbK_{p-3}(m_Ab)\right]. \tag{7.9}$$

Using the parametrisation eq. 7.7 is only valid in the Q^2 range where the form factor has been fitted and in particular lattice data is only avaliable in a limited Q^2 range (as seen in Chapter 4) with a $|Q^2|_{max}$ of $Q^2 = 1.29(\text{GeV})^2$. This corresponds to a limited resolution of order $(|Q^2|_{max})^{-\frac{1}{2}}$ on the impact parameter [136] and the results obtained on finite lattice volume can only give direct information on quark density behaviour at impact parameters of similar size to the lattice spacing. Regardless, we still wish to see physically plausible behaviour of the impact parameter density at small and large b, and so this parametrisation requires the relations

$$K_0(z) \underset{z\to 0}{\sim} log\frac{2}{z}, \qquad K_p(z) \underset{z\to 0}{\sim} \frac{2^{p-1}\Gamma(p)}{z^p} \text{ for } p > 0,$$
$$K_p(z) \underset{z\to\infty}{\sim} e^{-z}\sqrt{\frac{\pi}{2z}} \tag{7.10}$$

and $K_{-p}(z) = K_p(z)$. With this, for large b, each term in eq. 7.1 should fall off as $(m_Ab)^{p-3/2}e^{-m_Ab}$. In the limit as $b \to 0$, we expect that the terms should not diverge, with terms $b_\perp^j B'_{10}(b_\perp^2)$, $b_\perp^j \overline{B}'_{T10}(b_\perp^2)$ and $(2b^ib^j - b^2\delta^{ij})\tilde{A}''_{T10}(b_\perp^2)$ vanishing at $b = 0$, as they contain non-trivial dependence on the azimuthal angle ϕ. This brings a restriction to the power p in the parametrisations of our form factors to $p > 1$ for A_{10}, A_{T10} and $\tilde{A}_{T10}$, $p > 3/2$ for B_{10} and $p > 2$ for $\overline{B}_{T10}$. The terms A_{10}, A_{T10} and $\Delta_b\tilde{A}_{T10}$ then all have finite values at $b = 0$.

Thus for the next section, we choose the simplest parametrisation of eq. 7.7 based on the above limitations, where $p = 2$ for $A_{10}(Q^2)$, $B_{10}(Q^2)$ and $A_{T10}(Q^2)$, and $p = 3$ for $\tilde{A}_{T10}(Q^2)$ and $\overline{B}_{T10}(Q^2)$. This method limits us to fits using eq. 7.7, and so we will revisit the model dependence in a later section.

7.2 Lattice Results

7.2.1 Unpolarised

By choosing both $S_\perp^i$, $s_\perp^i = 0$, we can create a contour plot of the unpolarised transverse quark density where both the baryon and quark spin are unpolarised. In Fig.7.1, the x and y axes of the contour plot on the left display the perpendicular distance from the centre of the baryon b_x and b_y respectively, with the darkness of colour representing a higher quark probability density. In Fig. 7.1 and further figures to follow

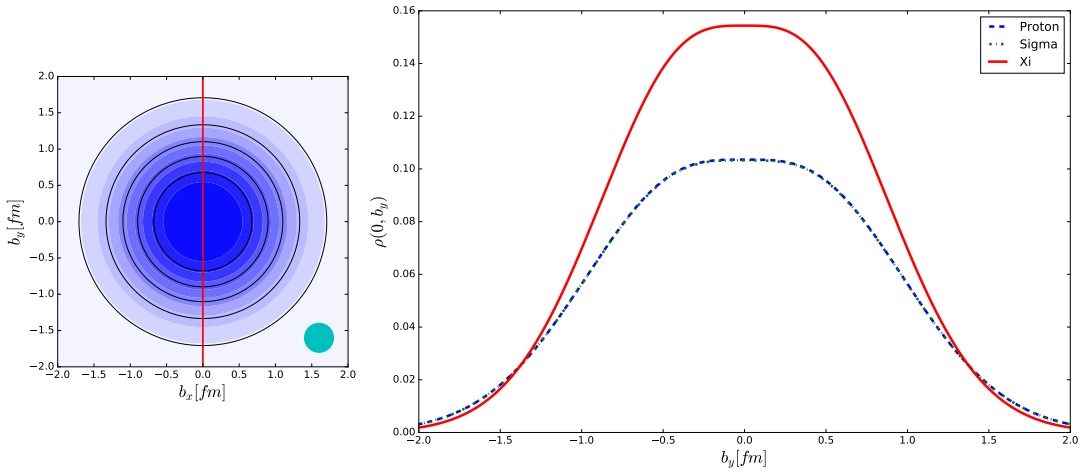

Figure 7.1: Quark density distribution of the doubly represented quark in the proton, sigma and cascade when both the baryon and quark spin are not polarised($S^i_\perp, s^i_\perp = 0$). The figure on the left is a contour plot showing the density distribution of the doubly represented u quark in the proton, $\rho(b_x, b_y)$, with a red line along the vertical at $b_x = 0$ to illustrate the cross-section shown in the right figure. The figure on the right shows a cross section of the density distribution down the $b_x = 0$ vertical axis, with the proton represented by a dashed line, the sigma by a dashed-dotted line, and the cascade by a full red line.

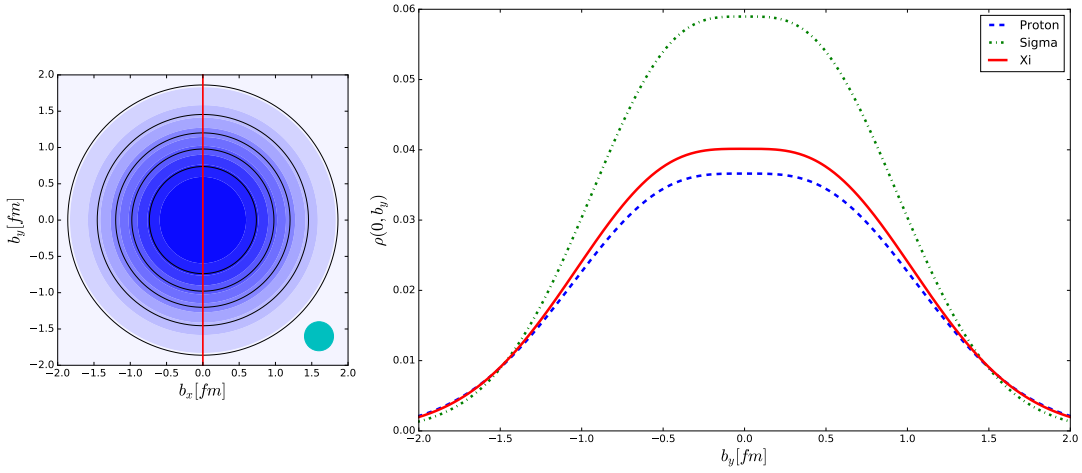

Figure 7.2: Similar to Fig. 7.1, only now showing the singly represented quark density distribution, for unpolarised baryon spin ($S^i_\perp = 0$) and unpolarised quark spin ($s^i_\perp = 0$).

in this chapter, the contour to the left will always be a representation of the quark density distribution of the proton. In the bottom right corner of the contour plot is a light blue circle, which will in the following plots display the spin polarisation of the quark and baryon, with an arrow within and outside the circle respectively, to display the direction of spin polarisation.The lack of such an arrow indicates the absence of polarisation. Thus when the baryon and up quark in the proton are both unpolarised in Fig.7.1, as we might naively expect, the position of the quarks are densely centred around the origin of the baryon. Since both spins are unpolarised, the only remaining term in the spin density eq. (7.1) is the $\frac{1}{2}A_{10}(b_\perp)$ term and so there is no distortion in the orbital symmetry. To the right of the contour plot is a cross-section plot represented by a red line down the centre of the contour plot, displaying the comparison between the proton and the sigma (Σ) and cascade (Ξ) hyperons.

This is a convenient way for us to display the difference in magnitude and the individual features. As we might expect, the heavier strange quark in the cascade baryon leads to a greater magnitude of quark density around the centre of the baryon, whilst the up quarks in the proton and sigma are almost identical. In Fig. 7.2 we show the singly represented case where we have a completely unpolarised quark and baryon, and again in this case, the singly represented strange quark in the sigma gives a greater magnitude in density, but here the presence of the two spectator strange quarks for the cascade, leads to a noticeable difference between the proton and the cascade, having the effect of pulling the singly represented up quark towards the centre of the cascade (Ξ).

7.2.2 Baryon Spin Polarised

We now allow the baryon spin to be polarised, and for example in Fig. 7.3 we orientate the baryon spin polarisation in the b_x-direction (i.e $S_x = 1, S_y = 0$) of the transverse plane as represented by the arrow in the bottom right corner on the outside of the light blue circle. This will bring into the equation the dipole term $\frac{b_\perp^j \epsilon^{ji}}{m} S_\perp^i B'_{10}(b_\perp^2)$, and thus in Fig.(7.3) we can instantly see that for an unpolarised doubly represented quark in the transversely polarised baryon, the density is shifted towards the upper half plane, perpendicular to the direction of the baryon's spin. Again, similar to Fig. 7.1 the strange quarks in the cascade lead to a greater magnitude and higher peak density, only this time the peak of our quark density is found at around $b_y \approx 0.25$ fm shifted in the positive b_y direction perpendicularly away from the direction of our baryon spin. In Fig. 7.3 we observe a similar magnitude at the centre of the baryon as to the unpolarised case in Fig. 7.1 forming an inflection point, showing that this distortion effect brought about by the $\frac{b_\perp^j \epsilon^{ji}}{m} S_\perp^i B'_{10}(b_\perp^2)$ term increases the likelihood of finding a quark in the upper half of the baryon, whilst decreasing the quark density in

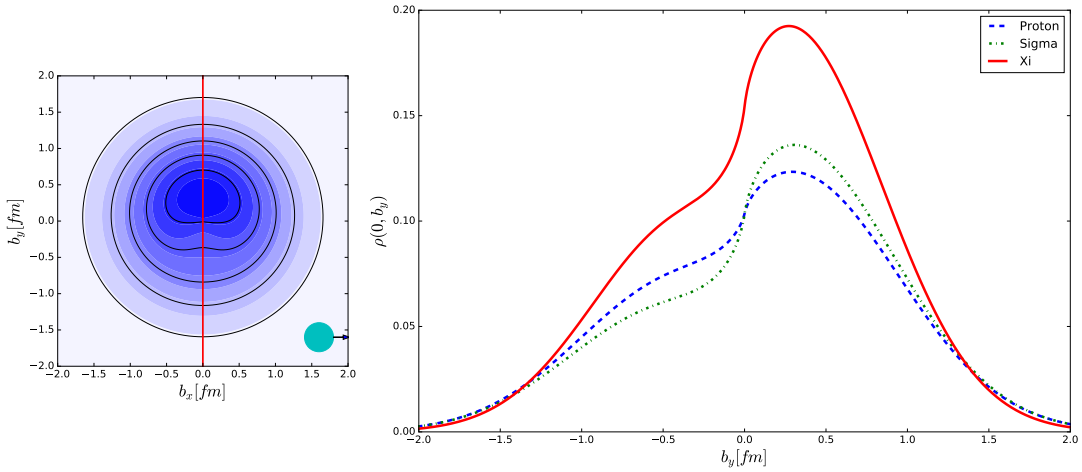

Figure 7.3: Similar to Fig. 7.1, only now showing the doubly represented quark density distribution, for a polarised baryon spin ($S_x = 1$) and unpolarised quark spin ($s^i_\perp = 0$).

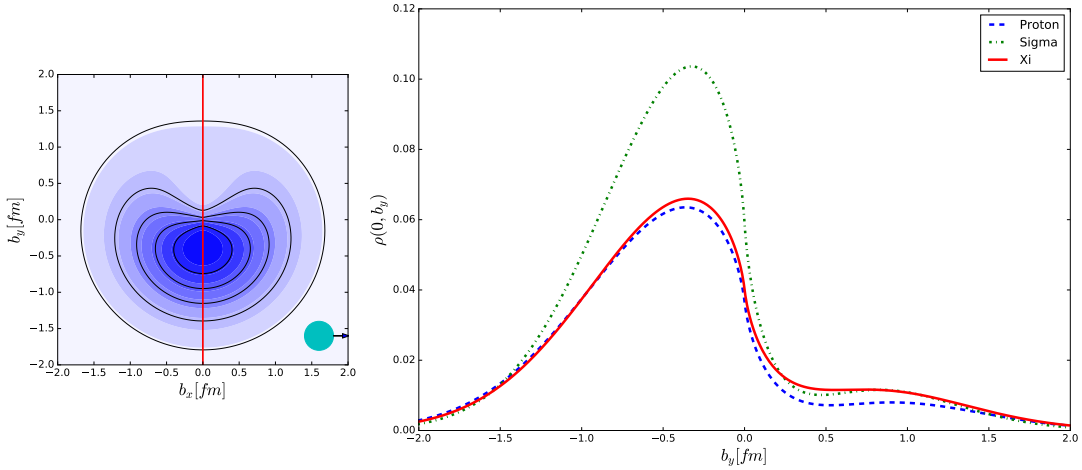

Figure 7.4: Similar to Fig. 7.1, only now showing the singly represented quark density distribution, for polarised baryon spin ($S_x = 1$) and unpolarised quark spin ($s^i_\perp = 0$).

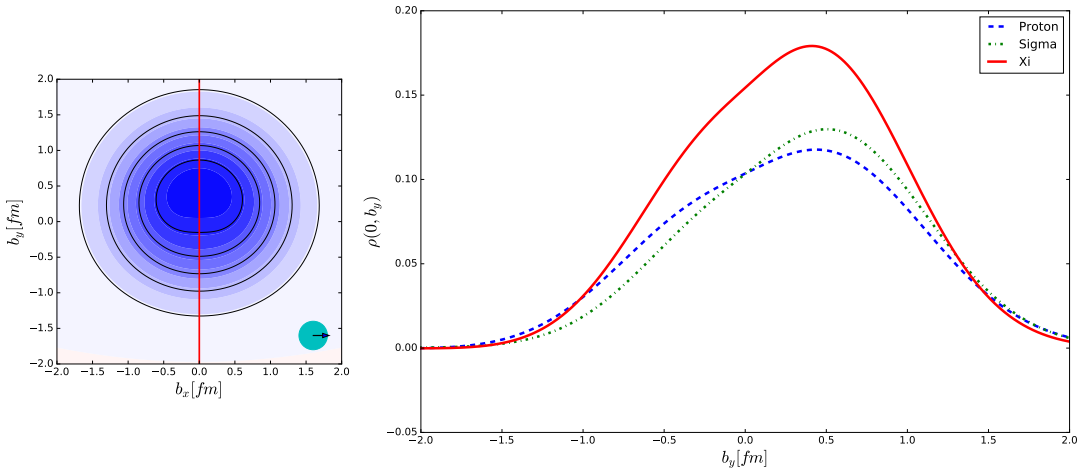

Figure 7.5: Similar to Fig. 7.1, only now showing the doubly represented quark density distribution, for unpolarised baryon spin ($S^i_\perp = 0$) and polarised quark spin ($s_x = 1$).

the lower half. We also see the spectator strange quark in the sigma has a much greater effect on density of the sigma compared to the proton, with a more pronounced effect from the inclusion of this dipole term.

In Fig. 7.4 we show the unpolarised singly represented quark in a polarised baryon, where here the density has shifted in the opposite direction to Fig. 7.3 and instead occupies the lower half of the plane. In this figure, we see a much lower plateau at the inflection point, with a much steeper drop in density at around the origin. This effect is due to the form of the Pauli form factor $F_2(Q^2)$, where if we recall back to Chapter 4 in Figs.(4.3 - 4.4), the singly represented quark contribution was negative as opposed to the positive doubly represented quark contribution, leading to either a shift up or down for the u and d quarks respectively.

7.2.3 Quark Spin Polarised

Now we look at the case where we allow only the quark spin polarisation to be non-zero with $s_x = 1$ in the b_x direction. In this case the second dipole term, $\frac{b^j_\perp \epsilon^{ji}}{m} s^i_\perp \overline{B}'_{T10}(b^2_\perp)$ is now effective. In Fig. 7.5 with now the quark spin polarisation represented by the arrow within the light blue circle in the bottom right of the contour plot, similarly to Fig. 7.3. The doubly-represented quark's density distribution has shifted into the upper half of the plane, with the peak now located further from the origin than the unpolarised and baryon spin cases at around $b_y \approx 0.5$ fm, where the shape of the distribution still resembles that of Fig. 7.3, only here we have a much gentler slope with a less perceptible inflection point.

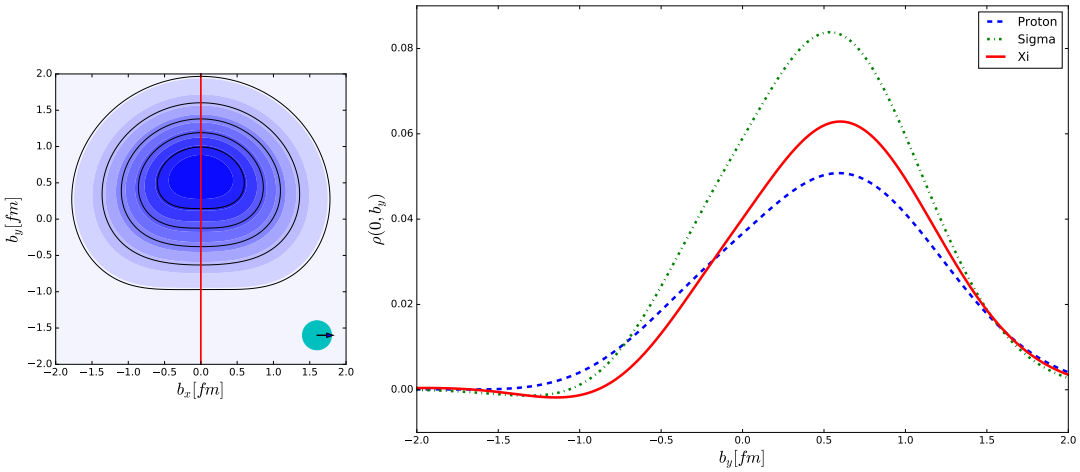

Figure 7.6: Similar to Fig. 7.1, only now showing the singly represented quark density distribution, for unpolarised baryon spin ($S^i_\perp = 0$) and unpolarised quark spin ($s_x = 1$).

In Fig. 7.6, we have the singly represented polarised quarks in the unpolarised baryon, and here we no longer find an inflection point as seen in the previous density plots, instead a single peak at around $b_y \approx 0.6$ fm with a much steeper decline. In this contour we see for the first time, the cascade and sigma drop below zero probability density at around the $b_y = -1$ fm point, and considering that our GPD moments are chiral-odd (quark minus antiquark), we may be observing an excess of right spin antiquarks. For the quark spin polarisation, both the doubly and singly represented quark distributions are shifted into the upper half of the plane perpendicular to the quark spin's polarisation. If we again recall from Chapter 4 in Figs. (F.3 - F.4), the doubly and singly represented $\overline{B}_{T10}$ form factor has the same sign and this reflects in the baryon spin structure.

It has been argued[134] that the distortions we see in the quark spin polarisations are related to the Boer-Mulders function [130] which has described the correlation between the transverse quark spin $s_\perp$ to the transverse momentum of the quark, and our result would suggest the Boer-Mulders function be negative for both the doubly and singly represented quarks [137].

7.2.4 Mixed Quark and Baryon Spin Polarisation

We are now interested in the effects of the quadrupole term $s^i_\perp \left(2b^i_\perp b^j_\perp - b^2_\perp \delta^{ij}\right) S^j_\perp \frac{1}{m^2} \tilde{A}''_{T10}(b^2_\perp)$ in eq. (7.2) and the second orbitally symmetric term $s^i_\perp S^i_\perp (A_{T10}(b^2_\perp) - \frac{1}{4m^2} \triangle_{b_\perp} \tilde{A}_{T10}(b^2_\perp))$ and their effect on the spin structure of the baryons. Thus we can approach this in two ways. Allow the baryon to have a fixed spin polarisation and

then vary the quark spin orientation to view the changes in the distribution, or vice versa fix the quark spin polarisation and vary the baryons spin orientation, where in our case we choose to demonstrate the latter.

We proceed by setting up three distinct polarisation states, where the quark and baryon are initially polarised in the same direction, then the second state where the quark or proton is perpendicular to the other, and finally the state where the quark and the proton are in opposite directions. This configuration of states will allow us to view the dependence on the quark spin in regards to the baryon spin when both spin polarisations are non-zero.

In Fig. 7.7, we consider the doubly represented contributions, where we have chosen to fix the quark spin polarisation $s_x = 1$ in the b_x direction, whilst varying the baryons spin direction as stated previously for parallel $S_\perp = (1, 0)$, perpendicular $S_\perp = (0, 1)$ and anti-parallel $S_\perp = (-1, 0)$ to the quark spin. In this figure, we show again the direction of the baryon spin by the direction of the arrow outside the blue circle in the bottom right corner, and the quark spin as the internal arrow. The first contour is a combination of Fig. 7.3 and Fig. 7.5, where the density has been shifted into the upper half-plane with a small distortion at the origin. The second contour plot shows the quark density start to shift around the centre of the baryon, with the peak located in the upper left plane as the baryon spin and quark spin become perpendicular, and here we see that the baryon spin is the dominant axis. In the third contour plot, we see that whilst the highest density region is still in the upper half-plane, we now have a strong dip around the origin, suggesting that in this situation, where the quark spin and baryon spin are anti-parallel to one another, there is a higher probability to find the doubly represented quarks in an almost donut off centre from the origin of the baryon, while still dominant in the upper half.

In Fig. 7.8, we now have the singly represented quark contributions for a similar situation to Fig. 7.7. Here for the first contour we see a situation similar to Fig. 7.4, where contribution from the dipole term $B'_{10}(b_\perp^2)$ is significant enough for the distortion into the lower half-plane and we see some slight similarities to the third contour of Fig. 7.7, with a slight decrease at the origin and a small rise opposite to the peak at $b_y = -0.5$ fm. In the second contour, much alike the second contour in Fig. 7.7 the density appears to have shifted again in a counter-clockwise fashion around the centre of the baryon, this time residing primarily in the positive right half-plane. And then finally for the third contour, we see a much clearer dip into the negative quark density even in the proton case, such that we have a visible red spot in our contour in a position mirroring that of the peak density for the singly represented quarks when the baryon spin and quark spin are anti-parallel. A combination of Figures 7.4 and 7.6 does not reveal whether either the baryon spin or quark spin stronly determines the shape of the spin density. However the first plot in Fig. 7.8 resembles that of Fig. 7.4 and the

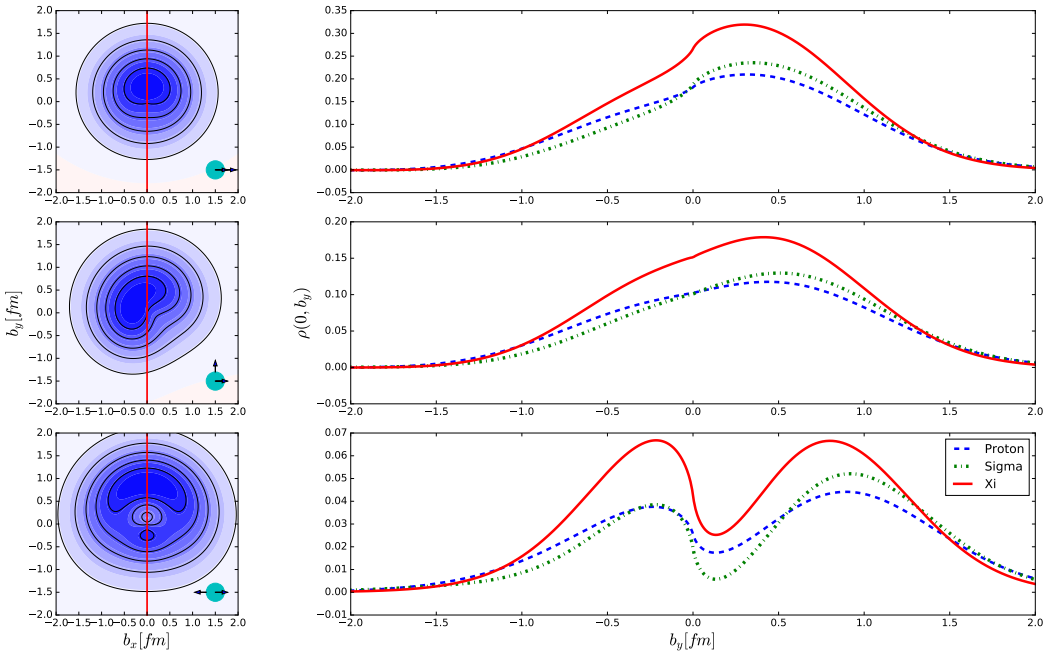

Figure 7.7: Similar to Fig. 7.1, only now showing the doubly represented quark density distribution, for a fixed quark spin polarisation ($s_x = 1$) and baryon polarisation of $S_\perp = (1, 0)$, $S_\perp = (0, 1)$ and $S_\perp = (-1, 0)$. The polarisation of each contour plot is shown by the teal circle in the bottom right corner, with the internal arrow showing the direction of the quark spin polarisation, and the external arrow showing that of the baryon spin polarisation.

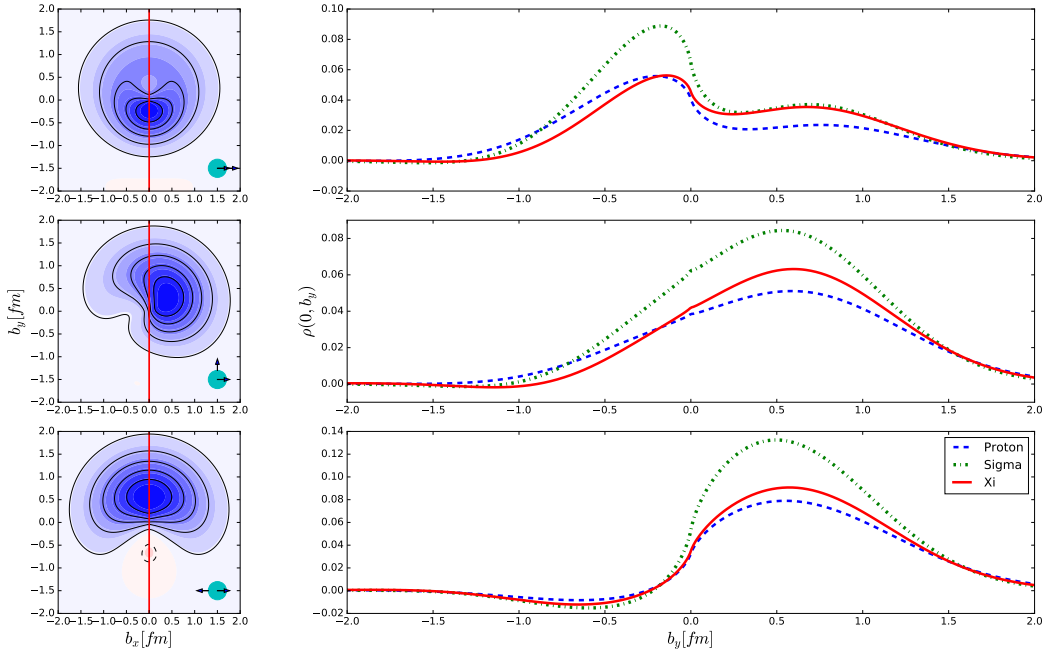

Figure 7.8: Similar to Fig. 7.7, only now showing the singly represented quark density distribution, for a fixed quark spin polarisation ($s_x = 1$) and baryon polarisation of $S_\perp = (1, 0)$, $S_\perp = (0, 1)$ and $S_\perp = (-1, 0)$.

baryon spin, in comparison to that of the quark spin, which signifies to us that the baryon spin is more dominant.

If in the case we had chosen to look at a fixed baryon spin polarisation with a varying quark spin polarisation, the results remain the same up to a rotation and reflection about the y-axis, with the alternate plots available in Appendix F.

7.3 Model Dependence

As mentioned previously, when transforming our form factors to the impact parameter space with dipole form in Q^2 in eq. 7.7, there are a variety of limitations we face when choosing our fit function for each of the form factors required to calculate the transverse spin density. Depending on the choice of model used to fit the form factors the effects that these models predict at high Q^2 and as $Q \to 0$, will translate into effects that will be seen in our density contour plots. Because of this model dependence, we wish to test what effects a variety of models will have on the spin structure predicted by the density equation (7.1). Thus in order to check this model dependence we consider the following models

$$\begin{array}{llll} \text{(a)} & \dfrac{a}{(1+bQ^2)^2} & \text{(b)} & \dfrac{a}{1+bQ^2+cQ^4} \\ \text{(c)} & \dfrac{a}{(1+bQ^2)^3} & \text{(d)} & ae^{bQ^2} \end{array} \tag{7.11}$$

where (a) is a standard dipole form we have used previously, (b) is a modified dipole form used for the Dirac form factor $F_1(Q^2)$ in Chapter 4, (c) is the tripole and (d) is an exponential form. In Figs. (7.9 - 7.10) we show the Pauli form factor $F_2(Q^2)$ or $B_{10}(Q^2)$ and the third tensor form factor $\overline{B}_{T10}(Q^2)$, where we have plotted each from our results calculated after extrapolation to the physical point in Chapter 6, with each of the fit functions defined in eq. 7.11. Here we show the dipole, in a solid blue line, the advanced dipole in a green dashed line, the tripole in a red dashed and dotted line, and the exponential in a black dotted line. Along with the fits we also show a simple goodness of fit χ^2/d.o.f. statistic, to show approximately how appropriate each fit function fits to the data. In the results shown earlier, we used the dipole fit for $B_{10}(Q^2)$ and the tripole fit for $\overline{B}_{T10}(Q^2)$, which although we can calculate these results analytically, their goodness of fit shows that they may not be the best fit functions to accurately describe our data. By computationally calculating the Fourier transform rather than computing the modified Bessel functions, we can show results for the unpolarised, baryon spin polarisation and quark spin polarisation, to see directly the effects of changing the fit functions we use on these two distributions.

In Fig. 7.11 we show the model dependence on the doubly represented u quark contribution in the proton to the Dirac form factor $F_1^u(Q^2)$, where similarly to the

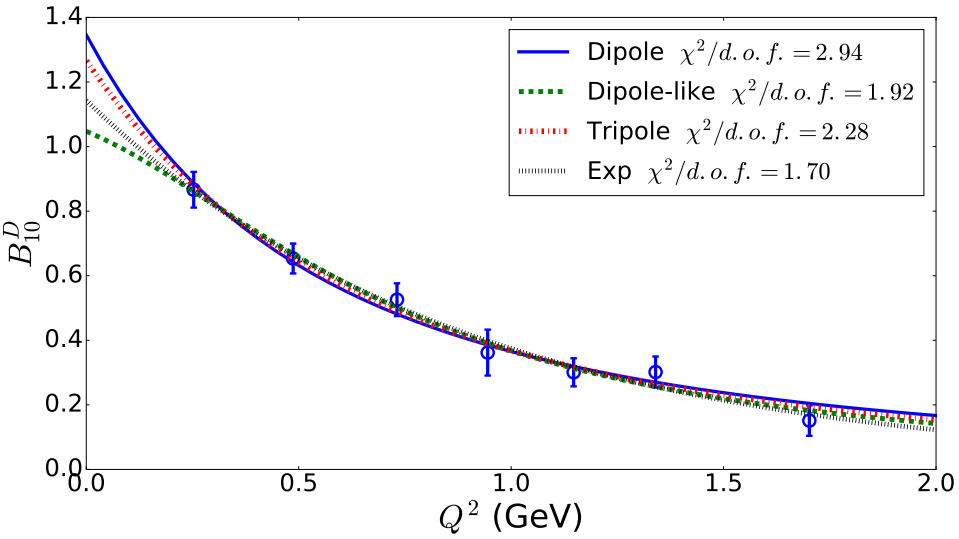

Figure 7.9: Showing the different fit functions for the B_{10} Pauli form factor for the doubly represented up quark of the proton. The solid blue line represents the dipole fit, the dashed green line representing a modified dipole fit, the red dashed and dotted line showing a tripole fit, and finally the black dotted line representing the exponential fit. Theres fit functions are defined in eq. 7.11. Each fit function is accompanied with a χ^2 per degree of freedom goodness of fit test statistic.

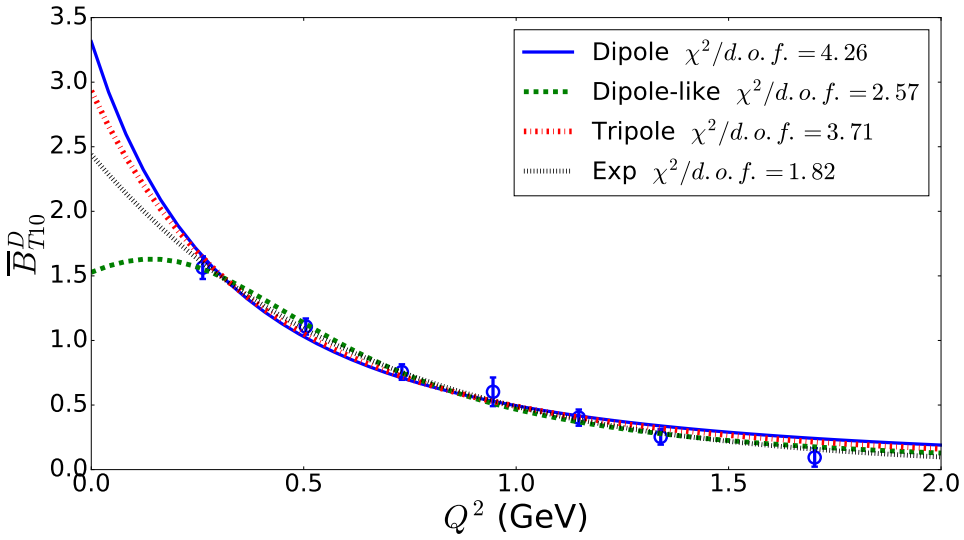

Figure 7.10: Similar to Figure 7.9, only now showing for the $\overline{B}_{T10}$ tensor form factor for the doubly represented up quark in the proton.

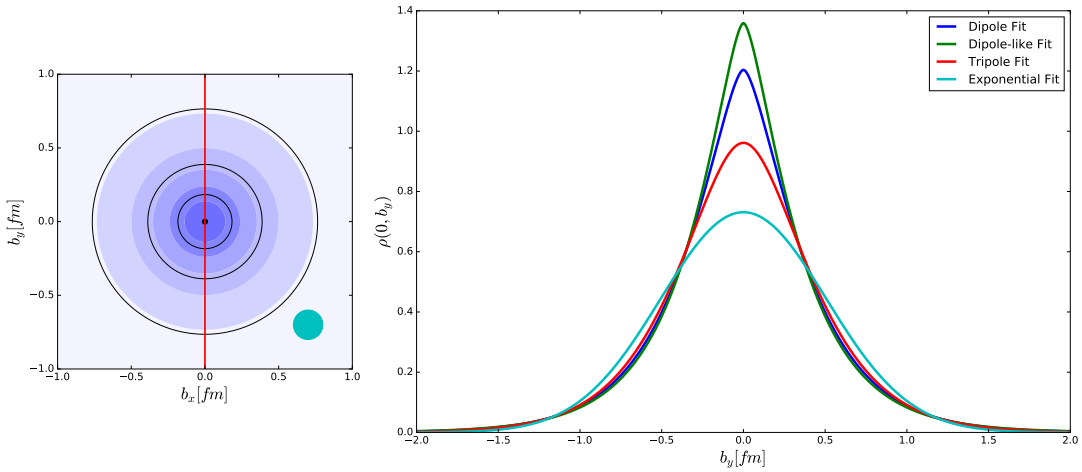

Figure 7.11: Similar to Fig. 7.1, only now showing how the model dependence of the form factor fits affects the quark density distribution of the doubly represented quarks of a proton with unpolarised baryon spin $S^i_\perp = 0$ and unpolarised quark spin $s^i_\perp = 0$. Here we see four potentially viable models for fitting the form factors, with the Dipole represented by blue, the dipole-like ansätze with green, the tripole in red and the exponential fit in teal.

previous figures, on the left we have a contour plot of the quark density distribution using the dipole fit function, and on the right we have a comparison to the four fit functions defined in eq.7.11 represented as a cross-section of each contour plot. As we can see, due to the orbitally symmetric nature of the $A_{10}(b^2_\perp)$ term in eq. 7.1, the major difference we see between the fit functions in an unpolarised proton with unpolarised quarks, is the magnitude and sharpness of its peak.

In Fig. 7.12 we show the effects of model dependence on the doubly represented u quarks in the proton when we set the baryon spin to $S_x = 1$ as we saw in Fig. 7.3. Here the main difference we see between the choice of fit function for the Pauli form factor $B_{10}(Q^2)$ determines the sharpness of the peak and the width of the plateau we see in the distortion towards the upper half-plane. Here the dipole-like fit (b) in eq. 7.11, gives us a sharp peak with no plateau, and the other fits each sacrifice the magnitude of their peak for an extended plateau each more exaggerated than before.

And finally in Fig. 7.13 we show the model dependence of the quark spin polarisation $s_x = 1$ in an unpolarised baryon, with the different choices of fit function for the form factor $\overline{B}_{T10}(Q^2)$. Again similar to Fig. 7.12 the general shape of each fit function is maintained, with the main difference been the location of the peaks and exaggeration of plateau.

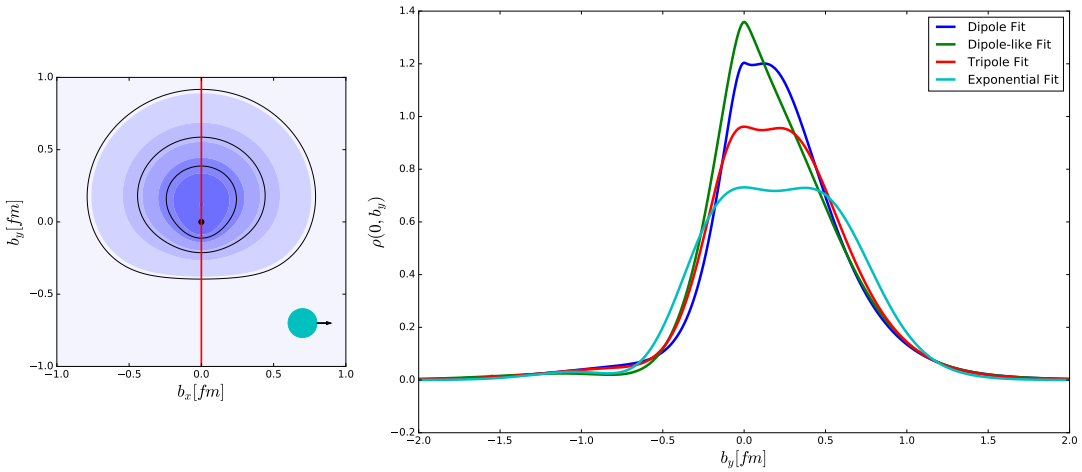

Figure 7.12: Similar to Fig. 7.11, only now showing how the model dependence of the form factor fits affects the quark density distribution of the doubly represented up quarks of a proton with baryon spin $S_x = 1$ and unpolarised quark spin $s^i_\perp = 0$.

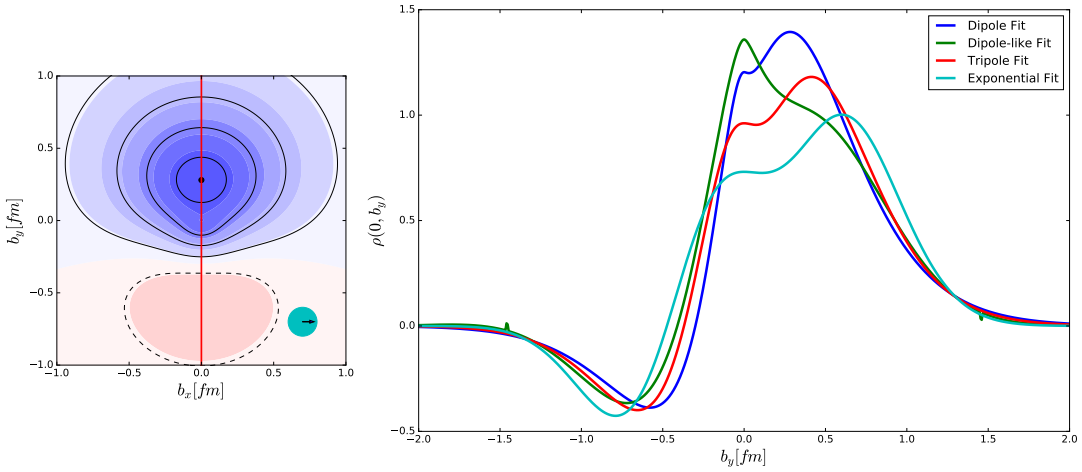

Figure 7.13: Similar to Fig. 7.11, only now showing how the model dependence of the form factor fits affects the quark density distribution of the doubly represented up quarks of a proton with unpolarised baryon spin $S^i_\perp = 0$ and polarised quark spin $s_x = 1$.

7.4 Summary

In this chapter we have used a combination of our results from Chapters 4, 5 and 6, in order to calculate the transverse spin density distributions of the quarks within the proton, sigma and cascade. By analytically solving the Fourier transform of eq. 7.7 into modified Bessel functions and choosing the lowest power parametrisation, we have transformed the Q^2 dependent form factors calculated in Chapter 4 and extrapolated to the physical point in Chapter 6, to impact parameter space. By doing so, we are able to use impact-parameter dependent form factors to construct the spin density equation eq. 7.1, in order to reveal a variety of transverse spin density distributions dependent on the choice of the baryon spin polarisation $S_\perp$ and the quark spin polarisation $s_\perp$.

By varying these two free parameters, we were able to display and compare the effects of baryon and quark spin on the density distribution of quarks within the baryon. We have been able to see the effects of the individual terms in eq. 7.1, seeing the quadrupole-esque term $s^i_\perp \left(2b^i_\perp b^j_\perp - b^2_\perp \delta^{ij}\right) S^j_\perp \frac{1}{m^2} \tilde{A}''_{T10}(b^2_\perp)$ ending up being less prominent and how the two dipole terms $\frac{b^j_\perp \epsilon^{ji}}{m} \left(S^i_\perp B'_{10}(b^2_\perp) + s^i_\perp \overline{B}'_{T10}(b^2_\perp)\right)$ dominate the structure of the distribution for transverse polarisation of both quark and proton spin, and how when the two are anti-parallel to one another, tend to cancel, leading to the unique effect in the third contour of Fig. 7.7, where the density is distributed around the centre of the baryon but less prominent directly in the centre. We have also looked into the model dependence of the parametrisation of the form factors, and how the resulting density can be sensitive to the choice of fit function. The general shape of the density is preserved, but the locations of the features are more dependent on the precision of each fit function.

We have only looked into the lowest moment of the transverse spin density, as we have only calculated the associated $n = 1$ electromagnetic and tensor form factors, but this analysis can be extended to the second or higher order x moments, with the additional calculation of terms such as A_{20} and A_{T20}, to give further insight into the internal structure of the baryon, with previous studies [135] showing similar results to the first order only tighter and more densely centred in the baryon.

In the next chapter, Chapter 8 we will look to the second moment of structure functions and the twist-3 matrix element d_2 to further our understanding of the internal structure of the a baryon.

Chapter 8

Revealing the Colour-Lorentz Force

The nucleon's second spin-dependent structure function g_2 is of considerable phenomenological interest. An analysis using the operator product expansion (OPE), briefly explained in Chapter 2, reveals that to leading order in $1/Q^2$, g_2 receives contributions from both twist-two and twist-three operators. Calculations of the structure function g_2 thus offer the unique possibility of directly assessing higher-twist effects [138]. Since g_2 involves higher twist, it does not have a simple parton interpretation as a single particle density, instead the twist-three contribution is related to quark-gluon correlations within the nucleon, the intuitive interpretation may not be immediately clear [139].

Since g_2 is related to the electromagnetic polarisabilities at low Q^2, these twist-3 matrix elements have been called colour polarisabilities in the literature [140]. However at high Q^2, the twist-3 component of g_2 is described by a local correlator, and this physical interpretation as a polarisability no longer applies, and instead is related to a decomposition of the colour electric and magnetic fields. This will then give the twist-3 component of g_2 the semi-classical interpretation as the average colour Lorentz force acting on the quark struck in a DIS experiment, the instant after being hit by a virtual photon.

In this chapter, we provide an updated lattice calculation of the $d_2^{(f)}$ reduced matrix element, including the appropriate renormalisation, and compare to earlier lattice calculations [141, 142]. We will then seek to explore an interpretation of these particular twist-3 matrix elements as a transverse 'force' [139], requiring us to calculate the off-forward matrix elements of a twist-3 operator and determine the associated form factors. These culminate in a two-dimensional Fourier transform analogue to the work done in Chapter 7, only now for these transverse 'force' spatial distributions.

8.1 Second Moment of the g_2 Structure Function

We begin by considering the polarised structure function, g_2, mentioned in Chapter 2, where by neglecting the quark masses and contributions of twist greater than two, one obtains the 'Wandzura-Wilczek' relation [45],

$$g_2(x,Q^2) \approx g_2^{WW}(x,Q^2) = -g_1(x,Q^2) + \int_x^1 \frac{dy}{y} g_1(y,Q^2), \tag{8.1}$$

which depends only on the nucleon's first spin-dependent structure function $g_1(x,Q^2)$. If we include the mass and gluon dependent terms up to twist-3, $g_2(x,Q^2)$ can be rewritten

$$g_2(x,Q^2) = g_2^{WW}(x,Q^2) + \overline{g_2}(x,Q^2), \tag{8.2}$$

where

$$\overline{g_2}(x,Q^2) = -\int_x^1 \frac{dy}{y}\frac{d}{dy}\left[\frac{m}{M}h_T(y,Q^2) + \zeta(y,Q^2)\right]. \tag{8.3}$$

Here the function $h_T(x,Q^2)$ denotes the transverse polarisation density with twist two, and $\zeta(x,Q^2)$ is the twist-3 term that arises from quark-gluon correlations. The $h_T(x,Q^2)$ term contains a quark to nucleon mass ratio m/M, which suppresses its contribution to g_2 for physical up and down quarks. By taking the moments of g_2 from eqs. 8.2 - 8.3 we obtain

$$\int_0^1 dx\ x^n g_2(x,Q^2) = \frac{n}{n+1}\Bigg\{ -\int_0^1 dx\ x^n g_1(x,Q^2) + \int_0^1 dx\ x^{n-1}\left[\frac{m}{M}h_T(x,Q^2) + \zeta(x,Q^2)\right]\Bigg\}. \tag{8.4}$$

Through a leading order OPE analysis with massless quarks, the moments of the structure function g_2 are given by [44, 143, 144]

$$2\int_0^1 dx x^n g_2(x,Q^2) = \frac{1}{2}\frac{n}{n+1}\sum_f (e^{(f)}_{g_2,n} d^{(f)}_n(\mu) - e^{(f)}_{g_1,n} a^{(f)}_n(\mu)) + O(1/Q^2), \tag{8.5}$$

for even $n \geq 2$, where f runs over the quark flavours, $a^{(f)}_n$ and $d^{(f)}_n$ are reduced matrix elements to be defined soon, $e^{(f)}_{g_1,n}$, $e^{(f)}_{g_2,n}$ are the Wilson coefficients that depend on the ratio of scales μ^2/Q^2, the running coupling constant $g(\mu)$ and the quark charges $\mathcal{Q}^{(f)}$,

$$e^{(f)}_{i,n}(\mu^2/Q^2, g(\mu)) = \mathcal{Q}^{(f)2}(1 + \mathcal{O}(g(\mu)^2)). \tag{8.6}$$

Here n is even and starts at $n = 2$ and so the reduced matrix elements $a^{(f)}_n$ and $d^{(f)}_n$, taken in a nucleon state with momentum p and spin vector s, are defined by [44]

$$\langle p,s|\mathcal{O}^{5(f)}_{\{\sigma\mu_1\ldots\mu_n\}}|p,s\rangle = \frac{1}{n+1}a^{(f)}_n\left[s_\sigma p_{\mu_1}\ldots p_{\mu_n} + \ldots - \text{traces}\right], \tag{8.7}$$

$$\langle p,s|\mathcal{O}^{5(f)}_{[\sigma\{\mu_1]\ldots\mu_n\}}|p,s\rangle = \frac{1}{n+1}d^{(f)}_n\left[(s_\sigma p_{\mu_1} - s_{\mu_1}p_\sigma)\,p_{\mu_2}\ldots p_{\mu_n} + \ldots - \text{traces}\right], \tag{8.8}$$

where

$$\mathcal{O}^{5(f)}_{\sigma\mu_1\ldots\mu_n} = \left(\frac{i}{2}\right)^n \overline{\psi}\gamma_\sigma\gamma_5 \overleftrightarrow{D}_{\mu_1}\ldots\overleftrightarrow{D}_{\mu_n}\psi - \text{ traces.} \tag{8.9}$$

Here $\overleftrightarrow{D} = \overleftarrow{D} - \overrightarrow{D}$ and the brackets $\{\ldots\}$ ($[\ldots]$) indicate symmetrisation (anti-symmetrisation) of the indices and the operator in eq. 8.7 has twist-two, whereas the operator in eq. 8.8 has twist-three.

In order to gain insights into what the twist-3 contribution to g_2 represents physically, we start by noting that the twist-3 operator $\mathcal{O}^{5(f)}_{[\sigma\{\mu_1]\ldots\mu_n\}}$ can be rewritten in terms of the QCD coupling g and the dual gluon field tensor $\tilde{G}_{\mu\nu} = \epsilon_{\mu\nu\rho\delta}G^{\rho\delta}$ using the equations of motion for massless QCD. For $n = 2$ we then find,

$$\mathcal{O}^{5(f)}_{[\sigma\{\mu_1]\mu_2\}} = -\frac{g}{6}\overline{\psi}\left(\tilde{G}_{\sigma\mu_1}\gamma_{\mu_2} + \tilde{G}_{\sigma\mu_2}\gamma_{\mu_1}\right)\psi - \text{ traces,} \tag{8.10}$$

which allows us to define the reduced matrix element d_2 at the chiral limit with

$$\begin{aligned} &-\frac{g}{6}\langle\vec{p},\vec{s}|\overline{\psi}\left(\tilde{G}_{\sigma\mu_1}\gamma_{\mu_2} + \tilde{G}_{\sigma\mu_2}\gamma_{\mu_1}\right)\psi - \text{ traces}|\vec{p},\vec{s}\rangle \\ &= \frac{1}{3}d_2\left[\left(s_\sigma p_{\mu_1} - s_{\mu_1}p_\sigma\right)p_{\mu_2} + \ldots \text{ traces}\right] \end{aligned} \tag{8.11}$$

For $\mu_1 = \mu_2 = 0$, d_2 parametrises the magnetic field component of the gluon field strength tensor, which is parallel to the nucleon spin. Furthermore

$$d_2 = 4\int_0^1 dx\ x\zeta(x), \tag{8.12}$$

and so a calculation of d_2 will provide insights into the size of the quark-gluon correlation term $\zeta(x)$.

8.2 Lattice Operator and Renormalization

In order to calculate the twist-3 matrix element d_2, we must split the process into two tasks, the first is to compute the nucleon matrix element of the appropriate lattice operator while the second is to renormalise the operator.

8.2.1 Renormalisation

For the calculation of the renormalisation constants, we employ the same technique used in Chapter 5, where we obtain a renormalised operator $\mathcal{O}(\mu)$ from the bare operator $\mathcal{O}(a)$, in the absence of mixing, via

$$\mathcal{O}(\mu) = Z_{\mathcal{O}}(a\mu)\mathcal{O}(a), \tag{8.13}$$

with lattice spacing a. The method previously used in chapter 5, does not account for the lower-dimensional operators that mix under renormalisation with the reduced matrix element $d_n^{(f)}$. A solution to this problem was presented in [141], and so we shall apply the same approach. This is achieved by imposing a (MOM-like) renormalisation condition [81, 145]

$$\frac{1}{4}\mathrm{Tr}\left[\Gamma_R(p)\Gamma_{Born}(p)^{-1}\right]_{p^2=\mu^2} = 1 \tag{8.14}$$

on the corresponding quark-quark vertex function in the Landau gauge. As in Chapter 5, $\Gamma_{Born}(p)$ is the Born (tree-level) contribution to the vertex function while the renormalised vertex function $\Gamma_R(p)$ and its precursor $\Gamma(p)$ are related by the multiplicative renormalisation from eq. 5.4.

For this calculation we shall use the first symmetric point mass configuration on Table 3.1 corresponding to $\kappa_{l,s} = 0.120900$, with a pion mass of 465 MeV. As was mentioned in Chapter 3, only the connected quark-line diagrams are considered in our lattice matrix element calculations.

Given Eq. 8.8, and choosing to calculate the matrix element of a nucleon with momentum in the x-direction $\vec{p} = (p, 0, 0)$, where $p = 2\pi/L$ denotes the smallest non-zero momentum available on our spatial lattice extent L, and spin polarisation in the z-direction $\Gamma_3 = \frac{1}{2}(1+\gamma_4)i\gamma_5\gamma_3$, we construct $\mathcal{O}^{[5]}$ from the following components:

$$\begin{aligned}
\mathcal{O}^5_{[3\{1\}4\}} &= \frac{1}{3}\left(2\mathcal{O}^5_{3\{14\}} - \mathcal{O}^5_{1\{34\}} - \mathcal{O}^5_{4\{13\}}\right) \\
&= \frac{1}{12}\overline{\psi}\Big(\gamma_3\overleftrightarrow{D}_1\overleftrightarrow{D}_4 + \gamma_3\overleftrightarrow{D}_4\overleftrightarrow{D}_1 - \frac{1}{2}\gamma_1\overleftrightarrow{D}_3\overleftrightarrow{D}_4 - \frac{1}{2}\gamma_1\overleftrightarrow{D}_4\overleftrightarrow{D}_3 \\
&\qquad - \frac{1}{2}\gamma_4\overleftrightarrow{D}_1\overleftrightarrow{D}_3 - \frac{1}{2}\gamma_4\overleftrightarrow{D}_3\overleftrightarrow{D}_1\Big)\gamma_5\psi \\
&=: \mathcal{O}^{[5]}.
\end{aligned} \tag{8.15}$$

This operator $\mathcal{O}^{[5]}$ belongs to the representation $\tau_1^{(8)}$ of the hypercubic group $H(4)$ [146, 147], with dimension five and C-parity +. There are then two more operators of dimension four and five respectively, that transform identically under $H(4)$ and have the same C-parity, with which our operator $\mathcal{O}^{[5]}$ can mix:

$$\frac{1}{12}\overline{\psi}\left(\sigma_{12}\overleftrightarrow{D}_1 - \sigma_{42}\overleftrightarrow{D}_4\right)\psi =: \mathcal{O}^{\sigma}, \tag{8.16}$$

$$\frac{1}{12}\overline{\psi}\left(\gamma_1\overleftrightarrow{D}_2\overleftrightarrow{D}_1 - \gamma_1\overleftrightarrow{D}_1\overleftrightarrow{D}_2 - \gamma_4\overleftrightarrow{D}_2\overleftrightarrow{D}_4 + \gamma_4\overleftrightarrow{D}_4\overleftrightarrow{D}_2\right)\psi =: \mathcal{O}^{0}, \tag{8.17}$$

with the definition $\sigma_{\mu\nu} = \frac{i}{2}[\gamma_\mu, \gamma_\nu]$. The operator $\mathcal{O}^0$ in eq. 8.17 mixes with $\mathcal{O}^{[5]}$ with a coefficient of order g^2 and vanishes in the tree approximation between quark states. We can then ignore its contribution to our renormalisation of $\mathcal{O}^{[5]}$. The second operator $\mathcal{O}^{\sigma}$

contributes to the mixing with a coefficient proportional to a^{-1}, and hence is required for the renormalisation. The renormalised operator is then written as,

$$\mathcal{O}^{[5]}(\mu) = Z^{[5]}(a\mu)\mathcal{O}^{[5]}(a) + \frac{1}{a}Z^{\sigma}(a\mu)\mathcal{O}^{\sigma}(a). \tag{8.18}$$

The renormalisation constant $Z^{[5]}$ and the mixing coefficient Z^{σ} are then determined by the conditions,

$$\frac{1}{4}\mathrm{Tr}\left[\Gamma^{[5]}_{R}(p)\Gamma^{[5]}_{Born}(p)^{-1}\right]_{p^2=\mu^2} = 1, \tag{8.19}$$

$$\frac{1}{4}\mathrm{Tr}\left[\Gamma^{[5]}_{R}(p)\Gamma^{\sigma}_{Born}(p)^{-1}\right]_{p^2=\mu^2} = 0, \tag{8.20}$$

as generalisations of eq. 8.14. We note that eq. 8.18 can be rewritten as

$$\mathcal{O}^{[5]}(\mu) = Z^{[5]}(a\mu)\left(\mathcal{O}^{[5]}(a) + \frac{1}{a}\frac{Z^{\sigma}(a\mu)}{Z^{[5]}(a\mu)}\mathcal{O}^{\sigma}\right), \tag{8.21}$$

hence $\mathcal{O}^{[5]}(\mu)$ will have multiplicative dependence on μ only if the ratio $Z^{\sigma}(a\mu)/Z^{[5]}(a\mu)$ does not depend on μ, which should be the case for large enough values of the renormalisation scale. The scale dependence will then completely reside in $Z^{[5]}$. The ratio has been calculated elsewhere for SLiNC fermions in lattice perturbation theory to one-loop [148], and takes the form

$$\begin{aligned}\frac{Z^{\sigma}(a\mu)}{Z^{[5]}(a\mu)} = -\frac{1}{16\pi^2}C_F g^2(11.795 - 44.841s_t - 9.537s_t^2 + c_{SW}(-6.322 + 21.047s_t \\ - 20.665s_t^2) + c_{SW}^2(-0.206 + 0.797s_t - 0.605s_t^2)) \approx 0.0549\end{aligned} \tag{8.22}$$

where $s_t = 0.1$ is the stout smearing parameter used in the SLiNC action, clover term $c_{SW} = 1$, $C_F = 4/3$ and $g^2 = 6/\beta$.

In order to extract the matrix elements for the operator $\mathcal{O}^{[5]}$, we discretise the derivative term $\overset{\leftrightarrow}{D}$ on the lattice, with working out shown in Appendix G. By following the procedure outlined in chapters 3,4 and 5, we calculate the renormalisation factors $Z^{[5]}$, and the matrix elements from $\mathcal{O}^{[5]}$ and $\mathcal{O}^{\sigma}$ in order to find the renormalised value of $d_2^{(f)}$, by applying eq. 8.21 to eq. 8.8. In Fig. 8.1, we show the renormalisation factor $Z^{[5]}$ using the RI'-MOM renormalisation scheme outlined in Chapter 5, along with a continuum extrapolation back to zero, where here we have set a cut-off at $(a\ p)^2 = 4$. It would be ideal to convert our results from RI'-MOM to the $\overline{\mathrm{MS}}$ scheme, but due to the complications of the mixing terms, the method to convert from one scheme to another becomes unclear, so we shall stick with the current RI'-MOM scheme.

Once the multiplicative renormalisation factors are applied, the value of $d_2^{(f)}$, for $f = u, d$ in the proton is given by

$$d_2^{(f)} = Z^{[5]}\left(d_2^{[5](f)} + \frac{1}{a}\frac{Z^{\sigma}}{Z^{[5]}}d_2^{\sigma(f)}\right). \tag{8.23}$$

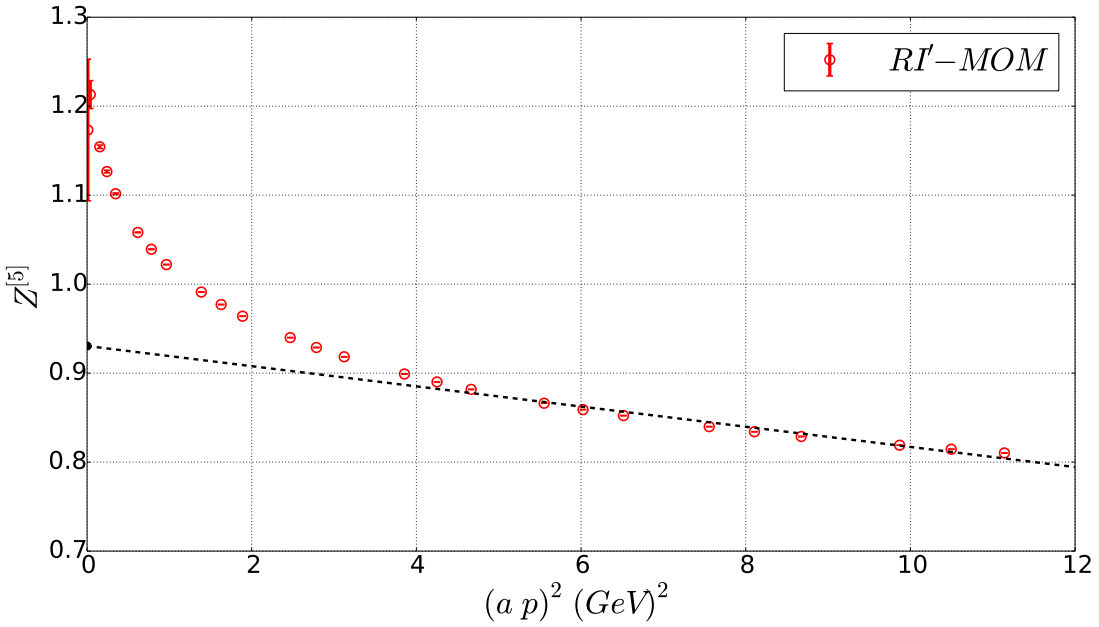

Figure 8.1: Renormalisation factor $Z^{[5]}$ using the RI'-MOM renormalisation scheme with a continuum extrapolation back to zero, with cutoff of $(a\ p)^2 = 4$, represented by the dashed black line.

8.2.2 Lattice Results

For this work, we use configuration 1 on Table. 3.1, where we work with $\beta = 5.5$, lattice volume $32^3 \times 64$ and spacing $a = 0.074$ fm. We used $N_{\text{conf}} \approx 1750$ configurations, with randomly selected source locations and a source-sink separation of at least $t_{\text{sink}} = 13$. We use polarisation in the z-direction $\Gamma_z = \frac{1}{2}(1+\gamma_4)i\gamma_5\gamma_3$ and momentum $\vec{p} = (p, 0, 0)$. Following the procedure layed out in Chapters 3 and 4, the nucleon matrix elements are determined from the ratio of three-point and two-point correlation functions,

$$R(t,\tau;p',p;\mathcal{O}) = \frac{C_{3pt}(\Gamma;\vec{p}\,',t;\vec{q},\tau;\mathcal{O}^{(q)})}{C_{2pt}(\Gamma;\vec{p},t)} \left[\frac{C_{2pt}(\Gamma;\vec{p}\,',\tau)C_{2pt}(\Gamma;\vec{p}\,',t)C_{2pt}(\Gamma;\vec{p},t-\tau)}{C_{2pt}(\Gamma;\vec{p},\tau)C_{2pt}(\Gamma;\vec{p},t)C_{2pt}(\Gamma;\vec{p}\,',t-\tau)}\right]^{\frac{1}{2}}. \tag{8.24}$$

In Fig. 8.2, we show the value of the up quark component of the unrenormalised matrix element $d_2^{[5]}$, where along the x-axis we show the lattice time extent t and the horizontal line is the plateau fit across the values of $t = [5, 9]$. The points here give a clear signal, and so its possible for us to get a good fit through the plateau, where we find the value

$$d_2^{[5]u} = -0.0037(3). \tag{8.25}$$

Figure 8.3 is similar to Fig. 8.2, only now we are showing the down quark component of the $d_2^{[5]}$ matrix element. The signal for the down quark component is much more

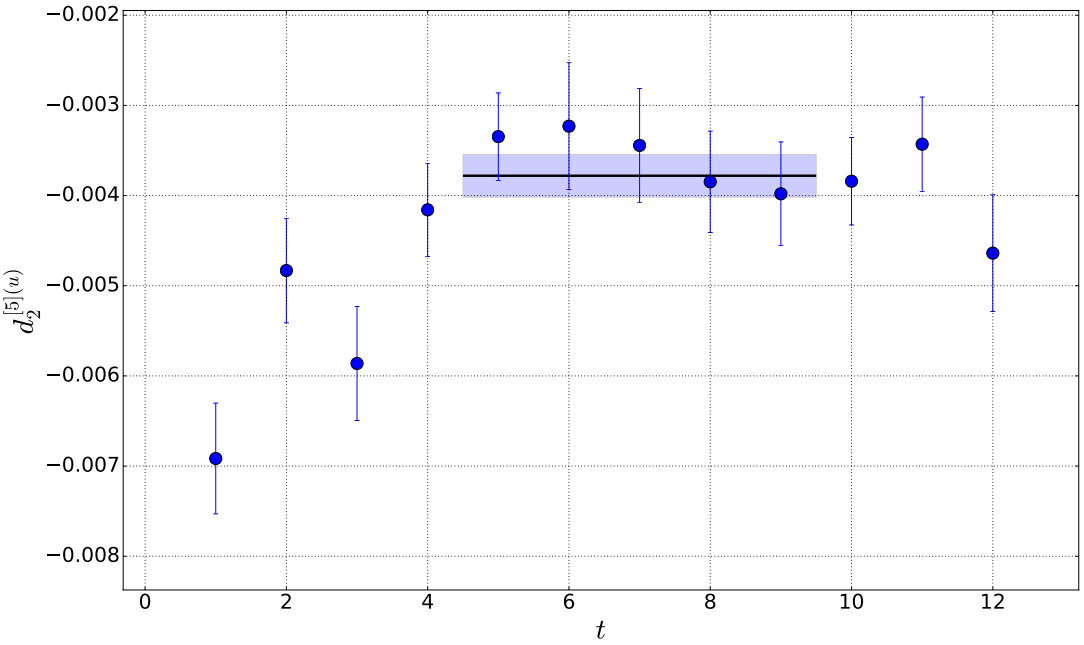

Figure 8.2: Unrenormalised calculation of the $d_2^{[5](u)}$ matrix element from the ratio 3.61 of two-point and three-point correlation functions. The x-axis shows the lattice time extent t and we show a plateau fit as a solid black bar with bootstrap error shaded blue, representing the value of the up quark component of $d_2^{[5]}$.

difficult to separate from noise, with the plateau of points $t = [4, 8]$ giving us the result

$$d_2^{[5](d)} = -0.00002(21). \tag{8.26}$$

The down quark result is consistent with zero and difficult to determine the appropriate result apart from the background noise, and so we shall instead focus on the much clearer up quark component. In Fig. 8.4, we show the result of the up quark component of the renormalisation matrix element d_2^{σ} divided by the lattice spacing a from eq. 8.23, where similar to Fig. 8.2, we show a fit through the plateau including points $t = [3, 8]$. This gives us the result

$$d_2^{\sigma(u)}/a = -0.0039(1). \tag{8.27}$$

By substituting the results from eq. 8.25 and eq. 8.27 into eq. 8.23, with the multiplicative renormalisation constant $Z^{[5]} \approx 0.931(6)$ from Fig. 8.1 and the mixing renormalisation $Z^{\sigma}/Z^{[5]}$ from eq. 8.22, we find the renormalised result of $d_2^{(u)}$ at $Q^2 = 0$ as

$$d_2^{(u)} = -0.00365(25). \tag{8.28}$$

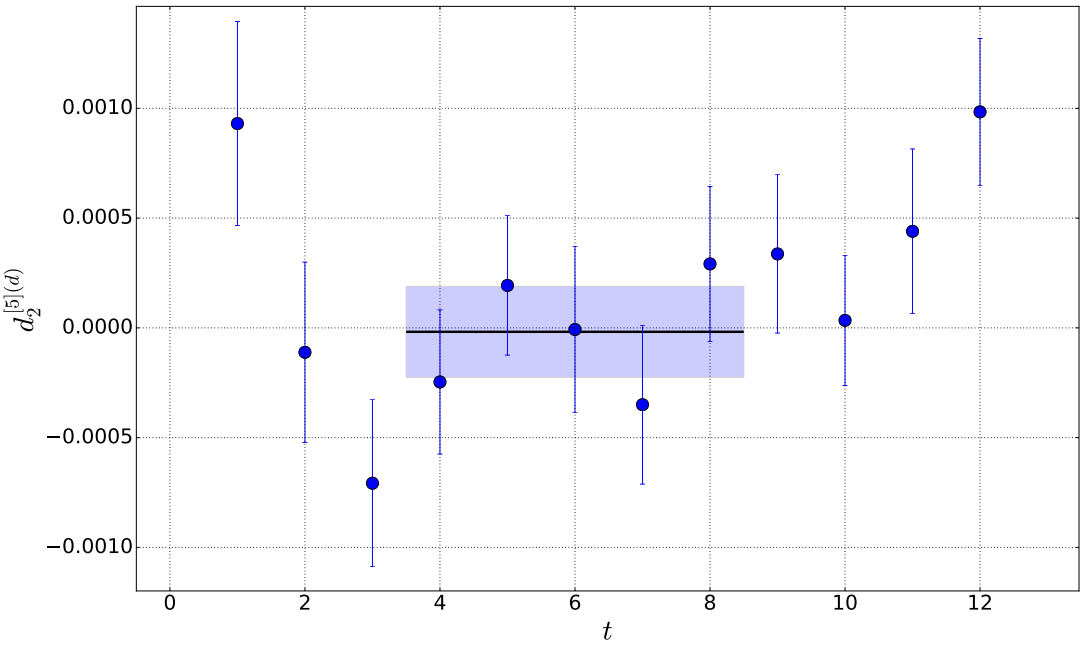

Figure 8.3: Similar to fig. 8.2, only now for the down quark component of $d_2^{[5]}$.

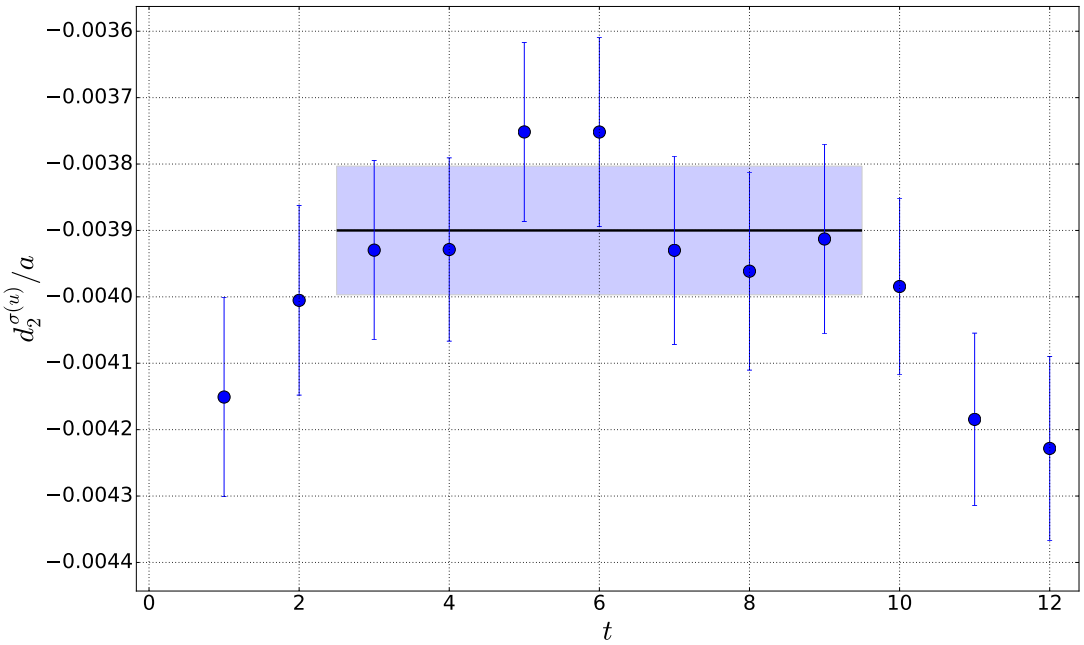

Figure 8.4: Similar to fig. 8.2, only now showing the result of the mixing operator $d^{\sigma(u)}/a$.

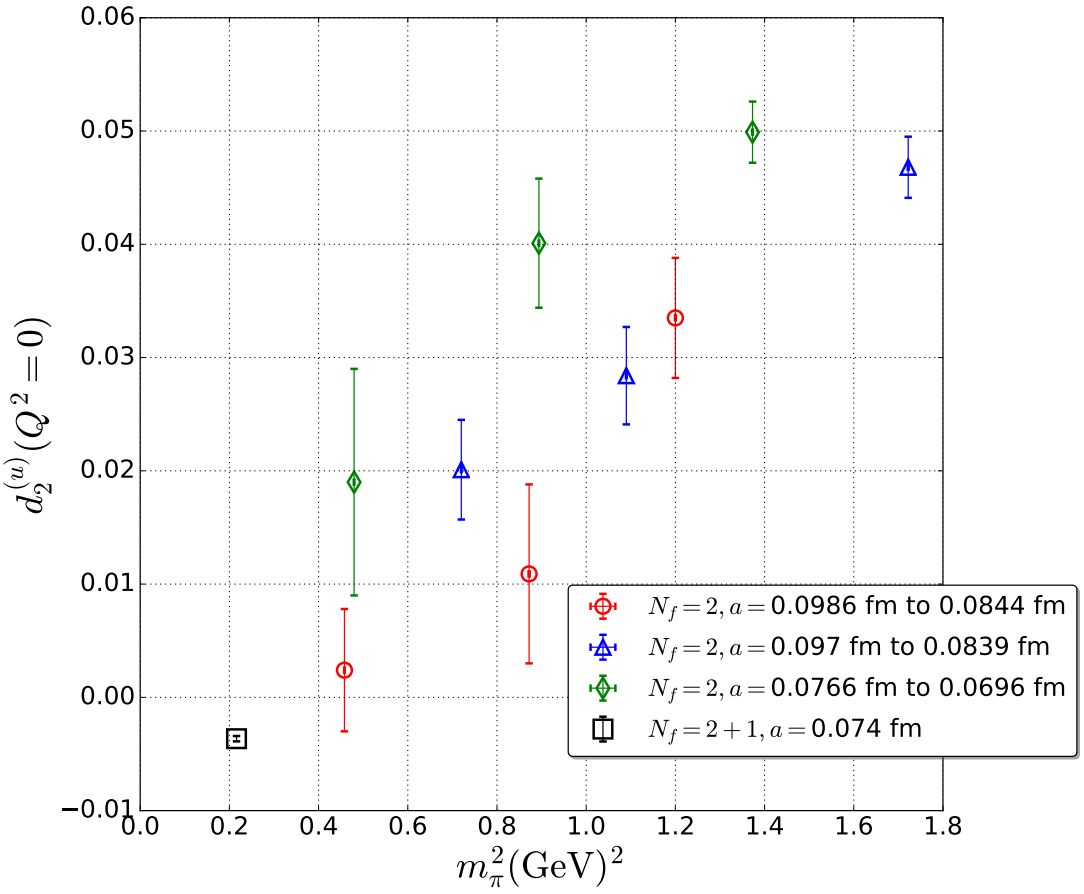

Figure 8.5: Various calculations of the renormalised $d_2^{(u)}$ matrix element at $Q^2 = 0$ plotted against m_π^2. The various shapes and colours representing differing $N_f = 2$ simulation sets from [142] for a range of lattice spacings, $a \approx 0.7$ to 0.9 fm. The black square is the $N_f = 2 + 1$ result from this work, with lattice spacing $a = 0.074$ fm.

In Fig. 8.5, we compare this result to previous calculations of the $d_2^{(u)}$, where in [142], a $N_f = 2$ lattice technique with lattice spacing ranging from $a \approx 0.7$ to 0.9 fm was used. This Figure shows the downward trend of the $d_2^{(u)}$ calculation as the pion mass decreases towards its physical value, where our result is shown as a black square, and for the first time drops below zero. The result seems to follow the logical progression of the calculations, only here we have a much smaller error in our calculation.

8.3 Transverse Force

We are interested in investigating a physical interpretation of these particular quark-gluon correlation twist-3 matrix elements. The twist-3 term $d_2^{(f)}$ from eq. 8.12, can be related to the following local matrix element [44, 149]

$$d_2^{(f)} = -\frac{1}{2M(P^+)^2 S^x}\langle P, S_T|\overline{q}(0)\gamma^+ g G^{+y}(0) q(0)|P, S_T\rangle, \tag{8.29}$$

where P^μ and M are the nucleon's four momentum and mass with a special choice for the vector $P = P^+(1,0,0,1)/\sqrt{2}$. Here we have now moved into light-cone coordinates, where we use a light-cone vector $n^\mu = (1,0,0,-1)/(\sqrt{2}P^+)$ with $n^2 = 0$, and $n \cdot P = 1$. S_T then refers to the transverse nucleon polarization vector, S^x is nucleon polarisation in the $\hat{x}$-direction and G^{+y} is the gluon field strength tensor. We can decompose the light-cone component of the gluon field strength tensor G^{+y} in terms of colour electric and magnetic fields [139],

$$\sqrt{2}G^{+y} = G^{0y} + G^{zy} = -E^y + B^x = -\left[\vec{E} + \vec{\nu} \times \vec{B}\right]^y \equiv F^{(f),y}, \tag{8.30}$$

for a quark moving with the velocity of light in the $\hat{z}$ direction, $\vec{\nu} = (0,0,-1)$, and where E and B are the chromo-electric and chromo-magnetic fields. This has the semi-classical interpretation as the average transverse colour Lorentz force acting on the struck quark in a DIS experiment the instant after being hit by a virtual photon. This suggests a connection between $d_2^{(f)}$ and this force

$$F^{(q),y}(0) = \sqrt{2}MP^+ S^x d_2^{(f)}. \tag{8.31}$$

While as we saw in Chapter 7, where the two-dimensional Fourier transforms of the form factors lead to impact parameter space distributions, these x^2 moments of the twist-3 $\overline{g}_2$ from eq. 8.3 can be related to the transverse colour Lorentz force [139]. This connection between the off-forward matrix elements and the transverse force [139], motivates us to calculate the off-forward matrix elements of the twist-3 operator in order to determine the associated form factors and explore the physical interpretation of their Fourier transform as the distribution of the average transverse colour Lorentz force on the transverse plane.

8.3.1 Transverse force form factors

In order to gain further insight into the distribution of the Lorentz force, we parametrize the general matrix element,

$$W^{\rho,\mu\nu}(p,p') = \langle p',s'|\overline{q}(0)\gamma^{\rho}igG^{\mu\nu}(0)q(0)|p,s\rangle \tag{8.32}$$

in terms of form factors. Following procedure outlined in [150], for general Lorentz indices, the matrix elements of the operator $\overline{q}(0)\gamma^{\rho}igG^{\mu\nu}(0)q(0)$ can be parametrised in terms of 8 form factors [151].

$$\begin{aligned} W^{\rho,\mu\nu}(P,\Delta) &= \langle p',s'|\overline{q}(0)\gamma^{\rho}igG^{\mu\nu}(0)q(0)|p,s\rangle = \overline{u}(p',\lambda') \\ &\left[\frac{1}{M^3}P^{\rho}(P^{\mu}\Delta^{\nu}-P^{\nu}\Delta^{\mu})F_1(t)+\frac{1}{M}(g^{\mu\rho}\delta^{\nu}-g^{\nu\rho}\Delta^{\mu})F_2(t)+\frac{1}{M}i\epsilon^{\rho\mu\nu\Delta}\gamma_5F_3(t)\right. \\ &+\frac{1}{M}P^{\rho}i\sigma^{\mu\nu}F_4(t)+\frac{1}{M}(P^{\mu}i\sigma^{\nu\rho}-P^{\nu}i\sigma^{\mu\rho})F_5(t)+\frac{1}{M^3}(P^{\mu}\Delta^{\nu}-P^{\nu}\Delta^{\mu})i\sigma^{\rho\Delta}F_6(t) \\ &\left.+\frac{1}{M^3}\Delta^{\rho}(P^{\mu}i\sigma^{\nu\Delta}-P^{\nu}i\sigma^{\mu\Delta})F_7(t)+\frac{1}{M^3}P^{\rho}(\Delta^{\mu}i\sigma^{\nu\Delta}-\Delta^{\nu}i\sigma^{\mu\Delta})F_8(t)\right]u(p,\lambda) \end{aligned} \tag{8.33}$$

where $P^{\mu}=(p'^{\mu}+p^{\mu})$ is the average nucleon momentum and $t=\Delta^2=(p'-p)^2$ is the invariant momentum transferred to the nucleon as we saw in Chapter 4. For the transverse force distribution, we are interested in the matrix elements of the operator $\overline{q}(0)\gamma^{+}gG^{+y}(0)q(0)$ from eq. 8.29, which is related to $d_2^{(f)}$. These are realised from eq. 8.33 and parameterized in the form of $\Phi_1(t),\ldots,\Phi_5(t)$, 5 independent linear combinations of the F form factors, as

$$\begin{aligned} &\langle p',s'|\overline{q}(0)\gamma^{+}gG^{+i}(0)q(0)|p,s\rangle = \\ &\quad\overline{u}(p',s')\left\{\frac{1}{M^2}\left[P^{+}\Delta^{i}_{\perp}-P^{\perp}\Delta^{+}\right]\gamma^{+}\Phi_1(t)+\frac{P^{+}}{M}i\sigma^{+i}\Phi_2(t)\right. \\ &\quad\left.+\frac{1}{M^3}i\sigma^{+\delta}\left[P^{+}\Delta^{i}_{\perp}\Phi_3(t)-P^{\perp}\Delta^{+}\Phi_4(t)\right]+\frac{P^{+}\Delta^{+}}{M^3}i\sigma^{i\Delta}\Phi_5(t)\right\}u(p,s), \end{aligned} \tag{8.34}$$

where i corresponds to a transverse index $i=x,y$. The form factor that we are interested in for our work is $\Phi_2(t)=(F_4(t)-F_5(t))$, where $d_2=\Phi_2(0)$, which requires a nucleon helicity flip and is thus sensitive to the transverse polarisation of the nucleon. Therefore a Fourier transform of Φ_2 describes a force field perpendicular to the transverse polarisation of the target [152], which could be interpreted as a transverse position resolved Sivers force [153].

8.3.2 Calculating the form factor Φ_2

In order for us to calculate these form factors, we must match up the lattice operator for $d_2^{(f)}$, $\mathcal{O}^{[5]}$ from eq. 8.10, with eq. 8.33, where in this case $\tilde{G}_{\mu\nu}\gamma_{\rho}\equiv\gamma_{\rho}\epsilon^{\mu\nu\rho\delta}G_{\rho\delta}$.

Hence for our operator $\mathcal{O}^{[5]}_{[3\{1]4\}}$, we end up with

$$\mathcal{O}^{[5]}_{[3\{1]4\}} = -\frac{g}{6}\overline{\psi}\left(\gamma_4 G_{42} + \gamma_1 G_{12}\right)\psi - \text{traces}. \tag{8.35}$$

It is now possible for us to match our lattice matrix elements to the form factors and calculate the left hand side of eq. 8.33 using the relation shown above in eq. 8.35. We now move away from the $Q^2 = 0$ limit that we calculated $d_2^{(f)}$ at previously and start to analyse the off-forward matrix elements, by choosing combinations of various insertion momenta q and polarisations including the the unpolarised $\Gamma_{\text{Unpol}} = \frac{1}{2}(1+\gamma_4)$, and polarisations in the x or z directions $\Gamma_x = \frac{1}{2}(1+\gamma_4)i\gamma_5\gamma_1$ and $\Gamma_z = \frac{1}{2}(1+\gamma_4)i\gamma_5\gamma_3$ respectively, in order to calculate values of the matrix element at non-zero Q^2. By calculating the pre-factors of each form factor using our chosen polarisations and momentum, we can pick out and choose the unique combinations that enable us to isolate the individual form factors. For example, the lowest non-zero $Q^2 = 0.26(\text{GeV})^2$ is constructed from the five combinations of polarisation and momenta, where we have polarisation Γ_x with momenta $\vec{p}_1 = (0,0,1)$ and $\vec{p}_2 = (0,1,0)$ and Γ_z with $\vec{p}_1$, $\vec{p}_2$ and $-\vec{p}_2$.

By extracting these unique combinations of matrix elements, we can then solve the linear equations for the 8 form factors and construct the linear combinations in eq. 8.34. By choosing different $\vec{q}$ values, we gain access to multiple values of Φ_2 away from $Q^2 = 0$ including the $d_2^{(u)}$ point calculated previously in eq. 8.28. In Fig. 8.6, we show these 6 values of $\Phi_2^{(u)}$ ranging from $Q^2 = 0$ to $Q^2 = 1.29\text{GeV}^2$ along with their bootstrap error and a dipole fit.

In addition to the $\Phi_2^{(u)}$ form factor, we are able to get the off-forward lattice calculations for up quark components of the form factors $\Phi_1^{(u)}$ and $\Phi_3^{(u)}$. In Figs. 8.7 and 8.8, we show the off-forward calculations of the $\Phi_1^{(u)}$ and $\Phi_3^{(u)}$ respectively. It is difficult to determine an appropriate fit for these form factors at the present time.

In order to compare the slope of the $\Phi_2^{(u)}$ form factor, we take the normalisation of $\Phi_2^{(u)}(Q^2)/\Phi_2^{(u)}(0)$ in order to set the value at $Q^2 = 0$ to 1, and compare this to the slope of the form factor of the $F_1^{(u)}$ electromagnetic Dirac form factor from Chapter 4, with a similar normalisation condition. In Fig. 8.9, we see this comparison, with our normalised $\Phi_2^{(u)}$ in blue compared to $F_1^{(u)}$ in red. This shows that the $\Phi_2^{(u)}$ form factor has a steeper slope than the Dirac form factor, which suggests the force is distributed more broadly than electric charge. This effect will be prominent when analysing the two-dimensional Fourier transform of this form factor, and the effect on the transverse force, as will be investigated in the next section.

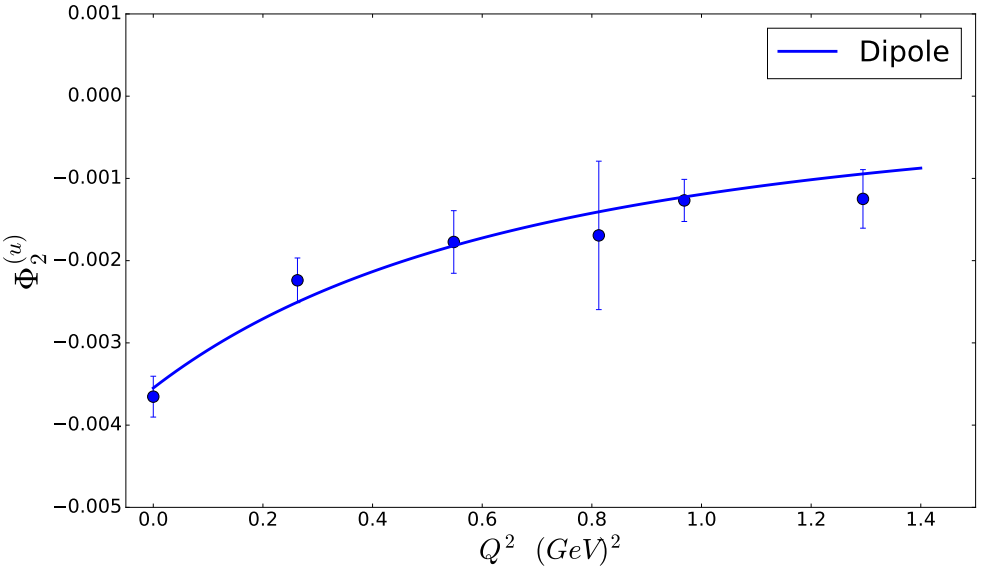

Figure 8.6: Transverse force form factor $\Phi_2^{(u)}(Q^2)$ from eq. 8.33, fitted with a dipole.

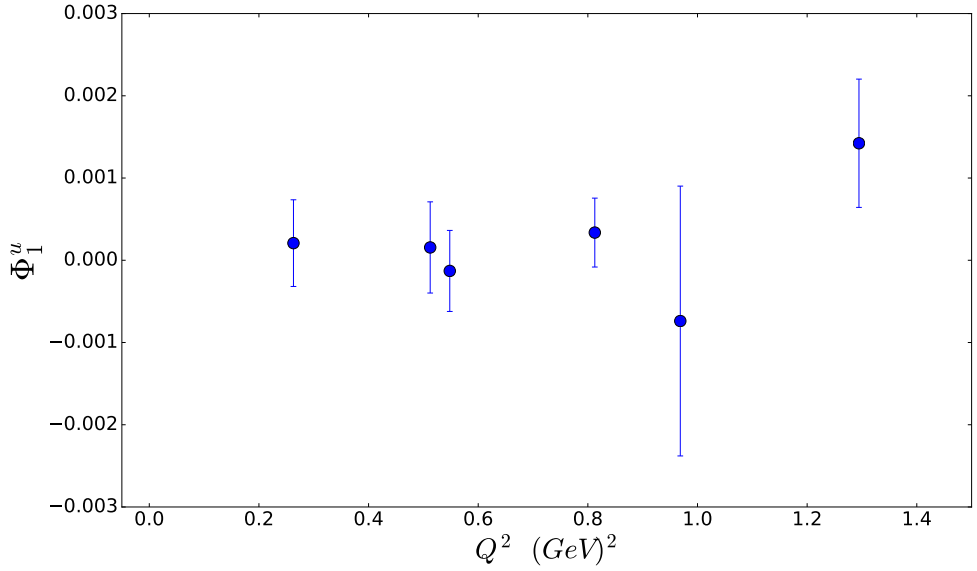

Figure 8.7: Transverse force form factor $\Phi_1^{(u)}(Q^2)$ from eq. 8.33.

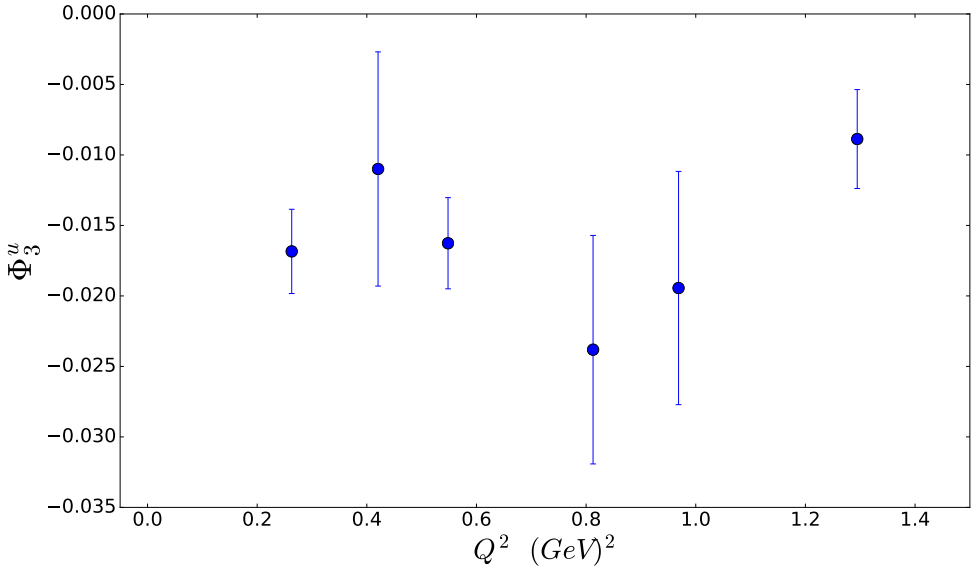

Figure 8.8: Transverse force form factor $\Phi_3^{(u)}(Q^2)$ from eq. 8.33.

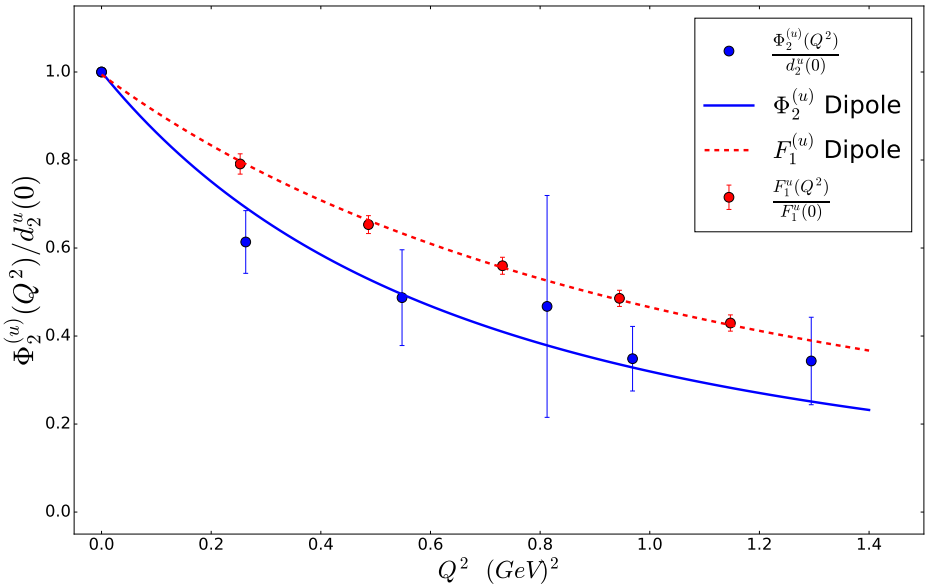

Figure 8.9: Transverse force form factor $\Phi_2^{(u)}(Q^2)$ for the up quark, normalised to one at $Q^2 = 0$, comparing the shape with the electromagnetic form factor $F_1^{(u)}(Q^2)$, similarly normalised.

8.3.3 Transverse Force Distribution

Just as the two-dimensional Fourier transform of our transverse spin dependent form factors gave us quark distributions dependent on the polarisation of the quark and nucleon spin in Chapter 7, the Fourier transform of the local matrix element in eq. 8.29 gives the distribution of the force in the transverse plane,

$$\mathcal{F}^i_{s's}(b_\perp) = \int \frac{d^2\Delta_\perp}{(2\pi)^2} e^{-ib_\perp\cdot\Delta_\perp} F^i_{s's}(\Delta_\perp) \tag{8.36}$$

with

$$F^i_{s's}(\Delta_\perp) = -\frac{1}{\sqrt{2}P+}\langle P^+, \frac{\Delta_\perp}{2}, s'|\overline{q}(0)\gamma^+ gG^{+i}(0)q(0)|P^+, -\frac{\Delta_\perp}{2}, s\rangle, \tag{8.37}$$

where s describes the transverse spin of the nucleon.

We require the vanishing skewness parameter in the limit $\xi \to 0$ [154] in order to develop a position space interpretation, thus the Δ^2 dependence of the form factors will be reduced to a transverse $\Delta^2_\perp$ dependence. Hence with $\Delta^+ = 0$ and $\xi = 0$, form factors Φ_4, Φ_5 and the second term in Φ_1 from eq. 8.33 no longer appear. Thus combining both eq. 8.34 and eq. 8.36 gives the spatial distributions of the force fields described by each form factor [155],

$$\begin{aligned}\mathcal{F}^i_{s's}(b_\perp) = \frac{i}{\sqrt{2}P+}\int \frac{d^2\Delta_\perp}{(2\pi)^2} e^{-ib_\perp\cdot\Delta_\perp}\overline{u}(p',s')\Bigg[&\frac{P^+\Delta^i_\perp}{M^2}\gamma^+\Phi_1(-\Delta^2_\perp) \\ &+\frac{P^+}{M}i\sigma^{+i}\Phi_2(-\Delta^2_\perp) + \frac{P^+\Delta^i_\perp}{M^3}i\sigma^{+\Delta}\Phi_3(-\Delta^2_\perp)\Bigg]u(p,s)\end{aligned} \tag{8.38}$$

with i again corresponding to the transverse index $i = x, y$.

By evaluating eq. 8.38, isolating only the second term and substituting in the dipole fit of $\Phi_2^{(u)}$ from Fig. 8.6, we are able to compute the Fourier transform as seen in Chapter 7 and plot the distribution of force, where since $\overline{q}(0)\gamma^+ gG^{+i}(0)q(0)$ is not sensitive to the polarisation of the quarks, the form factor describes the force acting on unpolarised quarks.

In Fig. 8.10, we show the Fourier transform of $\Phi_2^{(u)}(-\Delta^2_\perp)$ as a two dimensional density plot, where the length of the arrows displays the magnitude and their orientation represents the direction of the force. As the pre-factor to the Φ_2 term contains $\overline{u}(p',s')i\sigma^{i+}u(p,s)$, it requires a nucleon helicity flip and so is sensitive to the transverse polarisation of the nucleon, where here we have chosen a nucleon polarisation in the $x-$direction. Hence this Fourier transform describes the transverse force acting on the unpolarised quarks in a transversely polarised nucleon, and leads to the spatial distribution of the Sivers force [155].

If we compare this plot with the transverse spin density plots from chapter 7, we can see that unlike Fig. 7.3, in which we had unpolarised quarks in a polarised

proton, as is the case in Fig. 8.10, the transverse 'force' remains orbitally symmetric in magnitude around the point of origin, only in this case, the direction of the force is purely perpendicular in the positive direction to the polarisation of the nucleon spin.

As we noted in Fig. 8.9, the slope of the $\Phi_2^{(u)}$ form factor is steeper than that of the $F_1^{(u)}$ Dirac form factor, and so in comparison with the two-dimensional Fourier transform of the Dirac form factor demonstrated in Fig. 4.5, the density of the transverse force is more broadly distributed than that of the electric charge. From this one can begin to determine how the transverse force is dependent on the impact parameter $b_\perp$.

8.4 Summary

We have calculated the reduced matrix element $d_2^{(u)}$ using a $N_f = 2 + 1$ lattice at an unphysical quark mass and provided an updated result comparable to previous calculations. A key part of this calculation was the non-perturbative renormalisation and the inclusion of the operator mixing in our extraction of the twist-3 matrix element. The results for the d quark contribution to the $d_2^{(f)}$ were more consistent with zero. From here we moved on to looking at an interpretation of the quark-gluon correlations embodied in the twist-3 component of the x^2-moment of the g_2 structure function, d_2, identified with the color-Lorentz force acting on the struck quark in the instant after absorbing the virtual photon in a DIS experiment. This led to calculating the off-forward matrix elements of the local quark-gluon-quark correlator in order to determine the form factors that would describe the Lorentz force acting on the unpolarised quarks in a polarised proton, and yielded the first lattice calculation of the $\Phi_1^{(u)}$, $\Phi_2^{(u)}$ and $\Phi_3^{(u)}$ form factors.

We have shown that by taking a Fourier transform of these non-forward matrix elements, one can then determine how the transverse force depends on the impact parameter, $b_\perp$, and could lead to the spatial distribution of the Sivers force.

With future calculations, we hope to resolve these weak signal issues such that the down quark contributions, as well as the form factors of Φ_1 and Φ_3 can be improved. A greater understanding of these transverse 'force' form factors will lead to a significant conceptual advance in the understanding of the force mechanisms underlying confinement in QCD [156].

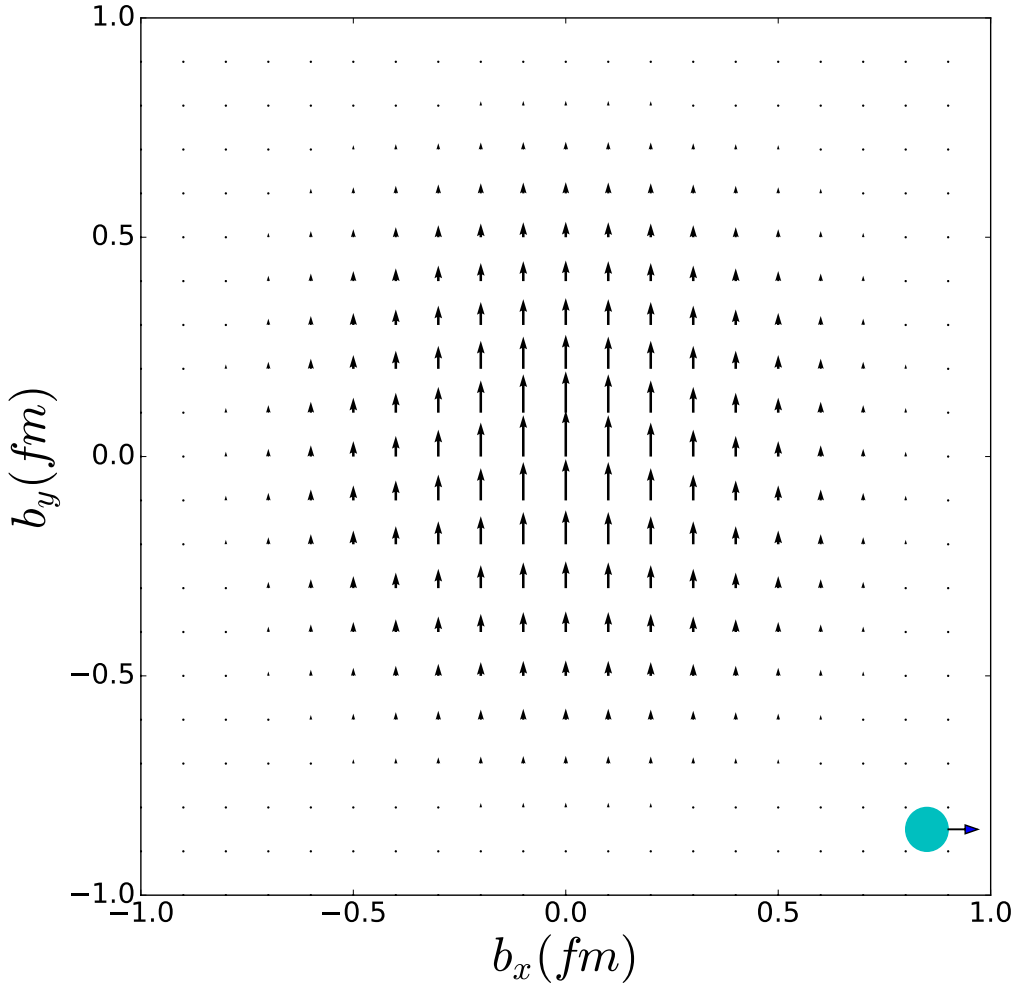

Figure 8.10: Transverse force field obtained from the form factor $\Phi_2^{(u)}$ in eq. 8.33. The orientation of the arrows represent the direction of the transverse force acting on the unpolarised quarks. The direction of the nucleon spin polarisation is denoted by the external arrow in the positive $x-$direction on the circle in the bottom right corner.

Chapter 9

Conclusion

In order for us to investigate the transverse properties of the octet baryons, we began with a brief overview of Quantum Chromodynamics in Chapter 2, and looked into the phenomenological processes that are used in experiments to extract useful quantities. From elastic scattering processes at smaller transfer momentum producing the electromagnetic form factors to later the larger momentum transfer collisions in deep in-elastic scattering (DIS) revealing the structure functions. With a brief look into the quantities that would assist us in uncovering the transverse properties of the baryons, we then had to introduce the lattice approach to calculating said quantities in Chapter 3, beginning with the discretisation of space-time, and the definition of the gluon and fermion actions. With randomly generated SU(3) gauge fields, particles are introduced into the system through the inversion of the Dirac matrix, forming the two-point quark propagators, and it is through these propagators that we can calculate useful quantities associated with the nucleons.

A two-point hadron correlator is the spatial Fourier transform of a combination of two-point quark propagators, and gives access to hadron masses and energies, however to probe their structure we require three-point correlators. With a third insertion point added to the two-point correlator on a single quark to construct the three-point correlator, we can extract quantities by fitting a plateau to a ratio function of the two and three-point correlators. It was through this technique that in Chapter 4, we demonstrated a calculation of the electromagnetic and tensor form factors, using one of the non-physical quark mass configurations. We also had an initial look into the transverse quark density distribution through a two-dimensional Fourier transform of the F_1 form factor, and saw the trivial transverse spin density of the unpolarised proton with its orbital symmetry about the origin of the proton. In order to improve the calculation of these non-physical configurations, in Chapter 5 we applied the RI'-MOM renormalisation scheme and then converted to the $\overline{\text{MS}}$ scheme in order to calculate the multiplicative renormalisation constants, required to remove divergent integrals from

our non-physical lattice configurations. Here we calculated the multiplicative renormalisation constants for a wide range of QCDSF lattice configurations, for multiple beta, lattice volumes and quark masses, allowing us to renormalise future lattice calculations done with these configurations.

Then in Chapter 6, we utilised the unique properties of SU(3) flavour symmetry breaking, that occurs as the lattice configurations move away from their mass symmetric point towards the physical mass. By considering this flavour expansion around the SU(3) flavour symmetric point, we were able to investigate the flavour breaking properties of the octet baryon matrix elements, and with the constraints on our hadron mass similarly constraining the expansion from the flavour breaking, were able to extrapolate our form factor results to the physical point. We observed strong flavour breaking effects in our 'fan' plots, where we could see as we moved closer to the physical mass of the pion, the heavier and lighter quarks diverged apart from the SU(3) symmetric point. We then went on to calculate the improvement coefficients, finding a 15% increase from the tree level value in our calculation of $\hat{b}_V$, and developing a new method to extrapolate results to the physical point. This was the first time these hadronic matrix elements have been extrapolated in this fashion alongside [1], and in this thesis, we have presented for the first time the extrapolation of the tensor form factor A_{T10} at the physical point.

By utilising the form factors, now extrapolated to the physical point in Chapter 6, we then presented results of the transverse quark density distributions of the octet baryons with respect to both the quark and nucleon spin polarisation in Chapter 7. By using analytically solving the Fourier transformation into a series of modified Bessel functions, we transformed our Q^2 dependent electromagnetic and tensor form factors into impact parameter space. Through the spin density equation, we were then able to present results revealing a variety of transverse spin dependent distributions, dependent on the choice of nucleon and quark spin polarisation. We were able to determine how the individual terms in the spin density equation impacted the quark density distribution through the quadrupole and dipole terms, and how the polarisation of the quarks and nucleon interact, as well as the difference between the proton, Σ and Ξ. Due to our lattice technique, we were able to calculate the 'doubly' and 'singly' represented quark contributions separately, and so when analysing the difference between the octet baryons, it was possible for us to take notice of the effect the spectator strange quarks had on the light quarks, where for the Cascade Ξ in the unpolarised case, the singly represented up quark would be more densely packed around the origin in comparison to the singly represented down quark in the proton, due to the presence of the two strange quarks. These spectator strange quark effects continue throughout the density calculations, and are exacerbated by the quark spin, increasing this distortion effect. We see interesting effects that occur when the quark spin and baryon spin polarisation

are both aligned or anti-aligned, where the baryon spin and quark spin polarisations interact with each other, leading to points of diminished quark density at the origin of the baryon, completely opposite to the unpolarised cases, with a clear dominance from the baryon spin when determining the density. An improved understanding of these transverse spin quark distributions will have implications when analysing the single-spin asymmetries observed in semi-inclusive deep in-elastic scattering (SIDIS) experiments, and hopefully with a deeper understanding of the baryon structure, we can better explain this phenomenology. We were able to determine that the transverse spin density distributions were rather sensitive to the fits of the form factors, and so further improvement to the calculation and extrapolation of the form factors will lead to further precision in our understanding of these densities.

Lastly we looked into the twist-3 component of the g_2 structure function, d_2 in Chapter 8. We first calculated a result for the reduced matrix element d_2 at $Q^2 = 0$ using our $N_f = 2 + 1$ lattice configuration alongside the renormalisation and were able to compare our result for the up quark component $d_2^{(u)}$ to a previous lattice result. Whilst we had issues with the signal coming through for the down quark component, the up quark component proved to follow the logical progression of previous calculations, vanishing as we head towards the chiral limit, where now we have crossed zero and found a negative result for the first time. Our goal for this calculation was to reveal the colour Lorentz force that the quark-gluon components embodied in the twist-3 component of the x^2-moment of the g_2 structure function could be interpreted as. To find the transverse 'force' density distribution, we calculated the off-forward matrix elements of the quark-gluon-quark correlator to determine the form factors that would describe the Lorentz force acting on unpolarised quarks in a polarised Proton. From this we were able to present the first lattice calculation of the $\Phi_2^{(u)}$ form factor, and through a Fourier transform, present the first look at a transverse distribution of the Lorentz force on the quarks, where we see the transverse 'colour' Lorentz force polarised perpendicular to the spin polarisation of the proton, and presented orbitally symmetric around the origin as it falls off away from the centre of the proton.

With improvements to the calculation of the off-forward matrix elements, in future we hope to solve the issues with the signal quality of the down quark contributions, and the Φ_1 and Φ_3 form factors. If these issues with signal strength can be solved, and the Fourier transforms of the Φ_1 and Φ_3 can be determined, this could lead to a significant advance into our conceptual understanding of the force mechanisms underlying confinement in QCD.

Appendix A

Metric and Dirac Matrices

A.1 Minkowski Spacetime

The metric in Minkowski space is chosen with the $(+1, -1, -1, -1)$ convention, so the metric tensor is defined as

$$g_{\mu\nu} = g^{\mu\nu} \equiv \begin{bmatrix} 1 & 0 & 0 & 0 \\ 0 & -1 & 0 & 0 \\ 0 & 0 & -1 & 0 \\ 0 & 0 & 0 & -1 \end{bmatrix} \tag{A.1}$$

The γ matrices generate a matrix representation of Clifford algebra $Cl_{1,3}(\mathbb{R})$,

$$\{\gamma^\mu, \gamma^\nu\} \equiv 2g^{\mu\nu}\mathbb{I}, \tag{A.2}$$

the fith Dirac matrix is then defined as

$$\gamma^5 \equiv i\gamma^0\gamma^1\gamma^2\gamma^3, \tag{A.3}$$

and the anti-symmetric matrices

$$\sigma^{\mu\nu} \equiv \frac{i}{2}\left[\gamma^\mu, \gamma^\nu\right]. \tag{A.4}$$

The set $\{\mathbb{I}, \gamma_\mu, \gamma_5, \gamma_\mu\gamma_5, \sigma_{\mu\nu}\}$ over the complex numbers forms a basis for the space of 4×4 complex matrices. Independent of the representation, the following identities

hold

$$\gamma^{5^2} = \mathbb{I}, \tag{A.5}$$
$$\left\{\gamma^5, \gamma^\mu\right\} = 0, \tag{A.6}$$
$$\mathrm{Tr}(\Gamma_i \Gamma_j) = 0 \forall i \neq j, \tag{A.7}$$
$$\mathrm{Tr}(\gamma^{\mu_1} \dots \gamma^{\mu_n}) = 0 \forall n \text{ odd}, \tag{A.8}$$
$$\mathrm{Tr}(\gamma^5 \gamma^{\mu_1} \dots \gamma^{\mu_n}) = 0 \forall n \text{ odd}, \tag{A.9}$$
$$\mathrm{Tr}(\gamma^\mu \gamma^\nu) = 4 g^{\mu\nu}, \tag{A.10}$$
$$\mathrm{Tr}(\gamma^5 \gamma^\mu \gamma^\nu) = 0, \tag{A.11}$$
$$\mathrm{Tr}(\gamma^\mu \gamma^\nu \gamma^\kappa \gamma^\lambda) = 4\left(g^{\mu\nu} g^{\kappa\lambda} - g^{\mu\kappa} g^{\nu\lambda} + g^{\mu\lambda} g^{\nu\kappa}\right), \tag{A.12}$$
$$\mathrm{Tr}(\gamma^5 \gamma^\mu \gamma^\nu \gamma^\kappa \gamma^\lambda) = -4i\epsilon^{\mu\nu\kappa\lambda}. \tag{A.13}$$

We make use of the standard Dirac basis unless otherwise stated,

$$\gamma_4 = \begin{bmatrix} \mathbb{I} & 0 \\ 0 & -\mathbb{I} \end{bmatrix}, \qquad \gamma_i = \begin{bmatrix} 0 & \sigma_i \\ -\sigma_i & 0 \end{bmatrix}, \qquad \gamma_5 = \begin{bmatrix} 0 & \mathbb{I} \\ \mathbb{I} & 0 \end{bmatrix}. \tag{A.14}$$

where σ_i are the Pauli matrices, defined in eq. C.5.

A.2 Euclidean Spacetime

In Euclidean space, the metric is defined as

$$\delta_{\mu\nu} \equiv \begin{bmatrix} 1 & 0 & 0 & 0 \\ 0 & 1 & 0 & 0 \\ 0 & 0 & 1 & 0 \\ 0 & 0 & 0 & 1 \end{bmatrix} \tag{A.15}$$

In the Wick rotation to Euclidean space, we choose the transformation

$$\gamma^\mu_{(\mathcal{M})} \equiv (\gamma^0_{(\mathcal{M})}, \gamma^i_{(\mathcal{M})}) \overset{\text{Wick}}{\to} \gamma_m u \equiv (\gamma_i, \gamma_4) = (-i\gamma^i_{(\mathcal{M})}, \gamma^0_{(\mathcal{M})}) \tag{A.16}$$

such that we obtain the correct relationship for Dirac matrices in Euclidean space,

$$\{\gamma_\mu, \gamma_\nu\} = 2\delta_{\mu\nu}\mathbb{I}. \tag{A.17}$$

With this convention, slashed quantities transform with a relative factor of i,

$$\not{x}_{(\mathcal{M})} \equiv \gamma^\mu_{(\mathcal{M})} g_{\mu\nu} x^\nu_{(\mathcal{M})} \overset{\text{Wick}}{\to} \not{x} \equiv \gamma_\mu \delta_{\mu\nu} x_\nu = i\not{x}_{(\mathcal{M})}, \tag{A.18}$$

and the slashed derivatives transform as

$$\not{\partial}_{(\mathcal{M})} \equiv \gamma_{\mu,(\mathcal{M})} g^{\mu\nu} \partial_{\nu,(\mathcal{M})} \overset{\text{Wick}}{\to} \gamma_\mu \delta_{\mu\nu} \partial_\nu = -i\not{\partial}_{(\mathcal{M})}. \tag{A.19}$$

We choose the fifth Dirac matrix

$$\gamma_5 \equiv \gamma_1\gamma_2\gamma_3\gamma_4 = -\gamma^5_{(\mathcal{M})}, \tag{A.20}$$

and the anti-symmetric tensor is defined as

$$\sigma_{\mu\nu} \equiv \frac{i}{2}\left[\gamma_\mu, \gamma_\nu\right], \tag{A.21}$$

and hence,

$$\sigma_{4i} = -i\sigma^{0i}_{(\mathcal{M})}, \tag{A.22}$$

$$\sigma_{ij} = -\sigma^{ij}_{(\mathcal{M})}. \tag{A.23}$$

Contractions between Lorentz vectors and the anti-symmetric tensor in Minkowski and Euclidean spacetime are related by

$$\sigma_{4\mu}\delta_{\mu\nu}q_\nu = i\sigma^{0\mu}_{(\mathcal{M})}g_{\mu\nu}x^\nu_{(\mathcal{M})}, \tag{A.24}$$

$$\sigma_{i\mu}\delta_{\mu\nu}q_\nu = \sigma^{i\mu}_{(\mathcal{M})}g_{\mu\nu}x^\nu_{(\mathcal{M})}, \tag{A.25}$$

The following identities hold independent of representation

$$\gamma_5^2 = \mathbb{I}, \tag{A.26}$$

$$\{\gamma_5, \gamma_\mu\} = 0, \tag{A.27}$$

$$\mathrm{Tr}(\Gamma_i\Gamma_j) = 0 \forall i \neq j, \tag{A.28}$$

$$\mathrm{Tr}(\gamma_{\mu_1}\dots\gamma_{\mu_n}) = 0 \forall n \text{ odd}, \tag{A.29}$$

$$\mathrm{Tr}(\gamma_5\gamma_{\mu_1}\dots\gamma_{\mu_n}) = 0 \forall n \text{ odd}, \tag{A.30}$$

$$\mathrm{Tr}(\gamma_\mu\gamma_\nu) = 4\delta_{\mu\nu}, \tag{A.31}$$

$$\mathrm{Tr}(\gamma_5\gamma_\mu\gamma_\nu) = 0, \tag{A.32}$$

$$\mathrm{Tr}(\gamma_\mu\gamma_\nu\gamma_\kappa\gamma_\lambda) = 4\left(\delta_{\mu\nu}\delta_{\kappa\lambda} - \delta_{\mu\kappa}\delta_{\nu\lambda} + \delta_{\mu\lambda}\delta_{\nu\kappa}\right), \tag{A.33}$$

$$\mathrm{Tr}(\gamma_5\gamma_\mu\gamma_\nu\gamma_\kappa\gamma_\lambda) = -4i\epsilon_{\mu\nu\kappa\lambda}. \tag{A.34}$$

In this thesis we use the transformed Dirac basis,

$$\gamma_4 = \begin{bmatrix}\mathbb{I} & 0\\ 0 & -\mathbb{I}\end{bmatrix}, \qquad \gamma_i = \begin{bmatrix}0 & -i\sigma_i\\ \sigma_i & 0\end{bmatrix}, \qquad \gamma_5 = \begin{bmatrix}0 & -\mathbb{I}\\ -\mathbb{I} & 0\end{bmatrix}, \tag{A.35}$$

where σ_i are the Pauli matrices, and all the matrices are Hermitian.

Appendix B

Levi-Civita Symbol

The Levi-Civita symbol in n dimensions is defined by total anti-symmetry in its indices, and the convention that

$$\epsilon^{12\ldots n} = +1. \tag{B.1}$$

These properties define the tensor for all other combinations of indices, with

$$\epsilon^{i_1 i_2 \ldots i_n} = \begin{cases} 0 & \text{any of } i_1, i_2, \ldots i_n \text{ are equal,} \\ +1 & \text{even permutation of } 1, 2, \ldots, n, \\ -1 & \text{odd permutation of } 1, 2, \ldots, n. \end{cases} \tag{B.2}$$

B.1 Minkowski Spacetime

In Minkowski spacetime, we define the Levi-Civita tensor with

$$\epsilon^{0123} = +1, \tag{B.3}$$

and the following identites hold,

$$\epsilon^{\mu\nu\kappa\lambda}\epsilon_{\mu\nu\kappa\lambda} = -24, \tag{B.4}$$

$$\epsilon^{\mu\nu\kappa\lambda}\epsilon_{\mu\nu\kappa\xi} = -6\delta^{\lambda}_{\xi}, \tag{B.5}$$

$$\epsilon^{\mu\nu\kappa\lambda}\epsilon_{\mu\nu\xi\eta} = -2(\delta^{\xi}_{\kappa}\delta^{\lambda}_{\eta} - \delta^{\kappa}_{\eta}\delta^{\lambda}_{\xi}), \tag{B.6}$$

$$\epsilon^{0ijk} = \epsilon_{ijk}, \tag{B.7}$$

where the last identity refers to the three-dimensional Euclidean tensor.

B.2 Euclidean Spacetime

In Euclidean spacetime, we choose the transformation

$$\epsilon^{\mu\nu\kappa\lambda}_{(\mathcal{M})} \overset{Wick}{\rightarrow} -\epsilon_{\mu\nu\kappa\lambda}, \tag{B.8}$$

so we have for the Levi-Civita tensor,

$$\epsilon_{1234} = +1 \tag{B.9}$$

and hence the following identities hold,

$$\epsilon_{\mu\nu\kappa\lambda}\epsilon_{\mu\nu\kappa\lambda} = 24, \tag{B.10}$$

$$\epsilon_{\mu\nu\kappa\lambda}\epsilon_{\mu\nu\kappa\xi} = -6\delta_{\lambda\xi}, \tag{B.11}$$

$$\epsilon_{\mu\nu\kappa\lambda}\epsilon_{\mu\nu\xi\eta} = -2(\delta_{\kappa\xi}\delta_{\lambda\eta} - \delta_{\kappa\eta}\delta_{\lambda\xi}), \tag{B.12}$$

$$\epsilon^{ijk4} = \epsilon_{ijk}, \tag{B.13}$$

where again the last identity refers to the three-dimensional Euclidean tensor.

Appendix C

Special Unitary Groups

The special unitary group of degree n, denoted by SU(n), is the non-Abelian Lie group of $n \times n$ unitary matrices with determinant 1 under multiplication. In the fundamental (or defining) representation, elements of SU(n) are generated by $n^2 - 1$ complex, traceless and Hermitian $n \times n$ matrices t^u, i.e. for each element Ω of SU(n),

$$\Omega = e^{i\omega^u t^u}, \tag{C.1}$$

for some real parameters ω^u. The generators t^u satisfy the commutation relation

$$[t^u, t^v] = if^{uvw}t^w, \tag{C.2}$$

where f^{uvw} are the fully antisymmetric structre constants of SU(n). The adjoint representation of SU(n) consists of $(n^2 - 1) \times (n^2 - 1)$ complex matrices, generated by matrices whose elements are given by the structure constants,

$$(T^u)^{vw} = -if^{uvw}. \tag{C.3}$$

C.1 SU(2) and the Pauli Matrices

In the fundamental representation, the three generators of SU(2) are

$$t^u = -\frac{i}{2}\sigma^u, \tag{C.4}$$

where σ^u are the Pauli matrices,

$$\sigma^1 = \begin{bmatrix} 0 & 1 \\ 1 & 0 \end{bmatrix}, \qquad \sigma^2 = \begin{bmatrix} 0 & -i \\ i & 0 \end{bmatrix}, \qquad \sigma^3 = \begin{bmatrix} 1 & 0 \\ 0 & -1 \end{bmatrix}. \tag{C.5}$$

The structure constants of SU(2) are given by

$$f^{uvw} = \epsilon^{uvw} \tag{C.6}$$

where ϵ^{uvw} is the anti-symmetric Levi-Civita tensor defined in eq. B.1.

C.2 SU(3) and the Gell-Mann Matrices

In the fundamental representation, the eight generators of SU(3) are

$$t^u = \frac{1}{2}\lambda^u, \tag{C.7}$$

where λ^u are the Gell-Mann matrices,

$$\begin{aligned}
\lambda^1 &= \begin{bmatrix} 0 & 1 & 0 \\ 1 & 0 & 0 \\ 0 & 0 & 0 \end{bmatrix}, \qquad \lambda^2 = \begin{bmatrix} 0 & -i & 0 \\ i & 0 & 0 \\ 0 & 0 & 0 \end{bmatrix}, \qquad \lambda^3 = \begin{bmatrix} 1 & 0 & 0 \\ 0 & -1 & 0 \\ 0 & 0 & 0 \end{bmatrix}, \\
\lambda^4 &= \begin{bmatrix} 0 & 0 & 1 \\ 0 & 0 & 0 \\ 1 & 0 & 0 \end{bmatrix}, \qquad \lambda^5 = \begin{bmatrix} 0 & 0 & -i \\ 0 & 0 & 0 \\ i & 0 & 0 \end{bmatrix}, \\
\lambda^6 &= \begin{bmatrix} 0 & 0 & 0 \\ 0 & 0 & 1 \\ 0 & 1 & 0 \end{bmatrix}, \qquad \lambda^7 = \begin{bmatrix} 0 & 0 & 0 \\ 0 & 0 & -i \\ 0 & i & 0 \end{bmatrix}, \qquad \lambda^8 = \frac{1}{\sqrt{(3)}} \begin{bmatrix} 1 & 0 & 0 \\ 0 & 1 & 0 \\ 0 & 0 & -2 \end{bmatrix}.
\end{aligned} \tag{C.8}$$

The structure constants of SU(3) are

$$\begin{aligned}
&f^{123} = 1, \\
&f^{147} = -f^{156} = f^{246} = f^{257} = f^{345} = -f^{367} = \frac{1}{2}, \\
&f^{458} = f^{678} = \frac{\sqrt{3}}{2},
\end{aligned} \tag{C.9}$$

with all other constants not related to these by permutations being zero.

Appendix D

Spin-Half Particles and the Dirac Equation

D.1 Minkowski Spacetime

In Minkowski spacetime, the four-spin vector is defined by the relations

$$p^\mu s_\mu = 0, \tag{D.1}$$

$$s^\mu s_\mu = -1. \tag{D.2}$$

The explicit form is given by

$$s^\mu(p,\sigma) = \left(\frac{\vec{p}\cdot s}{E}, s\right) = \left(\sigma\frac{\vec{p}\cdot\hat{e}}{m}, s\right), \tag{D.3}$$

where the relativistic three-spin is given by

$$s(p,\sigma) = \sigma\left[\hat{e} + \frac{\vec{p}\cdot\hat{e}}{m(E+m)}\vec{p}\right]. \tag{D.4}$$

Here $\hat{e}$ is the chosen spin-polarisation axis, and $\sigma = \pm 1$ is the spin quantum number. The Dirac equation for a free spin-half particle is given by

$$\left(i[\gamma^\mu]_{\alpha\beta}\partial_\mu - m\delta_{\alpha\beta}\right)[\psi(x)]_\alpha = 0, \tag{D.5}$$

where ψ is a four-component spinor. Assuming matrix-vector notation for the Dirac indices, and Feynman slash notation for the contraction with the γ matrix, this may be written in the more compact form

$$\left(i\partial\!\!\!/ - m\right)\psi = 0. \tag{D.6}$$

Positive and negative-energy solutions to the free Dirac equation are of the form

$$\psi = u(p,\sigma)e^{-ip\cdot x}, \tag{D.7}$$
$$\psi = v(p,\sigma)e^{+ip\cdot x}, \tag{D.8}$$

where the normalisation of the spinors is chosen to be

$$u(p,\sigma')\overline{u}(p,\sigma) = \left(\not{p} + m\right)\frac{1}{2}\left(\mathbb{I} + \gamma^5 \not{s}\right)\delta_{\sigma'\sigma}, \tag{D.9}$$
$$u(p,\sigma')\overline{v}(p,\sigma) = \left(\not{p} - m\right)\frac{1}{2}\left(\mathbb{I} + \gamma^5 \not{s}\right)\delta_{\sigma'\sigma}, \tag{D.10}$$

and the adjoint spinor is defined as

$$\overline{\psi} = \psi^\dagger\gamma^0. \tag{D.11}$$

Form the normalisation, we can derive the relations

$$\overline{u}(p,\sigma')u(p,\sigma) = 2m\delta_{\sigma'\sigma}, \tag{D.12}$$
$$\overline{u}(p,\sigma')\gamma^5 u(p,\sigma) = 0, \tag{D.13}$$
$$\overline{u}(p,\sigma')\gamma^\mu u(p,\sigma) = 2p^\mu\delta_{\sigma'\sigma}, \tag{D.14}$$
$$\overline{u}(p,\sigma')\gamma^\mu\gamma^5 u(p,\sigma) = 2ms^\mu\delta_{\sigma'\sigma}, \tag{D.15}$$
$$\overline{u}(p,\sigma')\sigma^{\mu\nu}u(p,\sigma) = 2\epsilon^{\mu\nu\kappa\lambda}s_\kappa p_\lambda\delta_{\sigma'\sigma}. \tag{D.16}$$

D.2 Euclidean Spacetime

After the Wick rotation to Euclidean spacetime, the four-spin vector is defined by the relations

$$p\cdot s = 0, \tag{D.17}$$
$$s^2 = 1. \tag{D.18}$$

The explicit form is given by

$$s_\mu(p,\sigma) = \left(s, i\frac{\vec{p}\cdot s}{E}\right) = (s, i\sigma\frac{\vec{p}\cdot\hat{e}}{m}), \tag{D.19}$$

where the relativistic three-spin

$$s(p,\sigma) = \sigma\left[\hat{e} + \frac{\vec{p}\cdot\hat{e}}{m(E+m)}\vec{p}\right]. \tag{D.20}$$

The Dirac equation for a free spin-half particle in Euclidean spacetime is given by

$$\left([\gamma^\mu]_{\alpha\beta}\partial_\mu + m\delta_{\alpha\beta}\right)[\psi(x)]_\alpha = 0, \tag{D.21}$$

which may be written in the compact form

$$\left(\not{\partial} + m\right)\psi = 0. \tag{D.22}$$

Positive and negative-energy solutions to the free Dirac equation are of the form

$$\psi = u(p,\sigma)e^{+ip\cdot x}, \tag{D.23}$$
$$\psi = v(p,\sigma)e^{-ip\cdot x}, \tag{D.24}$$

where the normalisation of the spinors is chosen to be

$$u(p,\sigma')\overline{u}(p,\sigma) = \left(-i\not{p} + m\right)\frac{1}{2}\left(\mathbb{I} + \gamma^5\not{s}\right)\delta_{\sigma'\sigma}, \tag{D.25}$$
$$u(p,\sigma')\overline{v}(p,\sigma) = \left(-i\not{p} - m\right)\frac{1}{2}\left(\mathbb{I} + \gamma^5\not{s}\right)\delta_{\sigma'\sigma}, \tag{D.26}$$

and the adjoint spinor is defined as

$$\overline{\psi} = \psi^\dagger\gamma_4. \tag{D.27}$$

Form the normalisation, we can derive the relations

$$\overline{u}(p,\sigma')u(p,\sigma) = 2m\delta_{\sigma'\sigma}, \tag{D.28}$$
$$\overline{u}(p,\sigma')\gamma_5 u(p,\sigma) = 0, \tag{D.29}$$
$$\overline{u}(p,\sigma')\gamma_\mu u(p,\sigma) = -2p_\mu\delta_{\sigma'\sigma}, \tag{D.30}$$
$$\overline{u}(p,\sigma')\gamma_\mu\gamma^5 u(p,\sigma) = 2ims_\mu\delta_{\sigma'\sigma}, \tag{D.31}$$
$$\overline{u}(p,\sigma')\sigma_{\mu\nu}u(p,\sigma) = 2i\epsilon_{\mu\nu\kappa\lambda}s_\kappa p_\lambda\delta_{\sigma'\sigma}. \tag{D.32}$$

Appendix E

Dirac Projectors and Traces

E.1 Projectors

Parity and spin projectors for spin-half baryon spectroscopy are defined as

$$\Gamma_{P_\pm} = \frac{1}{2}(\mathbb{I} \pm \gamma_4), \tag{E.1}$$

$$\Gamma_{S_\pm} = \frac{1}{2}(\mathbb{I} \mp i\hat{e}\cdot\vec{\gamma}\gamma_5), \tag{E.2}$$

where $\hat{e}$ is the chosen spin-polarisation axis. Commonly used combinations of these projectors for nucleon analyses are

$$\Gamma_{\text{unpol}} \equiv \Gamma_{P_+}\left(\Gamma_{S_+} + \Gamma_{S_-}\right) = \frac{1}{2}(\mathbb{I} + \gamma_4), \tag{E.3}$$

$$\Gamma_{\text{pol}} \equiv \Gamma_{P_+}\left(\Gamma_{S_+} - \Gamma_{S_-}\right) = -\frac{i}{2}(\mathbb{I} + \gamma_4)\hat{e}\cdot\vec{\gamma}\gamma_5, \tag{E.4}$$

$$\Gamma_{\text{pol}\pm} \equiv \Gamma_{P_+}\Gamma_{S_\pm} = \frac{1}{2}(\mathbb{I} + \gamma_4)\frac{1}{2}(\mathbb{I} \mp \hat{e}\cdot\vec{\gamma}\gamma_5) = \frac{1}{2}\left(\Gamma_{\text{unpol}} \pm \Gamma_{\text{pol}}\right). \tag{E.5}$$

$$\tag{E.6}$$

E.2 Traces

The function F_2 is defined by

$$F_2(\Gamma_{\text{proj.}};\vec{p},m) \equiv \frac{1}{4}\sum_\sigma [\Gamma_{\text{proj.}}]_{\alpha\beta} u_\alpha(p,\sigma)\overline{u}_\beta(p,\sigma) = \frac{1}{4}\text{Tr}\Gamma(-i\not{p} + m), \tag{E.7}$$

and is linear in $\Gamma_{\text{proj.}}$. For the basis of Dirac matrices, with kinematic inputs $\vec{p}$ and m assumed, it is given by

$$F_2(\mathbb{I}) = m, \tag{E.8}$$
$$F_2(\gamma_m u) = -ip_\mu, \tag{E.9}$$
$$F_2(\gamma_5) = F_2(\gamma_\mu\gamma_5) = F_2(\sigma_{\mu\nu}) = 0. \tag{E.10}$$

For the common Dirac projectors previously defined

$$F_2(\Gamma_{\text{Unpol}}) = \frac{1}{2}(E_X + m_X), \tag{E.11}$$
$$F_2(\Gamma_{\text{pol}}) = 0, \tag{E.12}$$
$$F_2(\Gamma_{\text{pol}\pm}) = \frac{1}{4}(E_X + m_X). \tag{E.13}$$

The function F_3 is defined as

$$\begin{aligned} F_3(\Gamma_{\text{proj.}}, \Gamma_{\mathcal{P},X}; \vec{p}', \vec{p}, m_X) &\equiv \frac{1}{4}\sum_{\sigma'\sigma}[\Gamma_{\text{proj.}}]_{\alpha\beta}u_\alpha(p',\sigma')\overline{u}(p',\sigma')\Gamma_{\mathcal{O},X}u(p,\sigma)\overline{u}_\beta(p,\sigma) \\ &= \frac{1}{4}\text{Tr}\Gamma_{\text{proj.}}\left(-i\not{p}' + m\right)\Gamma_{\mathcal{O},X}\left(-i\not{p} + m\right). \end{aligned} \tag{E.14}$$

In the basis of Dirac Matrices

$$F_3(\mathbb{I},\mathbb{I}) = -\frac{1}{2}(p'+p)^2 = m^2 - p'\cdot p, \tag{E.15}$$
$$F_3(\mathbb{I},\gamma_\mu) = -im(p'+p)_\mu, \tag{E.16}$$
$$F_3(\mathbb{I},\gamma_5) = 0, \tag{E.17}$$
$$F_3(\mathbb{I},\gamma_\mu\gamma_5) = 0, \tag{E.18}$$
$$F_3(\mathbb{I},\sigma_{\mu\nu}) = -i\left(p'_\mu p_\nu - p_\mu p'_\nu\right), \tag{E.19}$$
$$F_3(\gamma_m u,\gamma_\nu) = -\left[p'_\mu p_\nu + p_\mu p'_\nu + \frac{1}{2}\delta_{\mu\nu}(p'-p)^2\right], \tag{E.20}$$
$$F_3(\gamma_\mu,\gamma_5) = 0, \tag{E.21}$$
$$F_3(\gamma_\mu,\gamma_\nu\gamma_5) = -\epsilon_{\mu\nu\kappa\lambda}p'_\kappa p_\lambda, \tag{E.22}$$
$$F_3(\gamma_\mu,\sigma_{\kappa\lambda}) = -m\left[\delta_{\mu\kappa}(p'-p)_\lambda - \delta_{\mu\lambda}(p'-p)_\kappa\right], \tag{E.23}$$
$$F_3(\gamma_5,\gamma_5) = -\frac{1}{2}(p'-p)^2, \tag{E.24}$$
$$F_3(\gamma_5,\gamma_\mu\gamma_5) = -im(p'-p)_\mu, \tag{E.25}$$
$$F_3(\gamma_5,\sigma_{\mu\nu}) = -i\epsilon_{\mu\nu\kappa\lambda}p'_\kappa p_\lambda, \tag{E.26}$$
$$F_3(\gamma_\mu\gamma_5,\gamma_\nu\gamma_5) = -\left[p'_\mu p_\nu + p_\mu p'_\nu - \frac{1}{2}\delta_{\mu\nu}(p'+p)^2\right], \tag{E.27}$$
$$F_3(\gamma_\mu\gamma_5,\sigma_{\kappa\lambda}) = -m\epsilon_{\mu\kappa\lambda\xi}(p'+p)_\xi. \tag{E.28}$$

For the unpolarised projector, we have

$$F_3(\Gamma_{\text{Unpol}}, \mathbb{I}) = \frac{1}{2}\left[(E(\vec{p})+m)(E(\vec{p}')+m) - \vec{p}\cdot\vec{p}'\right], \tag{E.29}$$

$$F_3(\Gamma_{\text{Unpol}}, \gamma_4) = \frac{1}{2}\left[(E(\vec{p})+m)(E(\vec{p}')+m) + \vec{p}\cdot\vec{p}'\right], \tag{E.30}$$

$$F_3(\Gamma_{\text{Unpol}}, \gamma_i) = -\frac{i}{2}\left[(E(\vec{p})+m)\vec{p} + (E(\vec{p}')+m)\vec{p}'\right]_i, \tag{E.31}$$

$$F_3(\Gamma_{\text{Unpol}}, \gamma_5) = 0, \tag{E.32}$$

$$F_3(\Gamma_{\text{Unpol}}, \gamma_4\gamma_5) = 0, \tag{E.33}$$

$$F_3(\Gamma_{\text{Unpol}}, \gamma_i\gamma_5) = \frac{1}{2}\left[\vec{p}'\times\vec{p}\right]_i, \tag{E.34}$$

$$F_3(\Gamma_{\text{Unpol}}, \sigma_{4i}) = \frac{1}{2}\left[(E(\vec{p}')+m)\vec{p} - (E(\vec{p})+m)\vec{p}'\right]_i, \tag{E.35}$$

$$F_3(\Gamma_{\text{Unpol}}, \sigma_{ij}) = \frac{i}{2}\epsilon_{ijk}\left[\vec{p}\times\vec{p}'\right]_k, \tag{E.36}$$

and for the polarised projector

$$F_3(\Gamma_{\text{pol}}, \mathbb{I}) = \frac{i}{2}\hat{e}\cdot\vec{p}\times\vec{p}', \tag{E.37}$$

$$F_3(\Gamma_{\text{pol}}, \gamma_4) = -\frac{i}{2}\hat{e}\cdot\vec{p}\times\vec{p}', \tag{E.38}$$

$$F_3(\Gamma_{\text{pol}}, \gamma_i) = -\frac{1}{2}\left[(E(\vec{p})+m)\vec{p}'\times\hat{e} - (E(\vec{p}')+m)\vec{p}\times\hat{e}\right]_i, \tag{E.39}$$

$$F_3(\Gamma_{\text{pol}}, \gamma_5) = \frac{1}{2}\left[(E(\vec{p})+m)\vec{p}'\cdot\hat{e} - (E(\vec{p}')+m)\vec{p}\cdot\hat{e}\right], \tag{E.40}$$

$$F_3(\Gamma_{\text{pol}}, \gamma_4\gamma_5) = \frac{1}{2}\left[(E(\vec{p})+m)\vec{p}'\cdot\hat{e} + (E(\vec{p}')+m)\vec{p}\cdot\hat{e}\right], \tag{E.41}$$

$$F_3(\Gamma_{\text{pol}}, \gamma_i\gamma_5) = \frac{i}{2}\left[(E(\vec{p})+m)(E(\vec{p}')+m)\hat{e} + (\vec{p}\cdot\hat{e})\vec{p}' + (\vec{p}'\cdot\hat{e})\vec{p} - (\vec{p}'\cdot\vec{p})\hat{e}\right]_i, \tag{E.42}$$

$$F_3(\Gamma_{\text{pol}}, \sigma_{4i}) = -\frac{i}{2}\left[(E(\vec{p})+m)\hat{e}\times\vec{p}' + (E(\vec{p}')+m)\hat{e}\times\vec{p}\right], \tag{E.43}$$

$$F_3(\Gamma_{\text{pol}}, \sigma_{ij}) = -\frac{i}{2}\epsilon_{ijk}\left[(E(\vec{p})+m)(E(\vec{p}')+m)\hat{e} - +(\vec{p}\cdot\hat{e})\vec{p}' + (\vec{p}'\cdot\hat{e})\vec{p} - (\vec{p}'\cdot\vec{p})\hat{e}\right]_k. \tag{E.44}$$

In the Breit frame where $E(\vec{p}') = E(\vec{p}) = E$, it is convenient to work in terms of the kinematic variables

$$P \equiv \frac{1}{2}(p'+p), \tag{E.45}$$

$$q \equiv (p'-p). \tag{E.46}$$

For the unpolarised projector and Breit frame kinematics, we have

$$F_3^{\text{Breit}}(\Gamma_{\text{Unpol}}, \mathbb{I}) = m(E+m) + \vec{q}^2, \tag{E.47}$$
$$F_3^{\text{Breit}}(\Gamma_{\text{Unpol}}, \gamma_4) = m(E+m) + \vec{P}^2, \tag{E.48}$$
$$F_3^{\text{Breit}}(\Gamma_{\text{Unpol}}, \gamma_i) = -i(E+m)\vec{P}_i, \tag{E.49}$$
$$F_3^{\text{Breit}}(\Gamma_{\text{Unpol}}, \gamma_5) = 0, \tag{E.50}$$
$$F_3^{\text{Breit}}(\Gamma_{\text{Unpol}}, \gamma_4\gamma_5) = 0, \tag{E.51}$$
$$F_3^{\text{Breit}}(\Gamma_{\text{Unpol}}, \gamma_i\gamma_5) = \left[\vec{q} \times \vec{P}\right]_i, \tag{E.52}$$
$$F_3^{\text{Breit}}(\Gamma_{\text{Unpol}}, \sigma_{4i}) = -\left(E+m\right) q_i, \tag{E.53}$$
$$F_3^{\text{Breit}}(\Gamma_{\text{Unpol}}, \sigma_{ij}) = i\epsilon_{ijk}\left[\vec{P} \times \vec{q}\right]_k, \tag{E.54}$$

and for the polarised projector

$$F_3^{\text{Breit}}(\Gamma_{\text{pol}}, \mathbb{I}) = i\hat{e} \cdot \vec{P} \times \vec{q}, \tag{E.55}$$
$$F_3^{\text{Breit}}(\Gamma_{\text{pol}}, \gamma_4) = -i\hat{e} \cdot \vec{P} \times \vec{q}, \tag{E.56}$$
$$F_3^{\text{Breit}}(\Gamma_{\text{pol}}, \gamma_i) = (E+m)[\hat{e} \times \vec{q}]_i, \tag{E.57}$$
$$F_3^{\text{Breit}}(\Gamma_{\text{pol}}, \gamma_5) = (E+m)\hat{e} \cdot \vec{q}, \tag{E.58}$$
$$F_3^{\text{Breit}}(\Gamma_{\text{pol}}, \gamma_4\gamma_5) = -(E+m)\hat{e} \cdot \vec{P}, \tag{E.59}$$
$$F_3^{\text{Breit}}(\Gamma_{\text{pol}}, \gamma_i\gamma_5) = im(E+m)\left[\hat{e} + \frac{(\vec{P} \cdot \hat{e})\vec{P}}{m(E+m)} + \frac{\vec{q} \times (\hat{e} \times \vec{q})}{m(E+m)}\right]_i, \tag{E.60}$$
$$F_3^{\text{Breit}}(\Gamma_{\text{pol}}, \sigma_{4i}) = -(E+m)[\hat{e} \times \vec{P}]_i, \tag{E.61}$$
$$F_3^{\text{Breit}}(\Gamma_{\text{pol}}, \sigma_{ij}) = -\epsilon_{ijk}m(E+m)\left[\hat{e} + \frac{(\vec{q} \cdot \hat{e})\vec{q}}{m(E+m)} + \frac{\vec{P} \times (\hat{e} \times \vec{P})}{m(E+m)}\right]_k. \tag{E.62}$$

Appendix F

Additional Figures

F. ADDITIONAL FIGURES

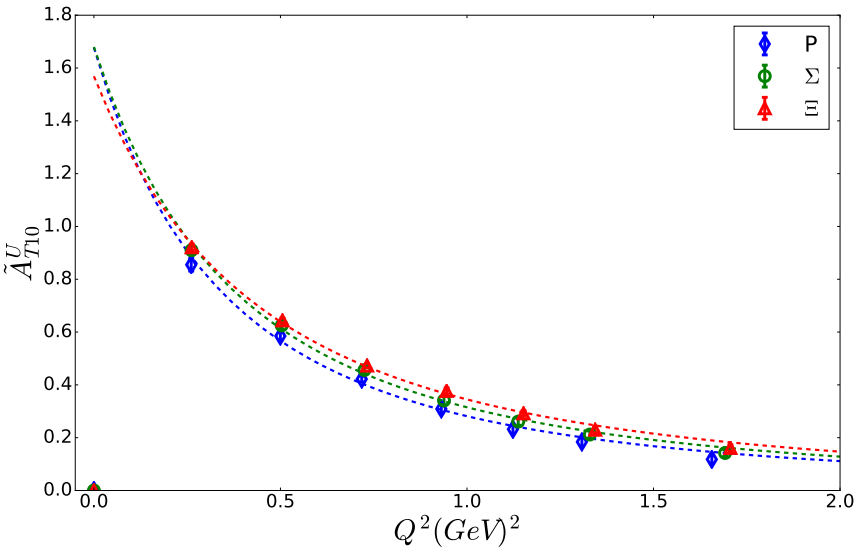

Figure F.1: The unrenormalised tensor form factor $\tilde{A}^u_{T10}(Q^2)$ for the $\kappa_l = 0.12104$, $\kappa_s = 0.12062$ lattice configuration. Comparing the Doubly represented quark contribution of the up quark in the Proton and Σ and the strange quark in the Ξ baryon.

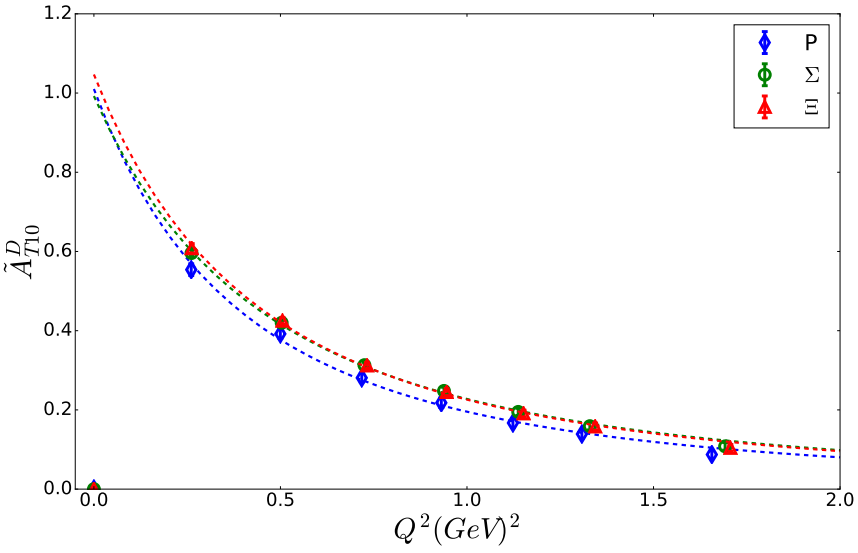

Figure F.2: The unrenormalised tensor form factor $\tilde{A}^d_{T10}(Q^2)$ for the $\kappa_l = 0.12104$, $\kappa_s = 0.12062$ lattice configuration. Comparing the Singly represented quark contribution of the down quark in the Proton, strange quark in the Σ and the up quark in the Ξ baryon.

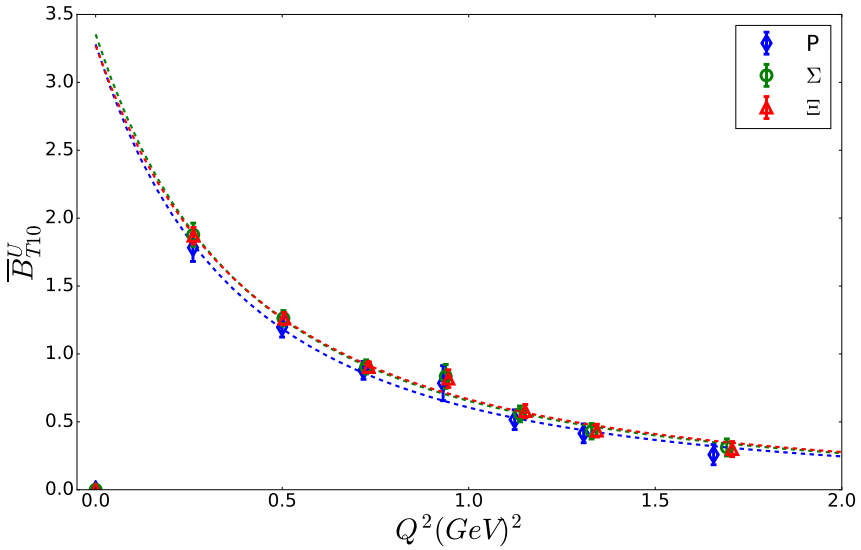

Figure F.3: The unrenormalised tensor form factor $\overline{B}^{u}_{T10}(Q^2)$ for the $\kappa_l = 0.12104$, $\kappa_s = 0.12062$ lattice configuration. Comparing the Doubly represented quark contribution of the up quark in the Proton and Σ and the strange quark in the Ξ baryon.

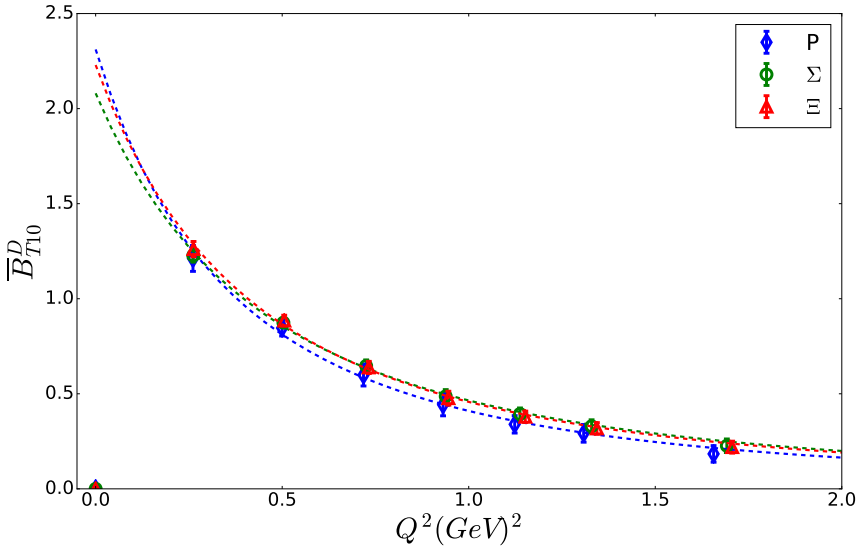

Figure F.4: The unrenormalised tensor form factor $\overline{B}^{d}_{T10}(Q^2)$ for the $\kappa_l = 0.12104$, $\kappa_s = 0.12062$ lattice configuration. Comparing the Singly represented quark contribution of the down quark in the Proton, strange quark in the Σ and the up quark in the Ξ baryon.

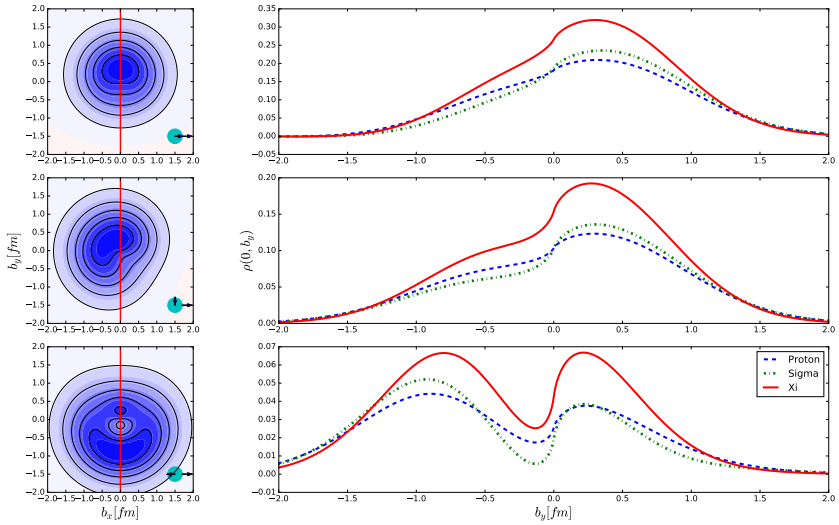

Figure F.5: Similar to Fig. 7.1, only now showing the doubly represented quark density distribution, for a fixed nucleon spin polarisation ($S_x = 1$) and quark polarisation of $s_\perp = (1, 0)$, $s_\perp = (0, 1)$ and $s_\perp = (-1, 0)$. The polarisation of each contour plot is shown by the teal circle in the bottom right corner, with the internal arrow showing the direction of the quark spin polarisation, and the external arrow showing that of the nucleon spin polarisation.

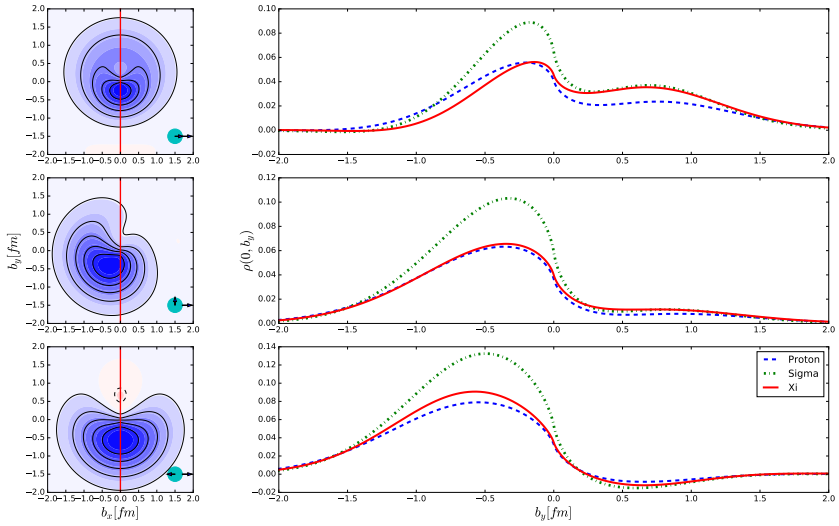

Figure F.6: Similar to Fig. F.5, only now showing the singly represented quark density distribution, for a fixed nucleon spin polarisation ($S_x = 1$) and quark polarisation of $s_\perp = (1, 0)$, $s_\perp = (0, 1)$ and $s_\perp = (-1, 0)$.

Appendix G

Discretising the derivative

We begin by using the definition

$$\overleftrightarrow{D} = \overrightarrow{D} - \overleftarrow{D} \tag{G.1}$$

where for the Twist 3 Matrix element d_2 we require the second derivative thus,

$$\begin{aligned} \overleftrightarrow{D}_\mu \overleftrightarrow{D}_\nu &= \left(\overrightarrow{D}_\mu - \overleftarrow{D}_\mu\right)\left(\overrightarrow{D}_\nu - \overleftarrow{D}_\nu\right) \\ &= \left(\overrightarrow{D}_\mu \overrightarrow{D}_\nu - \overrightarrow{D}_\mu \overleftarrow{D}_\nu - \overleftarrow{D}_\mu \overrightarrow{D}_\nu + \overleftarrow{D}_\mu \overleftarrow{D}_\nu\right) \end{aligned} \tag{G.2}$$

We discretise the derivatives

$$\begin{aligned} \overline{\psi}\Gamma\overrightarrow{D}_\mu\overrightarrow{D}_\nu\psi(x) = \frac{1}{4}\{ &- \overline{\psi}(x)\Gamma U_\mu^\dagger(x-\hat{\mu})U_\nu(x-\hat{\mu})\psi(x-\hat{\mu}+\hat{\nu}) \\ &+ \overline{\psi}(x)\Gamma U_\mu^\dagger(x-\hat{\mu})U_\nu^\dagger(x-\hat{\mu}-\hat{\nu})\psi(x-\hat{\mu}-\hat{\nu}) \\ &+ \overline{\psi}(x)\Gamma U_\mu(x)U_\nu(x+\hat{\mu})\psi(x+\hat{\mu}+\hat{\nu}) \\ &- \overline{\psi}(x)U_\mu(x)U_\nu^\dagger(x+\hat{\mu}-\hat{\nu})\psi(x+\hat{\mu}-\hat{\nu})\} \end{aligned}$$

$$\begin{aligned} -\overline{\psi}\Gamma\overleftarrow{D}_\mu\overrightarrow{D}_\nu\psi(x) = \frac{1}{4}\{ &- \overline{\psi}(x+\hat{\mu})\Gamma U_\mu^\dagger(x)U_\nu(x)\psi(x+\hat{\nu}) \\ &+ \overline{\psi}(x+\hat{\mu})\Gamma U_\mu^\dagger(x)U_\nu^\dagger(x-\hat{\nu})\psi(x-\hat{\nu}) \\ &+ \overline{\psi}(x-\hat{\mu})\Gamma U_\mu(x-\hat{\mu})U_\nu(x)\psi(x+\hat{\nu}) \\ &- \overline{\psi}(x-\hat{\mu})U_\mu(x-\hat{\mu})U_\nu^\dagger(x-\hat{\nu})\psi(x-\hat{\nu})\} \end{aligned}$$

$$
\begin{aligned}
-\overline{\psi}\Gamma\overrightarrow{D}_\mu\overleftarrow{D}_\nu\psi(x) = \frac{1}{4}\{ &-\overline{\psi}(x-\hat{\nu})\Gamma U_\mu^\dagger(x-\hat{\nu}-\hat{\mu})U_\nu(x-\hat{\nu}-\hat{\mu})\psi(x-\hat{\mu}) \\
&+\overline{\psi}(x+\hat{\nu})\Gamma U_\mu^\dagger(x+\hat{\nu}-\hat{\mu})U_\nu^\dagger(x-\hat{\mu})\psi(x-\hat{\mu}) \\
&+\overline{\psi}(x-\hat{\nu})\Gamma U_\mu(x-\hat{\nu})U_\nu(x-\hat{\nu}+\hat{\mu})\psi(x+\hat{\mu}) \\
&-\overline{\psi}(x+\hat{\nu})U_\mu(x+\hat{\nu})U_\nu^\dagger(x+\hat{\mu})\psi(x+\hat{\mu})\}
\end{aligned}
$$

$$
\begin{aligned}
\overline{\psi}\Gamma\overleftarrow{D}_\mu\overleftarrow{D}_\nu\psi(x) = \frac{1}{4}\{ &-\overline{\psi}(x+\hat{\mu}-\hat{\nu})\Gamma U_\mu^\dagger(x-\hat{\nu})U_\nu(x-\hat{\nu})\psi(x) \\
&+\overline{\psi}(x+\hat{\mu}+\hat{\nu})\Gamma U_\mu^\dagger(x+\hat{\nu})U_\nu^\dagger(x)\psi(x) \\
&+\overline{\psi}(x-\hat{\mu}-\hat{\nu})\Gamma U_\mu(x-\hat{\mu}-\hat{\nu})U_\nu(x-\hat{\nu})\psi(x) \\
&-\overline{\psi}(x-\hat{\mu}+\hat{\nu})U_\mu(x-\hat{\mu}+\hat{\nu})U_\nu^\dagger(x)\psi(x)\}
\end{aligned}
$$

If you sum over all x you get the same answer whichever of the four operators you choose.

$$
\sum_x \overline{\psi}\Gamma\overrightarrow{D}_\mu\overrightarrow{D}_\nu = \sum_x(-\overline{\psi}\Gamma\overleftarrow{D}_\mu\overrightarrow{D}_\nu) \tag{G.3}
$$

As shown,

$$
\begin{aligned}
\sum_x \overline{\psi}\Gamma\overrightarrow{D}_\mu\overrightarrow{D}_\nu\psi(x) = \frac{1}{4}\{ &-\sum_x \overline{\psi}(x)\Gamma U_\mu^\dagger(x-\hat{\mu})U_\nu(x-\hat{\mu})\psi(x-\hat{\mu}+\hat{\nu}) \\
&+\sum_x \overline{\psi}(x)\Gamma U_\mu^\dagger(x-\hat{\mu})U_\nu^\dagger(x-\hat{\mu}-\hat{\nu})\psi(x-\hat{\mu}-\hat{\nu}) \\
&+\sum_x \overline{\psi}(x)\Gamma U_\mu(x)U_\nu(x+\hat{\mu})\psi(x+\hat{\mu}+\hat{\nu}) \\
&-\sum_x \overline{\psi}(x)U_\mu(x)U_\nu^\dagger(x+\hat{\mu}-\hat{\nu})\psi(x+\hat{\mu}-\hat{\nu})\}
\end{aligned}
$$

here x is a dummy variable, which we can replace in the first two sums with $x = y+\hat{\mu}$, and in the second two sums with $x = y-\hat{\mu}$, such that

$$\begin{aligned}\sum_x \overline{\psi}\Gamma\overrightarrow{D}_\mu\overrightarrow{D}_\nu\psi(x) = \frac{1}{4}\{ &- \sum_y \overline{\psi}(y+\hat{\mu})\Gamma U_\mu^\dagger(y)U_\nu(y)\psi(y+\hat{\nu}) \\ &+ \sum_y \overline{\psi}(y+\hat{\mu})\Gamma U_\mu^\dagger(y)U_\nu^\dagger(y-\hat{\nu})\psi(y-\hat{\nu}) \\ &+ \sum_y \overline{\psi}(y-\hat{\mu})\Gamma U_\mu(y-\hat{\mu})U_\nu(y)\psi(y+\hat{\nu}) \\ &- \sum_x \overline{\psi}(y-\hat{\mu})U_\mu(y-\hat{\mu})U_\nu^\dagger(y-\hat{\nu})\psi(y-\hat{\nu})\} \\ = \sum_y(-\overline{\psi}\Gamma\overleftarrow{D}_\mu\overrightarrow{D}_\nu)\end{aligned}$$

This same proof works between any pair of operators, and so

$$\begin{aligned}\overleftrightarrow{D}_\mu\overleftrightarrow{D}_\nu &= \left(\overrightarrow{D}_\mu - \overleftarrow{D}_\mu\right)\left(\overrightarrow{D}_\nu - \overleftarrow{D}_\nu\right) \\ &= \left(\overrightarrow{D}_\mu\overrightarrow{D}_\nu - \overrightarrow{D}_\mu\overleftarrow{D}_\nu - \overleftarrow{D}_\mu\overrightarrow{D}_\nu + \overleftarrow{D}_\mu\overleftarrow{D}_\nu\right)\end{aligned}$$

reduces to

$$\begin{aligned}\overleftrightarrow{D}_\mu\overleftrightarrow{D}_\nu = \{ &- \overline{\psi}(x)\Gamma U_\mu^\dagger(x-\hat{\mu})U_\nu(x-\hat{\mu})\psi(x-\hat{\mu}+\hat{\nu}) \\ &+ \overline{\psi}(x)\Gamma U_\mu^\dagger(x-\hat{\mu})U_\nu^\dagger(x-\hat{\mu}-\hat{\nu})\psi(x-\hat{\mu}-\hat{\nu}) \\ &+ \overline{\psi}(x)\Gamma U_\mu(x)U_\nu(x+\hat{\mu})\psi(x+\hat{\mu}+\hat{\nu}) \\ &- \overline{\psi}(x)U_\mu(x)U_\nu^\dagger(x+\hat{\mu}-\hat{\nu})\psi(x+\hat{\mu}-\hat{\nu})\}\end{aligned} \tag{G.4}$$

Bibliography

[1] J. M. Bickerton, R. Horsley, Y. Nakamura, H. Perlt, D. Pleiter, P. E. L. Rakow, G. Schierholz, H. Stüben, R. D. Young, and J. M. Zanotti, "Patterns of flavor symmetry breaking in hadron matrix elements involving u , d , and s quarks", Phys. Rev. **D100**, 114516 (2019), arXiv:1909.02521 [hep-lat].

[2] S. Chatrchyan et al. (CMS), "Observation of a New Boson at a Mass of 125 GeV with the CMS Experiment at the LHC", Phys. Lett. B **716**, 30 (2012), arXiv:1207.7235 [hep-ex].

[3] G. Aad et al. (ATLAS), "Observation of a new particle in the search for the Standard Model Higgs boson with the ATLAS detector at the LHC", Phys. Lett. B **716**, 1 (2012), arXiv:1207.7214 [hep-ex].

[4] *Standard Model*, https://en.wikipedia.org/wiki/Standard_Model (Wikimedia Foundation, 2020 (accessed June 19, 2020)).

[5] K. Olive, "Review of Particle Physics", Chinese Physics C **38**, 090001 (2014).

[6] M. Rosenbluth, "High Energy Elastic Scattering of Electrons on Protons", Phys. Rev. **79**, 615 (1950).

[7] R. Hofstadter and R. McAllister, "Electron Scattering From the Proton", Phys. Rev. **98**, 217 (1955).

[8] M. Yearian and R. Hofstadter, "Magnetic Form Factor of the Neutron", Phys. Rev. **110**, 552 (1958).

[9] J. Arrington, C. Roberts, and J. Zanotti, "Nucleon electromagnetic form-factors", J. Phys. G **34**, S23 (2007), arXiv:nucl-th/0611050.

[10] J. Bernauer et al. (A1), "High-precision determination of the electric and magnetic form factors of the proton", Phys. Rev. Lett. **105**, 242001 (2010), arXiv:1007.5076 [nucl-ex].

[11] X. Zhan et al., "High-Precision Measurement of the Proton Elastic Form Factor Ratio $\mu_p G_E/G_M$ at low Q^2", Phys. Lett. B **705**, 59 (2011), arXiv:1102.0318 [nucl-ex].

[12] G. Ron et al. (Jefferson Lab Hall A), "Low Q^2 measurements of the proton form factor ratio $mu_p G_E/G_M$", Phys. Rev. C **84**, 055204 (2011), arXiv:1103.5784 [nucl-ex].

[13] M. Jones et al. (Jefferson Lab Hall A), "G(E(p)) / G(M(p)) ratio by polarization transfer in polarized e p —¿ e polarized p", Phys. Rev. Lett. **84**, 1398 (2000), arXiv:nucl-ex/9910005.

[14] C. Alexandrou, G. Koutsou, T. Leontiou, J. W. Negele, and A. Tsapalis, "Axial Nucleon and Nucleon to Delta form factors and the Goldberger-Treiman Relations from Lattice QCD", Phys. Rev. D **76**, [Erratum: Phys.Rev.D 80, 099901 (2009)], 094511 (2007), arXiv:0706.3011 [hep-lat].

[15] C. Alexandrou, G. Koutsou, J. W. Negele, and A. Tsapalis, "The Nucleon electromagnetic form factors from Lattice QCD", Phys. Rev. D **74**, 034508 (2006), arXiv:hep-lat/0605017.

[16] P. E. Shanahan, A. W. Thomas, R. D. Young, J. M. Zanotti, R. Horsley, Y. Nakamura, D. Pleiter, P. E. L. Rakow, G. Schierholz, and H. Stüben (CSSM, QCDSF/UKQCD), "Magnetic form factors of the octet baryons from lattice QCD and chiral extrapolation", Phys. Rev. **D89**, 074511 (2014), arXiv:1401.5862 [hep-lat].

[17] P. E. Shanahan, A. W. Thomas, R. D. Young, J. M. Zanotti, R. Horsley, Y. Nakamura, D. Pleiter, P. E. L. Rakow, G. Schierholz, and H. Stüben, "Electric form factors of the octet baryons from lattice QCD and chiral extrapolation", Phys. Rev. **D90**, 034502 (2014), arXiv:1403.1965 [hep-lat].

[18] H.-W. Lin, S. D. Cohen, R. G. Edwards, K. Orginos, and D. G. Richards, "Lattice Calculations of Nucleon Electromagnetic Form Factors at Large Momentum Transfer", (2010), arXiv:1005.0799 [hep-lat].

[19] H.-W. Lin, S. D. Cohen, R. G. Edwards, and D. G. Richards, "First Lattice Study of the N - P(11)(1440) Transition Form Factors", Phys. Rev. D **78**, 114508 (2008), arXiv:0803.3020 [hep-lat].

[20] M. Gockeler, T. Hemmert, R. Horsley, D. Pleiter, P. E. Rakow, A. Schafer, and G. Schierholz (QCDSF), "Nucleon electromagnetic form-factors on the lattice and in chiral effective field theory", Phys. Rev. D **71**, 034508 (2005), arXiv:hep-lat/0303019.

[21] P. Hagler et al. (LHPC), "Nucleon Generalized Parton Distributions from Full Lattice QCD", Phys. Rev. D **77**, 094502 (2008), arXiv:0705.4295 [hep-lat].

[22] H.-W. Lin, T. Blum, S. Ohta, S. Sasaki, and T. Yamazaki, "Nucleon structure with two flavors of dynamical domain-wall fermions", Phys. Rev. D **78**, 014505 (2008), arXiv:0802.0863 [hep-lat].

[23] K. Liu, S. Dong, T. Draper, and W. Wilcox, "Pi N N and pseudoscalar form-factors from lattice QCD", Phys. Rev. Lett. **74**, 2172 (1995), arXiv:hep-lat/9406007.

[24] S. Sasaki and T. Yamazaki, "Nucleon form factors from quenched lattice QCD with domain wall fermions", Phys. Rev. D **78**, 014510 (2008), arXiv:0709.3150 [hep-lat].

[25] P. Hagler, "Hadron structure from lattice quantum chromodynamics", Phys. Rept. **490**, 49 (2010), arXiv:0912.5483 [hep-lat].

[26] S. Boinepalli, D. Leinweber, A. Williams, J. Zanotti, and J. Zhang, "Precision electromagnetic structure of octet baryons in the chiral regime", Phys. Rev. D **74**, 093005 (2006), arXiv:hep-lat/0604022.

[27] T. Yamazaki, Y. Aoki, T. Blum, H.-W. Lin, S. Ohta, S. Sasaki, R. Tweedie, and J. Zanotti, "Nucleon form factors with 2+1 flavor dynamical domain-wall fermions", Phys. Rev. D **79**, 114505 (2009), arXiv:0904.2039 [hep-lat].

[28] S. Collins et al., "Dirac and Pauli form factors from lattice QCD", Phys. Rev. **D84**, 074507 (2011), arXiv:1106.3580 [hep-lat].

[29] H.-W. Lin and K. Orginos, "Strange Baryon Electromagnetic Form Factors and SU(3) Flavor Symmetry Breaking", Phys. Rev. D **79**, 074507 (2009), arXiv:0812.4456 [hep-lat].

[30] P. Wang, D. Leinweber, A. Thomas, and R. Young, "Chiral extrapolation of octet-baryon charge radii", Phys. Rev. D **79**, 094001 (2009), arXiv:0810.1021 [hep-ph].

[31] D. Diakonov, V. Petrov, P. Pobylitsa, M. V. Polyakov, and C. Weiss, "Nucleon parton distributions at low normalization point in the large N(c) limit", Nucl. Phys. B **480**, 341 (1996), arXiv:hep-ph/9606314.

[32] A. W. Schreiber, P. J. Mulders, A. Signal, and A. W. Thomas, "The Pion cloud of the nucleon and its effect on deep inelastic structure", Phys. Rev. D **45**, 3069 (1992).

[33] L. P. Gamberg, G. R. Goldstein, and K. A. Oganessyan, "Novel transversity properties in semiinclusive deep inelastic scattering", Phys. Rev. D **67**, 071504 (2003), arXiv:hep-ph/0301018.

[34] I. Cloet, W. Bentz, and A. W. Thomas, "Nucleon quark distributions in a covariant quark-diquark model", Phys. Lett. B **621**, 246 (2005), arXiv:hep-ph/0504229.

[35] I. Cloet, W. Bentz, and A. W. Thomas, "Transversity quark distributions in a covariant quark-diquark model", Phys. Lett. B **659**, 214 (2008), arXiv:0708.3246 [hep-ph].

[36] A. Bacchetta, F. Conti, and M. Radici, "Transverse-momentum distributions in a diquark spectator model", Phys. Rev. D **78**, 074010 (2008), arXiv:0807.0323 [hep-ph].

[37] C. Lorce, B. Pasquini, and M. Vanderhaeghen, "Unified framework for generalized and transverse-momentum dependent parton distributions within a 3Q light-cone picture of the nucleon", JHEP **05**, 041 (2011), arXiv:1102.4704 [hep-ph].

[38] H.-L. Lai, M. Guzzi, J. Huston, Z. Li, P. M. Nadolsky, J. Pumplin, and C.-P. Yuan, "New parton distributions for collider physics", Phys. Rev. D **82**, 074024 (2010), arXiv:1007.2241 [hep-ph].

[39] C. Adloff et al. (H1), "Measurement and QCD analysis of neutral and charged current cross-sections at HERA", Eur. Phys. J. C **30**, 1 (2003), arXiv:hep-ex/0304003.

[40] R. D. Ball, L. Del Debbio, S. Forte, A. Guffanti, J. I. Latorre, A. Piccione, J. Rojo, and M. Ubiali (NNPDF), "A Determination of parton distributions with faithful uncertainty estimation", Nucl. Phys. B **809**, [Erratum: Nucl.Phys.B 816, 293 (2009)], 1 (2009), arXiv:0808.1231 [hep-ph].

[41] A. Martin, W. Stirling, R. Thorne, and G. Watt, "Update of parton distributions at NNLO", Phys. Lett. B **652**, 292 (2007), arXiv:0706.0459 [hep-ph].

[42] J. Ashman et al. (European Muon), "An Investigation of the Spin Structure of the Proton in Deep Inelastic Scattering of Polarized Muons on Polarized Protons", Nucl. Phys. B **328**, edited by V. Hughes and C. Cavata, 1 (1989).

[43] K. G. Wilson, "Nonlagrangian models of current algebra", Phys. Rev. **179**, 1499 (1969).

[44] R. Jaffe, "g_2-The Nucleon's Other Spin-Dependent Structure Function", Comments Nucl. Part. Phys. **19**, 239 (1990).

[45] S. Wandzura and F. Wilczek, "Sum Rules for Spin Dependent Electroproduction: Test of Relativistic Constituent Quarks", Phys. Lett. B **72**, 195 (1977).

[46] K. G. Wilson, "Confinement of Quarks", edited by J. Taylor, 45 (1974).

[47] S. Syritsyn, "Review of Hadron Structure Calculations on a Lattice", PoS **LATTICE2013**, 009 (2014), arXiv:1403.4686 [hep-lat].

[48] M. Constantinou, "Hadron Structure", PoS **LATTICE2014**, 001 (2015), arXiv:1411.0078 [hep-lat].

[49] C. Alexandrou, "Hadron Structure in Lattice QCD", Prog. Part. Nucl. Phys. **67**, edited by A. Faessler and V. Rodin, 101 (2012), arXiv:1111.5960 [hep-lat].

[50] H.-W. Lin, "Review of Baryon Spectroscopy in Lattice QCD", Chin. J. Phys. **49**, 827 (2011), arXiv:1106.1608 [hep-lat].

[51] Z. Fodor and C. Hoelbling, "Light Hadron Masses from Lattice QCD", Rev. Mod. Phys. **84**, 449 (2012), arXiv:1203.4789 [hep-lat].

[52] D. Trewartha, W. Kamleh, D. Leinweber, and D. S. Roberts, "Quark Propagation in the Instantons of Lattice QCD", Phys. Rev. D **88**, 034501 (2013), arXiv:1306.3283 [hep-lat].

[53] D. Trewartha, W. Kamleh, and D. Leinweber, "Evidence that centre vortices underpin dynamical chiral symmetry breaking in SU(3) gauge theory", Phys. Lett. B **747**, 373 (2015), arXiv:1502.06753 [hep-lat].

[54] D. Trewartha, W. Kamleh, and D. Leinweber, "Centre vortex removal restores chiral symmetry", J. Phys. G **44**, 125002 (2017), arXiv:1708.06789 [hep-lat].

[55] H.-T. Ding, F. Karsch, and S. Mukherjee, "Thermodynamics of strong-interaction matter from Lattice QCD", Int. J. Mod. Phys. E **24**, 1530007 (2015), arXiv:1504.05274 [hep-lat].

[56] P. de Forcrand, J. Langelage, O. Philipsen, and W. Unger, "Lattice QCD Phase Diagram In and Away from the Strong Coupling Limit", Phys. Rev. Lett. **113**, 152002 (2014), arXiv:1406.4397 [hep-lat].

[57] C. S. Fischer, J. Luecker, and C. A. Welzbacher, "Phase structure of three and four flavor QCD", Phys. Rev. D **90**, 034022 (2014), arXiv:1405.4762 [hep-ph].

[58] R. Feynman, "Space-time approach to nonrelativistic quantum mechanics", Rev. Mod. Phys. **20**, 367 (1948).

[59] J. Smit, *Introduction to quantum fields on a lattice: A robust mate*, Vol. 15 (Cambridge University Press, Jan. 2011).

[60] C. Gattringer and C. B. Lang, *Quantum chromodynamics on the lattice*, Vol. 788 (Springer, Berlin, 2010).

[61] R. Gupta, "Introduction to lattice QCD: Course", in Les Houches Summer School in Theoretical Physics, Session 68: Probing the Standard Model of Particle Interactions (July 1997), pp. 83–219, arXiv:hep-lat/9807028.

[62] H. Rothe, *Lattice gauge theories: An Introduction*, Vol. 43 (1992).

[63] M. Luscher and P. Weisz, "On-Shell Improved Lattice Gauge Theories", Commun. Math. Phys. **97**, [Erratum: Commun.Math.Phys. 98, 433 (1985)], 59 (1985).

[64] S. Itoh, Y. Iwasaki, Y. Oyanagi, and T. Yoshie, "Renormalization Group Improved Lattice SU(3) Gauge Action and Hadron Spectrum in Quenched QCD on a 8**3 X 16 Lattice", Phys. Lett. B **148**, 153 (1984).

[65] *New Phenomena in Subnuclear Physics: Proceedings, International School of Subnuclear Physics, Erice, Sicily, Jul 11-Aug 1 1975. Part A*, Vol. 13 (Plenum, New York, USA, 1977).

[66] *New Phenomena in Subnuclear Physics. Part b. Proceedings, Second Half of the 1975 International School of Subnuclear Physics, Erice, Sicily, Jul 11-Aug 1 1975* (Jan. 1977).

[67] K. Symanzik, "Continuum Limit and Improved Action in Lattice Theories. 1. Principles and phi**4 Theory", Nucl. Phys. B **226**, 187 (1983).

[68] B. Sheikholeslami and R. Wohlert, "Improved Continuum Limit Lattice Action for QCD with Wilson Fermions", Nucl. Phys. B **259**, 572 (1985).

[69] H. W. Hamber and C. M. Wu, "Some Predictions for an Improved Fermion Action on the Lattice", Phys. Lett. B **133**, 351 (1983).

[70] M. G. Alford, T. Klassen, and G. Lepage, "Improving lattice quark actions", Nucl. Phys. B **496**, 377 (1997), arXiv:hep-lat/9611010.

[71] N. Cundy et al., "Non-perturbative improvement of stout-smeared three flavour clover fermions", Phys. Rev. D **79**, 094507 (2009), arXiv:0901.3302 [hep-lat].

[72] T. Harr, "Optimisations to Hybrid Monte Carlo for Lattice QCD", PhD thesis (University of Adelaide, 2019), eprint: http://hdl.handle.net/2440/119919.

[73] J. Dragos, "Improved Determination of Hadron Matrix Elements using the Variational Method", PhD thesis (University of Adelaide, 2016), eprint: http://hdl.handle.net/2440/106302.

[74] K. U. Can, A. Kusno, E. V. Mastropas, and J. M. Zanotti, "Hadron Structure on the Lattice", in Lecture series, University of Washington, Seattle, USA (2012).

[75] W. Bietenholz et al., "Flavour blindness and patterns of flavour symmetry breaking in lattice simulations of up, down and strange quarks", Phys. Rev. **D84**, 054509 (2011), arXiv:1102.5300 [hep-lat].

[76] R. Sommer, "Scale setting in lattice QCD", PoS **LATTICE2013**, 015 (2014), arXiv:1401.3270 [hep-lat].

[77] R. Horsley, J. Najjar, Y. Nakamura, H. Perlt, D. Pleiter, P. Rakow, G. Schierholz, A. Schiller, H. Stüben, and J. Zanotti (QCDSF-UKQCD), "SU(3) flavour symmetry breaking and charmed states", PoS **LATTICE2013**, 249 (2014), arXiv:1311.5010 [hep-lat].

[78] V. G. Bornyakov et al., "Wilson flow and scale setting from lattice QCD", (2015), arXiv:1508.05916 [hep-lat].

[79] W. Bietenholz et al., "Tuning the strange quark mass in lattice simulations", Phys. Lett. **B690**, 436 (2010), arXiv:1003.1114 [hep-lat].

[80] M. Luscher, "Volume Dependence of the Energy Spectrum in Massive Quantum Field Theories. 1. Stable Particle States", Commun. Math. Phys. **104**, 177 (1986).

[81] G. Martinelli, C. Pittori, C. T. Sachrajda, M. Testa, and A. Vladikas, "A General method for nonperturbative renormalization of lattice operators", Nucl. Phys. B **445**, 81 (1995), arXiv:hep-lat/9411010.

[82] C. Alexandrou, "Hadron deformation and form-factors from lattice QCD", AIP Conf. Proc. **904**, edited by C. N. Papanicolas and A. M. Bernstein, 49 (2007), arXiv:hep-lat/0608025.

[83] D. B. Leinweber, R. Woloshyn, and T. Draper, "Electromagnetic structure of octet baryons", Phys. Rev. D **43**, 1659 (1991).

[84] P. Shanahan, A. Thomas, and R. Young, "Sigma terms from an SU(3) chiral extrapolation", Phys. Rev. D **87**, 074503 (2013), arXiv:1205.5365 [nucl-th].

[85] I. Cloet, D. B. Leinweber, and A. W. Thomas, "Simple quark model with chiral phenomenology", Phys. Rev. C **65**, 062201 (2002), arXiv:hep-ph/0203023.

[86] A. W. Thomas, "Chiral extrapolation of hadronic observables", Nucl. Phys. B Proc. Suppl. **119**, edited by R. Edwards, J. W. Negele, and D. Richards, 50 (2003), arXiv:hep-lat/0208023.

[87] L. L. Foldy, "The Electromagnetic Properties of Dirac Particles", Phys. Rev. **87**, 688 (1952).

[88] M. Diehl and P. Kroll, "Nucleon form factors, generalized parton distributions and quark angular momentum", Eur. Phys. J. C **73**, 2397 (2013), arXiv:1302.4604 [hep-ph].

[89] B. J. Owen, W. Kamleh, D. B. Leinweber, M. S. Mahbub, and B. J. Menadue, "Transition of $\rho \to \pi\gamma$ in lattice QCD", Phys. Rev. D **92**, 034513 (2015), arXiv:1505.02876 [hep-lat].

[90] J. M. M. Hall, W. Kamleh, D. B. Leinweber, B. J. Menadue, B. J. Owen, A. W. Thomas, and R. D. Young, "Lattice QCD Evidence that the $\Lambda(1405)$ Resonance is an Antikaon-Nucleon Molecule", Phys. Rev. Lett. **114**, 132002 (2015), arXiv:1411.3402 [hep-lat].

[91] B. Owen, W. Kamleh, D. Leinweber, B. Menadue, and S. Mahbub, "Light Meson Form Factors at near Physical Masses", Phys. Rev. D **91**, 074503 (2015), arXiv:1501.02561 [hep-lat].

[92] B. J. Owen, J. Dragos, W. Kamleh, D. B. Leinweber, M. Mahbub, B. J. Menadue, and J. M. Zanotti, "Variational Approach to the Calculation of gA", Phys. Lett. B **723**, 217 (2013), arXiv:1212.4668 [hep-lat].

[93] J. Bulava, M. Donnellan, and R. Sommer, "On the computation of hadron-to-hadron transition matrix elements in lattice QCD", JHEP **01**, 140 (2012), arXiv:1108.3774 [hep-lat].

[94] B. Yoon et al., "Controlling Excited-State Contamination in Nucleon Matrix Elements", Phys. Rev. D **93**, 114506 (2016), arXiv:1602.07737 [hep-lat].

[95] D. S. Roberts, W. Kamleh, and D. B. Leinweber, "Nucleon Excited State Wave Functions from Lattice QCD", Phys. Rev. D **89**, 074501 (2014), arXiv:1311.6626 [hep-lat].

[96] C. Aubin and K. Orginos, "A new approach for Delta form factors", AIP Conf. Proc. **1374**, edited by D. Armstrong, V. Burkert, J.-P. Chen, W. Detmold, J. Dudek, W. Melnitchouk, and D. Richards, 621 (2011), arXiv:1010.0202 [hep-lat].

[97] J. Green, J. Negele, A. Pochinsky, S. Syritsyn, M. Engelhardt, and S. Krieg, "Nucleon electromagnetic form factors from lattice QCD using a nearly physical pion mass", Phys. Rev. D **90**, 074507 (2014), arXiv:1404.4029 [hep-lat].

[98] R. W. Schiel, "Expanding the Interpolator Basis in the Variational Method to Explicitly Account for Backward Running States", Phys. Rev. D **92**, 034512 (2015), arXiv:1503.02588 [hep-lat].

[99] M. Gockeler, P. Hagler, R. Horsley, D. Pleiter, P. E. L. Rakow, A. Schafer, G. Schierholz, and J. M. Zanotti (QCDSF, UKQCD), "Quark helicity flip generalized parton distributions from two-flavor lattice QCD", Phys. Lett. **B627**, 113 (2005), arXiv:hep-lat/0507001 [hep-lat].

[100] M. Constantinou, R. Horsley, H. Panagopoulos, H. Perlt, P. E. L. Rakow, G. Schierholz, A. Schiller, and J. M. Zanotti, "Renormalization of local quark-bilinear operators for N_f=3 flavors of stout link nonperturbative clover fermions", Phys. Rev. **D91**, 014502 (2015), arXiv:1408.6047 [hep-lat].

[101] G. Martinelli, C. Pittori, C. Sachrajda, M. Testa, and A. Vladikas, "A general method for non-perturbative renormalization of lattice operators", Nuclear Physics B **445**, 81 (1995), arXiv:hep-lat/9411010 [hep-lat].

[102] M. Göckeler, R. Horsley, Y. Nakamura, H. Perlt, D. Pleiter, P. E. L. Rakow, A. Schäfer, G. Schierholz, A. Schiller, H. Stüben, and et al., "Perturbative and nonperturbative renormalization in lattice qcd", Physical Review D **82** (2010), arXiv:1003.5756 [hep-lat].

[103] M. Constantinou, M. Costa, M. Gockeler, R. Horsley, H. Panagopoulos, H. Perlt, P. E. L. Rakow, G. Schierholz, and A. Schiller, *Perturbatively improving ri-mom renormalization constants*, 2013, arXiv:1303.6776 [hep-lat].

[104] M. Gockeler et al., "Perturbative and Nonperturbative Renormalization in Lattice QCD", Phys. Rev. D **82**, [Erratum: Phys.Rev.D 86, 099903 (2012)], 114511 (2010), arXiv:1003.5756 [hep-lat].

[105] A. I. Alekseev, "Strong coupling constant to four loops in the analytic approach to qcd", Few-Body Systems **-1**, 1 (2003), arXiv:hep-ph/0211339 [hep-ph].

[106] J. Gracey, "Three loop anomalous dimension of non-singlet quark currents in the ri' scheme", Nuclear Physics B **662**, 247 (2003), arXiv:hep-ph/0304113 [hep-ph].

[107] T. van Ritbergen, J. Vermaseren, and S. Larin, "The four-loop beta-function in quantum chromodynamics", Physics Letters B **400**, 379 (1997), arXiv:hep-ph/9701390 [hep-ph].

[108] K. Chetyrkin and A. Rétey, "Renormalization and running of quark mass and field in the regularization invariant and schemes at three and four loops", Nuclear Physics B **583**, 3 (2000), arXiv:hep-ph/9910332 [hep-ph].

[109] K. Chetyrkin, "Quark mass anomalous dimension to o (as4)", Physics Letters B **404**, 161 (1997), arXiv:hep-ph/9703278 [hep-ph].

[110] J. Vermaseren, S. Larin, and T. van Ritbergen, "The 4-loop quark mass anomalous dimension and the invariant quark mass", Physics Letters B **405**, 327 (1997), arXiv:hep-ph/9703284 [hep-ph].

[111] J. Gracey, "Three loop tensor current anomalous dimension in qcd", Physics Letters B **488**, 175 (2000), arXiv:hep-ph/0007171 [hep-ph].

[112] R. Horsley, J. Najjar, Y. Nakamura, H. Perlt, D. Pleiter, P. E. L. Rakow, G. Schierholz, A. Schiller, H. Stüben, and J. M. Zanotti, *Su(3) flavour symmetry breaking and charmed states*, 2013, arXiv:1311.5010 [hep-lat].

[113] C. Sachrajda and G. Villadoro, "Twisted boundary conditions in lattice simulations", Physics Letters B **609**, 73 (2005), arXiv:hep-lat/0411033 [hep-lat].

[114] R. Horsley et al., "Isospin splittings of meson and baryon masses from three-flavor lattice QCD + QED", J. Phys. **G43**, 10LT02 (2016), arXiv:1508.06401 [hep-lat].

[115] R. Horsley et al., "QED effects in the pseudoscalar meson sector", JHEP **04**, 093 (2016), arXiv:1509.00799 [hep-lat].

[116] R. Horsley et al. (CSSM, QCDSF, UKQCD), "Isospin splittings in the decuplet baryon spectrum from dynamical QCD+QED", (2019), arXiv:1904.02304 [hep-lat].

[117] T. Bhattacharya, R. Gupta, W. Lee, S. R. Sharpe, and J. M. S. Wu, "Improved bilinears in lattice QCD with non-degenerate quarks", Phys. Rev. **D73**, 034504 (2006), arXiv:hep-lat/0511014 [hep-lat].

[118] A. Gerardin, T. Harris, and H. B. Meyer, "Nonperturbative renormalization and $O(a)$-improvement of the nonsinglet vector current with $N_f = 2 + 1$ Wilson fermions and tree-level Symanzik improved gauge action", Phys. Rev. **D99**, 014519 (2019), arXiv:1811.08209 [hep-lat].

[119] T. Bakeyev, M. Gockeler, R. Horsley, D. Pleiter, P. E. L. Rakow, G. Schierholz, and H. Stuben (QCDSF-UKQCD), "Nonperturbative renormalization and improvement of the local vector current for quenched and unquenched Wilson fermions", Phys. Lett. **B580**, 197 (2004), arXiv:hep-lat/0305014 [hep-lat].

[120] N. Cundy et al. (QCDSF-UKQCD), "Clover improvement for stout-smeared 2+1 flavour SLiNC fermions: Non-perturbative results", PoS **LATTICE2008**, 132 (2008), arXiv:0811.2355 [hep-lat].

[121] R. Horsley, J. Najjar, Y. Nakamura, H. Perlt, D. Pleiter, P. E. L. Rakow, G. Schierholz, A. Schiller, H. Stüben, and J. M. Zanotti, "Lattice determination of Sigma-Lambda mixing", Phys. Rev. **D91**, 074512 (2015), arXiv:1411.7665 [hep-lat].

[122] T. Bhattacharya, R. Gupta, W. Lee, S. R. Sharpe, and J. M. S. Wu, "Improved bilinears in lattice qcd with nondegenerate quarks", Physical Review D **73** (2006), arXiv:hep-lat/0511014.

[123] K. Goeke, M. V. Polyakov, and M. Vanderhaeghen, "Hard exclusive reactions and the structure of hadrons", Prog. Part. Nucl. Phys. **47**, 401 (2001), arXiv:hep-ph/0106012.

[124] M. Diehl, "Generalized parton distributions", PhD thesis (2003), arXiv:hep-ph/0307382.

[125] A. Belitsky and A. Radyushkin, "Unraveling hadron structure with generalized parton distributions", Phys. Rept. **418**, 1 (2005), arXiv:hep-ph/0504030.

[126] R. Jaffe and X.-D. Ji, "Chiral odd parton distributions and polarized Drell-Yan", Phys. Rev. Lett. **67**, 552 (1991).

[127] J. C. Collins, L. Frankfurt, and M. Strikman, "Factorization for hard exclusive electroproduction of mesons in QCD", Phys. Rev. D **56**, 2982 (1997), arXiv:hep-ph/9611433.

[128] P. Hoodbhoy and X.-D. Ji, "Helicity flip off forward parton distributions of the nucleon", Phys. Rev. D **58**, 054006 (1998), arXiv:hep-ph/9801369.

[129] M. Diehl, "Generalized parton distributions with helicity flip", Eur. Phys. J. C **19**, 485 (2001), arXiv:hep-ph/0101335.

[130] D. Boer and P. Mulders, "Time reversal odd distribution functions in leptoproduction", Phys. Rev. D **57**, 5780 (1998), arXiv:hep-ph/9711485.

[131] D. W. Sivers, "Single Spin Production Asymmetries from the Hard Scattering of Point-Like Constituents", Phys. Rev. D **41**, 83 (1990).

[132] M. Diehl and P. Hagler, "Spin densities in the transverse plane and generalized transversity distributions", Eur. Phys. J. **C44**, 87 (2005), arXiv:hep-ph/0504175 [hep-ph].

[133] M. Burkardt, "Chromodynamic lensing and transverse single spin asymmetries", Nucl. Phys. A **735**, 185 (2004), arXiv:hep-ph/0302144.

[134] M. Burkardt, "Transverse deformation of parton distributions and transversity decomposition of angular momentum", Phys. Rev. D **72**, 094020 (2005), arXiv:hep-ph/0505189.

[135] M. Göckeler, P. Hägler, R. Horsley, Y. Nakamura, D. Pleiter, P. E. L. Rakow, A. Schäfer, G. Schierholz, H. Stüben, and J. M. Zanotti (QCDSF, UKQCD), "Transverse spin structure of the nucleon from lattice QCD simulations", Phys. Rev. Lett. **98**, 222001 (2007), arXiv:hep-lat/0612032 [hep-lat].

[136] M. Diehl, "Generalized parton distributions in impact parameter space", Eur. Phys. J. C **25**, [Erratum: Eur.Phys.J.C 31, 277–278 (2003)], 223 (2002), arXiv:hep-ph/0205208.

[137] L. P. Gamberg, G. R. Goldstein, and M. Schlegel, "Transverse Quark Spin Effects and the Flavor Dependence of the Boer-Mulders Function", Phys. Rev. D **77**, 094016 (2008), arXiv:0708.0324 [hep-ph].

[138] R. L. Jaffe, "Spin, twist and hadron structure in deep inelastic processes", in Ettore Majorana International School of Nucleon Structure: 1st Course: The Spin Structure of the Nucleon (Jan. 1996), pp. 42–129, arXiv:hep-ph/9602236.

[139] M. Burkardt, "Transverse force on quarks in deep-inelastic scattering", Phys. Rev. D **88**, 114502 (2013), arXiv:0810.3589 [hep-ph].

[140] B. Filippone and X.-D. Ji, "The Spin structure of the nucleon", Adv. Nucl. Phys. **26**, 1 (2001), arXiv:hep-ph/0101224.

[141] M. Gockeler, R. Horsley, W. Kurzinger, H. Oelrich, D. Pleiter, P. E. Rakow, A. Schafer, and G. Schierholz, "A Lattice calculation of the nucleon's spin dependent structure function g(2) revisited", Phys. Rev. D **63**, 074506 (2001), arXiv:hep-lat/0011091.

[142] M. Gockeler, R. Horsley, D. Pleiter, P. E. Rakow, A. Schafer, G. Schierholz, H. Stuben, and J. Zanotti, "Investigation of the second moment of the nucleon's g(1) and g(2) structure functions in two-flavor lattice QCD", Phys. Rev. D **72**, 054507 (2005), arXiv:hep-lat/0506017.

[143] R. Jaffe and X.-D. Ji, "Studies of the Transverse Spin Dependent Structure Function $g(2)$ (X, Q^2)", Phys. Rev. D **43**, 724 (1991).

[144] J. Blumlein and N. Kochelev, "On the twist -2 and twist - three contributions to the spin dependent electroweak structure functions", Nucl. Phys. B **498**, 285 (1997), arXiv:hep-ph/9612318.

[145] M. Gockeler, R. Horsley, H. Oelrich, H. Perlt, D. Petters, P. E. Rakow, A. Schafer, G. Schierholz, and A. Schiller, "Nonperturbative renormalization of composite operators in lattice QCD", Nucl. Phys. B **544**, 699 (1999), arXiv:hep-lat/9807044.

[146] M. Baake, B. Gemunden, and R. Odingen, "On the Relations Between Irreducible Representations of the Hyperoctahedral Group and O(4) and SO(4)", J. Math. Phys. **24**, 1021 (1983).

[147] J. E. Mandula, G. Zweig, and J. Govaerts, "Representations of the Rotation Reflection Symmetry Group of the Four-dimensional Cubic Lattice", Nucl. Phys. B **228**, 91 (1983).

[148] H. Pearlt, Private Communication, (August, 2018).

[149] E. V. Shuryak and A. Vainshtein, "Theory of Power Corrections to Deep Inelastic Scattering in Quantum Chromodynamics. 2. Q**4 Effects: Polarized Target", Nucl. Phys. B **201**, 141 (1982).

[150] S. Meissner, A. Metz, and M. Schlegel, "Generalized parton correlation functions for a spin-1/2 hadron", JHEP **08**, 056 (2009), arXiv:0906.5323 [hep-ph].

[151] M. Burkardt, F. P. Aslan, and M. Schlegel, "in preparation", (2020).

[152] F. P. Aslan, M. Burkardt, and M. Schlegel, "Transverse Force Imaging", in Probing Nucleons and Nuclei in High Energy Collisions: Dedicated to the Physics of the Electron Ion Collider (2020), pp. 186–189, arXiv:2001.05978 [hep-ph].

[153] D. W. Sivers, "Hard scattering scaling laws for single spin production asymmetries", Phys. Rev. D **43**, 261 (1991).

[154] M. Burkardt, "Impact parameter dependent parton distributions and off forward parton distributions for zeta —¿ 0", Phys. Rev. D **62**, [Erratum: Phys.Rev.D 66, 119903 (2002)], 071503 (2000), arXiv:hep-ph/0005108.

[155] F. P. Aslan, M. Burkardt, and M. Schlegel, "Transverse Force Tomography", Phys. Rev. D **100**, 096021 (2019), arXiv:1904.03494 [hep-ph].

[156] R. Young, Private Communication, (July, 2020).